

# A Data-Analysis and Sensitivity-Optimization Framework for the KATRIN Experiment

Zur Erlangung des akademischen Grades eines  
**Doktors der Naturwissenschaften**  
von der Fakultät für Physik  
des Karlsruher Instituts für Technologie  
genehmigte  
**Dissertation**

von

**Dipl.-Phys. Marco Kleesiek**

geb. Haag  
aus Heidelberg

Referent: Prof. Dr. Guido Drexlin  
Institut für Experimentelle Kernphysik, KIT  
Korreferent: Prof. Dr. Michael Feindt  
Institut für Experimentelle Kernphysik, KIT

Tag der mündlichen Prüfung: 14.07.2014



## Abstract

Presently under construction at the Karlsruhe Institute of Technology (KIT) in Germany, the Karlsruhe TRitium Neutrino (KATRIN) experiment is the next generation tritium  $\beta$ -decay experiment to perform a direct kinematical measurement of the electron neutrino mass with an unprecedented sensitivity of  $200 \text{ meV}/c^2$  at 90 % C.L.

This thesis describes the implementation of a consistent data analysis framework, addressing technical aspects of the data taking process and statistical challenges of a neutrino mass estimation from the  $\beta$ -decay electron spectrum. A new Monte Carlo method is presented, which optimizes the distribution of available measuring time and minimizes statistical uncertainties of involved fit parameters, allowing a reevaluation of the experiment's sensitivity.

## Erklärung der Selbstständigkeit

Hiermit versichere ich, die vorliegende Arbeit selbstständig angefertigt, alle dem Wortlaut oder Sinn nach entnommenen Inhalte anderer Werke an den entsprechenden Stellen unter Angabe der Quelle kenntlich gemacht und keine weiteren Hilfsmittel verwendet zu haben.

## Declaration of Authorship

I hereby assert, that I have written the enclosed thesis autonomously. Wherever contents from other publications are used, they are clearly attributed with their source indicated. No further means or sources were utilized.

Marco Kleesiek

Karlsruhe, 22. September 2014



---

## Introduction

---

Since their postulation in 1930, neutrinos have experienced a tremendous growth in scientific interest. They are by far the most abundant known fermionic matter particles in the universe and thus play a crucial role in cosmological structure formation as Dark Matter candidates. At the same time, neutrinos are the only charge-less fundamental fermions in the Standard Model of elementary particles, solely participating in weak interactions.

Various neutrino oscillation experiments have proven unambiguously, that neutrinos have non-zero masses. This phenomenon cannot be easily explained in the context of the established mass-generating Higgs mechanism of the Standard Model. Due to their intrinsic nature, oscillation experiments can only determine the mass splittings between the three active neutrino generations. Attempts of a direct measurement of the absolute mass scale and deductions from cosmological imprints have merely resulted in upper limits up to date, pointing towards sub-eV neutrino masses.

Even from our currently limited knowledge about neutrino properties, including their surprisingly light masses, it has become clear, that neutrinos stand very much apart from their fermionic partners. Neutrino masses clearly indicate physics beyond the Standard Model, possibly involving lepton number violation, new sources of CP violation, right-handed neutrino states and a new energy scale.

### Motivation

The Karlsruhe TRitium Neutrino (KATRIN) experiment is the next-generation tritium  $\beta$ -decay experiment to perform a direct kinematical and model-independent measurement of the effective electron neutrino mass  $m_{\nu_e}$  with an unprecedented sensitivity of  $m_{\nu_e} = 200 \text{ meV}/c^2$  at 90 % C.L. after five calendar years of data taking. Presently under construction at the Karlsruhe Institute of Technology (KIT) in Germany, KATRIN will use an ultra-luminous windowless gaseous tritium source, a large spectrometer with magnetic adiabatic collimation and electrostatic filtering, and a multi-pixel silicon detector to investigate the  $\beta$ -decay electron spectrum, looking for a minute shape distortion close to the tritium endpoint energy.

KATRIN aims to exceed its predecessor experiments in terms of mass sensitivity by one order of magnitude. Since in  $\beta$ -spectroscopy the squared neutrino mass  $m_{\nu_e}^2$  is the observable, this implies an improvement of the statistical accuracy and of many systematic

uncertainties by at least two orders of magnitude. This ambitious goal puts exceptional technological demands on the stability of experimental parameters, such as the tritium gas density, operating temperatures (from 3 K to room temperature), magnetic field strengths (from  $10^{-4}$  T up to several T) and high voltage potentials. Systematic effects have to be investigated as precisely as possible and must be accurately incorporated into the probabilistic model of the neutrino mass analysis.

With regard to the mass sensitivity, a series of yet unanswered statistical questions has to be addressed. The performance of the experiment significantly depends on the distribution of measuring time among different regions of the  $\beta$ -decay spectrum. An optimization of the measuring strategy can only be attempted however, if the statistical model is extended to incorporate various scenarios of systematic effects and backgrounds. Also, the possibility of detecting a sterile neutrino mass state will be of specific interest in this context.

Access and evaluation of recorded KATRIN data itself poses a challenge, but not due to the plain amount of data, which will be moderate in comparison to event-driven collider experiments like CMS or ATLAS. It is rather because of the huge number of diverse precision sensors and detectors distributed around the experimental apparatus, with literally thousands of variables being recorded continuously. Most of these data must be processed, calibrated and correctly related, before they can be reliably utilized in further analysis or as input to corresponding simulations.

### Objectives of this Thesis

With respect to these challenges, faced by the KATRIN data analysis chain in view of the upcoming neutrino mass measurements, the following objectives were set for the present doctoral thesis:

- A data processing and analysis framework should be implemented, providing analysts in the collaboration with a logical and uniform interface to various types of detector, sensor and calibration data. The system should on one hand incorporate existing analysis and simulation codes, and on the other hand provide a robust and extensible foundation for future tools.
- Strategies for the improvement of KATRIN's neutrino mass sensitivity should be explored, for instance through an optimization of the measurement time distribution. The probabilistic model, required for a neutrino mass inference from the observed data, should be revised and extended to incorporate critical systematic effects. It is desired to have the developed statistical methods and models assembled into a reusable toolkit, which integrates seamlessly with the above mentioned data analysis framework.

## Outline

In section 1 a brief introduction to the history of neutrinos, the phenomenology of neutrino flavor oscillations and a comparison of promising approaches for the determination of their absolute mass scale will be given.

KATRIN's working principle and experimental setup is outlined in section 2.

The IT infrastructure, which was implemented in the course of this thesis, is introduced in section 3.

Several data analysis and simulation applications, which are built upon the new software framework and were successfully utilized during recent commissioning measurements, are presented in section 4.

The calculation of  $\beta$ -decay spectra, together with the response of the KATRIN apparatus and incorporation of systematic effects is treated in section 5.

With this prerequisite, a new set of statistical tools, developed in the context of this thesis, is described in the following section 6. The presented methods cover Frequentist and Bayesian approaches of parameter inference, treatment of critical systematics, and are applied to the case of a sterile neutrino analysis. After introducing a new Markov Chain Monte Carlo driven optimization method, an adapted measuring strategy for KATRIN is proposed.

Based on these methods, a reevaluation of the neutrino mass sensitivity is performed in section 7, using background data from the first commissioning measurements of the spectrometer and detector section.

A recapitulation of the implemented work and an outlook on ensuing developments is given in section 8.



---

# Contents

---

<b>Introduction</b>	<b>i</b>
<b>1 Neutrino Physics</b>	<b>1</b>
1.1 Neutrinos in the Standard Model . . . . .	2
1.2 Neutrino Oscillations . . . . .	4
1.3 Massive Neutrinos . . . . .	10
1.4 Single Beta Decay Experiments . . . . .	16
1.5 Sterile Neutrinos . . . . .	21
<b>2 The KATRIN Experiment</b>	<b>25</b>
2.1 Measurement Principle . . . . .	26
2.2 MAC-E Filter Setup . . . . .	27
2.3 Tritium Source . . . . .	29
2.4 Transport Section . . . . .	30
2.5 Spectrometer Section . . . . .	31
2.6 Detector Section . . . . .	33
2.7 Monitoring . . . . .	34
2.8 Instrumentation and Data Producers . . . . .	35
2.9 Recent Commissioning Milestones . . . . .	37
<b>3 Data and Software Infrastructure</b>	<b>39</b>
3.1 Multi-Tier Architecture . . . . .	39
3.2 Source Code Standards and Organization . . . . .	41
3.3 Data Processing and Storage (Tier 1) . . . . .	46
3.4 Data Logic and Services (Tier 2) . . . . .	57
<b>4 Data Access and Analysis</b>	<b>65</b>
4.1 Web Frontends . . . . .	65
4.2 C++ Programming Interface to Data (Tier 3) . . . . .	69
4.3 Fast Analysis Examples . . . . .	77
4.4 Detector Analysis Suite . . . . .	80
4.5 Particle Tracking And Electromagnetic Field Simulation . . . . .	82

<b>5</b>	<b>Beta Spectrum Calculation</b>	<b>85</b>
5.1	Differential Beta Emission Spectrum . . . . .	86
5.2	Final States Distribution . . . . .	88
5.3	Doppler Effect . . . . .	93
5.4	Negative Squared Neutrino Masses . . . . .	93
5.5	Integrated Spectrum . . . . .	94
5.6	Sterile Neutrinos . . . . .	105
5.7	Floating-point Accuracy and Numerical Stability . . . . .	107
5.8	Detector Segmentation . . . . .	109
5.9	Background Models . . . . .	110
5.10	Measurement Simulation . . . . .	113
<b>6</b>	<b>Statistical Methods</b>	<b>117</b>
6.1	Parameter Inference . . . . .	118
6.2	Confidence Intervals . . . . .	126
6.3	Markov Chain Monte Carlo Methods . . . . .	134
6.4	Optimizing the Measuring Time Distribution . . . . .	143
6.5	Sterile Neutrino Sensitivity . . . . .	155
6.6	Correlated Systematics . . . . .	159
<b>7</b>	<b>Sensitivities Reevaluated</b>	<b>163</b>
7.1	SDS Background Measurements . . . . .	163
7.2	Measuring Time Optimization . . . . .	166
7.3	Background Radial Dependency . . . . .	167
<b>8</b>	<b>Summary and Conclusion</b>	<b>171</b>
	<b>Appendix</b>	<b>175</b>
	<b>Bibliography</b>	<b>181</b>
	<b>List of Figures and Tables</b>	<b>193</b>
	<b>Acronyms</b>	<b>199</b>
	<b>Index</b>	<b>201</b>
	<b>Acknowledgments</b>	<b>205</b>

# CHAPTER 1

---

## Neutrino Physics

---

In 1914 James Chadwick made the puzzling discovery, that the energy spectrum of electrons emitted in radium  $\beta$ -decay was of continuous nature [Cha14]. This finding could not be explained in a two-body decay model without breaking the fundamental laws of momentum and energy conservation. Wolfgang Pauli offered an elegant solution to this puzzle in 1930 by postulating a new spin  $\frac{1}{2}$  particle with no charge and very low mass, which he originally called a ‘neutron’. Emitted as an additional particle in a three-body decay, it could carry away additional momentum (and possibly mass) to explain the continuous  $\beta$ -decay spectrum.

Enrico Fermi formulated a coherent theory of nuclear  $\beta$ -decay in 1933 [Fer34], shortly after the discovery of today’s known actual neutron. He gave Pauli’s postulated particle the name of the ‘neutrino’  $\bar{\nu}_e$  and placed it in a point-like contact interaction of four particles:

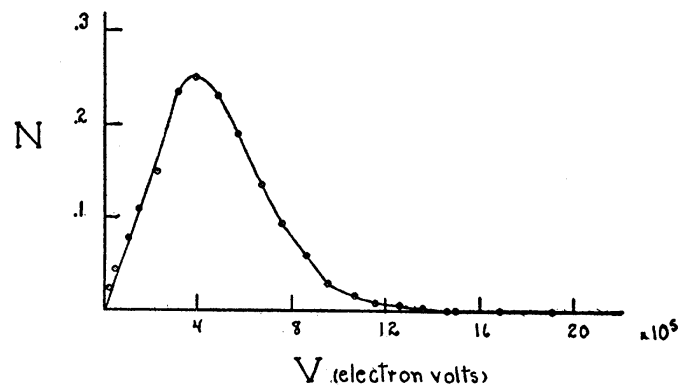
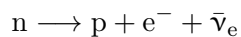


Figure 1.1: ‘Energy distribution curve of the beta-rays’ (radium). Figure taken from [Sco35].

Today Fermi's interaction is superseded in the Standard Model of elementary particles (SM) by electroweak theory.

The experimental discovery of the neutrino followed in 1956 in a series of 'Poltergeist' experiments by Reines and Cowan [Rei60], using the 'classical inverse  $\beta$ -decay' reaction

$$\bar{\nu}_e + p \longrightarrow e^+ + n .$$

With only a handful of events observed, a cross-section for this process in the order of  $\sigma \sim 10^{-43} \text{ cm}^2$  was derived, a typical scale for weakly interacting particles.

Evidence for an additional neutrino type, the muon neutrino  $\nu_\mu$ , was found in 1962 in an experiment at the Brookhaven synchrotron [Dan62]. The third type, the tau neutrino  $\nu_\tau$  was postulated following the discovery of the tau lepton in 1975, yet confirmed only 25 years later in the DONUT experiment at Fermilab [Kod01].

The total number of light neutrino flavors (at least of those actively participating in weak interaction), was determined at the LEP accelerator at CERN [Dec90] in 1989. The experimentally observed  $Z^0$  boson decay width could conclusively be matched with the theoretical expectation for  $N_\nu = 3$ .

## 1.1 Neutrinos in the Standard Model

In the Standard Model of elementary particles (SM) the three neutrino flavor states  $\nu_e, \nu_\mu, \nu_\tau$  are charge-less leptons, which are organized in three generations together with their charged leptonic partners  $e, \mu, \tau$ . Neutrinos are only known to undergo weak interactions, mediated by the  $W^\pm$  and  $Z^0$  bosons.

All leptons are spin  $1/2$  particles. A closely related property is the helicity, which defines the direction of a particle's spin relative to its momentum. The Goldhaber experiment from 1957 [Gol58] has shown, that naturally occurring neutrinos are always left-handed (spin and momentum in the same direction) while anti-neutrinos are right-handed (spin and momentum in opposite direction). One year before, the Wu experiment [Wu57] had proven, that the charged weak interaction violates parity maximally, meaning that only left-handed leptons and right-handed anti-leptons participate in charged weak interactions.

In the mathematical formulation of the SM as a chiral<sup>1</sup> field theory, the left-handed leptons are arranged in doublets  $(\nu_{eL}, e_L^-)$ , whereas right-handed leptons remain in singlets  $(e_R^-)$  with respect to the weak isospin  $SU(2)$  gauge symmetry. Together with the weak hypercharge symmetry  $U(1)$  the electromagnetic and weak interactions are unified under the electroweak  $SU(2) \times U(1)$  gauge group known as the Glashow-Weinberg-Salam model [Gla61; Sal68; Wei67].

---

<sup>1</sup> Chirality and helicity are closely related concepts. However, chirality is an inherently quantum mechanical property of a particle, which is invariant under Lorentz transformations.

Through spontaneous symmetry breaking, the Higgs mechanism [Hig64] allows to generate the massive  $W^\pm$  and  $Z^0$  bosons, while the photon  $\gamma$  stays massless. The fermions of the SM acquire their mass through interactions with the scalar Higgs boson, where they change their chirality in each vertex. These interactions are described in the Lagrangian density  $\mathcal{L}$  by Yukawa couplings with the Higgs doublet  $\phi_0 = \frac{1}{\sqrt{2}} \begin{pmatrix} 0 \\ v \end{pmatrix}$ ,  $v$  being the Higgs vacuum expectation value. In case of electrons, the corresponding Yukawa coupling terms [Zub11] are given by

$$\mathcal{L}_{\text{Yuk}} = -c_e \left[ \bar{e}_R \phi_0^\dagger \begin{pmatrix} \nu_{eL} \\ e_L \end{pmatrix} + (\bar{\nu}_{eL}, \bar{e}_L) \phi_0 e_R \right] \quad (1.1)$$

$$= -c_e \frac{v}{\sqrt{2}} [\bar{e}_R e_L + \bar{e}_L e_R], \quad (1.2)$$

where  $c_e$  is an arbitrary coupling constant. The electron mass is identified by  $m_e = c_e \frac{v}{\sqrt{2}}$ . Since right-handed neutrino singlet states  $\nu_R$  do not exist in the SM particle content, the theory predicts neutrinos to be massless.

An overview of the current particle content of the SM is given in figure 1.2. A scalar particle consistent with the properties of a Higgs boson was only recently discovered at the Large Hadron Collider (LHC) by the CMS [CMS12] and ATLAS [ATL12] collaborations.

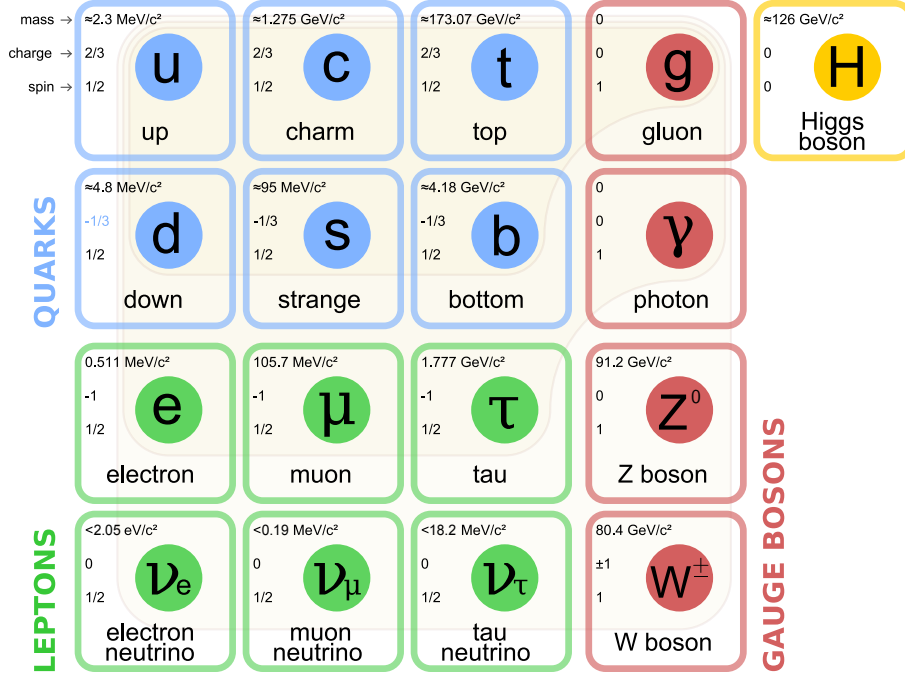


**Figure 1.2:** The Standard Model of elementary particles, with the three generations of matter (column 1 – 3), gauge bosons (column 4), and the Higgs boson (column 5). Graphical illustration derived from [Wik06], particle masses are taken from [Ber12].

## 1.2 Neutrino Oscillations

The phenomenon of neutrino oscillations has increased theoretical and experimental interest in neutrino physics during the last two decades. The underlying quantum mechanical effect, allowing a neutrino produced with one specific leptonic flavor ( $e$ ,  $\mu$ ,  $\tau$ ) to be measured as a different flavor after propagation, demands a non-zero neutrino mass. Since neutrino masses are not part of the SM, the discovery of neutrino oscillations is an important hint towards new physics beyond the SM.

### 1.2.1 The Solar Neutrino Problem

Soon after their discovery, neutrinos were realized to be ideal messenger particles to study hidden processes, such as the nuclear fusion processes in the core of our sun, where they are produced in huge numbers. The famous Homestake experiment was a chlorine-based detector, designed by Raymond Davis in the 60s [Dav94] with the intent of confirming the theoretical solar neutrino flux predicted by John Bahcall [Bah05]. However, a significant deficit in observed neutrino interactions was noticed in comparison to expectations from the standard solar model. Even though the results were at first challenged by the scientific community, they motivated a series of later solar neutrino experiments, such as the gallium-based GALLEX [Ham99], GNO [Alt05] and SAGE [Abd02] or water-based KamiokaNDE [Fuk96] and SNO [Ahm02] experiments.

An explanation of the *solar neutrino problem* was given by the theory of neutrino flavor oscillations, first developed by Pontecorvo [Gri69] and further elaborated by Maki, Nakagawa, and Sakata [Mak62]. In this scenario, electron neutrinos produced in the core of the sun would oscillate into another flavor while traveling from the sun to the observer.

The problem was finally resolved by the SNO experiment in 2001 [Ahm02]. The heavy water Cherenkov detector was capable of distinguishing between charged current (CC) interactions on deuterons and elastic scattering (ES) induced by electron neutrinos  $\nu_e$  on the one hand and neutral current (NC) interactions on deuterons involving all three flavors on the other hand. With an observed electron neutrino flux of about  $\frac{1}{3}$  of the total neutrino flux, clear evidence for neutrino flavor transitions was given. Finally, to give a more recent example, in 2013 the long-baseline T2K experiment conclusively observed muon neutrino to electron neutrino transformations [Abe13].

### 1.2.2 Theory of Neutrino Oscillations

Neutrino oscillations can be explained due to the mixture between *flavor eigenstates*  $|\nu_\alpha\rangle$  with  $\alpha = e, \mu, \tau$  and *mass eigenstates*  $|\nu_i\rangle$  with  $i = 1, 2, 3$ . When neutrinos are created in weak processes, they are produced in a well-defined flavor eigenstate, each of which is a different superposition of the three definite mass eigenstates. Because the masses  $m_i$  are slightly different, the quantum mechanical phases of neutrinos propagate at different rates. This leads to a change of the mass eigenstate mixture, which then corresponds to a different mixture of flavor eigenstates. For this reason, the probability of detecting the neutrino  $|\nu_\alpha\rangle$  in another flavor eigenstate  $|\nu_\beta\rangle$  after a certain propagation distance  $L$  will oscillate

periodically. The oscillation will continue for as long as the quantum mechanical state maintains coherent. Due to the tiny differences of squared masses this effect is observable on macroscopic scales: For instance, for atmospheric neutrinos the coherence length is  $L_{\text{coh}} > 10\,000\text{ km}$  [Zub11].

The mixture between flavor and mass eigenstates can be described as a unitary transformation with

$$|\nu_\alpha\rangle = \sum_i U_{\alpha i}^* |\nu_i\rangle \quad \text{and} \quad |\nu_i\rangle = \sum_\alpha U_{\alpha i} |\nu_\alpha\rangle . \quad (1.3)$$

$U_{\alpha i}$  is called the Pontecorvo-Maki-Nakagawa-Sakata (PMNS) matrix<sup>1</sup> or lepton mixing matrix, and can be written in the following parameterization

$$U = \begin{bmatrix} U_{e1} & U_{e2} & U_{e3} \\ U_{\mu1} & U_{\mu2} & U_{\mu3} \\ U_{\tau1} & U_{\tau2} & U_{\tau3} \end{bmatrix} \quad (1.4)$$

$$= \begin{bmatrix} 1 & 0 & 0 \\ 0 & c_{23} & s_{23} \\ 0 & -s_{23} & c_{23} \end{bmatrix} \begin{bmatrix} c_{13} & 0 & s_{13}e^{-i\delta} \\ 0 & 1 & 0 \\ -s_{13}e^{i\delta} & 0 & c_{13} \end{bmatrix} \begin{bmatrix} c_{12} & s_{12} & 0 \\ -s_{12} & c_{12} & 0 \\ 0 & 0 & 1 \end{bmatrix} \begin{bmatrix} 1 & 0 & 0 \\ 0 & e^{i\alpha_1} & 0 \\ 0 & 0 & e^{i\alpha_2} \end{bmatrix} \quad (1.5)$$

where  $c_{ij} = \cos \theta_{ij}$  and  $s_{ij} = \sin \theta_{ij}$ .

The phase factors  $\alpha_1$  and  $\alpha_2$  are only relevant if neutrinos are Majorana particles<sup>2</sup>. These Majorana phases do not enter into oscillation phenomena, but would cause cancellations in neutrino-less double beta decay (section 1.3.3) and influence the observable decay rate. A non-zero Dirac phase  $\delta$  would manifest leptonic CP symmetry violation, which is expected but has not been observed yet. If experimental data should show, that the  $3 \times 3$  mixing matrix is not unitary, it would imply the existence of one or more so-called sterile neutrinos, which participate in the mixing (see section 1.5).

A relevant quantity for oscillation experiments is the oscillation probability  $P$ . Its detailed derivation can be looked up in many textbooks like [Zub11], so only a short outline will be given here. According to the plane wave description of neutrino states, implied by the Schrödinger equation, the time evolution of a neutrino state  $|\nu_\alpha(t)\rangle$  with energy  $E$ , which was created with definite flavor  $\alpha$  at time  $t = 0$ , can be expressed as

$$|\nu_\alpha(t)\rangle = \sum_i U_{\alpha i}^* e^{-iE_i t} |\nu_i\rangle , \quad (1.6)$$

1 The PMNS matrix was introduced in 1962 by Ziro Maki, Masami Nakagawa and Shoichi Sakata [Mak62] to explain the neutrino oscillations predicted by Bruno Pontecorvo [Pon57].

2 A Majorana particle is identical to its own charge-conjugate or antiparticle respectively, as opposed to Dirac particles. The nature of neutrinos has not been determined yet, but is subject of recent neutrino-less double beta ( $0\nu\beta\beta$ ) decay experiments (section 1.3.3).

with  $c = \hbar = 1$ . From the transition amplitude

$$\langle \nu_\beta | \nu_\alpha(t) \rangle = \sum_i U_{\alpha i}^* U_{\beta i} e^{-iE_i t} \quad (1.7)$$

the probability  $P_{\alpha\beta} = |\langle \nu_\beta | \nu_\alpha(t) \rangle|^2$  for an initial flavor state  $\alpha$  to be detected as a flavor  $\beta$  can be calculated. In a relativistic approximation and assuming CP invariance ( $U_{\alpha i}$  real), it can be written as

$$P_{\alpha\beta}(t) = \delta_{\alpha\beta} - 4 \sum_{j>i} U_{\alpha i} U_{\alpha j} U_{\beta i} U_{\beta j} \sin^2 \left( \frac{\Delta m_{ij}^2 L}{4 E} \right), \quad (1.8)$$

with  $\Delta m_{ij}^2 = m_i^2 - m_j^2$  being the differences between the squared eigenstate masses and  $L \approx ct$  denoting the distance between source and detector. It becomes clear from equation 1.8, that oscillations require at least one mass to be different from zero and a non-diagonal mixing coefficient in  $U$ . As a result, oscillations are not sensitive to the absolute mass scale.

The general oscillation formulae for full three-flavor mixing are quite complex, but in most cases only one mass scale is relevant. For instance for atmospheric neutrinos with  $\Delta m_{\text{atm}}^2 = \Delta m_{32}^2 \approx \Delta m_{31}^2 \gg \Delta m_{21}^2$  the probability of a muon neutrino appearing as a tau neutrino can be simplified according to [Zub11]:

$$P_{\mu\tau} \approx \sin^2(2\theta_{23}) \cos^4(\theta_{13}) \sin^2 \left( \frac{\Delta m_{\text{atm}}^2 L}{4 E} \right) \quad (1.9)$$

The last  $\sin^2$  term in this example causes the periodic oscillation behavior in  $L$  with a so-called *oscillation length* of

$$L_{\text{osc}} = \frac{8\pi E}{m_{\text{atm}}^2}. \quad (1.10)$$

### MSW effect

The above described neutrino oscillation probabilities are modified in the presence of matter due to the Mikheyev-Smirnov-Wolfenstein (MSW) effect [Mik87; Wol78]. Sometimes referred to as a matter effect, it is very important to flavor transformations in the sun. The high electron densities allow electron neutrinos to participate in charged current coherent forward scattering, very similar to the electromagnetic process leading to the refractive index of light in a medium. For electron neutrinos the MSW effect leads to a modification of their effective masses, and this can cause a resonant transformation into muon or tau neutrinos. The predictions from the effect were confirmed by a suite of solar neutrino experiments, which measured a survival probability  $P_{ee} = \sin(2\theta_{12}) \approx 34\%$  for a solar mixing angle  $\theta_{12} = 34^\circ$  at high neutrino energies (MeV). These values are referred to as the MSW large mixing angle solution [Bah99].

## Neutrino Oscillation Parameters

During the last decades a considerable experimental effort has been made to determine the neutrino oscillation parameters: the mixing angles  $\theta_{12}, \theta_{23}, \theta_{13}$  and the differences of squared masses  $\Delta m_{21}^2, \Delta m_{32}^2$ . As can be seen from equation 1.8, one single experiment can only assess a certain combination of  $\theta_{ij}$  and  $\Delta m_{ij}^2$ , depending on its baseline  $L$  and the observed neutrino energy range  $E$ . For this reason a large diversity of experimental setups and complementary detection techniques is required to assemble the entire picture of all oscillation parameters.

Commonly the mixing in the first two generations  $\Delta m_{21}^2$  and  $\theta_{12}$  are referred to as *solar mixing* parameters  $\Delta m_{\text{sol}}^2$  and  $\theta_{\text{sol}}$ , because they are usually derived from a deficit of  $\nu_e$  produced in the solar core.  $\Delta m_{32}^2$  and  $\theta_{23}$  are referred to as *atmospheric mixing* parameters  $\Delta m_{\text{atm}}^2$  and  $\theta_{\text{atm}}$ , since they are determined investigating  $\nu_\mu$  produced in the earth's atmosphere by cosmic air showers.

It was not until 2012 that the last mixing angle  $\theta_{13}$  was determined by the Daya Bay Collaboration [An12] and other efforts. A summary of all parameters known to date is given in table 1.1. Most mixing angles and mass splittings have been measured with rather high precision, with the important exception of the CP-violating Dirac phase  $\delta$ . Also, the sign of  $\Delta m_{32}^2$  is not revealed yet, which leaves several open possibilities for the hierarchy of the neutrino mass spectrum:

Normal hierarchical

$$m_1 \ll m_2 < m_3 \quad \text{with} \quad \Delta m_{32}^2 = \Delta m_{\text{atm}}^2 > 0$$

Inverted hierarchical

$$m_3 \ll m_1 < m_2 \quad \text{with} \quad \Delta m_{\text{atm}}^2 < 0$$

Quasi-degenerate

$$m_1 \approx m_2 \approx m_3 \quad \text{with} \quad m_i^2 \gg |m_{\text{atm}}^2|$$

oscillation parameter	value
$\sin^2(2\theta_{12})$	$0.857 \pm 0.024$
$\Delta m_{21}^2$	$(7.50 \pm 0.20) \cdot 10^{-5} \text{ eV}^2$
$\sin^2(2\theta_{23})$	$> 0.95$
$ \Delta m_{32}^2 $	$2.32_{-0.08}^{+0.12} \times 10^{-3} \text{ eV}^2$
$\sin^2(2\theta_{13})$	$0.095 \pm 0.010$

**Table 1.1:** Neutrino oscillation parameters obtained through combined data analyses based on the 3-neutrino mixing scheme described in [Ber12].

Even though oscillation experiments cannot determine the absolute neutrino mass scale, a lower limit on the heaviest mass eigenstate  $m_i$  can be derived from the larger one of the two mass splittings:

$$m_3 > \sqrt{|\Delta m_{\text{atm}}^2|} \simeq 48 \text{ meV} \quad (1.11)$$

As argued before, a certain variety of oscillation experiments at different oscillation lengths and neutrino energy regimes is required to measure all parameters of the mixing matrix. The investigated neutrino sources are briefly summarized in the following:

### Solar neutrinos

Produced abundantly in different solar fusion cycles, solar neutrinos carry energies up to the MeV range. Their fluxes are predicted by the standard solar model (SSM) [Bah05]. With a baseline of 1 astronomical unit (AU), solar experiments are sensitive to the mixing angle  $\theta_{12}$  and mass difference  $\Delta m_{21}^2$ .

Radio-chemical experiments, already mentioned above (Homestake, Gallex, GNO, SAGE), were the first to establish a deficit in the measured  $\nu_e$  flux. The SNO experiment, introduced in section 1.2.1, used heavy water ( $\text{D}_2\text{O}$ ) to distinguish between neutral and charged current interactions and thus solved the solar neutrino problem by confirming the predicted SSM neutrino flux via neutral currents.

### Atmospheric neutrinos

Interactions of cosmic rays with the earth's atmosphere produce charged pions and muons, which decay into muon and electron (anti-)neutrinos in an expected ratio of  $\nu_\mu : \nu_e = 2 : 1$ .

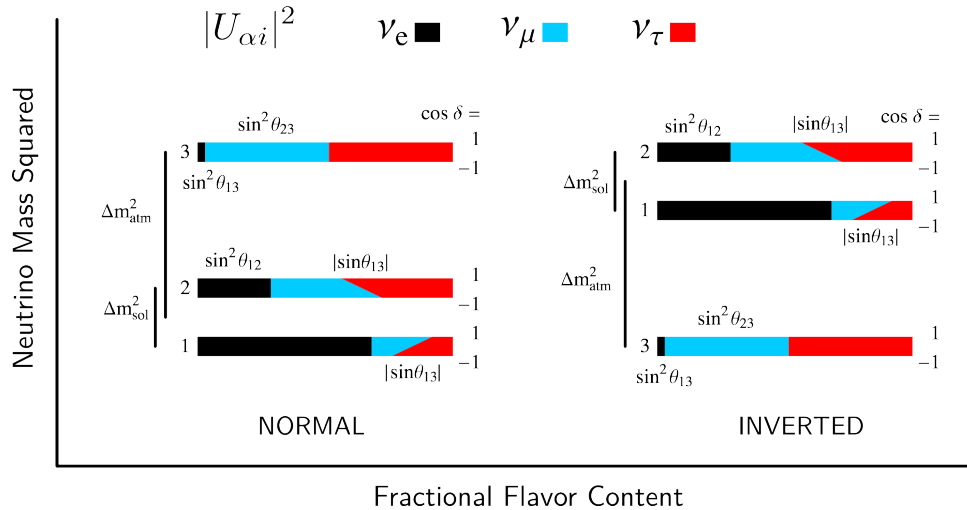


**Figure 1.3:** Flavor fraction of the three neutrino mass eigenstates showing the dependence on the cosine of the CP violating phase  $\delta$  and the mass hierarchy. Figure adapted from [Par08].

The Super-Kamiokande experiment [Fuk98], originally designed to observe proton decay, reconstructs both neutrino energy and direction from the characteristic Cerenkov light cones, emitted after neutrino-electron scattering in pure water. A deficit was observed for up-going atmospheric muon neutrinos (GeV scale), traveling through the earth ( $L \approx 13\,000$  km), when compared to down-going muon neutrinos, which travel only a much shorter distance ( $L \approx 15$  km). The result can be interpreted as oscillations of  $\nu_\mu \rightarrow \nu_\tau$ .

### Accelerator neutrinos

With artificial neutrino sources, such as GeV-scale  $\nu_\mu$  beams produced by particle accelerators, the baseline to energy ratio  $L/E$  can be tuned to achieve an even better sensitivity on the atmospheric oscillation parameters  $\theta_{23}$  and  $\Delta m_{32}^2$ .

The first long-baseline experiment was K2K [Ahn06], which ran from 1999 to 2005 and made use of a pulsed beam of muon neutrinos, directed from the proton synchrotron at the KEK facility towards the 250 km remote Super-Kamiokande detector, observing the  $\nu_\mu$  disappearance channel. The ongoing successor experiment T2K [Abe13] at an almost identical baseline of 295 km between the J-PARC accelerator in Tokai and Super-Kamiokande focused on the rare  $\nu_\mu \rightarrow \nu_e$  appearance oscillation. A first hint for a non-zero value of  $\theta_{13}$  was published by the T2K collaboration in 2011 [Abe11].

### Reactor neutrinos

Reactor neutrino experiments utilize the large flux of electron anti-neutrinos  $\bar{\nu}_e$ , produced by nuclear power plants, to assess the mixing angle  $\theta_{13}$ . Generally, both a far detector with a baseline of about 1 – 2 km, used to measure the disappearance of  $\bar{\nu}_e$ , and a second near detector to reduce systematic uncertainties on the source neutrino flux, are required.

The value of  $\theta_{13}$ , shown in table 1.1, has been obtained from three different experiments: Double Chooz [Ard06], Daya Bay [An12] and RENO [Ahn10], all of which provided very consistent results in 2012 [Ber12] with recent updates in 2014 [Neu14].

In figure 1.4 results from the KamLAND reactor neutrino experiment [Abe08] are shown. The detector at that time was surrounded by a large number of Japanese nuclear reactors, thus allowing to assemble a spectrum of  $\bar{\nu}_e$  rates at multiple baselines.

### Supernova neutrinos

The first real-time detection of astrophysical neutrinos from the supernova SN 1987A was performed by Kamiokande [Hir87] and the IMB experiment [Hai88], about three hours before the visible light from the explosion reached the earth. Not only did the observation confirm theoretical supernova type II models, in which 99 % of the energy of the massive star collapse is radiated away in neutrinos. The event also marked the beginning of the field of neutrino astronomy.

From the observed spread of the neutrino arrival times and the reconstructed neutrino energies, a time-of-flight analysis can be performed, giving a handle on determining the neutrino mass. In [Lor02] a Bayesian data analysis of about two dozen observed SN

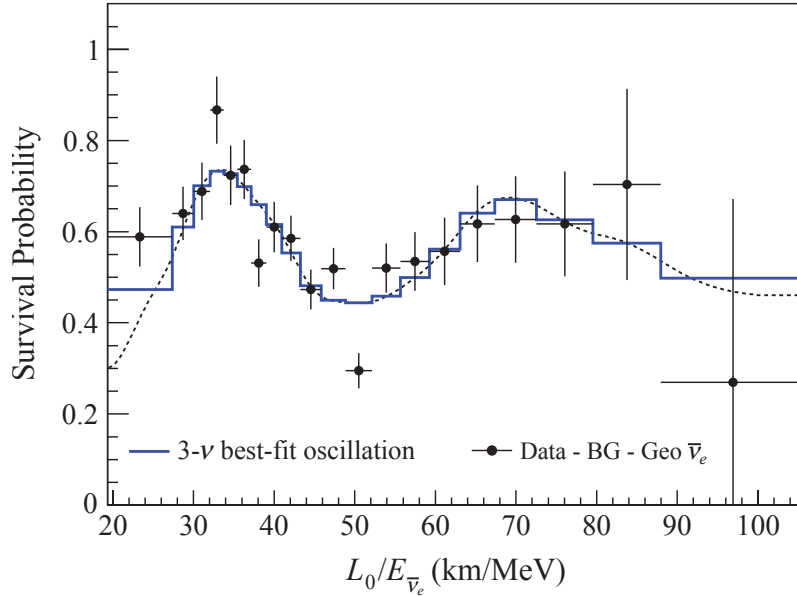


**Figure 1.4:** Ratio of the observed  $\bar{\nu}_e$  spectrum to the expectation for no-oscillation versus  $L_0/E$  from the KamLAND reactor neutrino experiment [Abe08].  $L_0 = 180$  km is the flux-weighted average reactor baseline. The 3- $\nu$  histogram is the best-fit survival probability curve for the mixing parameters  $\Delta m_{21}^2 = 7.54 \cdot 10^{-5} \text{ eV}^2$ ,  $\tan^2(\theta_{12}) = 0.481$ ,  $\sin^2(\theta_{12}) = 0.010$ . Figure taken from [Gan13].

1987A neutrinos results in an upper limit of

$$m_{\bar{\nu}_e} < 5.7 \text{ eV (95 \% C.L.)} . \quad (1.12)$$

However, this type of mass determination strongly depends on the choice of the neutrino emission model in supernova explosions, and is not competitive with direct kinematical techniques, which will be discussed in section 1.4.

### 1.3 Massive Neutrinos

Experimental observations have provided impressive evidence for the phenomenon of neutrino oscillations, which require neutrinos to have mass. Although the oscillation observables are not sensitive to the absolute mass scale, it is known from cosmological and laboratory data, that the heaviest neutrino mass resides in the sub-eV range.

#### 1.3.1 Neutrino Mass Beyond the SM

As explained in section 1.1, the SM does not incorporate a generation mechanism for neutrino masses. A possible extension within the Higgs mechanism would be the introduction of a right-handed neutrino singlet state  $\nu_R$ , which does not participate in weak interactions (sterile neutrino). However, in this case the corresponding Yukawa coupling constant  $c_\nu$  would be about six orders of magnitude smaller compared to charged fermions [Moh07].

### The Seesaw Mechanism

Another possible mechanism for the generation of neutrino masses arises from a combination of Dirac and Majorana mass terms. Charged fermions can only acquire Dirac-type masses:

$$\mathcal{L} = m_D \bar{\psi} \psi = m_D (\bar{\psi}_L \psi_R + \bar{\psi}_R \psi_L) \quad (1.13)$$

$\psi_R$  and  $\psi_L$  are the chiral components (right-handed and left-handed) of the spinor representation  $\psi$  of the corresponding fermionic field.

For charge-less particles like the neutrino, Majorana-type masses can be introduced, but only under the condition, that the particles are their own anti-particle  $\psi = \psi^c$ :

$$\mathcal{L} = \frac{1}{2} (m_L \bar{\psi}_L \psi_R^c + m_R \bar{\psi}_L^c \psi_R) + \text{h.c.}^1 \quad (1.14)$$

Here,  $\psi^c$  is the charge conjugate with  $\psi_{L,R}^c = (\psi^c)_{R,L} = (\psi_{R,L})^c$ .

Coming back to neutrinos, we denote  $\psi_L = \nu_L$ ,  $\psi_R^c = \nu_R^c$ ,  $\psi_R = N_R$ ,  $\psi_L^c = N_L^c$ , the latter two being sterile neutrinos, which do not participate in weak interactions. In this notation the combination of Dirac (equation 1.13) and Majorana (equation 1.14) masses becomes [Zub11]:

$$\mathcal{L} = \frac{1}{2} [m_D (\bar{\nu}_L N_R + \bar{N}_L^c \nu_R^c) + m_L \bar{\nu}_L \nu_R^c + m_R \bar{N}_L^c N_R] + \text{h.c.} \quad (1.15)$$

$$= \frac{1}{2} (\bar{\nu}_L, \bar{N}_L^c) \begin{pmatrix} m_L & m_D \\ m_D & m_R \end{pmatrix} \begin{pmatrix} \nu_R^c \\ N_R \end{pmatrix} + \text{h.c.} \quad (1.16)$$

An interesting scenario arises, when the Majorana mass  $m_L$  for the left-handed neutrino  $\nu_L$  is zero ( $m_L = 0$ ), but  $m_R$  for the right-handed sterile neutrino  $N_R$  is very large ( $m_R \gg m_D$ ). Then the following two mass eigenvalues can be obtained from the  $2 \times 2$  mass matrix:

$$m_\nu = \frac{m_D^2}{m_R} \quad \text{and} \quad (1.17)$$

$$m_N \approx m_R \quad (1.18)$$

Under the assumption that the Dirac mass terms  $m_D$  are of the order of charged fermion masses (MeV to GeV) and the mass of the sterile neutrino  $m_N$  is of the order of the GUT-scale ( $\sim 10^{16}$  GeV), the above mechanism naturally leads to the very small observable neutrino masses. This is also called the *seesaw* mechanism (type I) for the production of small neutrino masses [Gel79].

---

1 h.c. signifies the Hermitian conjugate.

In this type I seesaw the neutrino masses would scale with the charged fermion masses, leading to a hierarchical mass scenario. If the upper left entry of the  $2 \times 2$  matrix,  $m_L$  is not exactly zero, equation 1.17 is extended by an additional term, including the vacuum expectation value of the Higgs field. In that case, the resulting neutrino masses are quasi-degenerate, which is sometimes referred to as the type II seesaw.

Further approaches of introducing neutrino masses ‘beyond the Standard Model’ involve Higgs triplet states [Sch80], supersymmetry [Moh06] or extra spatial dimensions [Ark02], just to name a few.

### 1.3.2 Cosmology

The determination of the neutrino mass and its origin is of huge interest not only to elementary particle physics. Also cosmology would greatly benefit from a more precise knowledge of the neutrino mass and its resulting contribution to the total matter density and evolution of structures in the Universe.

#### Cosmic Neutrino Background

Similar to the cosmic microwave background (CMB), being one of the pillars of the  $\Lambda$ CDM cosmological model<sup>1</sup> [Ber03], a cosmic neutrino background (CvB) is predicted. The CvB consists of relic neutrinos, which have decoupled from thermal equilibrium with matter in the very early Universe. This ‘freeze-out’ happened when the Universe was about one to two seconds old at a decoupling temperature of  $T \approx 1$  MeV [Les06], which today corresponds to a relic neutrino black body temperature of 1.95 K.

Since neutrinos only interact weakly and gravitationally, they are a prototype of the many dark matter candidates proposed today, and so far the only one, known to exist. In figure 1.5 the contribution of the neutrino energy density  $\Omega_\nu$  to the total energy density  $\Omega_{\text{tot}}$  is shown. It depends on their number density per neutrino flavor  $n_\nu = (3/11)n_\gamma = 339 \text{ cm}^{-3}$  [Les06], which can be derived from the primordial abundances of light elements. Their energy density  $\Omega_\nu$  is given by the sum of the neutrino mass eigenstates

$$\Omega_\nu = \frac{\sum m_i}{93.14 h^2 \text{ eV}/c^2} \quad (1.19)$$

with the dimensionless Hubble parameter  $h = H_0/(\text{km s}^{-1} \text{ Mpc}^{-1}) = 0.673 \pm 0.012$ . Relic neutrinos are not only among the oldest messengers from the Big Bang, they are also by far the most abundant known fermionic particles in the Universe. Within the mass regime, which will be explored by the KATRIN experiment ( $\sum m_i < 600 \text{ meV}$ ), neutrinos could constitute a considerable contribution to the total energy density in the Universe (see figure 1.5).

---

1 The standard model of cosmology  $\Lambda$ CDM is based on the concept of a hot Big Bang, from which our Universe has evolved to its present cold state, dominated by dark energy ( $\Lambda$ ) and dark matter (CDM).

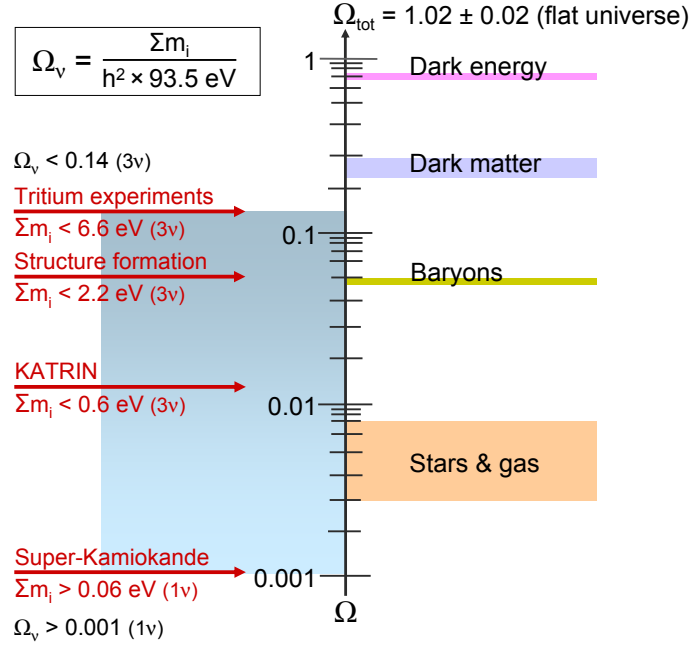


**Figure 1.5:** Neutrino energy density contribution  $\Omega_\nu$  to the total energy density  $\Omega$  of the Universe in comparison to the contribution from dark energy  $\Omega_\Lambda$ , dark matter  $\Omega_{\text{DM}}$  and baryons  $\Omega_b$ . The experimentally constrained contribution  $\Omega_\nu$  from neutrino hot dark matter to the total matter energy density  $\Omega$  spans two orders of magnitude. The lower bound on  $\Omega_\nu$  stems from the analysis of atmospheric neutrino oscillation. Figure adapted from [KAT05].

### Structure Formation

After thermal decoupling, relativistic neutrinos can move collision-free on a free-streaming length  $\lambda_{\text{FS}}$  before becoming non-relativistic. In a non-relativistic approximation [Les06], the free-streaming length can be written as

$$\lambda_{\text{FS}} = 8 \frac{1+z}{\sqrt{\Omega_\Lambda + \Omega_m(1+z)^3}} \left( \frac{\text{eV}}{m_\nu} \right) h^{-1} \text{Mpc} , \quad (1.20)$$

where  $\Omega_\Lambda$  and  $\Omega_m$  are the density fraction of the cosmological constant and matter. The red-shift is denoted by  $z$ .

As a consequence of free-streaming, light neutrinos can escape areas of high density without interaction and effectively dampen or even erase gravitational perturbations up to a scale of about  $\lambda_{\text{FS}} \simeq 1230 \left( \frac{\text{eV}}{m_\nu} \right) \text{Mpc}$  [Zub11]. The suppression of small-scale density fluctuations and correlated effects on the evolution of larger structures are stronger with large  $m_\nu$  and  $\Omega_\nu$ .

### Indirect Constraints on Neutrino Mass

The substantial influence of massive neutrinos on cosmological observables allows to derive constraints on the total sum of neutrino masses, even though with certain limitations. A recent combined analysis of cosmological data published in [Bat14] yielded an upper limit of

$$\sum m_i \leq (320 \pm 81) \text{ meV} . \quad (1.21)$$

Observations of the angular power spectrum of temperature anisotropies in the CMB from the Planck satellite [Ade13] were used in combination with polarization measurements from WMAP [Ben13] and observations of baryonic acoustic oscillations (BAO) [Beu11].

A caveat of these indirect cosmological constraints are the large dependencies on model assumptions. The achieved neutrino mass limits can vary by up to an order of magnitude, depending on the combination of selected data sets and cuts. A complementary direct mass measurement is imperative in order to reduce the cosmological model parameter degeneracy and relieve some of the existing tensions between various data sets.

#### 1.3.3 Neutrino-less Double Beta Decay

The observation of the hypothetical neutrino-less double  $\beta$ -decay ( $0\nu\beta\beta$ ) would not only establish the Majorana nature of the neutrino ( $\nu = \bar{\nu}$ ), but imply lepton number violation as well. It could also provide access to the absolute neutrino mass scale.

Double  $\beta$ -decay with neutrino emission ( $2\nu\beta\beta$ ) is a second order weak nuclear process, involving the simultaneous transmutation of two neutrons into two protons:

$$2n \longrightarrow 2p + 2e^- + 2\bar{\nu}_e , \quad (1.22)$$

This process is observable when single  $\beta$ -decay is energetically forbidden (as for the even-even isotopes  $^{76}\text{Ge}$  or  $^{136}\text{Xe}$ ). The energy spectrum of the two emitted electrons, as shown in figure 1.6, is continuous, since the neutrinos carry away part of the decay energy  $Q$ .

Neutrino-less double  $\beta$ -decay ( $0\nu\beta\beta$ ) is an alternative process, first suggested by G. Racah in 1937 [Rac37], shortly after E. Majorana had introduced a theoretical description for neutrinos to be their own antiparticle. The two neutrons decay without the emission of neutrinos:

$$2n \longrightarrow 2p + 2e^- \quad (1.23)$$

The two  $\beta$ -decays are mediated by the exchange of a virtual Majorana-type neutrino. This hypothetical process clearly implies the violation of lepton number conservation with  $\Delta L = 2$ . Furthermore it requires the neutrino to have mass: The right-handed anti-neutrino

$\bar{\nu}_e$  emitted in one  $\beta$ -decay has to be absorbed as a left-handed neutrino  $\nu_e$  in the second inverse  $\beta$ -decay. Only if  $m_\nu > 0$ , the helicity (spin projection onto the momentum vector) has a finite chance to flip and change its sign<sup>1</sup>.

Since the emitted electrons carry all the decay energy, the energy spectrum of double  $\beta$ -decay is modified by the appearance of comparatively small peak at the decay endpoint  $Q$ , the typical signature for  $0\nu\beta\beta$  decay. It is strongly suppressed compared to  $2\nu\beta\beta$  decay, which is why a major effort of such experiments is the reduction or distinction from background.

In  $0\nu\beta\beta$  decay experiments an effective Majorana mass  $\langle m_{\beta\beta} \rangle$  is measured, which is a coherent sum of the neutrino mass eigenstates:

$$\langle m_{\beta\beta} \rangle = \left| \sum_i U_{ei}^2 m_i \right| = \left| \sum_i |U_{ei}|^2 m_i e^{i\alpha_i} \right| \quad (1.24)$$

Since the CP-violating Majorana phases  $\alpha_i$  can lead to cancellations, it is well possible that  $\langle m_{\beta\beta} \rangle < m_i$ . The effective mass is obtained by observing the half-life  $T_{1/2}^{0\nu}$  of the decay

$$\left( T_{1/2}^{0\nu} \right)^{-1} = G^{0\nu}(Q, Z) \cdot |M^{0\nu}|^2 \frac{\langle m_{\beta\beta} \rangle^2}{m_e^2}, \quad (1.25)$$

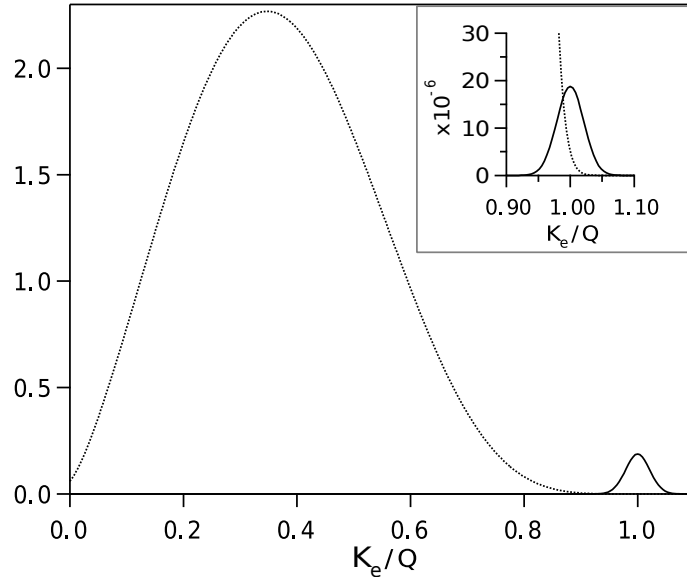


**Figure 1.6:** Illustration of the summed electron energy spectrum  $K_e$  ( $Q$  is the endpoint) for  $0\nu\beta\beta$  (solid curve) and  $2\nu\beta\beta$  decays (dotted curve). The  $0\nu\beta\beta$  spectrum is normalized to  $10^{-2}$ . Figure according to [Eli02].

<sup>1</sup> The  $0\nu\beta\beta$  decay process can theoretically be enabled by alternative mechanisms, such as a right-handed W boson [Bog85].

where  $G^{0\nu}$  is a phase space factor depending on the endpoint energy  $Q$  and the atomic charge  $Z$ . The largest uncertainties arise from the calculation of the nuclear transition matrix elements  $M^{0\nu}$ . Recent model predictions still differ by a factor of 2 – 3 [Dev13].

In 2013 the GERDA collaboration published the so far most stringent limit on the  $0\nu\beta\beta$  half-life of germanium  $^{76}\text{Ge}$  from their first measurement phase [Dev13] with a detector mass of 18 kg of enriched  $^{76}\text{Ge}$ . The measured half-life is

$$T_{1/2}^{0\nu} (^{76}\text{Ge}) = 2.1 \cdot 10^{25} \text{ y at } 90\% \text{ C.L.} \quad (1.26)$$

which translates into an Majorana mass limit of

$$\langle m_{\beta\beta} \rangle = 250 - 520 \text{ meV} , \quad (1.27)$$

depending on the nuclear matrix element calculation. With this result the GERDA experiment has started to disprove the only claimed observation of  $0\nu\beta\beta$  decay in  $^{76}\text{Ge}$  to date, which was made by a subgroup of the Heidelberg-Moskow experiment in 2003 [Kla04].

## 1.4 Single Beta Decay Experiments

So far the most promising model-independent access to the absolute neutrino mass scale is made possible through the kinematical investigation of weak  $\beta^-$  decays:

$$n \longrightarrow p + e^- + \bar{\nu}_e \quad (1.28)$$

The experimental method purely relies on the kinematic properties of this physical process: energy and momentum conservation. The energy spectrum of the emitted  $\beta$  electron is analyzed close to the endpoint energy of the emitting radioactive isotope, where a shape distortion due to a non-zero electron-neutrino mass is most apparent. No model assumptions about the Dirac or Majorana nature of the neutrino has to be made.

### 1.4.1 Beta Decay Kinematics

In  $\beta^-$  decay the energy released by the nucleus is shared between the outgoing  $\beta$  particle (the electron) and the anti-neutrino  $\bar{\nu}_e$ . The kinetic energy spectrum of the emitted particles therefore is continuous, ranging up to the maximal available energy  $Q$ , usually referred to as the endpoint energy  $E_0$ .

Starting from Fermi's golden rule [Fer34]

$$\frac{dN}{dE} = \frac{2\pi}{\hbar} |M|^2 \rho(E) , \quad (1.29)$$

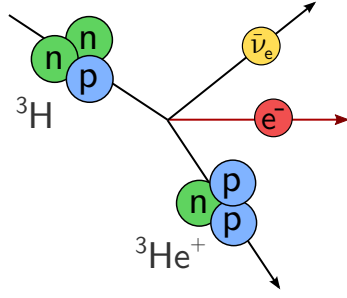


**Figure 1.7:** Schematic of the tritium  $\beta$ -decay.

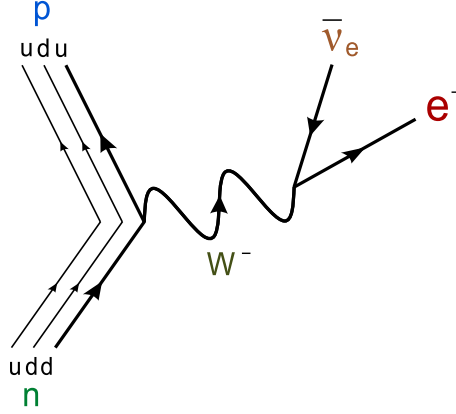


**Figure 1.8:** Feynman diagram of a  $\beta^-$  decay from neutron into proton, involving the charged current  $W^-$  boson.

with the transition matrix element  $M$  and the density of final states  $\rho(E)$ , the electron energy spectrum of nuclear  $\beta$ -decay can be written down in the following form [Ott08], with units  $\hbar = c = 1$ :

$$\frac{dN}{dE} = \frac{G_F^2 \cos^2 \theta_C}{2\pi^3} |M|^2 S(E) F(Z, E) p(E + m_e) \cdot \sum_i \sum_f |U_{ei}|^2 P_f \varepsilon_f \sqrt{\varepsilon_f^2 - m_i^2} \Theta(\varepsilon_f - m_i) \quad (1.30)$$

$G_F$  is the Fermi coupling constant,  $\theta_C$  the Cabibbo angle and  $M$  the nuclear matrix element of the transition.  $S(E)$  is a shape factor, required if the transition is of the forbidden type.

The Fermi function  $F(Z, E)$  accounts for the nuclear Coulomb interaction with the emitted electron, and  $p(E + m_e)$  gives the phase space factor of the outgoing electron. The phase space of the emitted neutrino is the product of the neutrino energy  $\varepsilon_j = E_0 - E_f - E$  and the neutrino momentum  $\sqrt{\varepsilon_f^2 - m_i^2}$ , which determines the shape of the spectrum near the tritium endpoint  $E_0$ . Energy conservation is ensured by inclusion of the step function  $\Theta$ .

The neutrino phase space factor has to be summed over all final states  $E_f$  (excitations) of the daughter state (atom, molecule), populated with probabilities  $P_f$ , and over the neutrino mass eigenstates  $m_i$ .

In case of tritium  $\beta$ -decay an important simplification applies. The transition is super-allowed, with the ground state wave function of the parent nucleus  $T$  being identical to the daughter nucleus  ${}^3\text{He}^+$ . As a consequence, the nuclear matrix element  $M$  is energy independent and its calculation well known. The shape factor  $S(E)$  equals 1 for super-allowed transitions.

The mass splittings, well known from oscillation experiments [Nak10], are too small to be resolved experimentally from a  $\beta$ -decay spectrum at present. The observable  $m_{\nu_e}^2$ , which can be extracted from the spectral shape near the endpoint, is given by the incoherent sum over the mass eigenstates weighted by the matrix elements  $U_{ei}$  of the PMNS mixing matrix (see section 1.2.2):

$$m_{\nu_e}^2 = \sum_i |U_{ei}|^2 m_i^2 \quad (1.31)$$

$\beta$ -decay experiments are called model-independent, since their observable does not depend on the neutrino being a Majorana or Dirac particle. This is in contrast to  $0\nu\beta\beta$  experiments, where the observable  $m_{\langle\beta\beta\rangle}$  is a coherent sum, and partial cancellation of the mass terms due to imaginary Majorana phases  $\alpha_i$  can arise (see equation 1.24 for comparison).

The effect of a non-zero neutrino mass  $m_{\nu_e}$  on the shape of the tritium  $\beta$ -decay spectrum is illustrated in figure 1.9.

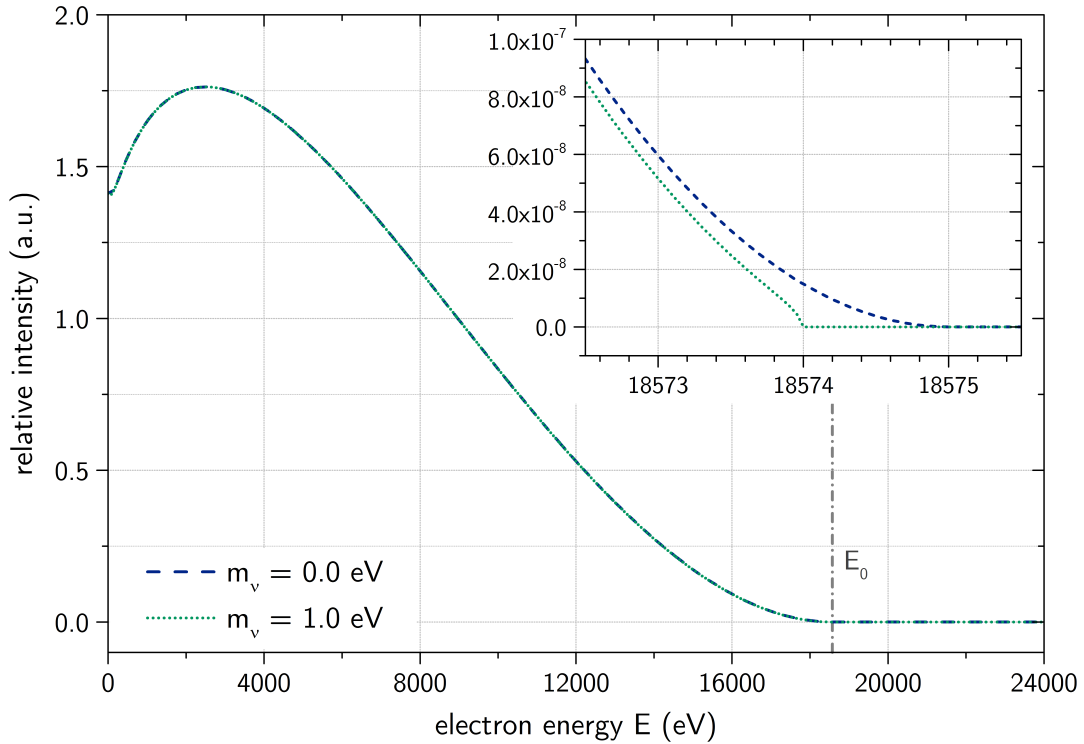


**Figure 1.9:** Differential tritium  $\beta$ -decay electron energy spectrum. The endpoint region is enlarged to show the effect of a non-zero neutrino mass on the spectrum shape. Only a tiny fraction of  $\sim 2 \cdot 10^{-13}$  of the emitted electrons fall into the last eV interval below the endpoint (enlarged inset).

### 1.4.2 Rhenium and Holmium Experiments

An alternative approach to spectrometry is the use of cryogenic bolometers (similar to those used in some  $0\nu\beta\beta$  decay experiments) for the kinematic investigation of single  $\beta$ -decays. In a calorimetric setup the entire decay energy is released in the detector, eliminating some of the systematic uncertainties arising from an external electron source. Also, the use of micro-calorimeters provides a certain degree of scalability of the experimental setup.

Rhenium  $^{187}\text{Re}$  has been a promising isotope with a low endpoint of  $Q = 2.67\text{ keV}$  for a long time. On the downside it has an exceedingly long half-life of  $T_{1/2}^{0\nu} = 4.3 \cdot 10^{10}\text{ y}$ , which requires an experiment to install large amounts of the isotope for a sufficiently high source activity. The MILANO experiment [Sis04] used an array of 10 micro-calorimeters, each containing 250 – 300  $\mu\text{g}$  of  $\text{AgReO}_4$  crystals, and published an upper limit on the electron neutrino mass of

$$m_{\bar{\nu}_e} < 15\text{ eV (90\% C.L.)} . \quad (1.32)$$

The successor experiment MARE plans an extension of the array to improve the sensitivity down to the sub-eV range [Nuc12], however it will also investigate other  $\beta$  isotopes, such as holmium  $^{163}\text{Ho}$ .

Another possibility of a direct neutrino mass measurement is pursued by the ECHo and HOLMES collaborations [Bla13], using a calorimetric measurement of the holmium  $^{163}\text{Ho}$  electron capture:



$^{163}\text{Ho}$  decays by capturing an electron from the inner atomic shells to an excited state of the dysprosium  $^{163}\text{Dy}$  atom with a half-life of  $T_{1/2} \approx 4570\text{ y}$  and a low  $Q$ -value of  $Q \approx 2.3 - 2.8\text{ keV}$ . The neutrino mass can be obtained from a calorimetric measurement of the continuous  $^{163}\text{Dy}$  de-excitation spectrum close to the  $Q$ -value. In order to push the sensitivity below the 1 eV range, a more precise determination of the mass difference  $Q$  between  $^{163}\text{Ho}$  and  $^{163}\text{Dy}$  is planned in dedicated Penning trap measurements.

### 1.4.3 Tritium as Beta Emitter

Since several decades, tritium  $\text{T} = {}^3_1\text{H}$  is considered as the most promising candidate in spectroscopic, direct neutrino mass measurements:



Its ideal characteristics have led to a series of tritium-based  $\beta$ -decay experiments in the past five decades. Crucial advantages of tritium are:

### Low endpoint energy

The endpoint energy  $E_0 \approx 18.6$  eV is comparatively low. This leads to a favorable decay phase space in the endpoint region of the electron energy spectrum, which is of major interest in a neutrino mass search. Here the relative fraction of observable  $\beta$  electrons scales with  $1/E_0^3$ . Also there are technical benefits: The retarding voltage required for electrostatic spectroscopy has to meet the energy scale of the emitter's endpoint. Stringent requirements on the voltage stability and challenges, arising from the possibility of vacuum discharges, are less of a concern with a correspondingly lower endpoint energy.

### Short half life

A very short half-life  $T_{1/2} = (4500 \pm 8) \text{ d} \approx 12.3 \text{ y}$  [Luc00] leads to high decay rates and limits the adequate amounts of source material. KATRIN will make use of only 20  $\mu\text{g}$  in its source to achieve a  $\beta$ -decay intensity of  $10^{11} \text{ s}^{-1}$ .

### Super-allowed decay

The parent and daughter states are mirror nuclei with identical wave functions. The nuclear matrix element  $|M|$  then becomes energy-independent and no intermediate states have to be included in the theoretical description.

### Low nuclear charge

Due to its low charge  $Z = 1$  and simple atomic shell, interactions between  $\beta^-$  electrons and nuclei in the source become rare and can be accurately computed.

### Gaseous hydrogen isotope

In case of gaseous molecular tritium, many well studied properties from hydrogen are transferable to tritium as a hydrogen isotope. Also, for a gaseous emitter no solid state effects have to be taken into account.

For gaseous molecular tritium, a will be used for the KATRIN experiment, the decay is denoted as



Due to its molecular structure, the daughter ion  ${}^3\text{HeT}^+$  will typically be in a rotationally and vibrationally excited state, in addition to the usual electronic excitations. These final states modify the spectrum of  $\beta$ -decay electrons and have to be accounted for in a neutrino mass analysis (section 5.2).

#### 1.4.4 Current Beta Decay Neutrino Mass Limits

The two most recent tritium  $\beta$ -decay experiments, currently holding the most sensitive model-independent neutrino mass result, are the 'Mainz neutrino mass experiment', concluded in 2001, and the 'Troitsk neutrino mass experiment', which is still operational. Both experiments make use of a high resolution spectrometer of the Magnetic Adiabatic Collimation combined with an Electrostatic (MAC-E) filter type, a principle that the KATRIN experiment will push to its technological limits (section 2.2).

At the Mainz experiment, a solid quench-condensed tritium source was used. While avoiding the gasdynamical complexities of a gaseous tritium source, technical challenges arose from the surface wetting and charging of the tritium substrate, the latter due to remaining  ${}^3\text{HeT}^+$  ions. Their final neutrino mass results were published in 2005 [Kra05]:

$$m(\bar{\nu}_e)^2 = -0.6 \pm 2.2(\text{stat}) \pm 2.1(\text{sys}) \text{ eV}^2 \quad (1.36)$$

$$m(\bar{\nu}_e) < 2.3 \text{ eV (95 \% C.L.)} \quad (1.37)$$

The Troitsk experiment employs a windowless gaseous tritium source, as will the KATRIN experiment. One recent result, published in 2011 [Ase11], is:

$$m(\bar{\nu}_e)^2 = -0.67 \pm 1.89(\text{stat}) \pm 1.68(\text{sys}) \text{ eV}^2 \quad (1.38)$$

$$m(\bar{\nu}_e) < 2.05 \text{ eV (95 \% C.L.)} \quad (1.39)$$

A combined analysis by the Particle Data Group [Ber12] yields the currently lowest limit from direct neutrino mass measurements:

$$m(\bar{\nu}_e) < 2.0 \text{ eV (95 \% C.L.)} \quad (1.40)$$

## 1.5 Sterile Neutrinos

The seesaw mechanism introduced in section 1.3.1 is an appealing way to generate small neutrino masses, required to explain neutrino mixing phenomena, as observed by a large number of oscillation experiments. By adding right-handed *sterile* neutrino partners (weak isosinglets with no charge) to the SM matter content and introducing related Majorana mass terms, the small masses of the known three active neutrino generations can be generated. So from a theoretical point of view, sterile neutrinos are a natural occurrence.

When seesaw mass generation is put in the context of grand unification or leptogenesis, it is tempting to relate the sterile mass states to high energies ( $\gg 100 \text{ GeV}$ ) well above the electroweak energy scale. But technically, any values are possible and a priori not defined by the model. Low-energy seesaw scenarios can be motivated by a series of profound problems in particle physics and astrophysics, since the corresponding right-handed neutrino states remain kinematically accessible through mixing. This is in particular true for keV-scale neutrinos, which are discussed as possible warm dark matter candidates [Bar12].

The possible existence of a light sterile neutrino ( $m \sim 1 - 10 \text{ eV}$ ) was first suggested by the LSND short-baseline neutrino oscillation experiment [Ath98], which observed an excess of  $\bar{\nu}_e$  in a  $\bar{\nu}_\mu$  beam from  $\Pi^+$  decay. The results could not entirely be ruled out by the KARMEN and MiniBooNE experiments [Agu09; Arm03]. Interestingly, claims for eV-scale sterile neutrinos were further backed by the calibration of gallium solar neutrino experiments [Abd09]. Recent re-evaluations of nuclear reactor anti-neutrino flux predictions have lead to an overall deficit in the observed flux of reactor neutrino experiments, known as the *reactor antineutrino anomaly* [Men11] (see figure 1.10). It is compatible with sterile neutrinos having

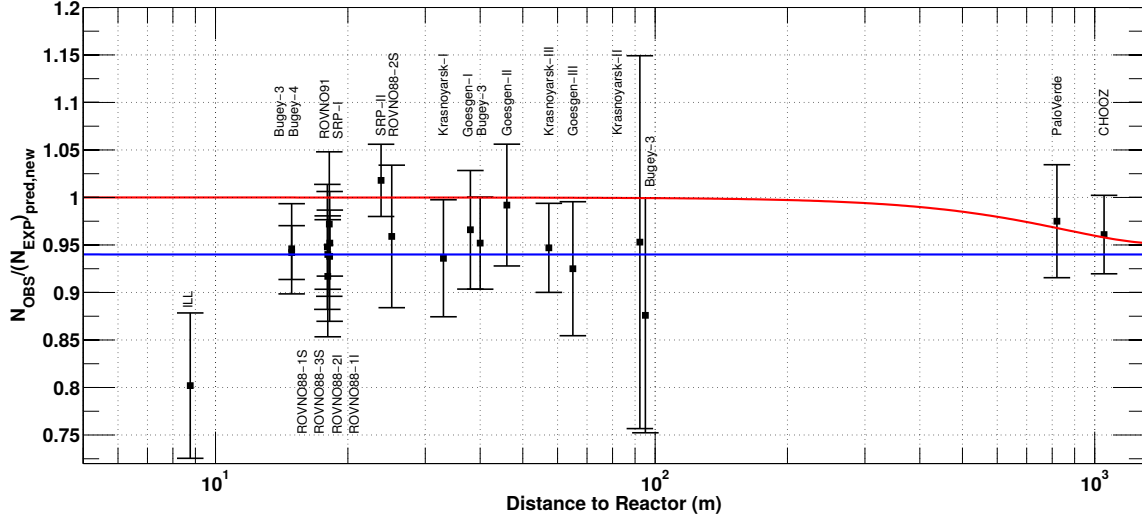


**Figure 1.10:** Illustration of the short baseline reactor antineutrino anomaly. Experimental results are compared with the predictions from a 3 active neutrino mixing solution (red line) and an alternative prediction including a new neutrino mass state (blue line) with  $|\Delta m_s^2| > 1 \text{ eV}^2$  and  $\sin^2(\theta_s) = 0.12$ . Figure taken from [Men11].

a mass with difference from the largest active neutrino mass eigenstate of  $\Delta m_s^2 > 1 \text{ eV}^2$ . In figure 1.11 the oscillation parameter space, favored by a combined analysis of recent reactor data, gallium solar neutrino calibration experiments and MiniBooNE- $\nu$  data, is depicted.

Cosmological data, mainly from observations of the cosmic microwave background and large scale structures, do not firmly exclude the hypothesis of a fourth neutrino, however they favor its mass to be  $m_s < 1 \text{ eV}$  [Bat14; Wym14].

A promising probe of the absolute mass scale of an eV sterile neutrino is made possible by tritium  $\beta$ -decay experiments, where an additional kink in the observed electron spectrum close to the tritium endpoint would be expected. In section 6.5 of this theses it is shown, that KATRIN will be capable of investigating the admixture of a fourth sterile mass state to the electron anti-neutrino with an unprecedented sensitivity, covering most of the parameter space (sterile neutrino mass and mixing) favored by the reactor anti-neutrino anomaly.

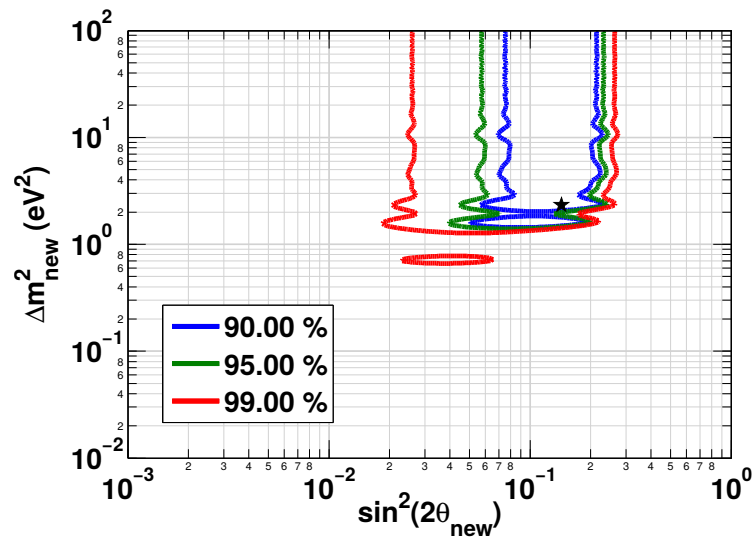


**Figure 1.11:** Allowed regions for a sterile neutrino (3+1 neutrino hypothesis) from the combination of reactor, MiniBooNE, Gallex and Sage data. The no-oscillation hypothesis is disfavored at 99.8% C.L. Constraints on the oscillation parameters can be stated with  $|\Delta m_s^2| > 1.5 \text{ eV}^2$  and  $\sin^2(2\theta_s) = 0.14 \pm 0.08$  (95% C.L.). Each experiment fitted separately leads to similar bounds, but without strong significance. Figure adapted from [Men11].



# CHAPTER 2

---

## The KATRIN Experiment

---

The Karlsruhe TRitium Neutrino (KATRIN) experiment is the next generation tritium  $\beta$ -decay experiment, targeted to perform a direct model-independent measurement of the absolute neutrino mass scale. With an envisaged sensitivity of 200 meV at 90 % C.L. (350 meV at 95 % C.L.) after five calendar years of operation, KATRIN will improve the current neutrino mass limits obtained by its predecessors by one order of magnitude (see section 1.4.4). Presently under construction at the Karlsruhe Institute of Technology (KIT) in Germany, the experimental apparatus will consist of a Windowless Gaseous Tritium Source (WGTS), two spectrometers of the Magnetic Adiabatic Collimation combined with an Electrostatic (MAC-E) filter type, a differential and cryogenic pumping section and a multi-pixel silicon detector. An overview of the setup is given in figure 2.2.



**Figure 2.1:** Official logo of the KATRIN collaboration.

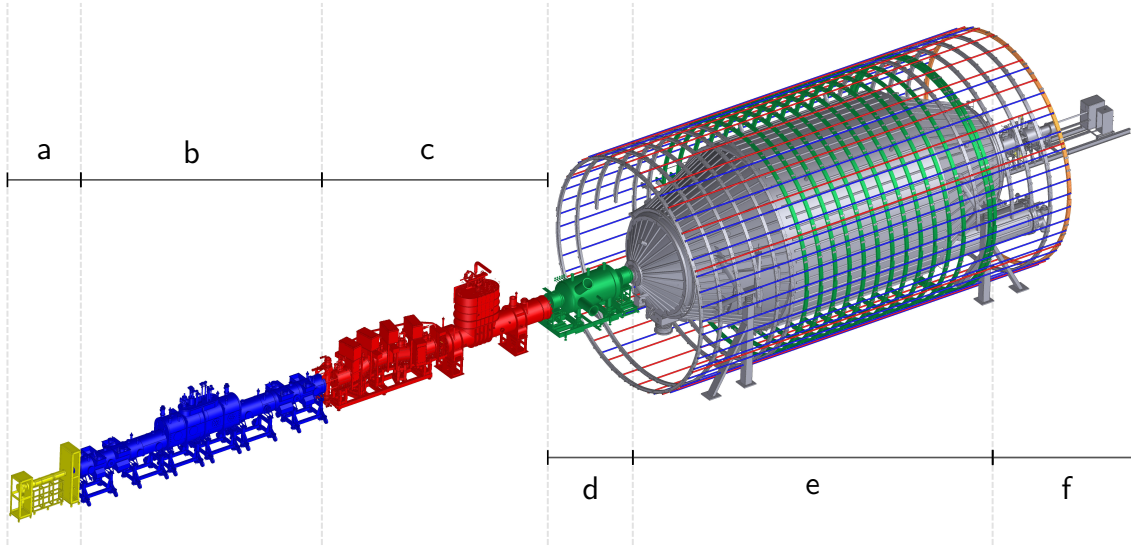


**Figure 2.2:** The KATRIN experimental setup, 70 m in length.

- (a) rear section, source monitoring and calibration
- (b) windowless gaseous tritium source (WGTS)
- (c) differential and cryogenic pumping section, removal of tritium
- (d) pre-spectrometer, filtering of low-energy  $\beta$  electrons
- (e) main spectrometer, high resolution  $\beta$  spectroscopy in the tritium endpoint region
- (f) detector section, position resolved counting of transmitted electrons

## 2.1 Measurement Principle

The fundamental measurement principle of KATRIN is high precision  $\beta$ -decay spectroscopy. Using an electrostatic high-pass filter, the energy of emitted  $\beta$ -decay electrons is analyzed to look for a distortion of the energy spectrum in the tritium endpoint region. A shape analysis of the observed spectrum allows a measurement of the effective electron neutrino mass  $m_{\nu_e}^2$ , an incoherent sum over the mass eigenstates  $m_i$ :

$$m_{\nu_e}^2 = \sum_{i=1}^3 |U_{ei}|^2 m_i^2 \quad (2.1)$$

KATRIN will upscale the dimensions of previous experimental setups considerably. In order to improve the sensitivity on  $m_{\nu_e}$  by one order of magnitude, many key parameters of the experiment have to be enhanced by two orders of magnitude, since the observable is the squared neutrino mass  $m_{\nu_e}^2$ . In order to push forward into the sub-eV regime, the KATRIN design does not only require better source statistics but foremost very tight constraints on critical systematic parameters of the apparatus, which will be outlined in the following sections.

## 2.2 MAC-E Filter Setup

So far, the Magnetic Adiabatic Collimation combined with an Electrostatic (MAC-E) filter type is the most promising measurement principle in model-independent neutrino mass experiments. It was successfully tested for the first time in Russia at Troitsk in the mid-eighties [Lob85] and independently at Mainz in the late eighties [Pic92].

A typical MAC-E filter experiment features the following components: A stable high luminosity source with well controlled systematics regarding solid-state effects, temperature and density fluctuations (figure 2.2 b). A transport system, separating the source from the analyzing spectrometer, which has to be under ultra high vacuum (UHV) conditions and free of any interfering residual tritiated gas (figure 2.2 c). A spectrometer, operating as a MAC-E filter, has to guarantee a high energy resolution (figure 2.2 e). Finally, a detector for counting the transmitted signal electrons (figure 2.2 f).

$\beta$ -decay electrons, produced in the source section, are emitted isotropically. In order to guide as many electrons as possible to the spectrometer, strong magnetic fields of a few T are set up in the source and transport section by superconducting solenoids. The Lorentz force guides the electrons onto a cyclotron motion along the longitudinal field lines, eventually leading the forward-emitted electrons towards the MAC-E filter. The kinetic energy  $E_{\text{kin}}$  of the electrons can be decomposed into a transversal  $E_{\perp}$  and a longitudinal component  $E_{\parallel}$ :

$$E_{\text{kin}} = E_{\perp} + E_{\parallel} \quad (2.2)$$

The MAC-E filter is elevated onto a negative potential through applying high voltage to the vessel itself and a wire electrode, attached to the inner walls of the spectrometer. The potential is typically within a narrow interval close to the tritium endpoint  $U \approx 18.6 \text{ keV}$ . With the source and detector section on ground potential, this configuration creates an electro-static retarding field, which runs parallel to the guiding magnetic field lines. The middle of the spectrometer, where the retarding field is strongest, is referred to as the *analyzing plane* (see figure 2.3). Electrons with a longitudinal kinetic energy  $E_{\parallel} > qU$  can overcome the potential barrier and be counted by the detector, while the rest will be reflected.

Only  $E_{\parallel}$  can be analyzed, which poses a problem for most of the isotropically emitted electrons with a considerable transversal energy fraction. The solution is an adiabatic conversion of  $E_{\perp}$  into  $E_{\parallel}$  while leaving the total electron energy  $E_{\text{kin}}$  unchanged. This is achieved by reducing the magnetic field strength  $B_{\text{max}} = 6 \text{ T}$  from the entrance (or exit) of the spectrometer by several orders of magnitude to the analyzing plane with  $B_{\text{min}} = 3 \cdot 10^{-4} \text{ T}$ . In doing so, the spectrometer is designed to avoid strong field gradients and provide adiabatic conditions (no significant change of magnetic fields along one cyclotron cycle). Then the magnetic moment  $\mu = \frac{E_{\perp}}{B}$  is guaranteed to be a conserved quantity in non-relativistic approximation. As the magnetic field strength  $B$  becomes lower, also  $E_{\perp}$  is decreased and adiabatically transformed into longitudinal direction.

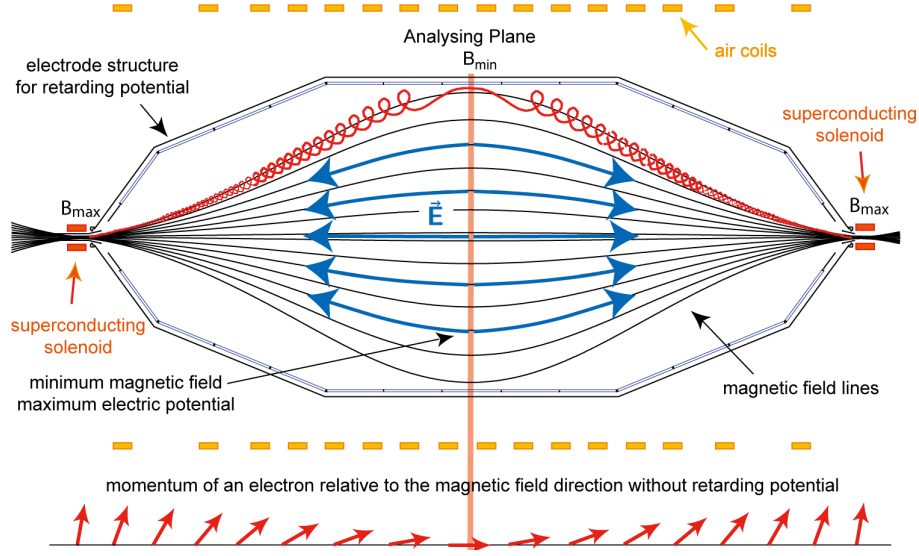


**Figure 2.3:** Working principle of a MAC-E filter. Electrons traveling on cyclotron paths along the guiding magnetic field lines undergo an adiabatic momentum transformation. The direction of their momentum vector is being parallelized along the field lines in regions of low magnetic field strength (analyzing plane), where the electrons can be precisely analyzed by the electrostatic retarding potential. Figure adapted from [Hug08].

The transformation from transversal to longitudinal momentum cannot be perfect, since a minimum field strength  $B_{\min} > 0$  in the analyzing plane is required to keep the magnetic flux tube contained inside the spectrometer vessel. The maximum transversal energy  $E_{\perp}$ , that an electron can keep, defines the energy resolution  $\Delta E$  of the spectrometer:

$$\frac{\Delta E}{E} = \frac{B_{\min}}{B_{\max}} \quad (2.3)$$

For isotropically emitted electrons with an energy close to the tritium endpoint  $E_0 = 18.6$  keV, the maximum fraction of energy not visible to the filter is

$$\Delta E = 18\,600 \text{ eV} \cdot \frac{3 \cdot 10^{-4} \text{ T}}{6 \text{ T}} = 0.93 \text{ eV} . \quad (2.4)$$

Essentially the MAC-E acts as an *integrating high-pass filter*. Its transmission characteristics are summarized by the so-called transmission function (see section 5.5.1), with its shape being defined by the configuration of electric and magnetic fields. Varying the retarding voltage and shifting the electrostatic barrier gives access to the shape of the energy spectrum of analyzed  $\beta$ -decay electrons. Due to the MAC-E filtering principle, an integrating measurement of the spectrum is performed:

$$N(qU) \propto t_{qU} \int_{qU}^{E_0} \frac{dN}{dE} (E, m_{\nu}^2) R(E, qU) dE \quad (2.5)$$

$N(qU)$  denotes the number of expected signal electrons at a given retarding energy  $qU$  for a measuring time  $t_{qU}$ . In order to reveal information about the differential spectrum  $dN/dE$ , not only a substantiated knowledge of  $\beta$ -decay theory is required. The response of the apparatus  $R$ , describing the probability for an emitted  $\beta$  electron to be detected, has to be known precisely (section 5.5.4). It comprises all characteristics of the experimental setup, which influence the observed signal, including the transmission function  $T$  of the spectrometer (section 5.5.1).

The energy resolution  $\Delta E$  of the MAC-E filter does not ultimately limit the neutrino mass sensitivity, which for KATRIN is anticipated to be much smaller. A non-zero neutrino mass does not only cause a shift of the observable spectrum endpoint, but a characteristic shape distortion of the integrated spectrum, reaching several eV below the endpoint. This feature allows the extraction of a neutrino mass estimate with higher accuracy.

Not all  $\beta$  electrons with emission direction in the forward half sphere are allowed to reach the detector. High polar emission angles imply larger transversal momentum and increased electron path lengths through the source tube due to their cyclotron motions. Such trajectories are less desirable, since they come with a higher probability of electrons scattering with tritium molecules and enhanced synchrotron radiation losses. Here the experiment exploits the *magnetic mirror* effect [Hig07] to reject electrons with a high polar (or pitch) angle  $\theta$ . With a lower magnetic field strength in the source  $B_S = 3.6$  T and a maximum field strength  $B_{\max} = 6.0$  T in the transport and spectrometer section, the polar emission angle is constrained to

$$\theta_{\max} = \arcsin \left( \sqrt{\frac{B_S}{B_{\max}}} \right) \approx 50.8^\circ. \quad (2.6)$$

### 2.3 Tritium Source

The Windowless Gaseous Tritium Source (WGTS) is a high luminosity  $\beta$  emitting source, embedded in a complex cryostat. In its center the WGTS contains a stainless steel beam tube (length  $l = 10$  m, diameter  $d = 90$  mm), where high purity gaseous tritium is injected at the middle. The gas will diffuse to both ends of the tube, where it is pumped out by twelve Turbo Molecular Pumps (TMPs) in total, reducing the gas flow by a factor of  $10^2$ . The pumps are housed by the rear and front differential pumping sections (DPS1-F, DPS1-R), which increase the total length of the source section to 16 m. The pumped out gas is collected, reprocessed and reinjected via a closed cycle, the inner loop system. This pumping method avoids windows at the end of the source, which could inflict energy losses on the emitted  $\beta$  electrons.

To achieve reasonable gas densities of  $\rho \approx 5 \cdot 10^{14} \text{ cm}^{-3}$  at moderate throughput, the beam tube is operated at  $T = 30$  K. With an injection pressure of  $p_{\text{inj}} \approx 3 \cdot 10^{-3}$  mbar, the corresponding reference value for the column density  $\rho d = 5 \cdot 10^{17} \text{ cm}^{-2}$  can be adjusted. This choice of a nearly opaque source is motivated by the requirement of a high source activity  $A \approx 10^{11}$  Bq, while keeping scattering probabilities of  $\beta$  electrons as low as possible.

The source section is a critical component in terms of systematic effects. It contributes a large fraction to the overall systematic uncertainty budget:

- Due to the thermal and bulk motion of tritium molecules, the electron spectrum is modified by a Doppler shift during  $\beta$ -decay (section 5.3). To minimize this effect, the beam tube is cooled down to 27 – 30 K.
- The column density needs to be precisely known and controlled at a  $10^{-3}$  level. A stable pressure profile of  $p = 3 \cdot 10^{-3}$  mbar at the injection point to  $p < 10^{-4}$  mbar at the pump ports is established by constant injection and pumping rates.
- The demanded stability of the column density requires the temperature over the whole beam tube to be stable within  $\pm 30$  mK. This challenge is met with a two-phase neon cooling system, which has already been successfully tested and commissioned [Gro11].
- A reliable near-time monitoring of the isotopic tritium purity ( $\varepsilon_T \approx 95\%$ ) is provided by a dedicated Laser Raman system LARA [Sch13b].

## 2.4 Transport Section

The transport section joins to the front end of the Windowless Gaseous Tritium Source (WGTS) cryostat and consists of two functional units: The differential pumping section (DPS2-F) and the cryogenic pumping section (CPS). While signal electrons must be guided from the source to the spectrometer section undistorted, both tritium retention systems together have to reduce the tritium gas flow by 14 orders of magnitude (in combination with the differential pumps of the WGTS). Thus the partial pressure of tritium in the main spectrometer is pushed below  $10^{-20}$  mbar and the background due to tritium  $\beta$ -decay in the spectrometer is kept below the design limit [Mer13].

The DPS2-F differential pumping section connects five beam tubes tilted by  $20^\circ$  against each other to avoid a direct line of sight for neutral tritium molecules. This way the pumping of the four large TMPs, housed in pump ports between the beam tube elements, is more efficient, with a gas flow reduction by 5 orders of magnitude. A system of superconducting solenoids with field strengths up to  $B = 5.5$  T guides the signal electrons adiabatically through the 7 m long unit.

The adjoining CPS cryogenic pumping section will provide a tritium flow reduction by another 7 orders of magnitude. Based on the principle of cryo-sorption, tritium molecules are adsorbed by argon frost at 3 K on the inner surface parts of the CPS beam tube. As with the DPS2-F, the beam tube elements form a chicanery to guarantee that residual gas will make contact with the surface at least once.

Charged tritium ions, which are guided by the magnetic field lines and cannot be pumped, have to be removed by a system of electric dipoles [Jan]. A diagnostic unit using the FT-ICR (Fourier Transform-Ion Cyclotron Resonance) detection technique will be installed in the DPS2-F to monitor the ion content originating from the source section [Ubi09].

## 2.5 Spectrometer Section

The energy of  $\beta$ -decay electrons from the transport section is analyzed by a tandem setup of electrostatic spectrometers, both implementing the MAC-E filter principle explained in section 2.2.

### 2.5.1 Pre-Spectrometer

The pre-spectrometer with a length of  $l = 2.4$  m and diameter  $d = 1.7$  m can be operated as a filter for the low-energy part of the  $\beta$  electron spectrum, up to an adjustable potential barrier of 18.3 keV. The high-energy part of the spectrum, which is relevant for KATRIN analysis (starting at 50 eV below  $E_0$ ), would not be affected by this operation mode. In this case, the overall electron flux can be reduced by up to 7 orders of magnitude, minimizing the chance of additional background due to residual gas ionization [Pra11]. However, when operated as pre-filter, a large Penning trap will be formed, which can be avoided by operating the pre-spectrometer at very low potential [Fra14]. Until 2011 the pre-spectrometer was operated as a standalone unit to study electron transport and background characteristics [Frä10].

### 2.5.2 Main Spectrometer

With a length of  $l = 23.3$  m and a central diameter of  $d = 9.8$  m the main spectrometer is one of the largest and most prominent components of the experimental setup. Here the high precision energy analysis of  $\beta$  electrons is performed.

The MAC-E filter configuration is realized by superconducting magnets on either side of the spectrometer with field strengths up to  $B_{\max} = 6$  T. In the center of the spectrometer, the so-called analyzing plane, the field strength drops by a factor of 20 000 to  $B_A = 3 \cdot 10^{-4}$  T. As explained in section 2.2, this ratio determines the energy resolution of the filter. It also leads to a significant broadening of the magnetic flux tube and necessitates the size of the tank. With an effective area of the analyzing plane  $A_P = 63.6$  m<sup>2</sup>, the magnetic flux transported through the spectrometer is  $\phi = B_A \cdot A_P = 0.01908$  Tm<sup>2</sup>. Fine-shaping of the magnetic field configuration and compensation of the earth magnetic field is realized with a large-volume air coil system [Glü13].

The retarding potential is defined by a precision high voltage (HV) system, where the vessel itself is elevated to act as Faraday cage. The final HV precision is achieved through electrodes inside the tank, implemented as a complex two-layer wire electrode system, which is installed with only few centimeters of distance from the inner walls [Val10]. Set on a slightly higher negative potential with respect to the vessel, the wires allow fine tuning of the electrostatic field and provide shielding against background electrons ejected from the 690 m<sup>2</sup> vessel wall by throughgoing cosmic ray muons.

### Pumping Systems

Any collision of signal electrons with residual gas within the main spectrometer clearly has to be avoided, which is why the entire vessel with a volume of 1250 m<sup>3</sup> is operated at UHV conditions of  $p < 10^{-11}$  mbar. This low pressure regime is achieved by a cascaded pumping

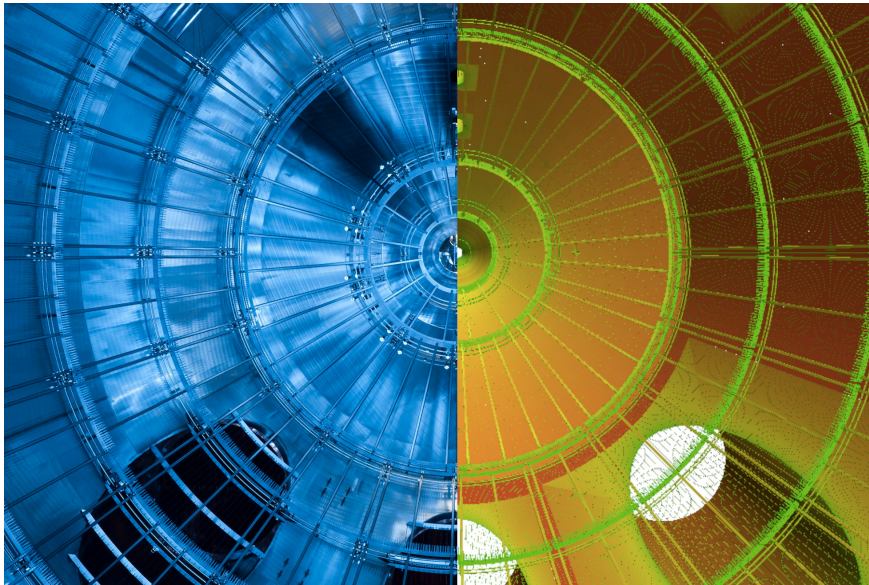


**Figure 2.4:** View into the main spectrometer along the beam axis facing towards the detector. The inner surface is covered with the two-layer wire electrode system. In this picture the three pump ports, visible at the bottom, are still empty. The left half shows a real photograph, while the right half depicts a discretized 3D model with the color indicating the electric potential calculated with the KATRIN field solving software KEMField. By courtesy of T.J. Corona [Cor14].

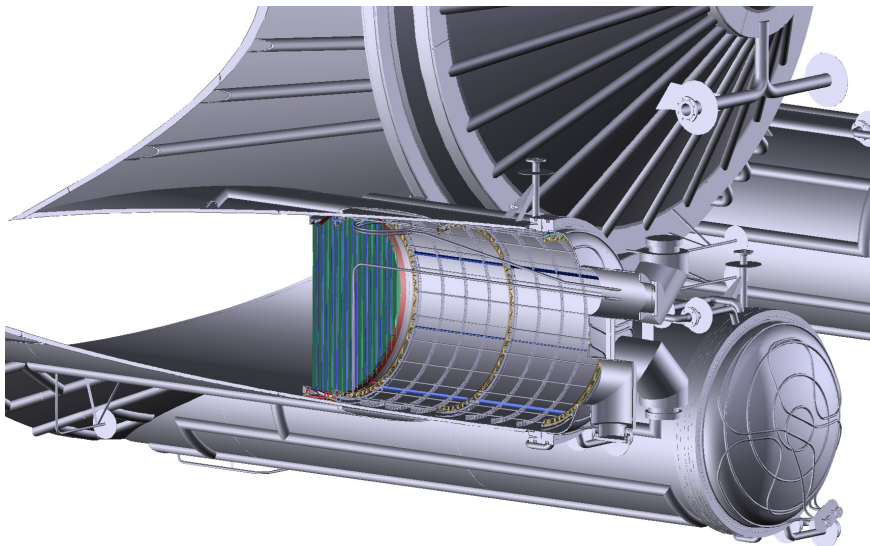


**Figure 2.5:** Cross section through one of the three main spectrometer pump ports, exposing the non-evaporable getter (NEG) pump and the liquid nitrogen cooled baffles (vertical blue blades on the left end of the pump port).

system [Wol09], keeping the partial pressure from outgassing  $H_2$  and other gas species at a minimal level. In each of the vessel's three pump ports, large amounts of non-evaporable getter (NEG) strips (totaling a length of 3 km) are installed to absorb hydrogen with high efficiency. Additionally, each getter pump is supported by two TMPs.

Previous investigations have revealed, that the NEG strips with their large porous surface (in addition to the inner spectrometer surface) release substantial amounts of radon  $^{219}Rn$ , which gives rise to an increased background, if it decays in the spectrometer volume (also see section 5.9.2). A suppression technique, which was successfully installed and tested in the current setup, are the liquid nitrogen  $LN_2$  cooled copper baffles [Goe14], visible in figure 2.5. They consist of V-shaped cooper blades acting as apertures, which block the direct line of sight between the NEG strips and the inner spectrometer volume. Being cooled with liquid nitrogen, the baffles are capable of cryo-condensing nearly all emanated radon atoms on their cold surface.

## 2.6 Detector Section

Electrons, which pass the analyzing plane of the main spectrometer, are re-accelerated and guided onto the focal plane detector (FPD) or simply main detector [Ams14]. The system 'merely' acts as an electron counting device – the energy resolution is performed by the main spectrometer. The detector wafer, as shown in figure 2.7, consists of a monolithic silicon PIN (positive-intrinsic-negative) diode array, segmented into 148 pixels, with a sensitive area of 90 mm in diameter. Thanks to the segmentation, the electron trajectories along the fieldlines through the spectrometers and the source section can be reconstructed during the analysis.

A schematic of the detector section setup is given in figure 2.6. With a moderate energy resolution of  $\sim 1.6$  keV for signal electrons at 18.6 keV, the detector performance can be improved by a post-acceleration electrode, yielding a potential offset to signal electrons for better discrimination from the continuum Compton background. Shielding from gamma

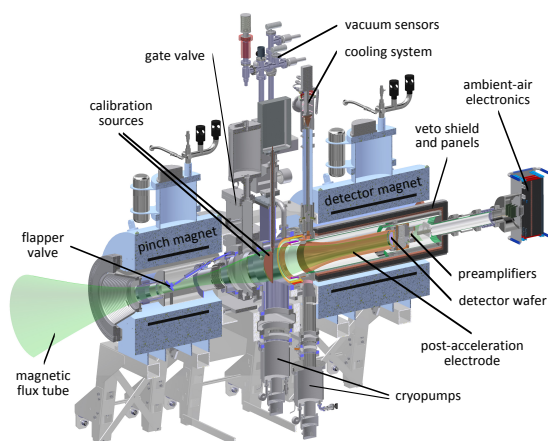


**Figure 2.6:** Focal plane detector setup.



**Figure 2.7:** 148 pixel silicon wafer, each pixel having equal surface area.

radiation and cosmic background is provided by passive copper and lead shells and an active plastic scintillator veto system, which allows the rejection of coincident detector events. The setup is equipped with two energy calibration systems, an americium  $^{241}\text{Am}$  gamma source and an UV-illuminated titanium disk.

## 2.7 Monitoring

### 2.7.1 Rear Section

Continuous monitoring of critical source parameters is guaranteed by the rear section. The rear wall of the WGTS will be used to control the electric potential of the source plasma and to monitor tritium activity via  $\beta$  induced x-ray spectroscopy (BIXS) [Röl12]. Additionally, a high-intensity angular-selective electron gun will be installed [Val11]. By sending a stable beam of electrons through a hole in the rear wall, the column density of the source gas and the scattering characteristics of electrons in the source can be measured repeatedly (see section 5.5.6). Magnetic dipoles will allow to shift the electron beam across the magnetic flux tube and provide a radial and azimuthal coverage of these measurements.

### 2.7.2 Monitor Spectrometer

In parallel to the main beam line the former Mainz spectrometer is installed as the monitor spectrometer of the KATRIN setup [Erh14]. A schematic of the monitor spectrometer is depicted in figure 2.8. Being connected to the same high voltage supplies as the main beam

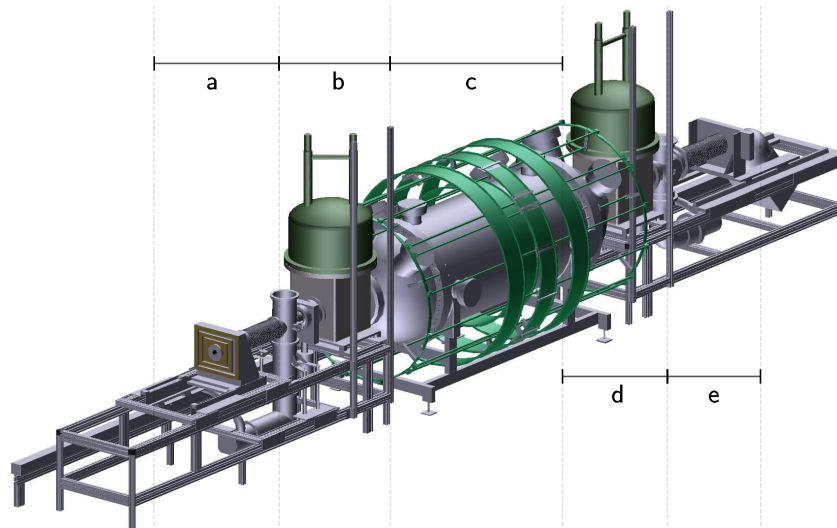


**Figure 2.8:** Monitor spectrometer setup, consisting of  
 (a) the solid state source holder,  
 (b+d) superconducting solenoids,  
 (c) a spectrometer (MAC-E filter) with air coils for field adjustment in the analyzing plane and earth magnetic field compensation,  
 (e) the housing for the five-pixel silicon detector.

line, it is used to monitor the stability of the main spectrometer retarding potential with high precision. By continuously measuring the width and position of the K-32 conversion line of a solid-state krypton  $^{83\text{m}}\text{Kr}$  source, drifts or fluctuations in the retarding voltage can be detected on the ppm-scale.

## 2.8 Instrumentation and Data Producers

### 2.8.1 Detector Data Acquisition System

The silicon detectors utilized by KATRIN (focal-plane, veto, monitor spectrometer, beam profile monitoring detector) produce raw data rates at a signal bandwidth of several MHz in up to 148 channels each. This amount of data is processed by a Detector Data Acquisition (DAQ) system, which was originally developed by the Institute for Data Processing and Electronics (IPE) at Karlsruhe Institute of Technology (KIT) for the Pierre-Auger-Observatory [Aug96]. The Field Programmable Gate Array (FPGA) based architecture allows data preprocessing at a wide range of event rates from mHz to MHz with a timing resolution of 50 ns.

The electronics consist of first-level trigger (FLT) and second-level trigger (SLT) cards. Each FLT card handles 24 channels of analog signal conditioning and processing. An additional central-control FPGA performs time synchronization and readout for each card. In case of the focal-plane detector system, 8 FLT cards serve the main detector, while two serve the veto. A single SLT card provides a single-board computer, which coordinates all FLT cards and communicates with the DAQ operating computer via a fast Ethernet interface. A synchronization unit, equipped with a high-precision clock, synchronizes the internal counters of the DAQ electronics with a 10 MHz signal.

The operator interface and run-based data recording is provided by the Object-oriented Real-time Control and Acquisition (ORCA) software, which was designed by KATRIN collaborators at the University of Washington at Seattle and at the University of North Carolina [Phy14]. It comes with the required libraries to interface with the DAQ hardware outlined above and allows interpretation of the recorded data in C++ based analysis tools. A screenshot of the graphical user interface is shown in figure 2.9.

A list of the detector systems operated by ORCA and a description of the recorded physical data will be given in section 3.3.2.

### 2.8.2 Slow Control Systems

The KATRIN experiment is a complex apparatus with thousands of system variables, which require constant monitoring and automated control. A distributed system, which handles these tasks running on independent controller hardware, is commonly referred to as *Slow Control* system. On the one hand, it is a crucial aspect of the experiment's safety concept, if one thinks of the challenges of maintaining the so-far largest UHV system, dealing with superconducting magnetic fields, high voltages and cryogenic temperatures. On the other hand, the Slow Control System (SCS) has to provide the necessary flexibility in scientific operation and ensure reliable monitoring of a large number of sensors.

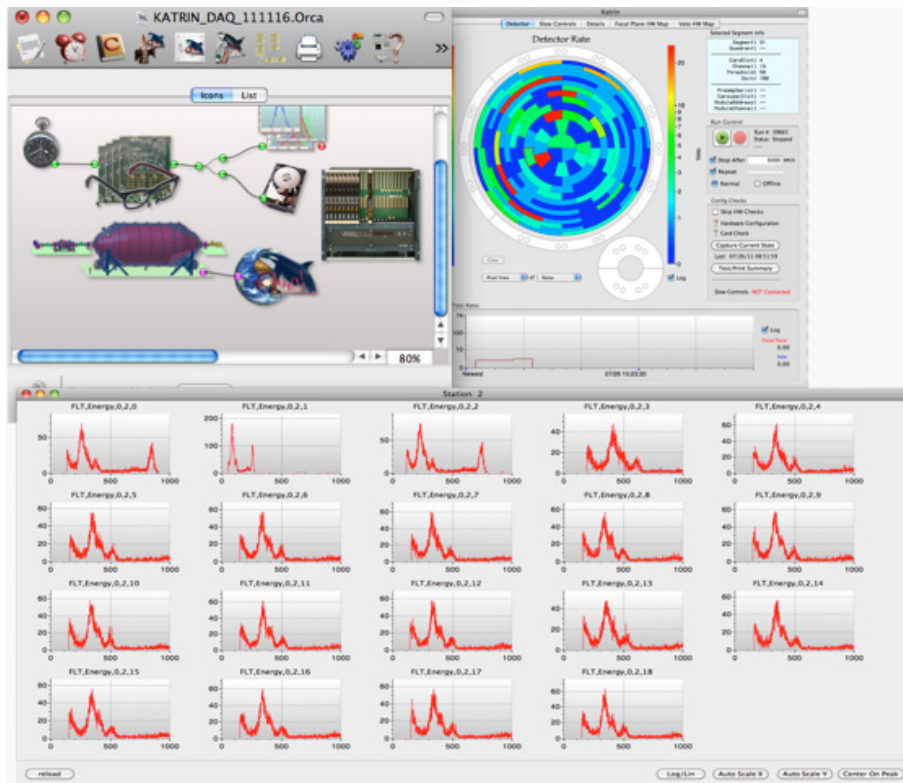


**Figure 2.9:** Screenshot of ORCA’s graphical user interface, showing real time event monitoring of the focal-plane detector system.

Experimental control and monitoring is maintained by the IPE and in large parts realized with Siemens SIMATIC Process Control System 7 (PCS7) and the Central Acquisition and Control (ZEUS) system, the latter being a KIT development, based on National Instruments’ LabView. Both systems store the recorded data in various formats and in multiple databases. The IPE maintains a PHP [PHP14] based server software called Advanced Data Extraction Infrastructure (ADEI) [Chi14], which collimates the Slow Control data from its heterogeneous source systems into a single MySQL [Ora14] database in a unified format.

The web interface provided by ADEI (see figure 2.10) allows close to real time visualization of Slow Control data with a latency of about one second. A central SQL database, maintained and synchronized by ADEI, is used by KATRIN’s analysis infrastructure to perform further processing in conjunction with sensor calibration data, and to provide Slow Control access for external client software.

A more comprehensive list of KATRIN Slow Control data producers will be given in section 3.3.3.

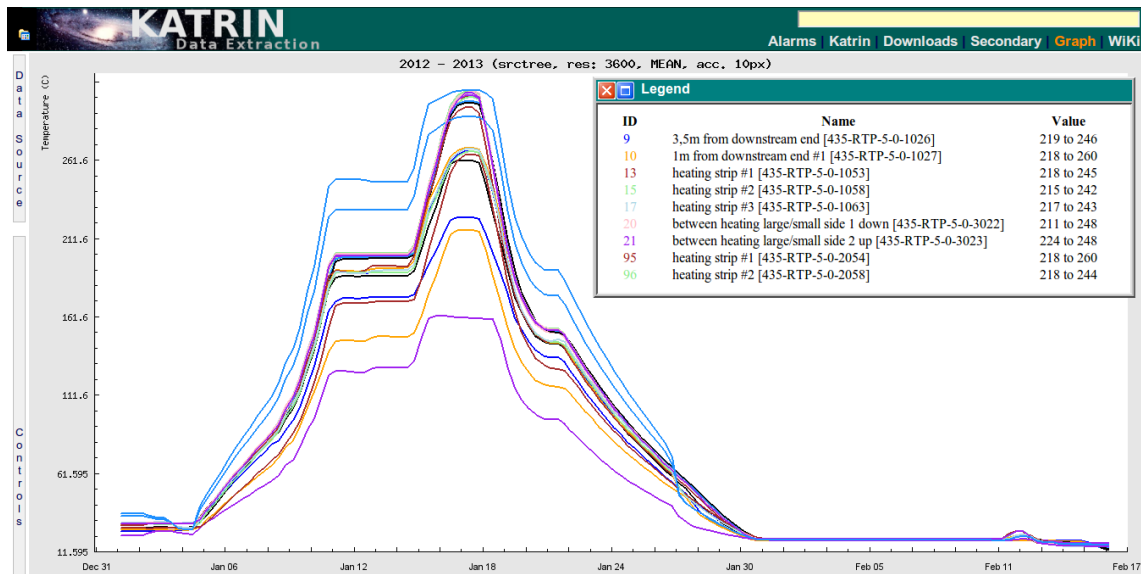


**Figure 2.10:** ADEI web frontend showing a graph of several temperature sensors (in °C) during the spectrometer bake-out in January 2013.

## 2.9 Recent Commissioning Milestones

The low field air coil system (LFCS), allowing for fine shaping of the magnetic field in the spectrometer section and compensation of the earth magnetic field (EMCS) [Glü13], has been installed in mid-2011. The two-layer wire electrode consisting of 23 440 wires, which covers the inside of the main spectrometer vessel and prevents secondary electrons produced by cosmic radiation from entering the flux tube, was installed in mid-2012 [Val10]. In January 2013 the main spectrometer was successfully baked out to a temperature of 300 °C.

The detector section and the main spectrometer were connected and an angular resolved egun [Val11] was installed on the source side of the spectrometer in May 2013 to start an initial commissioning phase, referred to as the Spectrometer and Detector Section (SDS) commissioning phase I (SDS-I). These measurements verified system functionality, while performing successful tests on the spectrometer transmission properties, detailed background studies, as well as hardware and software optimization.



# CHAPTER 3

---

## Data and Software Infrastructure

---

The KATRIN experiment is a large apparatus with literally thousands of distributed sensors. Data formats as well as recording intervals and accumulated amounts of data per sensor are as diverse as the physical quantities, that are being monitored. Some data require a considerable amount of processing, format conversion and calibration, before they can be used by the analyst.

Most of these procedures should preferably be performed automatically, without the user (e.g. a physics graduate student) having to deal with the laborious details of how and where the particular data of interest are stored. At the same time, any manipulation of raw data should be documented, traceable and reversible, giving a more demanding user enough freedom to work with raw data directly and apply custom calibration if necessary.

One of the goals, set for the present thesis, was to design and implement an infrastructure, which not only can handle the logistical challenge of processing and organizing thousands of distributed sensors reliably, but also providing an intuitive and consistent interface to different types of data used in analysis. In this chapter an outline will be given over KATRIN's recently introduced IT infrastructure, covering the data processing chain, distribution mechanisms and software organization.

### 3.1 Multi-Tier Architecture

A design decision, which was made in the very early stages of this work, was to physically separate the analysis software chain into a client and server layer. The implemented software architecture pattern is commonly called a three-tier model:

#### Data tier (1)

This layer involves processing and persistence (storage) of KATRIN data (section 3.3).

### Server logic tier (2)

The logical layer comprises those software modules, that are allowed to directly operate on the data, and manage incoming write or read requests from client applications. Usually these tasks are fulfilled by service applications (section 3.4), running on a remote server.

### Client tier (3)

Those parts of the software that provide a user interface and are used to request data for analysis or to initiate modifications to the database, belong to the client tier (section 4).

The approach of such a modular client-server architecture has significant advantages over a classical design, where the user must access the data directly and manually. By restricting direct control over the data to an intermediate service layer, one can consistently regulate how and by whom data should be accessed (user authorization). Modifications can be backtraced and logged.

What may seem like a restriction at first glance is actually a great benefit for the data consumer. He is given a clean and well defined interface to the data. How the data are accumulated, organized and calibrated, does not necessarily have to be of his concern anymore. The technical details of transferring data to the user are also greatly simplified, as will be described in more detail in section 3.4.

Another aspect of the modular multi-tier design is its flexibility. As long as the interface definition between server and client remains unchanged, the actual implementation of either one can be upgraded or replaced independently. Client analysis code and server-side data management code can run on different platforms and could theoretically be implemented in different programming languages.

### Short History of Development

The development process of the presented architecture involved contributions from a number of collaborators. Between the years 2010 and 2012 working prototypes of the data processing facilities, the data management services and the data access logic were established and tested in a joint effort with Sebastian Vöcking from the University of Münster. Considerable parts of the former code base were written in the context of his doctoral thesis [Vöc], which the reader may refer to for more information about the prototype system.

From 2013 to 2014 all three layers of the architecture underwent a substantial redesign as part of this present thesis. Some modifications to the data acquisition software did not allow full backwards compatibility, so the opportunity was taken to rework critical details of the framework, implement new functionality and redefine user interfaces in order to incorporate experiences from two years of testing phases. The new setup was successfully taken into operation during the SDS commissioning phase in mid 2013 (see section 2.9). In the following sections of chapter 3 and 4 an outline of the software architecture in its current operational stage will be given.

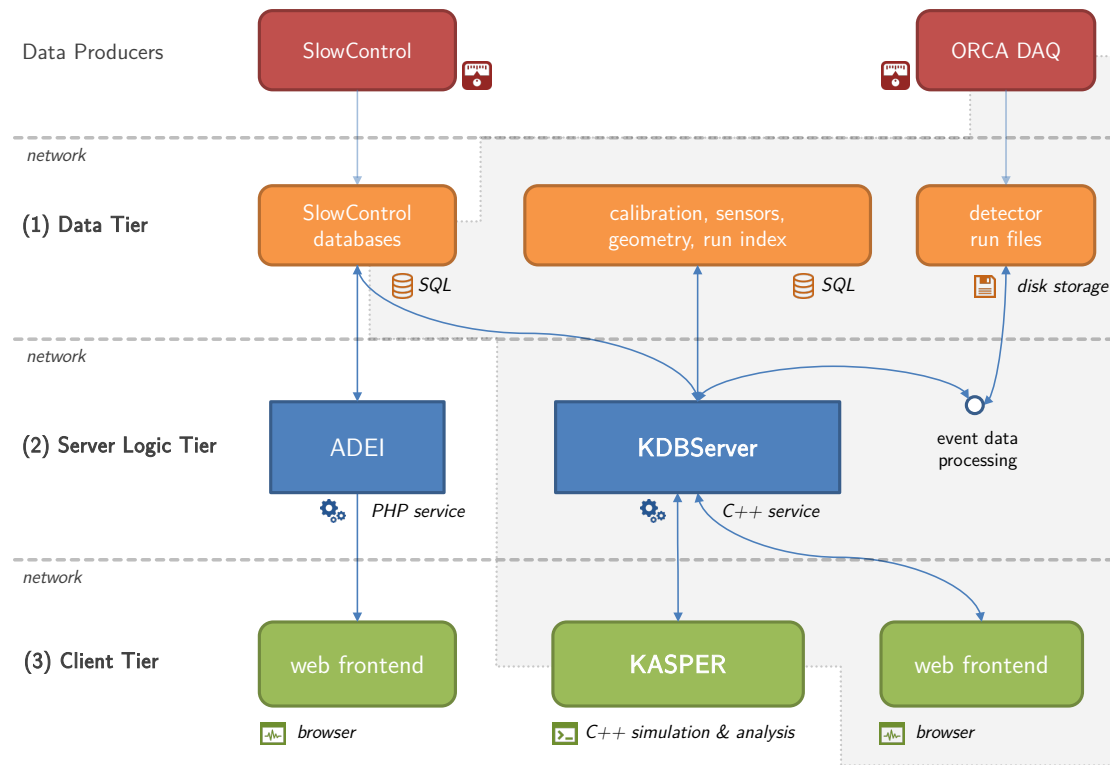


**Figure 3.1:** Diagram of the multi-tier IT infrastructure of the KATRIN experiment. A detailed explanation of the individual components is given in chapter 3 (tier 1 and 2) and chapter 4 (tier 3). Components within the shaded area were designed and in large parts implemented as part of this thesis.

### 3.2 Source Code Standards and Organization

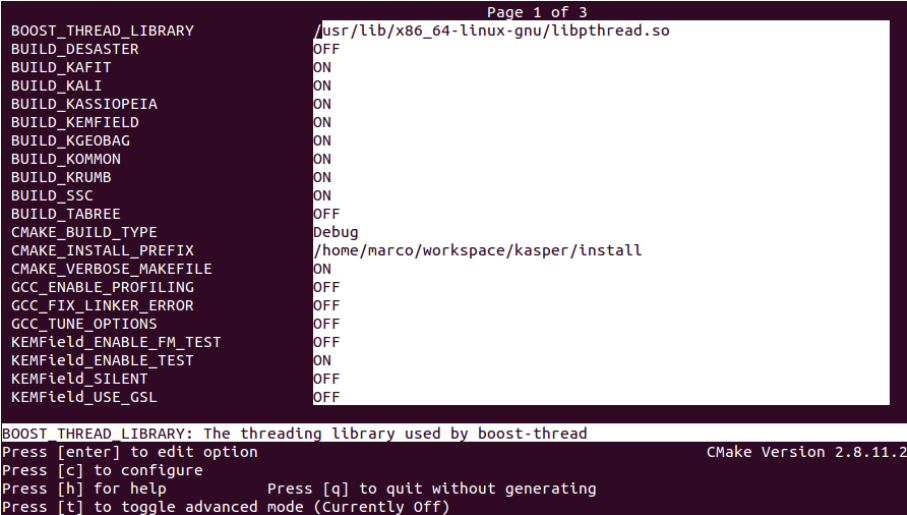
In 2011 software developers from the KATRIN collaboration made a coordinated effort of introducing common coding standards and moving all crucial software into one coherent framework. The situation before was not uncommon, but nevertheless unsatisfying. Collaborators working on their own specific problem, for example field solving, would be pretty much unaware of developments in other areas, such as detector data analysis. This naturally led to a lot of redundant code development and misconception. Developers would address similar problems in parallel, but solve them in a technically incompatible way. Interfacing simulation and analysis was an unpleasant challenge and in some cases not even possible technically.

### 3.2.1 KASPER - Unified Analysis and Simulation Package

It was agreed to organize most of the existing crucial analysis and simulation tools in one common C++ software framework called *KASPER*. Currently supported operating systems are Linux and MacOS<sup>1</sup>. For specific tasks a limited number of external open source libraries is required. The popular general-purpose *boost* library [Daw14] is included for features like linear algebra, statistical distributions, unit testing, cross-platform file system operations and multi-threading. The *ROOT* analysis library from CERN [Ant09] is utilized by some of the *KASPER* modules for event data representation and graphical output. Code documentation is automatically generated from C++ source code annotations using *Doxygen* [Hee08].

Each module within *KASPER* can be compiled individually with minimal dependencies, if required. This is important, for instance, when code must be executed on Graphics Processing Unit (GPU) clusters with tight constraints on third party libraries. However, most users can compile the *KASPER* package as a whole. On the one hand, the common build system enforces all parts of the analysis and simulation code to remain compatible and to be linked correctly against each other. On the other hand it makes the installation and configuration process (figure 3.2) more comfortable for new users of the framework.

*KASPER* has grown into a comprehensive library, utilizing modern C++ techniques. It unifies common tasks and features, required by many of its components. Currently it is subdivided into the following list of modules:



```

Page 1 of 3
BOOST_THREAD_LIBRARY /usr/lib/x86_64-linux-gnu/libpthread.so
BUILD_DESASTER OFF
BUILD_KAFIT ON
BUILD_KALI ON
BUILD_KASSIOPEIA ON
BUILD_KEMFIELD ON
BUILD_KGEOBAG ON
BUILD_KOMMON ON
BUILD_KRUMB ON
BUILD_SSC ON
BUILD_TABREE OFF
CMAKE_BUILD_TYPE Debug
CMAKE_INSTALL_PREFIX /home/marco/workspace/kasper/install
CMAKE_VERBOSE_MAKEFILE ON
GCC_ENABLE_PROFILING OFF
GCC_FIX_LINKER_ERROR OFF
GCC_TUNE_OPTIONS OFF
KEMField_ENABLE_FM_TEST OFF
KEMField_ENABLE_TEST ON
KEMField_SILENT OFF
KEMField_USE_GSL OFF

BOOST_THREAD_LIBRARY: The threading library used by boost-thread
Press [enter] to edit option
Press [c] to configure
Press [h] for help
Press [q] to quit without generating
Press [t] to toggle advanced mode (Currently Off)
CMake Version 2.8.11.2

```

**Figure 3.2:** CMake [Kit14] configuration dialog of the *KASPER* package. Individual modules can be activated and configured to meet the user’s needs and requirements of his operating system.

<sup>1</sup> Recommended and tested compilers are GCC (4.5+) and Clang (3.0+). The build system CMake (2.6+) [Kit14] is used to package and compile the code.

**Kommon**

This basic module provides very common functionality, such as physics constants definitions, mathematical utilities, IO tools, logging facilities and an extensible random number generator.

**Kassiopeia**

Particle tracking Monte Carlo (MC) simulation, see section 4.5.1.

**KEMField**

Electro-magnetic field solving algorithms with optional parallelization on GPU clusters [Cor14].

**KGeoBag**

Geometry definitions and logic.

**SSC**

Source modeling and  $\beta$ -decay spectrum calculation, section 5.

**KaLi**

Data access library, providing definitions of data formats, access to the KATRIN data base through a web service layer, and basic analysis logic, section 4.2.1.

**BEANS**

Comprehensive suite of detector analysis tools and detector electronics simulation (DRIPS), section 4.4.

**KaFit**

Statistical tools and probability models to study the impact of systematics and measurement strategy on the neutrino mass sensitivity, section 6.

**KTrap**

Spectrometer transmission analysis and simulation [Gro15].

Some of the above listed KASPER modules will be explained in more detail, including physics examples, in later chapters of this thesis. Figure 3.3 provides a graphical overview of the most important modules and their relationships.

Novice users can start with one of the ready-to-use executables, included in KASPER. Most of the provided analysis and simulation tools can be customized with simple XML configuration files. For developers of new analysis or simulation logic, KASPER provides a consistent and documented set of object-oriented libraries. With these, all of KASPER's functionality can be combined within one compilation unit or executable program respectively. The resulting application can range from detector readout, Slow Control access, to simulation of magnetic fieldlines and estimation of a neutrino mass from generated or real

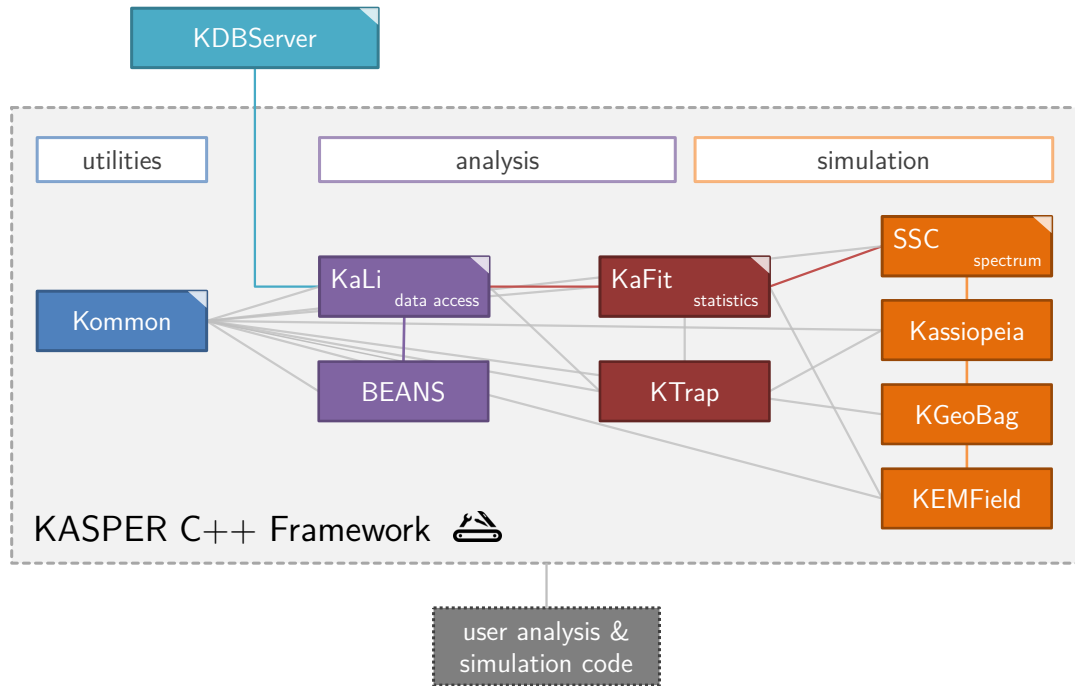


**Figure 3.3:** Schematic overview of KASPER’s main components and their relation to each other. A brief explanation of each individual module is given in the main text (section 3.2.1). Modules tagged with a white triangle were developed or significantly extended in the course of this thesis (Kommon, KaLi, KDBServer, SSC, KaFit).

data. All involved parts of the code rely on common physics constants and random numbers produced by one single generator. Input of configuration files and output of results can be realized consistently with common utilities shared across the entire project.

Since KASPER mainly comprises analysis and simulation tools running on a user’s local computer, it belongs to *tier 3* of KATRIN’s IT infrastructure.

### 3.2.2 KDBServer - Database Management and Data Access Services

The KDBServer package is a C++ project linking against KASPER. It is the server-side counterpart to the data consumer KASPER, since it implements the functionalities of KATRIN’s *tier 2*, the data management layer. In principle it is equipped with all of KASPER’s analysis capabilities, but comes with some important additions. It is designed to run as a web server application on KATRIN’s central data servers, where it handles automated data processing and serves user requests for all of KATRIN’s accumulated experimental data. KDBServer is organized as an external software package outside KASPER, since it holds very specific code logic related to database and web technologies, requiring additional third party libraries.

module / package	code lines	total lines	C++ files
<b>Kommon</b>	20 652	27 587	188 <sup>1</sup>
Kassiopeia	34 482	47 023	365
KEMField	62 850	90 757	565
KGeoBag	58 141	78 510	614
<b>SSC</b>	8618	14 995	99 <sup>1</sup>
<b>KaLi</b>	13 023	19 537	139 <sup>2</sup>
BEANS	35 035	44 843	348
<b>KaFit</b>	12 672	19 867	107 <sup>2</sup>
<b>KDBServer</b>	19 311	28 617	240 <sup>2</sup>
	264 784	371 736	2665 <sup>2</sup>

**Table 3.1:** Source code metrics for modules of the simulation and analysis package KASPER and the server side data processing package KDBServer. CMake code (configuration and build system), documentation, configuration, input data and any form of generated code are *excluded* from the statistics.

<sup>1</sup> The modules Kommon and SSC were modified and extended for this thesis.

<sup>2</sup> The modules KaLi (2.0), KaFit and the web service KDBServer (2.0) were designed and implemented from scratch in the course of this thesis.

A more thorough and technical outline of KDBServer can be found in section 3.4, along with a discussion of the chosen programming language and technologies. In the IT landscape, C++ is a rather unpopular choice for a web service application, as opposed to more ‘modern’ programming languages like Java, PHP or Python. For a physics experiment like KATRIN however, the call for C++ comes with considerable benefits regarding interoperability and consistency of the overall analysis chain, and last but not least, performance and scalability.

### 3.2.3 Code Management, Revision Control, Bug Tracking

Most software projects in KATRIN, including the client analysis / simulation package KASPER and the server software KDBServer, are hosted on a *Git* repository server, maintained by collaborators from the University of Münster [Beh]. In software development, Git is a distributed revision control and source code management system [Sof14]. Git was initially designed and developed by Linus Torvalds for Linux kernel development in 2005.

Every project is assigned to its own repository, where changes to the code have to be documented by each individual developer and can be tracked throughout the complete history of the project. One particularly powerful feature of Git is the *branching* paradigm. If a developer plans to introduce critical changes to the project, he or she can create a linked duplicate of the working directory. Modifications in a personal branch do not affect

the *master* branch used by others, therefore new features can safely be introduced and tested. Once the changes are considered mature enough, they can be *merged* back into the *master* in a controlled manner.

Each *commit* (a documented set of changes) to the repository is communicated to other developers via email notifications. In addition, a bug-tracking system called ‘trac’ [Tra14] was set up to allow users to report problems with the code on a central website and provide feedback to developers.

### 3.3 Data Processing and Storage (Tier 1)

This section provides a brief overview of KATRIN related data sources which are most relevant for actual data analysis during commissioning and the later neutrino mass measurements. Furthermore, an outline is given of the processing and calibration procedures and the data storage scheme, comprising the so-called *data tier* of the experiment’s IT infrastructure.

The data accumulated during the operation of KATRIN can in general be divided into three categories:

#### Run based data

This category refers to self-contained sequences of event-triggered data. The recording is explicitly triggered or scheduled by an operator with a defined recording time and usually results in binary files written to a hard drive. For KATRIN the most important run based data is taken by the silicon detector systems, controlled by dedicated computers running the ORCA DAQ software (section 2.8.1). Throughout this document, this type of run based data will be referred to as detector DAQ data or ORCA data.

#### Slow Control data

Information recorded by the distributed SCS (section 2.8.2), covering magnetic, electric, pressure and temperature sensors, falls into this category. Sensor readout is in most cases performed by LabView or Siemens based hardware, aggregated into groups of sensors. For each so-called ‘log group’, sensor values are usually taken continuously at fixed intervals and stored as floating point values (plus status bits) in an SQL database.

#### User generated and KATRIN specific meta data

Additional information required for analysis and simulation, that is not gathered from any of the above mentioned sensors, is organized in a set of related SQL tables (figure 3.8). That information includes a sensor and positioning catalog, an index of processed ORCA runs, calibration data and more.

A basic graphical overview of the various data sources around the experimental setup is given in figure 3.4.

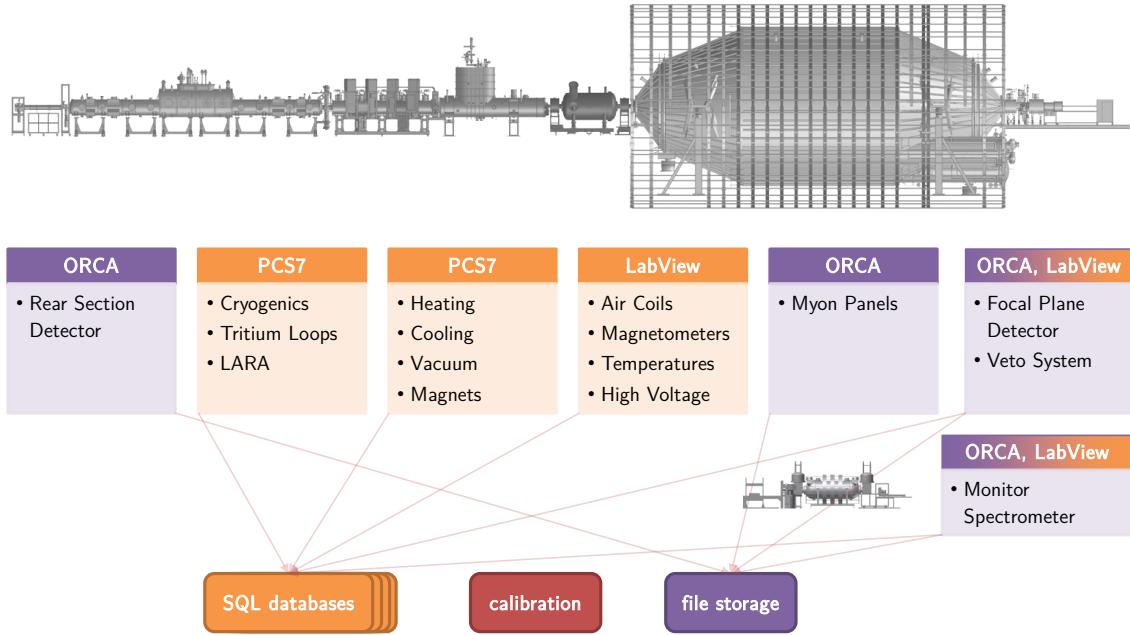


**Figure 3.4:** Illustration of various KATRIN data producers categorized by data acquisition system.

### 3.3.1 KATRIN numbering scheme

All components of the KATRIN experiment are uniquely indexed and logically categorized by a KATRIN specific identifier, the so-called *KATRIN number*. The numbering system is applied to most pieces of equipment like valves, cables, computers, cabinets, pumps and sensors. This indexing scheme is not merely used for bookkeeping. It is also implemented throughout the database and the analysis software as a means of identifying detector pixels, sensor channels, the corresponding calibration data, and sections of the geometry, as defined by internal KATRIN documents [Bor10; Wol12]. A KATRIN number has the following form:

$$NNN - XXXX - M - nnnn - ZZZZ$$

*NNN* is the system structure number, denoting the basic section of the experiment, like 200 for the WGTS, 300 for the transport system, 400 for the spectrometer, 500 for the detector and so on.

*XXX* is a redundant alphabetic descriptor. PTM for instance denotes a turbo-molecular pump.

*M* is a global functionality indicator, e.g. 1 for magnet.

*nnnn* is a serial number for sub-components of a main system *NNN*. The triplet of *NNN*, *M* and *nnnn* has to be unique for each component.

$ZZZZ$  can be used to further sub-divide a component or sensor. For the analysis this digit is commonly used to denote a specific readout channel of one sensor, like the axis of magnetometer or a status bit.

For instance, the longitudinal z-component readout channel ( $ZZZZ = 5$ ) of magnetometer number 4, installed on ring 3 ( $nnnn = 8340$ ) of the main spectrometer air coil system ( $NNN = 433$ ) is identified by the number 433-RBY-1-8340-0005.

### 3.3.2 ORCA Run File Repository

Currently there are three detector systems running at KATRIN, which are operated by Macintosh computers running the ORCA DAQ software (section 2.8.1):

- The 148 pixel focal plane silicon detector together with a 32 channel plastic scintillator veto (section 2.6).
- A set of 8 plastic scintillator muon panels, used to monitor the cosmic muon flux close the main spectrometer [Rov13].
- The 5 pixel silicon detector of the monitor spectrometer (section 2.7.2).

During an active detector data taking run, ORCA writes the event data, recorded by the DAQ hardware (section 2.8.1), to a binary file on a local harddrive connected to the DAQ computer. In addition, the run files contain comprehensive headers with information about the systems configuration and condition. Optionally, a run can be structured into subruns: In that case, additional headers are inserted into the data stream, whenever the run configuration changes and a new subrun is started.

The recorded data rate depends on the DAQ mode, chosen by the experimenter: *Energy mode* is the default data taking mode, which stores the energy and timing for each detector event (12 B per event). *Trace mode* adds a 2048-point ADC waveform for each event to the data stream (4 kB per event). For very high rates an alternative *histogram mode* can be chosen, where a 2048-bin energy histogram is filled for each channel or pixel respectively (8 kB per channel). Typical run file sizes can range from 100 MB up to 2000 MB, and on rare occasions even more.

### Run File Processing

Once a run has completed on one of the ORCA systems, the utility program ‘rsync’ [Tri03] synchronizes the DAQ machine’s locally stored run files with a central Redundant Array of Independent Disks (RAID) storage system over the internal network. The rsync process, receiving the file on the target machine, invokes an automated processing chain, controlled by a modular script, written in the Python language [Oli07].

A comprehensive basis for the processing script and a great deal of advice regarding its extensible design were kindly given by Sanshiro Enomoto, the author of the BEANS analysis suite. The run processing sequence is designed to be modular and flexible enough to deal with all incoming run based data formats. An outline of the involved processing steps is given in figure 3.5.

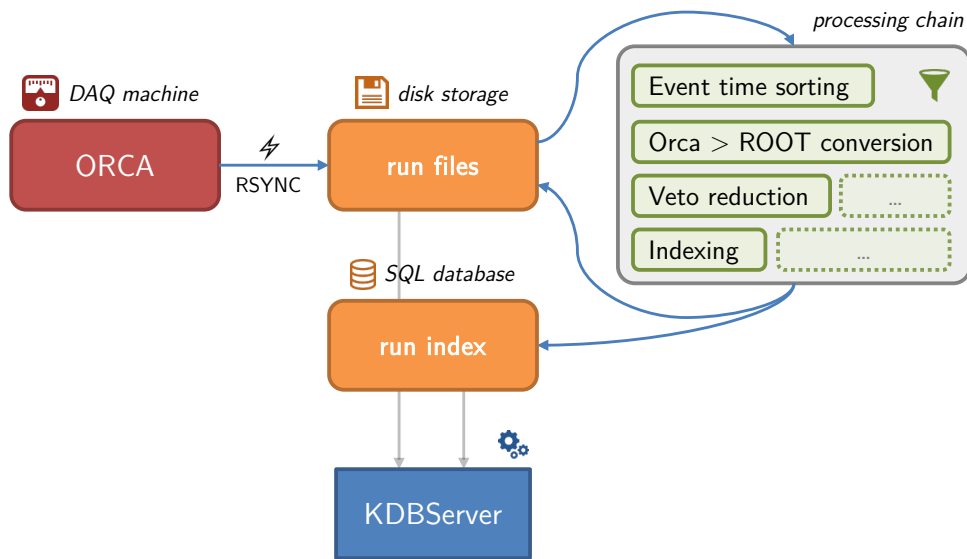


**Figure 3.5:** Flow diagram of the automated run processing chain. Once the DAQ machine has finished a data-taking run, the raw data is ‘rsynced’ to central file storage. The processing script performs various conversion / indexing steps and writes the converted data to the file storage and SQL databases, where it can be accessed by the service layer (KDBServer).

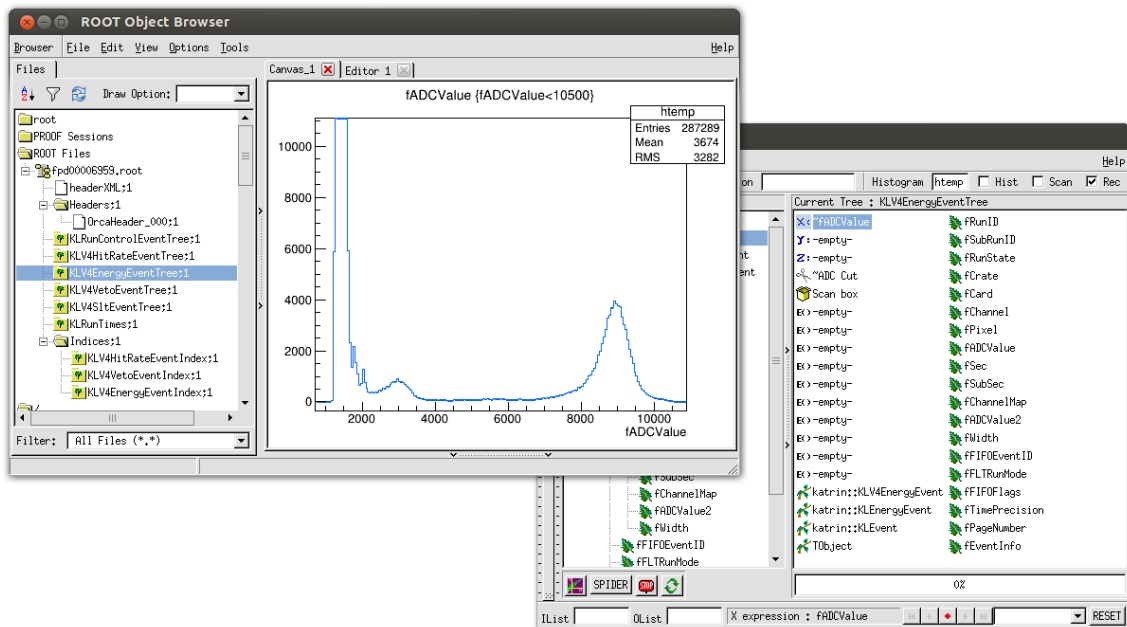


**Figure 3.6:** Structure of ORCA detector data in ROOT compatible format, opened with the TTreeView tool provided by ROOT. A histogram of energy ADC values can easily be obtained with only a handful of mouse clicks.

- First, the event information in an ORCA file is checked for consistency and a time sorting algorithm is applied<sup>1</sup>.
- In the next step the raw event data is converted into a ROOT compatible format, with each event type being stored in its own TTree, a ROOT-specific data structure (figure 3.6).
- If applicable, veto information from the focal plane detector system is used to identify coincidences and generate a veto-reduced copy of the run file.
- The converted ROOT files are extended with an event index, making the navigation through the event data by later analysis code as convenient and performant as possible.
- Both the original raw data and the processed files are stored in an organized directory tree, together with additional header information and log files, documenting the processing status.
- After run processing is completed, basic meta data about the run structure and configuration is written to a dedicated table of the SQL database (section 3.3.4), thereby registering the run as being ‘available’ for offline access and analysis.

### 3.3.3 Slow Control Database

The central storage of Slow Control data is in most parts handled by the PHP server application ADEI (section 2.8.2). ADEI is responsible for gathering the raw data from the local databases (most of them running on Microsoft SQL servers) and caching it into one common MySQL database, which makes the data accessible to KATRIN’s analysis logic.

Similar sensors, which are read out by one hardware controller, are usually collimated into a so-called *log group*, typically composed of 20 up to 150 channels. Each log group is written to its own database table. One entry corresponds to a new line or row in that table, with the number of columns given by the number of sensor channels collimated by the log group, plus optional status information.

Figure 3.7 shows an exemplary Slow Control cache table, as it is created by ADEI and provided to KATRIN’s software infrastructure. Each single channel of data corresponds to one column, prefixed with the letter *v* in an SQL cache table. The value of the *id* column is given by the sensor readout time in nanoseconds since the epoch (01.01.1970). Table 3.2 summarizes all categories of Slow Control channels, that are currently monitored and accessible through the KATRIN analysis framework.

---

<sup>1</sup> The working principle of the detector electronics requires time sorting of recorded events, since the event buffers on the employed FPGAs behave like a stack. If two or more events are recorded within the buffer time of 50 ns, they are read out and streamed to the data file in reverse order.

<b>sensor / device type</b>	<b>number of channels</b>
actuation switch	19
field point unit status	8
thermo controller status	154
electronic cabinet / circuit board status	22
power supply, high voltage	50
power supply, low voltage	176
electrical heater	1647
electrical exchanger	15
electric motor	24
pump / compressor	89
turbo molecular pump	361
sensor, B-field	510
sensor, electrical property	150
sensor, flow controller	48
sensor, flow rate	31
sensor, geometrical properties	77
sensor, level	88
sensor, moisture	1
sensor, pressure	940
sensor, temperature	2586
valve, automatic	682
valve, manual	609
safety valve	8
	<b>8295</b>

**Table 3.2:** Summary of active Slow Control channels, as of June 2014. The list covers the pre-spectrometer, main spectrometer, detector section and monitor spectrometer.

The screenshot shows a SQL Editor window with a table structure for Slow Control data. The table is named 'cache0\_md5\_00bce3a35e17f4fe7450b059931442b1'. The columns are: #, id, time, ns, subcache, v0, v1, v2, v3, v4, v5. The data is sorted by id, showing a range from 1 to 34. The table is cached and pre-processed by ADEI.

#	id	time	ns	subcache	v0	v1	v2	v3	v4	v5
1	135168530650000000	2012-10-31 12:08:26	500000000	0	10000.0009765625	64	6.3484774194491e17	50177	192	6.3487200729255e17
2	135168531500000000	2012-10-31 12:08:31	500000000	0	10000.0009765625	64	6.3484774194491e17	50177	192	6.3487200729255e17
3	1351685314515625000	2012-10-31 12:08:36	515625000	0	10000.0009765625	64	6.3484774194491e17	50177	192	6.3487200729255e17
4	1351685321515625000	2012-10-31 12:08:41	515625000	0	10000.0009765625	64	6.3484774194491e17	50177	192	6.3487200729255e17
5	1351685326531250000	2012-10-31 12:08:46	531250000	0	10000.0009765625	64	6.3484774194491e17	50177	192	6.3487200729255e17
6	1351685331546875000	2012-10-31 12:08:51	546875000	0	10000.0009765625	64	6.3484774194491e17	50177	192	6.3487200729255e17
7	1351685336546875000	2012-10-31 12:08:56	546875000	0	10000.0009765625	64	6.3484774194491e17	50177	192	6.3487200729255e17
8	1351685341562500000	2012-10-31 12:09:01	562500000	0	10000.0009765625	64	6.3484774194491e17	50177	192	6.3487200729255e17
9	1351685346578125000	2012-10-31 12:09:06	578125000	0	10000.0009765625	64	6.3484774194491e17	50177	192	6.3487200729255e17
10	1351685351578125000	2012-10-31 12:09:11	578125000	0	10000.0009765625	64	6.3484774194491e17	50177	192	6.3487200729255e17
11	1351685356593750000	2012-10-31 12:09:16	593750000	0	10000.0009765625	64	6.3484774194491e17	50177	192	6.3487200729255e17
12	1351685361609375000	2012-10-31 12:09:21	609375000	0	10000.0009765625	64	6.3484774194491e17	50177	192	6.3487200729255e17
13	1351685366609375000	2012-10-31 12:09:26	609375000	0	10000.0009765625	64	6.3484774194491e17	50177	192	6.3487200729255e17
14	1351685371625000000	2012-10-31 12:09:31	625000000	0	10000.0009765625	64	6.3484774194491e17	50177	192	6.3487200729255e17
15	1351685376625000000	2012-10-31 12:09:36	625000000	0	10000.0009765625	64	6.3484774194491e17	50177	192	6.3487200729255e17
16	1351685381640625000	2012-10-31 12:09:41	640625000	0	10000.0009765625	64	6.3484774194491e17	50177	192	6.3487200729255e17
17	1351685386656250000	2012-10-31 12:09:46	656250000	0	10000.0009765625	64	6.3484774194491e17	50177	192	6.3487200729255e17
18	1351685391656250000	2012-10-31 12:09:51	656250000	0	10000.0009765625	64	6.3484774194491e17	50177	192	6.3487200729255e17
19	1351685396671875000	2012-10-31 12:09:56	671875000	0	10000.0009765625	64	6.3484774194491e17	50177	192	6.3487200729255e17
20	1351685401687500000	2012-10-31 12:10:01	687500000	0	10000.0009765625	64	6.3484774194491e17	50177	192	6.3487200729255e17
21	1351685406687500000	2012-10-31 12:10:06	687500000	0	10000.0009765625	64	6.3484774194491e17	50177	192	6.3487200729255e17
22	1351685411703125000	2012-10-31 12:10:11	703125000	0	10000.0009765625	64	6.3484774194491e17	50177	192	6.3487200729255e17
23	1351685416703125000	2012-10-31 12:10:16	703125000	0	10000.0009765625	64	6.3484774194491e17	50177	192	6.3487200729255e17
24	1351685421718750000	2012-10-31 12:10:21	718750000	0	10000.0009765625	64	6.3484774194491e17	50177	192	6.3487200729255e17
25	1351685426734375000	2012-10-31 12:10:26	734375000	0	10000.0009765625	64	6.3484774194491e17	50177	192	6.3487200729255e17
26	1351685431734375000	2012-10-31 12:10:31	734375000	0	10000.0009765625	64	6.3484774194491e17	50177	192	6.3487200729255e17
27	1351685436750000000	2012-10-31 12:10:36	750000000	0	10000.0009765625	64	6.3484774194491e17	50177	192	6.3487200729255e17
28	1351685441765625000	2012-10-31 12:10:41	765625000	0	10000.0009765625	64	6.3484774194491e17	50177	192	6.3487200729255e17
29	1351685446765625000	2012-10-31 12:10:46	765625000	0	10000.0009765625	64	6.3484774194491e17	50177	192	6.3487200729255e17
30	1351685451781250000	2012-10-31 12:10:51	781250000	0	10000.0009765625	64	6.3484774194491e17	50177	192	6.3487200729255e17
31	1351685456781250000	2012-10-31 12:10:56	781250000	0	10000.0009765625	64	6.3484774194491e17	50177	192	6.3487200729255e17
32	1351685461796875000	2012-10-31 12:11:01	796875000	0	10000.0009765625	64	6.3484774194491e17	50177	192	6.3487200729255e17
33	1351685466812500000	2012-10-31 12:11:06	812500000	0	10000.0009765625	64	6.3484774194491e17	50177	192	6.3487200729255e17
34	1351685471812500000	2012-10-31 12:11:11	812500000	0	10000.0009765625	64	6.3484774194491e17	50177	192	6.3487200729255e17

Figure 3.7: SQL table structure for Slow Control data, cached and pre-processed by ADEI.

### 3.3.4 KATRIN SQL Database

The KATRIN SQL database basically stores all additional information, which is needed for analysis and simulation besides ORCA run event data or raw Slow Control data. An important difference here is how information to this database is added or modified. While run and Slow Control data are generated by a clearly defined number of system processes and usually never modified again, the KATRIN SQL database is required to allow various forms of user-generated input and consequent updates.

In the context of this work, the complete database scheme as outlined in figure 3.8, was set up and made available for the KATRIN analysis framework. Currently the database consists of 14 different tables, a number which is likely to grow in the future, when new data types are required to be managed centrally (for instance complex simulation results). For the purposes of this dissertation however, we will focus on to those parts of the database, that are most relevant to the present work.

#### Modification History and Version Control

Most database tables have a few columns (or fields) in common. The *user\_id* and *entry\_time* fields keep track of the user and the creation time of an entry. In addition, a more elaborate comment on a new database entry can be added to the *history* table for the purpose of documentation.

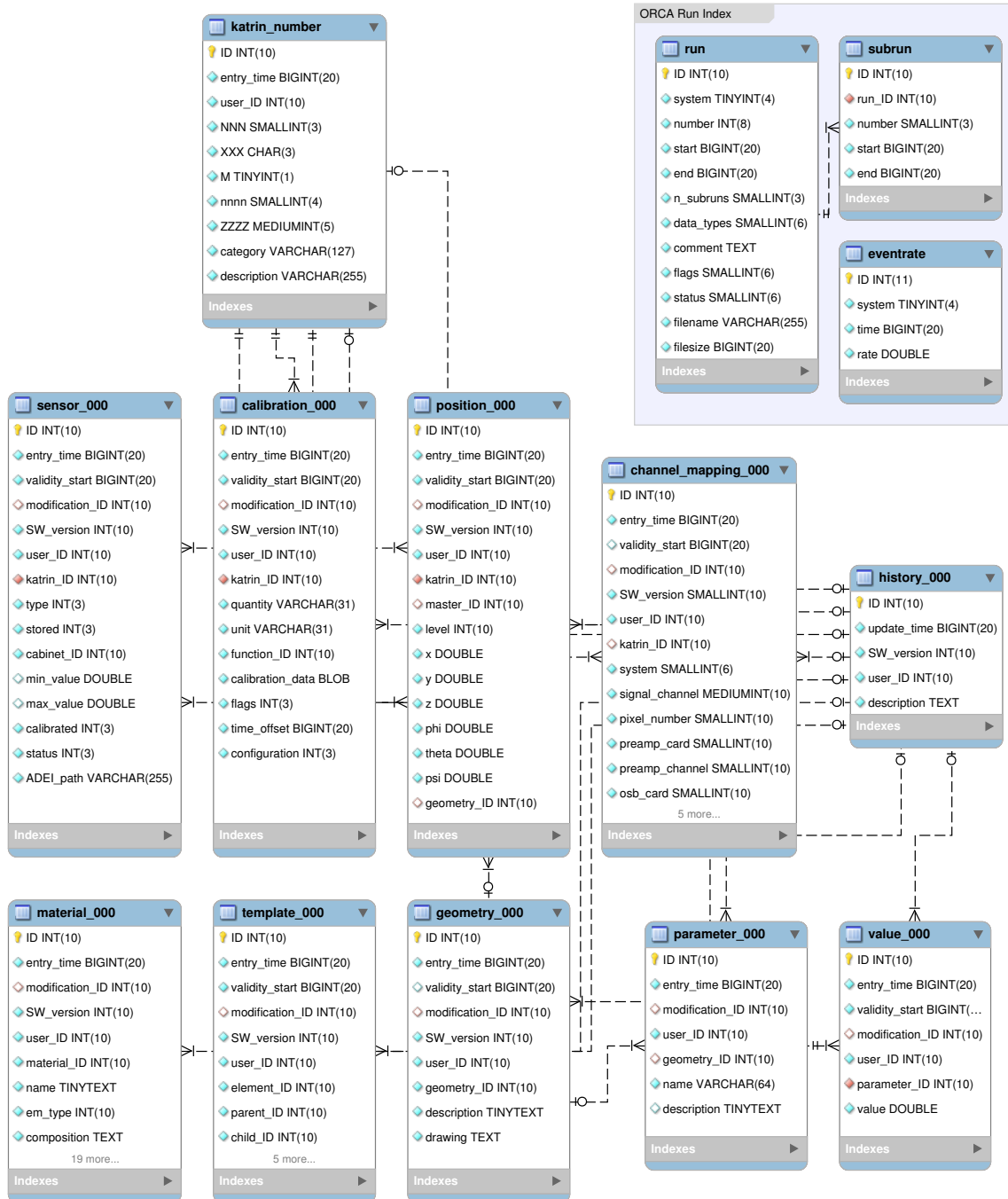


Figure 3.8: KATRIN database containing all data indexed by the KATRIN numbering scheme and ORCA run information (upper right corner).

Deletion or modification of an existing entry in the KATRIN database is generally prohibited. The *calibration* table gives a good explanation, why. Any analysis that is once performed on a particular data set and possibly published, needs to be reproducible. Funding agencies strictly require, that any sort of raw data or calibration, used in a scientific publication, must be stored away for at least 10 years. Therefore, tables like *calibration* have a second time-stamp field *validity\_start*, indicating the time interval, for which this particular data entry is valid. If for instance, a later calibration procedure requires an update of a prior data entry, a new data entry is added with an equal *validity\_start*, but more recent *entry\_time*. Due to this mechanism, raw data can always be re-analyzed with updated, more accurate calibration, or with the older dataset, which was once used for a publication.

### KATRIN Numbers - Surrogate vs. Natural Key

Each device or sensor channel in KATRIN is identified by a KATRIN number like 433-RBY-1-8340-0005 (see section 3.3.1). In relational databases this kind of user-defined identifier is called a *natural key*. For an SQL database however an integral *surrogate key* is more feasible. It is not derived from the data and usually generated internally.

The *katrin\_number* table essentially is a mapping between the technical surrogate key (*ID*) and our natural key, which in the present database representation is divided into five separate columns (*NNN*, *XXX*, *M*, *nnnn*, *ZZZZ*).

Relations between tables are established by the database through surrogate keys, indicated in figure 3.8 by dashed lines. A very important feature of relational databases comes into play here, which are *foreign key constraints*. If deletion or modification of an entry in one table would break the relation to an entry in another table, the database itself can refuse such an action. That way, a fundamental degree of data consistency can be guaranteed without any external programming logic involved.

### Sensor Catalog

Sensor channels, which need to be available within the analysis framework, are indexed in the *sensor* table. An important link is established by this catalog: The KATRIN number of a sensor channel is mapped to an ADEI specific descriptor (*ADEI\_path*), which is required to retrieve Slow Control data associated with a sensor channel from the correct Slow Control cache table.

### Calibration

The table *calibration* is designed to hold various forms of calibration data in a binary format. In most cases, a set of calibration data consists of a list of real numbers, which can be applied to raw Slow Control or detector ADC data, according to a functional expression defined by the field *function\_ID*. But the code accessing the table is extensible and flexible enough to account for more complex data. Data can be written and retrieved either by the user through a web interface or by automatic processes through the client-side analysis logic (section 4.2.8).

### Position

Position and orientation of a sensor, or any other component of the KATRIN experimental setup can be stored and tracked in the *position* table with a set of Euler coordinates  $(x, y, z, \phi, \theta, \psi)$ . The information can be arranged in a hierarchical structure, since this table is capable of describing child-to-parent relations via the field *master\_ID*.

### Channel Mappings

Channel Mappings are used to map detector pixels with ADC channels and specific components of the DAQ electronics to the appropriate KATRIN numbers. Such a mapping allows for calibration data (energy calibration in particular) to be associated with the ADC values recorded by each detector pixel.

### Run Data Index

The two run index tables *run* and *subrun* hold information about complete and processed ORCA runs. Start and stop times for a run itself and its subdivision into subruns, DAQ recording modes, file sizes and status indicators from recording and conversion processes are stored here, providing a basic dissection of an ORCA run's properties. In addition, event rates recorded by the corresponding detector system are extracted during run processing and written to the *eventrate* table with a 10 s binning.

#### 3.3.5 Expected Amounts of Data

From extrapolations of recorded data during the recent SDS commissioning measurements, a rough estimate on the expected amounts of data and the required disk storage can be given. The accumulated event data from all ORCA detector systems is anticipated to be about 2 TB per year. Slow Control systems are expected to produce an amount of roughly 1 TB per year, once all sensors of the experimental setup, relevant for analysis, are operational and recording data. Other data types will most likely constitute negligible amounts in comparison.

#### 3.3.6 Planned Extensions

The processing and management layer was set up with extensibility in mind, not only limited to the addition of further Slow Control sensors or detectors managed by ORCA.

### Mobile Magnetic Sensor Unit System

A non-ORCA based system, which is planned to be integrated into KATRIN's infrastructure in the near future, is the mobile magnetic sensor unit system (MobSU) [Osi12]. It consists of up to 14 autonomous mobile units with magnetic field sensors, which make use of the holding structure of the air coil system, to circulate the main spectrometer during specific measurement phases. These units allow to scan the magnetic field setup in greater detail than the limited number of static sensors installed around the spectrometer.

Each circular run of a single unit will result in a binary file which will be handled by the same processing chain currently responsible for detector runs (section 3.3.2). After applying calibration to the recorded field strengths and transformation into a global coordinate system, the results will either be written to a dedicated table of the KATRIN SQL database or the central Slow Control database.

### Laser Raman System

The Laser Raman (LARA) system will determine the isotopic composition of the source gas, which is critical information for the analysis [Sch13b]. It is installed with optical access to a buffer cell in the inner loop system of the WGTS. Using Raman spectroscopy, characteristic wavelength shifts between laser light and scattered photons allow a distinction and quantitative analysis of the six different hydrogen isotopologues, as well as other gas species, such as methane.

Current plans foresee the integration of LARA information as a Slow Control like system into the data flow, making it available to near-time monitoring tools and offline analysis based on the common KASPER framework.

### 3.4 Data Logic and Services (Tier 2)

The C++ project named KDBServer implements all functionality accounted to KATRIN's data logic layer, in software engineering sometimes referred to as the middle or *logic tier*. KDBServer is a web service in the sense, that it runs on a server machine and exposes its functionality, such as data access, through a well-defined interface over the network for client applications, which are executed on a user's local computer.

In the context of the present thesis the need for an intermediate data logic layer was first brought up for discussion. Following the reasoning at the beginning of this chapter, the multi-tier architecture with KDBServer in its middle was eventually considered as the most sensible design choice. Coordinated with KATRIN's data producers (section 3.3) and data consumers (section 4) KDBServer ultimately evolved into a crucial, and now continuously operating part of the data analysis chain.

#### 3.4.1 KDBServer - KATRIN's Web Service

KDBServer has full control over all KATRIN data sources, including the run file repositories and SQL databases, described in section 3.3. It is responsible for keeping the data consistent upon modifications and restricts access and operations to authorized users. In general it fulfills two tasks: Firstly, it generates an interactive web interface for users to manage database contents, such as calibration and positioning information, and to obtain basic analysis of detector data (section 4.1). Secondly, KDBServer acts as a mediator between KATRIN data and the user's analysis code, providing a well defined and consistent programming interface for remote data access.

#### Technical Design Aspects

For both tasks, C++ seems a rather peculiar choice of the programming language. When it comes to networking and web applications, Java, PHP and Python along with many more modern languages, have become very popular choices, usually offering a vast selection of well documented libraries and frameworks. For KATRIN however, C++ already was the dominating language in most simulation and analysis applications. Introducing an additional programming language into the analysis chain, would probably have led to redundancies and an increased maintenance effort of the overall system.

Technically KDBServer builds directly on top of the comprehensive KASPER library, utilizing available analysis and simulation logic, which was originally developed for offline execution. This leaves the future possibility to successively move more and more analysis procedures from the client to the server side, having it executed automatically in real-time.

KDBServer can either be compiled to run as a FastCGI [Bro96] application from any common Hypertext Transfer Protocol (HTTP) server, or as an independent light-weight multi-threaded server. Either way, the web service implementation has proven to run responsive and stable during daily operation, in particular during the recent SDS-I commissioning measurements. It also scaled well in the sense that concurrent data requests from multiple users (and from several institutes) were handled robustly.

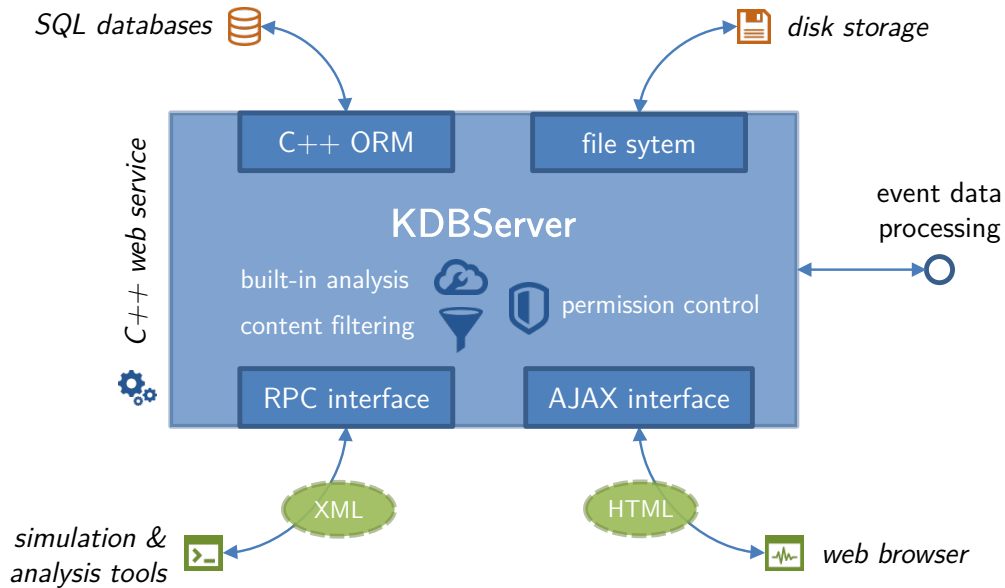


**Figure 3.9:** KDBServer comprises KATRIN’s middle tier, managing data source and controlling data access. It is implemented as an object-oriented C++ web service. An Object-Relational Mapping (ORM) is used to transparently convert SQL data into C++ objects. The Remote Procedure Call (RPC) interface offers access to the service’s functionalities through a standards compliant XML protocol. A dynamic Asynchronous JavaScript and XML (AJAX) enabled web browser interface is provided for online monitoring and administrative tasks.

Two external C++ libraries, *Wt* and *gSOAP*, were used to implement KDBServer as a standards-compliant web application. They provide crucial functionalities and enable some of the core concepts of KDBServer. In the following, their working principles and use within the KATRIN data analysis chain will be outlined briefly.

#### Wt - A C++ Web Application Toolkit

Wt (pronounced ‘witty’) [Emw14] is an open source C++ web application framework. It provides a widget-centric Application Programming Interface (API) with an event-driven signal/slot programming model.

The library allows the development of rich user interfaces in a way resembling the better known C++ library Qt. But the exceptional feature of Wt is its ability to translate the application into a web browser compatible, AJAX powered format, using most recent HTML5 rendering techniques.

Furthermore, Wt includes a compact C++ Object-Relational Mapping (ORM) layer, which is used by KDBServer to map KATRIN C++ data types to Structured Query Language (SQL) database tables. Major database systems like MySQL/MariaDB, PostgreSQL or Sqlite3 are supported out of the box.

### gSOAP - Toolkit for SOAP Web Services and XML-Based Applications

gSOAP is a platform-independent toolkit for developing web services based on C and C++ applications [Van08; Van02]. It provides a Remote Procedure Call (RPC) compiler, which produces the stub and skeleton routines to integrate existing C++ logic into Simple Object Access Protocol (SOAP)/Extensible Markup Language (XML) web services and enables direct SOAP/XML messaging over HTTP. As a result, standards compliant data transfer can be achieved with a manageable API, relieving the developer and user from the burden of dealing with the underlying transport protocols, compression or encryption mechanisms.

The toolkit allows KATRIN data to be accessed through industry-standard SOAP 1.1/1.2 and Web Services Description Language (WSDL) 1.1 protocols, in conjunction with on-the-fly Zlib compression [Deu96], Secure Sockets Layer (SSL) encryption and authentication. Smaller data types are transferred in human-readable SOAP/XML format. Binary data, like larger blocks of slow control or run data, are streamed as Direct Internet Message Encapsulation (DIME) attachments.

#### 3.4.2 Object Relational Mappings

In order to access contents from SQL databases, KDBServer utilizes the *Object-Relational Mapping (ORM)* layer, provided by the Wt library. ORM denotes a programming technique, which describes mapping schemes between objects of a programming language, in our case C++ data types, and the corresponding columns of a relational SQL database table. This concept bears practical benefits. The SQL-related C++ code gains better readability and the database queries become less error-prone, since parts of the database logic are now validated during compile-time. In addition, the system is practically invulnerable to certain types of external exploits, such as SQL code injection.

All KATRIN data types shown in figure 3.8, are represented with an ORM mapping, sharing common C++ base classes. This way, most of the required filtering and processing logic, concerning calibration, positioning or sensor information, can be shared among similar data types throughout the code. A more detailed explanation of the ORM concept, including a simple code example, can be found in the appendix A.1.

#### Transaction Safety

A feature, which is enforced throughout all server-side processes, is transaction safety. The purpose of a database *transaction* is to handle a series of changes to the database as one single consistent operation. If somehow one of the steps associated with these changes fails, the database is able to ‘roll back’ all changes made as part of the transaction. This is important to ensure referential integrity between related tables of a database. Furthermore, transactions provide *isolation* between concurrent requests from multiple users. For this reason, transaction safety is an essential feature, when the integrity of the data and consistency of requests on the data are to be guaranteed.

### 3.4.3 Service Oriented Architecture

Remote user access to KATRIN data is provided by a web service implementation within KDBServer, also completely written in C++. This implementation is realized with the well-documented and actively maintained open source library gSOAP, already introduced above.

SOAP is an XML based protocol, used to establish communication with a web service. Messaging is performed through the remote procedure calling (RPC) technique: A software running on the user's client machine invokes a function (e.g. asking for sensor or detector data), which then is not executed on the client machine but translated into an XML message and sent over the network to the web service. After verifying the message, the service evaluates the function call, translates the return value into XML and sends it back to the client. The client software now ends the function call and returns the data to the user in a programmable format, for example a C++ object.

A detailed explanation of how KATRIN's analysis and simulation software realizes communication with KDBServer, and what benefits the technique holds from a user's perspective, will be given in section 4.2.1.

A more technical example, providing some insight into the XML content exchanged between KDBServer and client applications, can be found in the appendix A.2.

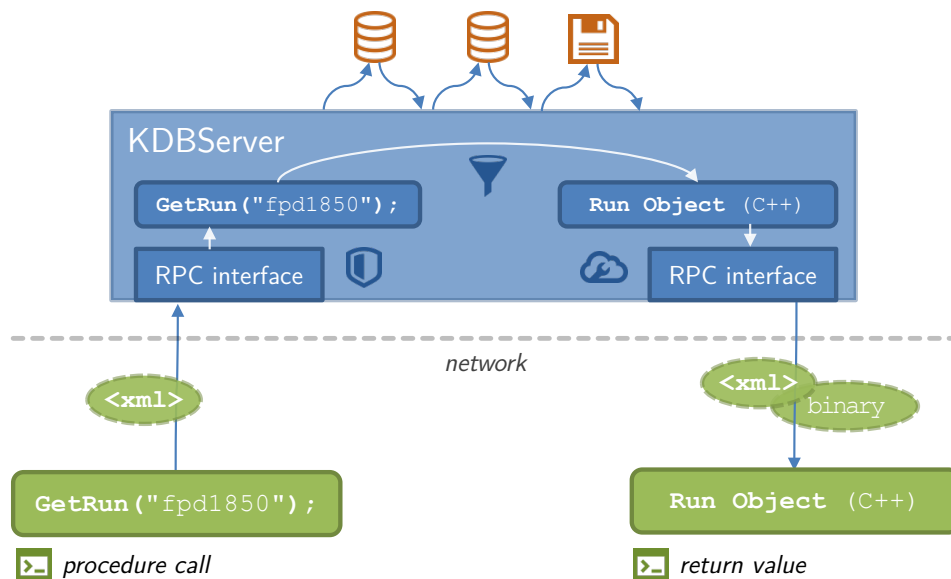


**Figure 3.10:** A client tool invokes a function, which is translated into a XML message. KDBServer parses the request, checks user permissions and assembles the data. The result is converted into an XML response (with binary attachments if necessary) and returned to the client.

### Data Compression

The gSOAP library provides built-in Zlib compression algorithms, which have proven to be quite effective, not only on XML data, but especially on detector event data. ORCA run files, which are transferred as binary DIME attachments, can gain sizes well above 5 GB. With activated compression, such event data files are reduced to about one third of their original size during network transfer.

### Security

As more collaborators require access to KATRIN data from remote locations, certain restrictions, especially on write operations, have to be enforced. User authentication is realized through basic HTTP user/password authentication or SSL certificates. The KATRIN web service can selectively decide, which user to grant write or read permission, and it can track all modifications of database contents back to the responsible author.

### Interoperability

Currently, most access to the web service and analysis of data is performed with the KATRIN C++ client code KaLi (section 4.2.1), which has been developed in tandem with the web service KDBServer. It uses the same underlying gSOAP library to handle serialization and communication.

Client applications, communicating with the data service, do not necessarily have to be written in C++. SOAP implementations are available in most modern programming languages, including C#, Java, Python and PHP. By exposing (making available) all functionality of the KATRIN web service through a standardized SOAP interface, client analysis tools in nearly any language are thinkable.

#### 3.4.4 Slow Control Processing

Resolving and processing Slow Control data is one of the more complex tasks for KDBServer. Reading sensor values from a single Slow Control channel involves querying at least a handful of different database tables and requires many careful consistency checks, before the data can be assembled and sent to the user.

When a user or client analysis tool asks for a series of Slow Control values or an averaged value over a given time interval, the following steps have to be performed by KDBServer:

- The web service receives a data request for one or more *KATRIN numbers*, which identify the sensor channels of interest, and a time interval.
- From KATRIN's sensor table, a mapping is generated, relating KATRIN numbers to *ADEI paths*, which are the storage descriptors of actual Slow Control data. The mapping procedure has to consider the specified time intervals and take into account possible changes in the storage path of the data during that time.

- *Calibration data* for the selected sensor channels and time interval are collected from KATRIN's calibration table.
- Validity of the storage descriptors and *availability* of Slow Control data in ADEI's data tables are *verified*. Time intervals are adjusted if certain interpolation options were selected by the user, or if the calibration data demand a correction.
- Now the concerned Slow Control tables are read, using SQL statements, prepared in advance. ROOT TTree data structures are used to hold the *raw Slow Control data*.
- The response message for the user is assembled. KATRIN numbers, sensor information and calibration data are wrapped in a response *XML envelope*. The ROOT TTree structure is appended as a binary attachment.
- Using on-the-fly compression and optional encryption, the response is sent to the client machine.

#### 3.4.5 Run File Repository Organization

The directory structure and naming scheme for raw and processed run files are defined in such a way, that KDBServer can reliably resolve their location after processing and archiving. When a user requests a specific run file through the web interface or the programming interface, KDBServer is able to deliver any of the requested run formats in raw and processed versions within minimal response time.

Many operations regarding detector event data, however, do not require the user to download a run file at all. The web service provides a set of functions to search and filter the list of available runs, ask for configuration details, recording modes, file sizes and event rates. For such tasks the dynamically generated run index tables in the KATRIN database are sufficient, with no time-consuming parsing of large binary files required.

#### 3.4.6 Performance and Scalability

Most data requests to KDBServer are usually processed in under 50 ms, including response times in a local network. When larger amounts of data are queried, for instance in the case of overnight event data runs, the transfer time is longer, depending on the available network bandwidth. More complex Slow Control queries, involving sensor data spanning several years (often corresponding to several 100 000 readout values), can be condensed to reasonably smaller amounts, using fast averaging algorithms on the SQL database level.

The systems benefits enormously from using highly optimized compiled C++ code a light-weight database back-end on the server side, not only performance-wise, but also in terms of memory usage. A single KDBServer process rarely demanded more than 4 MB of working memory. Concurrent request from tens of users during measurement phases were handled robustly without ever utilizing the full CPU capacity of the host system, driven by a four-core Intel® Xeon™ E5620 @ 2.4 GHz.

### 3.4.7 System Replication and Backup

The system was designed to allow full replication of the web service functionality. At KIT two machines are redundantly processing data and providing access to file repositories and databases, synchronizing data modifications between each other. Further machines will be set up in the near future at collaborating US institutions to provide faster access to the data for local users.

Backups of all file repositories and databases are performed on a daily basis to local hard drive RAID systems. KATRIN's projected requirements on disk space during commissioning or measurement phases is about 5 TB per year. Long term archiving is planned to be realized with the Large Scale Data Facility (LSDF) at KIT [Gar11].



# CHAPTER 4

---

## Data Access and Analysis

---

The previous chapter described various data sources of the experiment and the web service component `KDBServer`, which is responsible for pre-processing and managing data. This chapter concentrates on the other end of the analysis chain, describing how users of KATRIN software can access the data and use the available infrastructure to develop their own tools.

Essentially, two different methods of accessing the service layer have been implemented as part of this thesis: Firstly, a web interface for basic monitoring and administrative tasks, which can be accessed from conventional web browsers on desktop computers or mobile devices, and secondly, a C++ programming interface providing full access to all available data types with fundamental data selection and analysis capabilities.

### 4.1 Web Frontends

The C++ `KDBServer` package (section 3.4.1), running on the KATRIN data servers, employs the underlying `Wt` library to dynamically render an interactive web interface. Using a web technology called `AJAX`, user interactions on interface widgets like buttons and form elements, are processed and responded without requiring a reload of the web page. Graphical elements, such as plots, are not generated through intermediate raster graphics, but directly drawn on the web browser's canvas, using most recent `HTML5` rendering methods.

#### 4.1.1 ORCA Run Browser

The web interface shows a permanent navigation bar at the top of the page, giving access to all available subsections. A run list view, shown in figure 4.1, provides a sortable listing of all processed ORCA runs. The user can comfortably select a specific date or one of the active ORCA systems (focal plane detector, muon panels, monitor spectrometer).

System	End	#SubRuns	DataTypes	Flags	Status	FileSize
(1) fpd   Focal Plane Detector	2013-10-01 23:38:14	1	5264	0	0	55 288 KB
(1) fpd   Focal Plane Detector	2013-10-01 21:35:42	1	5264	0	0	54 804 KB
(1) fpd   Focal Plane Detector	2013-10-01 19:35:37	1	5264	0	0	54 793 KB
(1) fpd   Focal Plane Detector	2013-10-01 17:35:31	1	5264	0	0	54 563 KB
(1) fpd   Focal Plane Detector	2013-10-01 15:25:54	1	5264	0	0	341 728 KB
(1) fpd   Focal Plane Detector	2013-10-01 15:04:34	1	5264	0	0	345 313 KB
(1) fpd   Focal Plane Detector	2013-10-01 14:43:13	1	5264	0	0	345 454 KB
(1) fpd   Focal Plane Detector	2013-10-01 14:21:53	1	5264	0	0	347 399 KB
(1) fpd   Focal Plane Detector	2013-10-01 14:00:33	1	5264	0	0	346 633 KB
(1) fpd   Focal Plane Detector	2013-10-01 13:39:12	1	5264	0	0	347 605 KB
(1) fpd   Focal Plane Detector	2013-10-01 13:17:53	1	5264	0	0	347 611 KB
(1) fpd   Focal Plane Detector	2013-10-01 12:56:34	1	5264	0	0	343 041 KB
(1) fpd   Focal Plane Detector	2013-10-01 12:35:15	1	5264	0	0	345 071 KB
(1) fpd   Focal Plane Detector	2013-10-01 12:13:56	1	5264	0	0	348 733 KB
(1) fpd   Focal Plane Detector	2013-10-01 11:52:37	1	5264	0	0	350 380 KB

**Figure 4.1:** Web interface for browsing and selecting processed ORCA runs.

Clicking on a row in the listing will switch the interface to a detailed view of the corresponding run, shown in figure 4.2. The user can quickly assess basis configuration parameters, recording times and DAQ modes, the sub-run structure and an event-rate display. Furthermore, direct download links to the actual run files in several formats are provided, as well as run headers and log files.

#### 4.1.2 Database Viewer and Administrator

Other parts of the database can also be examined with the same web interface, including all registered KATRIN numbers, a sensor catalog, calibration data, positioning data and detector channel mappings. Figure 4.3 shows a listing of positioning data for magnetometers. This particular information is used in the analysis chain to transform measured field vectors into a common coordinate system. Such tables can be sorted dynamically for each column and filtered for specific KATRIN numbers or sections of the experiment.

Wherever applicable, the web interface features editing capabilities for authorized administrators of the database. For most data types a corresponding form is provided, which allows editing of existing or creation of new entries. Many form fields are backed by automatic drop down lists, showing suggestions of available values, and are validated in real-time with immediate response for the editor. An exemplary creation dialog for sensor entries is pictured in figure 4.4.

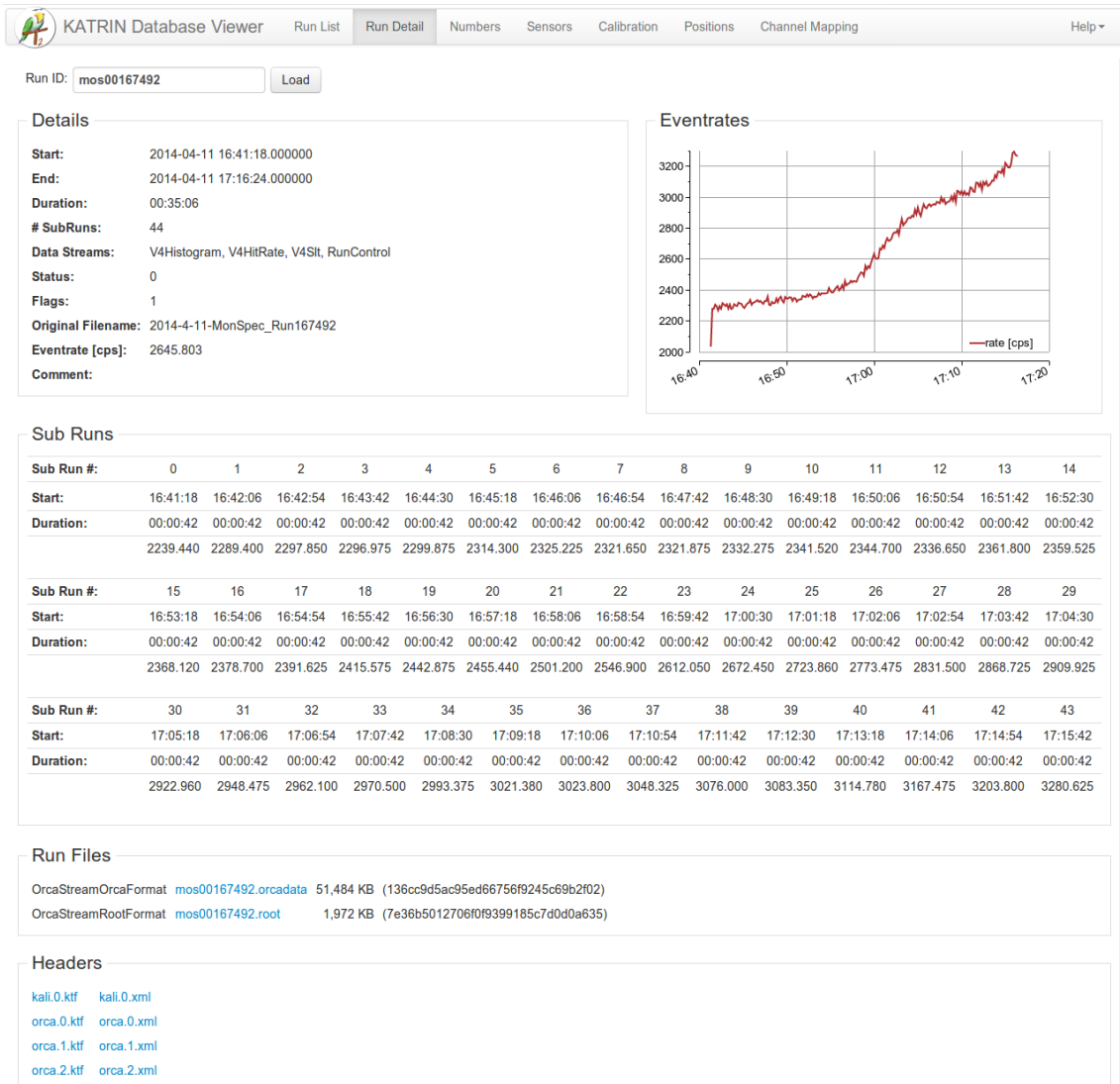


Figure 4.2: Web interface for ORCA run details, event display and run file download links.

KATRIN Database Admin    Katrin Numbers    Sensor    Calibrations    **Positions**    ChannelMappings    Help ▾

Katrin Number	EntryTime	ValidityStart	Master	Level	X	Y	Z	Phi	Theta	Psi	Geometry	Category	Description
433-RBY-1-8410-0003	2013-06-14 12:32:45	NULL	432-TVV-3-0000-0000	1	-3.71	-3.71	3.60...	-225	0	0	NULL	magnetometer	Ring04
433-RBY-1-8410-0005	2013-06-14 12:33:04	NULL	432-TVV-3-0000-0000	1	-3.71	-3.71	3.60...	-225	0	0	NULL	magnetometer	Ring04
433-RBY-1-8420-0001	2013-06-14 12:33:22	NULL	432-TVV-3-0000-0000	1	-5.25	0	3.60...	-180	0	0	NULL	magnetometer	Ring04
433-RBY-1-8420-0003	2013-06-14 12:33:40	NULL	432-TVV-3-0000-0000	1	-5.25	0	3.60...	-180	0	0	NULL	magnetometer	Ring04
433-RBY-1-8420-0005	2013-06-14 12:33:58	NULL	432-TVV-3-0000-0000	1	-5.25	0	3.60...	-180	0	0	NULL	magnetometer	Ring04
433-RBY-1-8430-0001	2013-06-14 12:34:18	NULL	432-TVV-3-0000-0000	1	-3.71	3.71	3.60...	-135	0	0	NULL	magnetometer	Ring04
433-RBY-1-8430-0003	2013-06-14 12:34:39	NULL	432-TVV-3-0000-0000	1	-3.71	3.71	3.60...	-135	0	0	NULL	magnetometer	Ring04
433-RBY-1-8430-0005	2013-06-14 12:34:58	NULL	432-TVV-3-0000-0000	1	-3.71	3.71	3.60...	-135	0	0	NULL	magnetometer	Ring04
433-RBY-1-8440-0001	2013-06-14 12:35:26	NULL	432-TVV-3-0000-0000	1	0	5.25	3.60...	-90	0	0	NULL	magnetometer	Ring04
433-RBY-1-8440-0003	2013-06-14 12:35:43	NULL	432-TVV-3-0000-0000	1	0	5.25	3.60...	-90	0	0	NULL	magnetometer	Ring04
433-RBY-1-8440-0005	2013-06-14 12:36:05	NULL	432-TVV-3-0000-0000	1	0	5.25	3.60...	-90	0	0	NULL	magnetometer	Ring04
433-RBY-1-8450-0001	2013-06-14 12:42:25	NULL	432-TVV-3-0000-0000	1	3.71	3.71	3.60...	-45	0	0	NULL	magnetometer	Ring04
433-RBY-1-8450-0003	2013-06-14 12:36:31	NULL	432-TVV-3-0000-0000	1	3.71	3.71	3.60...	-45	0	0	NULL	magnetometer	Ring04
433-RBY-1-8450-0005	2013-06-14 12:36:53	NULL	432-TVV-3-0000-0000	1	3.71	3.71	3.60...	-45	0	0	NULL	magnetometer	Ring04

KatrinNumber Filter:  Apply     Only most recent ValidityStart.    RowCount: 97

New Entry    Delete Selected    Reload

**Figure 4.3:** Web interface for the administration of KATRIN's database tables. Here a list of geometric positions is shown, sorted by KATRIN numbers.

KATRIN Database Admin    Katrin Numbers    Sensor    Calibrations    **Positions**    ChannelMappings    Help ▾

Katrin Number	EntryTime	ValidityStart	MinValue	MaxValue	Adc	AdcPath	Category	Description
123-ABC-0-1111-0001	2013-08-15 05:09:17	2011-12-31					PumpP...	vacuum gauge actual pressure ...
432-RPI-3-3110-0001	2014-01-30 14:28:27	NULL					umpPo...	vacuum gauge MKS Inv-Magn...
432-RPP-3-2320-0001	2012-11-15 13:23:07	2012-10-31					PumpP...	TEMP vacuum g... mainspec coldc...
432-RPP-3-2320-0002	2013-08-21 14:07:30	2012-10-31						
433-ELV-1-0100-0001	2013-03-17 13:40:54	NULL						
433-ELV-1-0101-0001	2012-12-11 09:48:03	NULL					aircoils	SW Currents act...
433-ELV-1-0200-0001	2013-03-17 13:44:17	NULL					aircoils	SW Currents act...
433-ELV-1-0201-0001	2012-12-11 09:48:08	NULL					aircoils	aircoil 1 current ...
433-ELV-1-0301-0001	2012-12-11 09:46:50	NULL					aircoils	aircoil 2 current ...
433-ELV-1-0401-0001	2011-11-22 15:48:53	2010-12-31					aircoils	aircoil 3 current ...
433-ELV-1-0501-0001	2011-11-29 07:50:10	2010-12-31					aircoils	aircoil 4 current ...
433-ELV-1-0601-0001	2012-12-11 09:46:55	NULL					aircoils	aircoil 5 current ...
433-ELV-1-0701-0001	2012-12-11 09:47:00	NULL					aircoils	aircoil 6 current ...
433-ELV-1-0801-0001	2012-12-11 09:47:05	NULL					aircoils	aircoil 7 current ...
433-ELV-1-0901-0001	2012-12-11 09:47:11	NULL					aircoils	aircoil 8 current ...

**Create New Sensor Entry**

KatrinNumber:

Validity Start:

Stored:

Cabinet ID:

Minimum Value:

Maximum Value:

Calibrated:

Adei Path:

Category:

Description:

Save    Cancel

KatrinNumber Filter:  Apply    AdcPath Filter:  Apply     Only most recent ValidityStart.    RowCount: 501

New Entry    Delete Selected    Reload

**Figure 4.4:** Web interface showing a dialog for the creation of a new sensor entry.

## 4.2 C++ Programming Interface to Data (Tier 3)

In this section the last logical layer of KATRIN's IT infrastructure is introduced. For users of the software framework KASPER, who require access to any kind of KATRIN data, it is a crucial and frequently used software component.

### 4.2.1 KaLi

The C++ programming interface for data access and selection is integrated in the global software framework KASPER as the module called *KaLi*<sup>1</sup> (also see figure 3.3 on page 44).

The ground work for KaLi was originally laid by Sebastian Vöcking [Vöc], who first advocated the concept of accessing data via a C++ programming interface. In a joint effort the code was developed to serve as an interface to KATRIN's data service KDBServer (section 3.4.1) and feature basic data selection and analysis logic.

In the course of the present thesis, KaLi underwent a thorough and complete rewrite with the aim to provide coherent interfaces and clean data structures, which integrate seamlessly with other KATRIN simulation and analysis code. Many enhanced data access and analysis functionalities were added during this code refactoring in order to comply with the increasing demands from analyses performed during the first SDS commissioning phase in 2013. In conjunction with the server-side enhancements, outlined in section 3.4.6, many demanding operations (comprehensive Slow Control queries in particular) could be accelerated by about an order of magnitude.

Most common analysis tasks at KATRIN can now be realized with less than  $\sim 100$  lines of code in a very straightforward manner. This is made possible by the extensive data processing and access logic behind KaLi and the web service framework KDBServer, both of which consist of nearly  $\sim 35\,000$  lines of code. While the backbone of KaLi utilizes rather advanced programming techniques, such as template metaprogramming, the users of the code usually only have to work with the most basic and quickly learnable language constructs. Its basic usage and working principle will be illustrated in the following with the aid of a few short code examples.

### 4.2.2 Data Format Definitions

One of KaLi's tasks is the definition of KATRIN's basic data formats in the form of C++ class declarations. The definitions cover all data types held in our databases, such as sensors, calibration, geometry and others (section 3.3.4). In addition, many auxiliary data types are defined, which are required to perform data requests and file system operations,

---

<sup>1</sup> The name KaLi is an acronym standing for 'KAtrIN LIbrary'. Although its meaning is not perfectly accurate anymore, since KaLi constitutes a specific part of the overall library, the name was kept for historical reasons.

such as KATRIN numbers, timestamps (UTC time with nanosecond precision), IO helpers and wrappers for run header information. For most data types serialization within the ROOT framework is supported<sup>1</sup>.

More sophisticated class structures are provided for the representation of Slow Control data and ORCA run files, allowing for convenient and fast navigation through larger amounts of information. Basic analysis logic is included, allowing users to quickly accumulate statistical quantities or apply custom calibration algorithms to raw data. All KaLi data types which require an iteration over a sequence of data entries, implement an iterator interface which is in compliance with the C++ Standard Template Library (STL) library. Thus the data can be navigated and transformed with most common C++ algorithms.

### 4.2.3 Unified RPC Interface

KaLi's core feature certainly is the client interface to the data inventory of the experiment. The interface is implemented upon the same gSoap library, used in KDBServer to expose its data services to client applications (section 3.4.1). Therefore, KaLi is not only the logical but also the technically consistent counterpart of KDBServer. As the name gSoap suggests, communication with the server is established through the SOAP protocol, meaning that client and server exchange information via XML messages over standard (or secure) HTTP connections.

From a user's or developer's point of view, the rather complex network operation is treated as a Remote Procedure Call (RPC). The user working on the client side can be indulged in the illusion of an ordinary local function call. One does not have to worry about the technical details of network communication or how the result of a data request has to be assembled from various sources, processed, serialized and transported over the network. No prior knowledge about web technologies or databases is required, in order to use the interface. A very basic understanding of C++ programming is sufficient.

#### A Short RPC Example

The following code example should illustrate, how simple a request for Slow Control data turns out to be for a KaLi user in practice. The complex task of resolving the correct data source and applying valid calibration data (see section 3.4.4), is entirely handled remotely on the server-side.

```
1 // instantiate a data manager
2 KLDataManager myDataManager;
3
4 // select and specify data
5 KLSlowControlFilter dataFilter;
6 dataFilter.AddKatrinNumber( "433-RBY-1-8420-0001" );
7 dataFilter.AddKatrinNumber( "433-RBY-1-8420-0003" );
8 dataFilter.SetTimeInterval( "2013-09-08 12:00:00", "2013-09-11 22:00:00" );
```

---

1 Serialization is the decomposition of an object into its data members, so that it can be written to disk.

```

9
10 // invoke the remote procedure call and get the result data
11 KLSlowControlPtr myScData = myDataManager.GetSlowControl( dataFilter );
12
13 // output the median of channel 0 of the calibrated sensor value to console:
14 cout << myScData->Accumulate( KLAccumulator::eMedian ).GetCalibrated(0) << endl;

```

In line 11 of the above example, a local function call is invoked, which triggers the RPC process, requests data from the remote server, interprets the response and returns the result value. And in fact, from the user's perspective, this whole process requires only *one single line of code*.

KLDataManager is the class which implements all read and write operations offered by KATRIN's web service KDBServer. Each data type has its own interface method and selection arguments, but all of them are structured according to a consistent pattern. Object-oriented class inheritance is applied throughout the code, to establish a logical grouping of data types. No matter how diverse the different data types and their source locations are (section 3.3), all of them are accessed and used through one unified interface.

An exemplary diagram, depicting the communication process behind KLDataManager, is shown in figure 4.5.

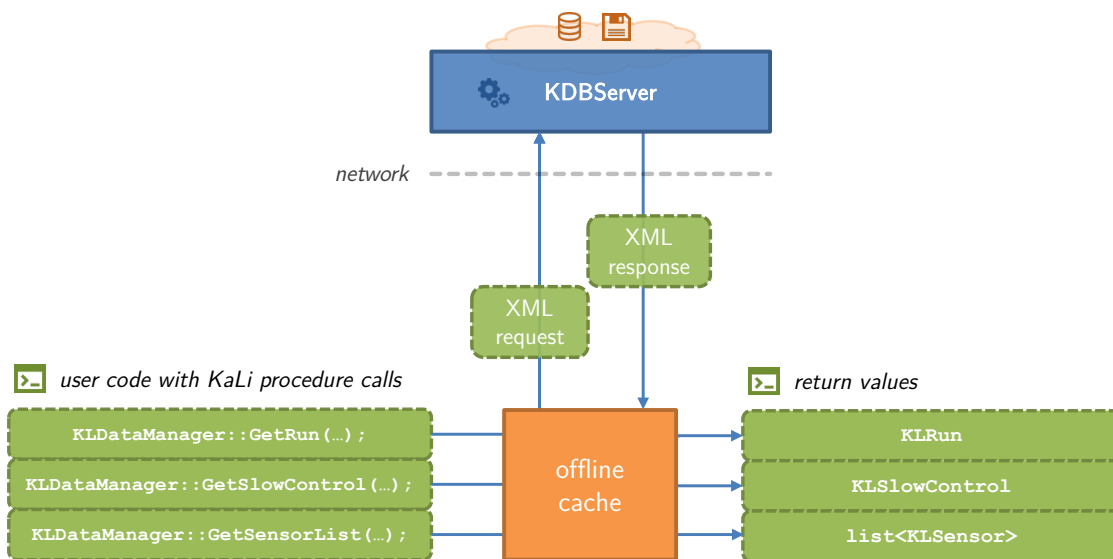


**Figure 4.5:** Data operations articulated to KLDataManager via function calls are accumulated into as little XML requests as possible. The returned data is intercepted by KaLi's caching mechanism and stored on the user's harddrive. When the request is repeated while a network connection is unavailable, KaLi will automatically attempt to fall back to cached data and return a result.

## Reducing Communication Overhead

Response times of RPC calls are generally well below 100 milliseconds, including network connection and data transfer durations. The underlying KaLi code uses a smart pointer technique to automatically collect multiple calls to `KLDataManager` into a single request bundle, thus reducing the number of subsequent network connections and the related protocol overhead.

Typical use cases would be, for instance, a series of simple calibration and positioning queries or more complex searches for detector data combined with Slow Control. Only when one of the returned data structures is accessed (dereferenced) for the first time, an actual data transfer between the user's local machine and the data server takes place.

In addition, on-the-fly Zlib data compression [Deu96] is applied during transfer, which is not only effective with respect to the exchanged XML information, but also reduces the transfer volume for binary files by a factor of up to 3.

### 4.2.4 Offline Caching

Many analysis tasks in KaLi can be performed without depending on the RPC interface. KaLi provides the necessary functions to load run files or serialized Slow Control data directly from local disk. However, the function set provided by `KLDataManager` is the easiest way to access most recent data, while at the same time writing the least amount of code to do so.

An important question at this point is: What happens to the analysis logic, when the client computer has no network connection? Does the RPC interface become useless and the code, depending on it, non-functional? Fortunately, this is not the case. KaLi's `KLDataManager` features a transparent caching mechanism for read operations. Most of the analysis code built upon KaLi will continue to work unperturbed, even when disconnected from network.

The working principle of the caching mechanism is outlined in figure 4.5. Every outgoing request is intercepted and distinctly indexed with a hash identifier. The corresponding response message from the server is then labeled with the hash identifier and stored in a cache directory on the client machine. This principle is applied to all outgoing and incoming communication, with the exception of those requests explicitly demanding real-time data.

If the network connection is down or even severed during execution of the code, `KLDataManager` attempts to recover data, which matches the request hash and has been downloaded before, from the local cache directory. The program will seamlessly continue execution with a short notification on the user's console. No modification of the analysis code or interaction from the operator is required to make use of this feature.

To keep the local cache directory organized and clean, KaLi can be configured to restrict the maximum age and size of cached data. If not instructed otherwise, the cache directory is cleaned automatically from outdated files before the termination of the user's program.

### 4.2.5 Database Browsing

A list of available KATRIN numbers, registered sensors, as well as calibration and positioning data can fairly easily be queried through `KLDataManager`. The user can select specific data by constructing a `KLDatabaseFilter` and specifying KATRIN number ranges, time intervals or a filter criterion for a specific author.

```

1 // get accustomed to KATRIN numbers
2 KLLKatrinNumber someNumber("436-WHV-0-9999-0001");
3 KLLKatrinNumber sameNumber(436, "WHV", 0, 9999, 1);
4 // this should be true
5 assert( someNumber == sameNumber );
6
7 KLLKatrinNumber invalidNumber("435-UIAOK");
8 // this number must be invalid
9 assert( !invalidNumber.IsValid() );
10
11 // get a list of all registered KATRIN numbers from the database
12 list< KLLKatrinNumber > numberList = myDataManager.GetKatrinNumberList();
13
14 // output the number of result entries to console
15 cout << "# of katrin number entries: " << numberList.size() << endl;
16
17 // now query a selection of registered sensors
18 KLDatabaseFilter dbFilter;
19 // constrain the date, since they were entered in the database
20 dbFilter.SetEntryInterval( KLTimeStamp(2013, 01, 01), KLTimeStamp::Max() );
21 // only return entries in a katrin number range 433-RBY-0 to 433-RBY-9
22 dbFilter.SetKatrinNumberInterval( KLLKatrinNumber(433, "RBY", 0, 0, 0),
23 KLLKatrinNumber(433, "RBY", 9, 9999, 9999) );
24
25 list< KLSensor > sensorList = myDataManager.GetSensorList( dbFilter );
26
27 // output the number of result entries to console
28 cout << "# of selected sensor: " << sensorList.size() << endl;
29
30 // get the positioning information for the last sensor in the list
31 dbFilter.SetKatrinNumber( sensorList.back().GetKatrinNumber() );
32 KLPosition sensorPosition = myDataManager.GetPosition( dbFilter );
33
34 // output the position to console
35 cout << sensorPosition.GetX() << ", " << sensorPosition.GetY() << ", " <<
36 sensorPosition.GetZ() << endl;

```

### 4.2.6 Run File Analysis

The run file interface is a bit more complex and the following example only scratches the surface of the logic provided for searching and navigating through detector event data (see figure 3.6). If the user knows the specific run number of interest, he can directly request

and download the binary file and start his analysis. If not, he can start with a search for certain run criteria and request a lightweight list of run information, before deciding to initiate a larger file transfer.

```

1 // clean up files in my local cache, that are older than 2 weeks
2 myDataManager.CleanupCache( KLWeeks(2) );
3
4 // query a list of focal plane detector runs, starting January 2013
5 KLRunFilter runFilter;
6 runFilter.SetOrcaSystem( KLEOrcaSystem::FPD );
7 runFilter.SetTimeInterval( KLTimeStamp(2013, 8, 1), KLTimeStamp::Now() );
8
9 // start data transfer
10 KLRunIdList runIdList = myDataManager.GetRunIdList( runFilter );
11
12 // output the number of results to console
13 cout << "# of FPD runs since 2013.08: " << runIdList.size() << endl;
14
15 // let's pick the last (most recent) run and download the event data
16 KLRunId myRunId = runIdList.back();
17 KLRunPtr myRun = myDataManager.GetRun( myRunId, KLERunFileType::
  OrcaStreamRootFormat );
18
19 // iterate over all recorded energy events and output the ADC values:
20 KLEventSequence< KLEnergyEvent > myEventSequence = myRun->GetEventSequence<
  KLEnergyEvent >();
21
22 for (int i = 0; i < myEventSequence.size(); ++i)
23 {
24     cout << "event " << i << " ADC value: " << myEventSequence[i].GetADCValue()
  << endl;
25 }

```

#### 4.2.7 Slow Control Analysis

KaLi features a readily comprehensible interface for working with Slow Control data. The complicated processing of diverse raw data formats, non-standard timestamps and synchronization with KATRIN's sensor and calibration database is done on the server side. However, the user has the freedom to investigate and manipulate any kind of calibration applied to raw Slow Control data, if desired.

Once a set of KATRIN numbers for the selected readout channels and a time interval have been specified, the user can choose to request either data for a sensor's actual acquisition rate or a reduced amount of data. In case of the latter, the server performs an interpolation by averaging sensor values over a specified time duration.

The returned data can be navigated by the user in a table-like structure. Each row holds a UTC time stamp and one raw and calibrated value per channel. An accumulation logic is included to allow for quick extraction of common statistical quantities without the need of

iterating through the whole data set by hand. The following quantities can be calculated: Row count, standard deviation, unbiased error of mean, kurtosis, maximum, mean, median, minimum, skewness, sum and unbiased variance.

The following code example illustrates the brief analysis of a single channel one month interval of Slow Control data:

```

1 // configure the data filter
2 KLSlowControlFilter dataFilter;
3 dataFilter.SetTimeInterval( "2013-11-01 08:00:00", "2013-12-01 08:00:00" );
4 dataFilter.AddKatrinNumber( "436-WHV-0-9999-0001" );
5
6 // let the server interpolate the data within 5 minute intervals
7 dataFilter.SetResampling( KLMinutes(5) );
8
9 // query the data
10 KLSlowControlPtr myScData = myDataManager.GetSlowControl( dataFilter );
11
12 // quit the program in case no data was returned
13 if (myScData->IsEmpty())
14 {
15     cerr << "No Slow Control data was received." << endl;
16     return -1;
17 }
18
19 // iterate over all slow control values
20 for (KLSlowControlEntry& entry : *myScData)
21 {
22     // print the timestamp, raw value and calibrated value to console
23     cout << entry.GetTimeStamp() << "\t"
24          << entry.GetRaw() << "\t"
25          << entry.GetCalibrated() << endl;
26 }
27
28 // accumulate some statistical quantities
29 KLSlowControlEntry min      = myScData->Accumulate( KLEAccumulator::Min );
30 KLSlowControlEntry max      = myScData->Accumulate( KLEAccumulator::Max );
31 KLSlowControlEntry mean     = myScData->Accumulate( KLEAccumulator::Mean );
32 KLSlowControlEntry median   = myScData->Accumulate( KLEAccumulator::Median );
33 KLSlowControlEntry variance = myScData->Accumulate( KLEAccumulator::Variance );

```

#### 4.2.8 Custom Calibration Functions

The database provides access to any form of calibration data: Lists of float / integer values or more complex binary data. When such an entry is requested from the database, it comes with a definition of how to apply the calibration to raw data and what format the resulting value should have.

Aside from predefined calibration functions like polynomials or vector transformations, the user can implement custom calibration logic and apply it to any raw data downloaded with KLDataManager, including Slow Control, or data generated locally.

```
1 /**
2  * Custom calibration function for the Monitor Spectrometer Fluke voltage.
3  * @param input Raw value.
4  * @return  $f(x) = (p_0 + x) * p_1 * p_2$ 
5  */
6 template<>
7 double KLCalibration< KLECalibrationType::MonSpecVoltmeter >::Calibrate(double
8 input) const
9 {
10 // container holding 3 calibration values from the database
11     vector<double> p = this->GetCalibrationData();
12     p.resize(3, 0.0);
13 // custom calibration logic
14     return (p[0] + input) * p[1] * p[2];
15 }
```

#### 4.2.9 Documentation

The source code of KaLi is documented using ‘doxygen’ [Hee08] annotations. When compiling and installing the code, the user can choose to generate a full API reference documentation along with it, explaining the usage of each class, method, and function arguments.

In order to make first steps with the code easier for beginners, a set of commented example programs is delivered with the installation of KaLi, illustrating recommended methods and patterns for common analysis tasks. One of these examples is the detector energy calibration tool presented in the following section.

### 4.3 Fast Analysis Examples

In the following, three exemplary data monitoring and analysis programs are presented, which were developed and tested along with the C++ client library KaLi, making use of the same convenient data selection and analysis features.

#### 4.3.1 Focal Plane Detector Energy Calibration

Figure 4.6 shows the output from an analysis tool, performing an energy calibration of the focal plane detector. For this purpose, the detector system is operated in a special mode, where photo electrons emitted from a calibration titanium disk are recorded by the detector. KaLi downloads the corresponding run file and generates a histogram of ADC values. A Gaussian function is fitted to determine the mean ADC value. The Slow Control voltages of the titanium disk and a few other electric components are queried to calculate the energy of the incident electrons, which can then be related to the corresponding ADC values.

The amount of code required for this sort of analysis is only about 100 lines long, including the logic to request data, perform fitting of ADC values and painting of the result graphs. Three Slow Control data sets and one run file have to be downloaded (total size  $\sim 20$  MB) or retrieved from cache. On a common Intel® Core i5™ desktop computer with access to the data server on the same local area network, the total execution time is about 5 seconds.

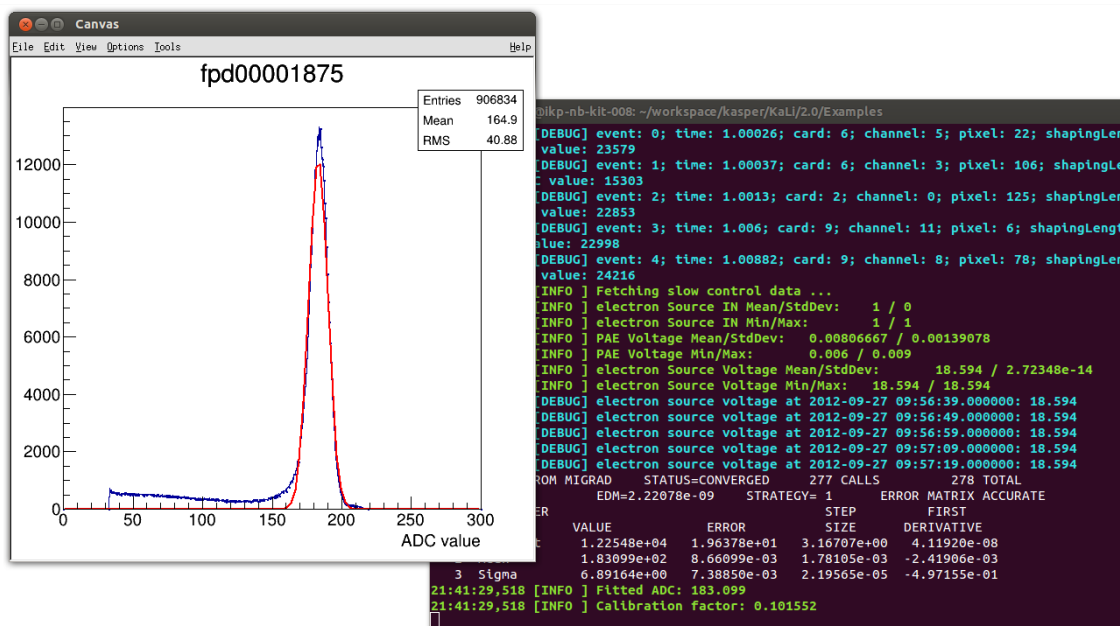
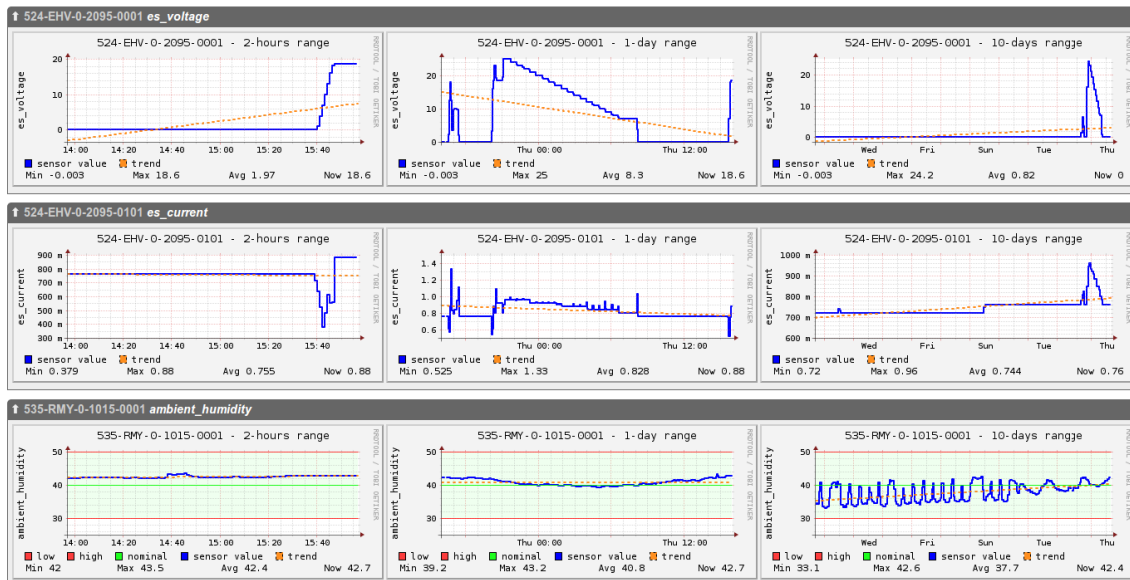


Figure 4.6: Energy calibration of the focal plane detector, purely built on KaLi analysis logic.

### 4.3.2 Slow Control Monitor

As outlined in section 4.2.7, using the Slow Control functionality provided by KaLi, data from thousands of sensors can be accessed in a consistent manner and with little amount of effort. The proper calibration data sets are applied automatically.

While in many use cases sensor readout will most likely be directly incorporated in an analysis, the KaLi interface can also be used to store selected data in ASCII or ROOT compatible file formats, or to generate graphical output. In figure 4.7 a Slow Control monitoring application, written by Jan Behrens [Beh], is shown, which is built upon the KaLi library. In regular intervals, the tool requests data from a predefined set of sensors (KATRIN numbers) and publishes a collection of graphs on an internal webpage for monitoring purposes.



**Figure 4.7:** A series of regularly updated slow control graphs for predefined KATRIN numbers. Script written by Jan Behrens [Beh].

### 4.3.3 Monitor Spectrometer Analysis

The MAC-E filter based monitor spectrometer (section 2.7.2) is targeted to monitor the energy scale stability of the KATRIN experiment. Rubidium  $^{83}\text{Rb}$ , implanted into a solid substrate, decays into krypton  $^{83}\text{Kr}$ , which serves as electron emitter. By monitoring the position of the K-32 conversion line in the obtained electron spectrum, the energy scale of the retarding potential can be reliably determined [Erh14; Sle13].

Figure 4.8 shows the output of the analysis package ‘createfilterspec’. The tool gathers the required detector event data (typically  $\sim 20$  MB) and 60 minutes of Slow Control data for three voltage meters through the KaLi interface. In a local network the execution time is about 5 seconds, including data transfer time, fitting of the line shape and plotting.

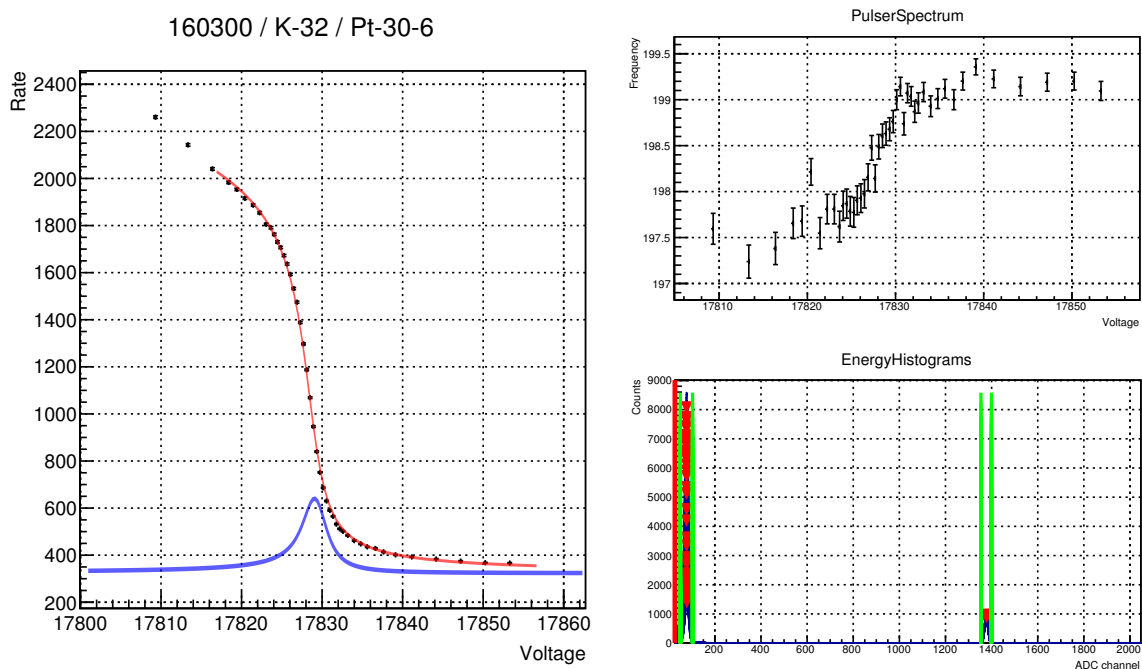


**Figure 4.8:** Monitor spectrometer filter spectrum (red line) and a fit of the K-32 conversion line (blue). Script written by Martin Slezák [Sle].

#### 4.4 Detector Analysis Suite

The BEANS (Building Analysis Sequence) package is a suite of detector analysis tools which is based on a toolkit originally developed for the focal plane detector commissioning in 2012. In addition to detector event data analysis it contains a utility to perform electronics readout simulations (DRIPS). The design goal of BEANS is to automatize tasks that are performed on a regular basis and to minimize the amount of code development time, usually required for more complex physics analysis logic. The conceptual structure of BEANS resembles a very mathematical or functional way of programming, which is different from the paradigm of imperative programming, common in C++.

```
1 KDBeans beans;  
2 // prepare analysis chain  
3 (beans  
4   // readout event data recorded in 'energy mode'  
5   .Append(new KDEnergyEventReadout())  
6   // create an ADC histogram  
7   .Append((new KDAdcHistogram())  
8     ->SetBin(300, 0, 300)  
9     ->SetTitle("ADC")  
10  )  
11  // prepare histograms and graphs for drawing  
12  .Append(new KDDraw())  
13 );  
14 // execute analysis  
15 beans.Build(argc, argv).Start();
```

BEANS has been developed by Sanshiro Enomoto from the University of Washington, Seattle [Cen14]. His work motivated many of the design decisions made for the data processing framework of KATRIN and the data access module KaLi. All offline analyses performed with BEANS rely on the RPC interface provided by KaLi (section 4.2.3) to read from KATRIN data sources and in some cases write to the database. The offline caching functionality of KaLi enables most scripts written for BEANS to reproduce an analysis without network connection from local data.

Figure 4.9 shows the graphical result of a typical BEANS analysis, composed of multiple reusable analysis components, arranged in a linear sequence.

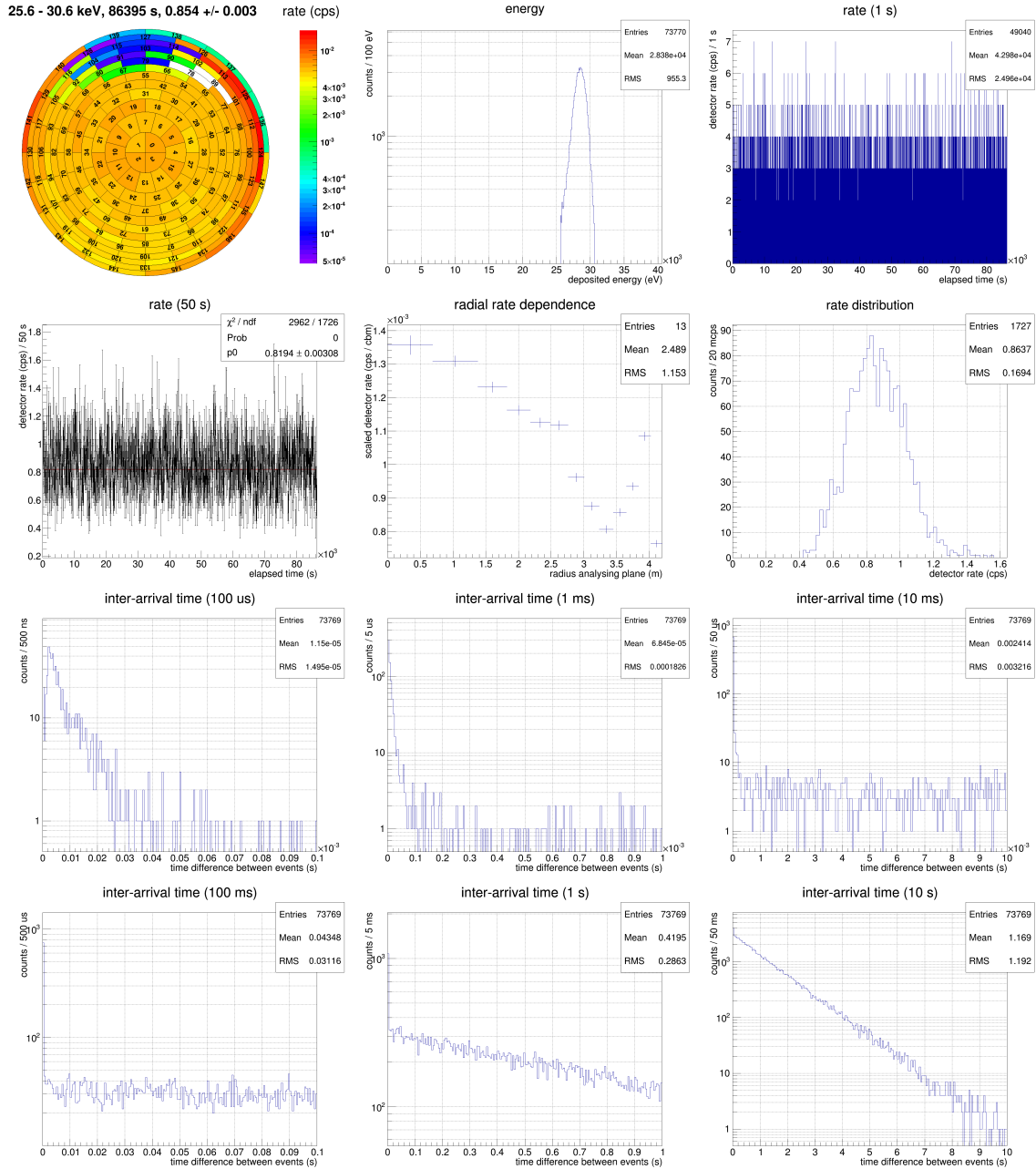


**Figure 4.9:** An exemplary set of detector analysis plots, generated by BEANS. This summary features hit rate, energy and inter-arrival time distributions. The plotted data was recorded by the focal plane detector in run number 6959, a background measurement during the spectrometer commissioning phase.

## 4.5 Particle Tracking And Electromagnetic Field Simulation

### 4.5.1 Kassiopeia

Kassiopeia is a particle tracking framework, originally developed for the KATRIN experiment. The targeted physics problem is the simulation of particle trajectories in electromagnetic fields, which require solving of complex differential equations of motion and involve stochastic processes, such as bulk scattering, decay and potential surface processes. These computations are backed by a fully-featured geometry package KGeoBag and a versatile electromagnetic field simulation library KEMField (section 3.2.1). A detailed publication is in preparation [Fur14], which will be accompanied by the release of Kassiopeia as an independent tool for general use.

For KATRIN, Kassiopeia is utilized to simulate trajectories of charged particles through the experimental setup. Such simulations are crucial for the understanding of the transmission characteristics of the apparatus and for the identification of sources of possible background, such as trapped particles. In figure 4.10 a simulated track of an electron, stored in the main spectrometer, is visualized.

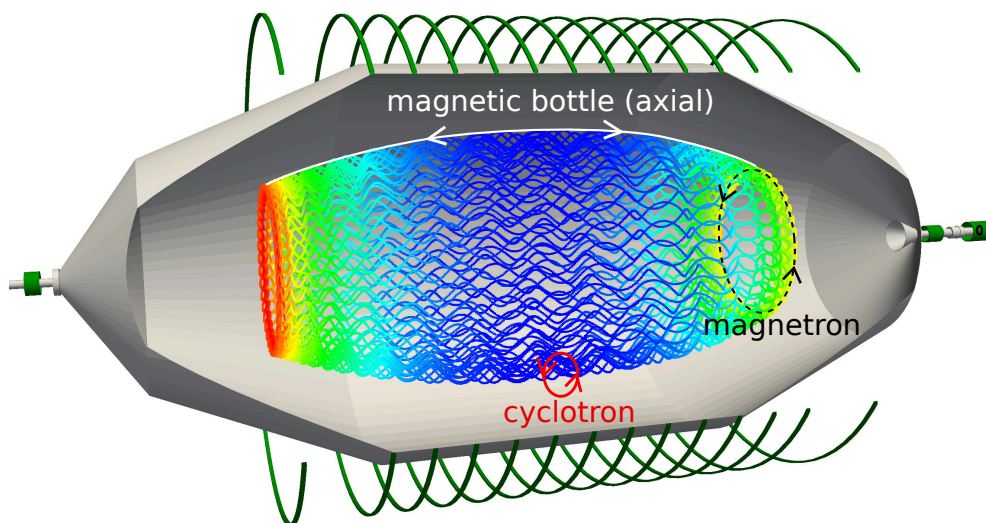


**Figure 4.10:** Track of a stored particle inside the main spectrometer, simulated with Kassiopeia and visualized with ParaView [Ced06]. Graphic by courtesy of Stefan Groh, KIT [Gro15].

## 4.5.2 Fieldline Monitoring

Kassiopeia uses the data interface provided by KaLi to access Slow Control data, such as solenoid currents and magnetic field sensor data. Thus, field calculations can be performed for the actual electromagnetic setup, monitoring the field in nearly real-time (<1 min). A fieldline snapshot of the KATRIN setup during the SDS commissioning phase is shown in figure 4.11.

The current development of Kassiopeia aims to integrate particle tracking and field simulations even better with the information provided by KATRIN's database. Accurate and current positioning data and geometric information will then be directly incorporated into the simulations.

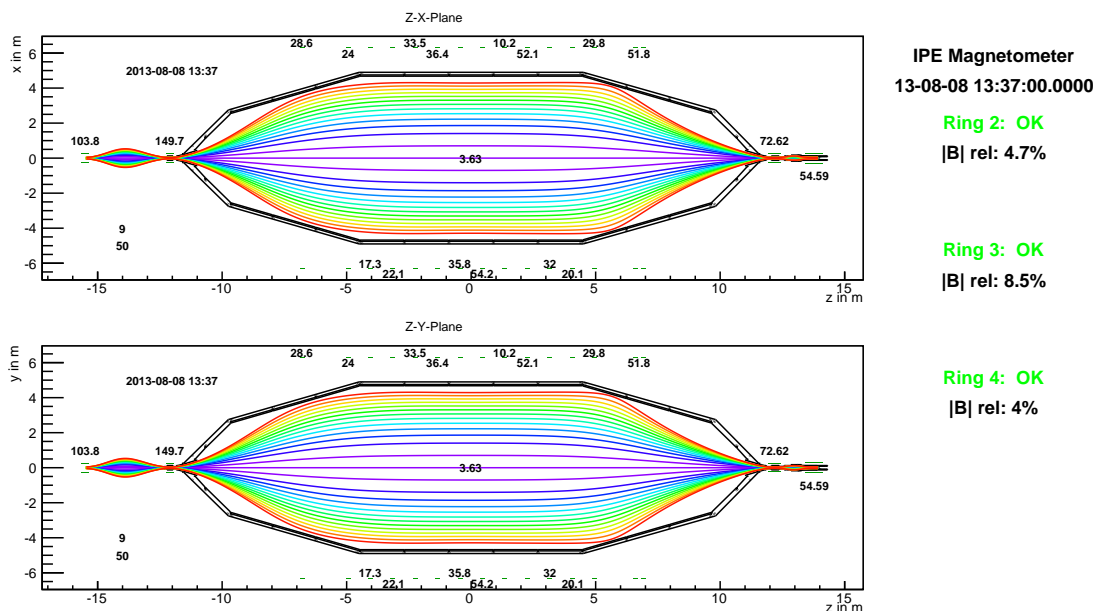


**Figure 4.11:** Near-time magnetic fieldline monitoring. The magnetic field calculation is based on real-time magnetometer data from 72 channels, accessed through the KaLi data interface.



# CHAPTER 5

---

## Beta Spectrum Calculation

---

In this chapter those parts of the KASPER framework are presented, which implement  $\beta$ -decay theory and KATRIN specific characteristics of the experimental setup in order to reliably compute the expected count rates of the experiment. The calculations described in the following sections are thus an essential basis for any further statistical studies, including a neutrino mass analysis.

### SSC

The Source and Spectrum Calculation (SSC) module implements the computation of differential and integrated tritium  $\beta$  decay spectra. In order to do so, it has to model the electromagnetic and gasdynamic properties of the source section, compute the response function of the apparatus and map the flux of electrons onto the pixels of the silicon detector, residing at the opposite end of the KATRIN beamline.

One important difference with respect to the particle tracking module KASSIOPEIA is the fact, that SSC does *not* perform Monte Carlo simulations. The kinetic electron energy spectrum is calculated analytically according to  $\beta$ -decay theory and then numerically integrated, incorporating source and transmission properties. This distinction is important with regard to later statistical analyses, where the spectrum has to be recalculated for varying input parameters over and over again: The analytical computation of expected count rates is performed faster by orders of magnitude, compared to a full-blown MC particle tracking simulation.

Nevertheless, the two software modules share a lot of overlap: Source spectra computed by SSC can serve as input to particle tracking simulation. Vice versa, detailed and computationally intense transmission function simulations from KASSIOPEIA are used to model an accurate analytical description of the transmission function, which is required by SSC as input to compute the integrated  $\beta$  spectrum.

Two former doctoral students at KIT, W. Käfer and M. Hötzel, provided the ground work for the source modeling and spectra calculation code as part of their theses [Höt12; Käf12]. Since then, the code has undergone some substantial changes and additions, which were demanded by increasingly complex statistical questions. In the following, the core functionality of SSC is briefly summarized, but with emphasis on recent changes to the code, including additional systematic effects and numerical tools for better performance and accuracy.

## KaFit

The software module KaFit does not only contain the statistical methods, described in the following chapter 6. It provides additional features, which fill the gap between the calculation of an integrated  $\beta$  spectrum and the prediction of an actual event count number for a data-taking run period.

KaFit implements several models of geometry-dependent background and provides the logic to define a run interval strategy in conjunction with a given total measurement time distribution. In this way the code can be used to predict the expected event count on each pixel of the detector for various configurations, and to simulate a complete set of KATRIN data taking runs.

### 5.1 Differential Beta Emission Spectrum

The differential  $\beta$  spectrum is calculated according to classical Fermi theory, which was already outlined in section 1.4.1. Modifications and approximations to the analytical description of the energy spectrum were chosen to maximize the accuracy close to the endpoint region. According to equation 1.30, the electron energy spectrum can be calculated as:

$$\begin{aligned} \frac{dN}{dE} &= C F(Z, E) p(E + m_e) \\ &\sum_f |U_{ei}|^2 P_f f_{\text{rad}}(E - E_f) \varepsilon_f \sqrt{\varepsilon_f^2 - m_i^2} \Theta(\varepsilon_f - m_i), \\ \varepsilon_j &= E_0 - E_f - E \end{aligned} \quad (5.1)$$

In this notation the constant  $C$  absorbs all energy independent factors:

$$C = \frac{G_F^2 \cos^2 \theta_C}{2\pi^3} |M|^2 \quad (5.2)$$

The sum over all probabilities  $P_f$  of the Final State Distributions (FSDs) (section 5.2) has to be unity, so that  $\sum_f P_f = 1$ .

### 5.1.1 Radiative Corrections

Electrons, emitted within a Coulomb field of a nucleus, experience subtle energy losses due to their interaction with virtual and soft real photons. This correction, accounted for by the energy dependent factor  $f_{\text{rad}}(E - E_f)$ , only becomes relevant close to the tritium endpoint. In our case,  $f_{\text{rad}}$  is implemented as recommended by [Rep83].

### 5.1.2 Fermi Function

The Coulomb interaction between the outgoing electron with energy  $E$  and the daughter nucleus with charge  $Z$  is described by the Fermi function  $F(Z, E)$ . In case of tritium  $\beta$ -decay, the attraction of the electron by the positively charged nucleus can be accounted for by an empirical, non-relativistic approximation, as outlined in [Sim81],

$$F(Z, E) = \frac{x}{1 - \exp(-x)} \left( 1.002037 - 0.001427 \frac{v_e}{c} \right); \quad x = \frac{2\pi Z \alpha}{v_e/c} \quad (5.3)$$

with the fine-structure constant  $\alpha$  and electron velocity  $v_e$ .

### 5.1.3 Nuclear Recoil

Within the center-of-momentum frame of a tritium molecule  $\text{T}_2$ , the daughter molecule  $(^3\text{HeT})^+$  experiences a recoil after the decay and carries away a small amount of kinetic energy. According to [KAT05], the recoil energy  $E_{\text{rec}}$  can be approximated by

$$E_{\text{rec}} = E \frac{m_e}{M_{(^3\text{HeT})^+}}. \quad (5.4)$$

With the electron mass  $m_e$  and the daughter molecule mass  $M_{(^3\text{HeT})^+}$ , the recoil energy shows a linear dependence on the kinetic electron energy  $E$ . Close to the endpoint  $E_0 \approx 18.6$  keV and a few eV below,  $E_{\text{rec}}$  yields a nearly constant value of  $\approx 1.7$  eV. For practical reasons, within our calculations the parameter  $E_{\text{rec}}$  for the recoiling  $(^3\text{HeT})^+$  ion and the slightly lower recoil energies for the isotopologues  $(^3\text{HeD})^+$  and  $(^3\text{HeH})^+$  are incorporated by the final states  $E_f$ .

A comparison of differential  $\beta$  spectra for different values of  $m_\nu$  without the inclusion of final states or the Doppler effect (see section 5.3) is shown in figure 5.1.

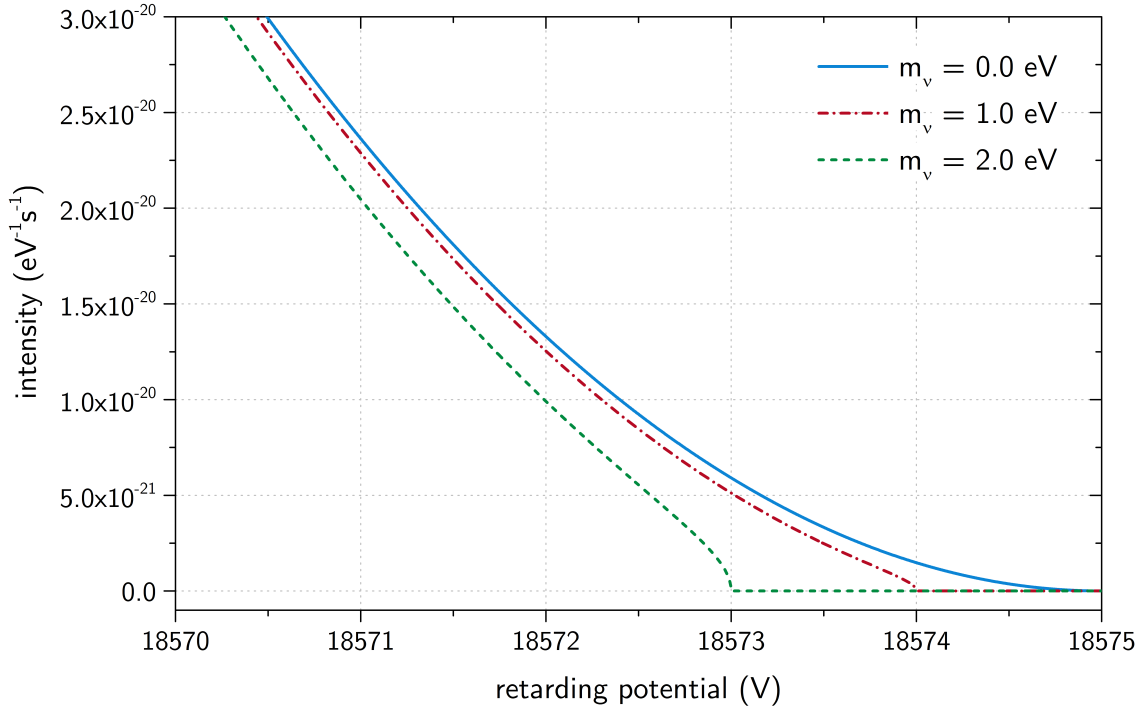


**Figure 5.1:** Comparison of differential  $\beta$  decay spectra. Final states and the Doppler effect have been deactivated to better emphasize the characteristic shape distortion due to a non-zero neutrino mass.

## 5.2 Final States Distribution

The  $\beta$ -emitter in the WGTS consists of molecular states of the tritiated hydrogen isotopologues  $T_2$ ,  $DT$  and  $HT$ , which decay into  $(^3\text{HeT})^+$ ,  $(^3\text{HeD})^+$  and  $(^3\text{HeH})^+$  respectively. After the decay, the daughter molecule may be left in a rovibronic (rotational and vibrational) and excited electronic final state. These discrete states of excitation are represented by a comprehensive set of Final State Distributions (FSDs), characterized by an excitation energy  $E_f$  and probability  $P_f$ .

Although sometimes incorrectly referred to as a systematic effect, the final states clearly have a non-negligible impact on the shape of the  $\beta$  spectrum, as the maximum available energy for the  $\beta$ -decay electron is decreased by the excitation energy  $E_f$ .

In fact, the effective  $\beta$  spectrum has to be calculated as a superposition of many single  $\beta$ -decay branches, each one with a lower effective endpoint  $E_{0,\text{eff}} = E_0 - E_f$ , weighted by  $P_f$  (see equation 5.1). For this purpose our code applies a set of pre-packaged FSDs, which were created according to most recent calculations in [Dos08; Dos06; Sae00].

The abundance of each hydrogen isotopologue has to be specified as input parameter to the spectrum calculation (like the tritium purity  $\varepsilon_T$ ), and the corresponding final states have to be weighted accordingly. Reliable monitoring of these abundances during measurements is the objective of dedicated Laser Raman measurements (section 2.3).

Each isotopologue is further subdivided into several distributions, each one corresponding to an initial angular momentum  $J = 0, 1, 2, 3$  of the parent molecule. Each species of  $J$  has to be weighted according to a Boltzmann distribution:

$$P_J(T) = \frac{g_s g_J \exp\left(-\frac{\Delta E_J}{k_B T}\right)}{Q} \quad (5.5)$$

$T$  is the temperature of the source gas,  $k_B$  the Boltzmann constant,  $\Delta E_J$  the energy difference to the ground state, and  $Q$  is a normalizing constant, such that  $\sum P_J = 1$ . The rotational degeneracy of the distribution is given by the factor  $g_J = (2J + 1)$ .

$g_s$  accounts for the spin-degeneracy of the nuclei. For heteronuclear molecules (DT, HT) without spin coupling and therefore no spin-degeneracy,  $g_s = 1$  [Lon02]. For a homonuclear molecule like  $T_2$ ,  $g_s$  is determined by the ratio of ortho and para states occupied by the molecule (see the following section 5.2.1).

### 5.2.1 Ortho-Para Ratio of Molecular Tritium

Within a  $T_2$  molecule the spins  $I = 1/2$  of both nuclei can couple to form a triplet state with both spins aligned parallel (ortho) or a singlet state with both spins aligned anti-parallel (para).

The triplet ortho state has a total spin of 1 and a spin degeneracy of 3. The corresponding nuclear spin wave functions are

$$|\uparrow\uparrow\rangle, \quad \frac{1}{\sqrt{2}}(|\uparrow\downarrow\rangle + |\downarrow\uparrow\rangle) \quad \text{and} \quad |\downarrow\downarrow\rangle.$$

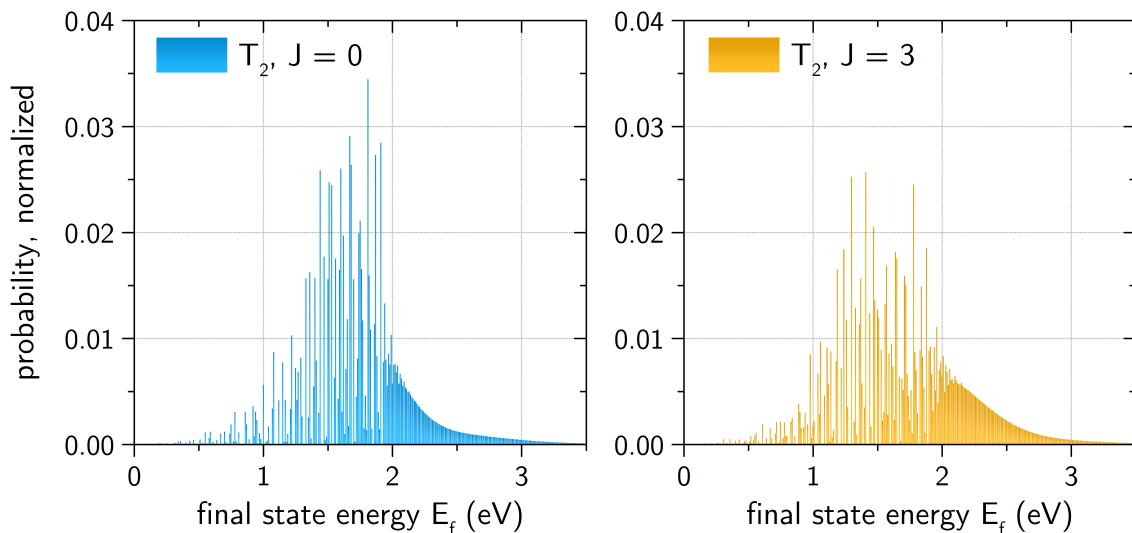


**Figure 5.2:** Comparison of normalized  $T_2$  final states distributions with angular momentum  $J = 0$  (left) and  $J = 3$  (right).

The singlet para state on the other hand is non-degenerate with a total spin of 0. The nuclear wave function is

$$\frac{1}{\sqrt{2}} (|\uparrow\downarrow\rangle - |\downarrow\uparrow\rangle).$$

Due to the permutational antisymmetry of the total wave function of the tritium molecule, only certain rotational states  $J$  can be adopted by the spin states. Ortho tritium has a symmetric nuclear spin wave function and therefore can only have rotational wave functions, that are antisymmetric with respect to permutation of the two nuclei. Thus the ortho state can only adopt rotational states with  $J = \text{odd}$ . Accordingly, for the para state only rotational states with  $J = \text{even}$  are possible [Atk06].

At standard room temperature and pressure the ratio between ortho and para  $r_{op}$  is about 3:1, which reflects the ratio of spin degeneracies. At low temperatures however, the para form dominates, as it is the configuration with the lower energy. A conversion from one state to another is a forbidden process, leading to very low conversion rates in the order of days [Fuk13].

Up to now, most calculations involving the decay of molecular tritium have been performed under the assumption of an ortho-para ratio  $\lambda = 3 : 1 = 0.75$  [Dos08]. Having the ortho-para ratio  $\lambda$  as a free input parameter for the calculation of the FSD weights is one the recent additions to the spectrum calculation code SSC.

In the recent bachelor thesis of Andrei Krochin [Kro14], the assumption of  $\lambda = 0.75$  during  $\beta$ -decay was investigated in greater detail, and found to be accurate for the KATRIN setup: Within the tritium loop of the WGTS, the source gas is forced into thermal equilibrium at room temperature  $T = 300$  K by a permeator membrane. The process of cooling the gas

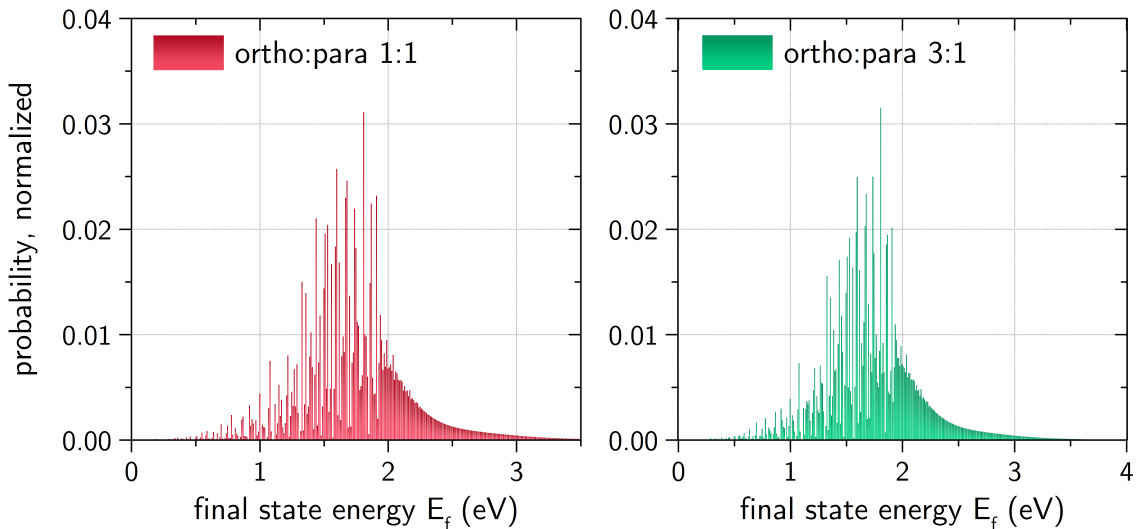


**Figure 5.3:** Comparison of normalized  $T_2$  final states distributions with ortho:para ratio 1:1 (left, expected at  $T \approx 30$  K) and ortho:para ratio 3:1 (right, expected at  $T \approx 300$  K).

down to  $T = 30$  K, injection and pumping out of the beam tube takes only about 1.5 s. A conversion from para into ortho states within this short period of time was estimated to be very unlikely ( $p < 3\%$ ), even when catalytic conversion mechanisms are considered. It was found that the corresponding change in the FSDs and shift of the measured neutrino mass would be negligible with  $\Delta m_\nu^2 = (0.48 \pm 0.07) \cdot 10^{-3} \text{ eV}^2$ .

### 5.2.2 Rebinning

Eventually, the calculation of the differential spectrum requires the inclusion of several FSDs: 3 sets of distributions for the molecular isotopologue, with each set containing up to 4 partial distributions for the angular momenta  $J$ . This sums up to 12 distributions, which have to be weighted dynamically according to their isotopical abundances and the local temperature  $T$  within each source segment. The electronic excitations make up one additional distribution to be included.

The energy binning of the FSDs, provided by [Sae00], is quite detailed with  $\Delta E_f = 10$  meV. In order to calculate the differential spectrum at  $E = E_0 - 30$  eV, the summation over the final states  $f$  (equation 5.1) has to be performed  $13 \times 3000$  times. Each summand involves the evaluation of a radiative correction term  $f_{\text{rad}}(E - E_f)$  and a square-root term  $\sqrt{\varepsilon_f^2 - m_i^2}$ .

Profiling the code thoroughly (investigating the computation time per line of code) revealed, that the final state summation had become the dominating bottleneck of the spectrum calculation code, claiming about 80% of the overall computation time.

Considering that the Doppler effect (see section 5.3) effectively causes a broadening of the differential spectrum on a scale of about 130 meV, it is evident, that the detailed binning of the provided FSD is not necessary. In order to increase performance, a new rebinning scheme was implemented.

#### Original Binning Scheme

The FSDs, as calculated by [Dos08; Sae00], are provided in the form of ASCII files, one for each molecular isotopologue and angular momentum. Each line within a file describes a bin with two values: the weighted mean energy  $E_f$  of all final states, that are summed up within a bin, and the probability  $P_f$  for a transition into one of these states. Even though the binning size is similar for all input files, the mean energies  $E_f$  are not.

If a detailed, non-homogeneous source model is used for the simulations, the temperature-dependent weighing of distributions  $f$  for a specific angular momentum  $J$  has to be performed individually for every segment (voxel) of the tritium source. As a consequence the computationally demanding summation in equation 5.1 has to be executed for each file separately.

### Dynamic Runtime Rebinning

During the initialization phase of the spectrum calculation code, the binning width of all loaded partial FSDs is adjusted according to a user-defined value and matched among all input files.

A second optimization is performed immediately before the summation in 5.1: Based on the local temperature of a source segment and the maximum relevant FSD energy  $E_f^{\max} = E_0 - qU$ , a single condensed FSD is calculated. One bin of the condensed distribution is composed out of the corresponding 13 resized partial distribution bins, which are weighted according to angular momentum and molecular abundance. The partial probabilities  $P_f$  are summed up and the effective weighted center of energy  $E_f$  is recalculated.

Thanks to this strategy, the calculation of the differential spectrum rate can be performed over a single condensed FSD with negligible loss in precision. The rebinning width can be chosen by the user depending on the desired accuracy. A reasonable width of 100 meV, which does not result in a significant change of the calculated (Doppler broadened) spectrum, leads to a computational speedup of about two orders of magnitude.

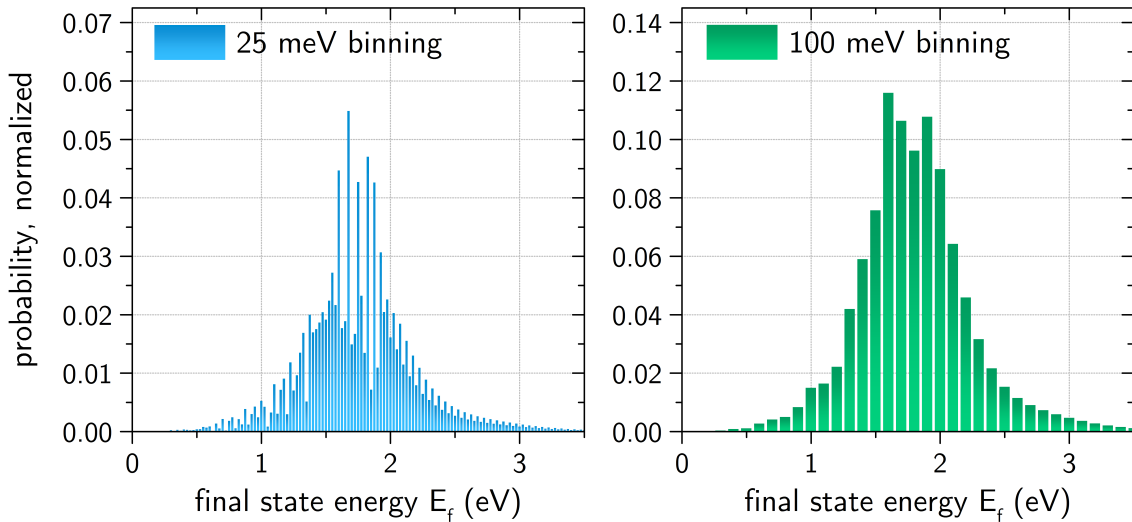


**Figure 5.4:** Comparison of different binning sizes (100 meV left, 25 meV right). All final states distributions are combined and weighted for a tritium purity of  $\varepsilon_T = 0.95$  and temperature  $T = 30$  K with an ortho:para ratio of 3:1.

### 5.3 Doppler Effect

The thermal motion of  $\beta$ -emitting tritium molecules leads to a broadening of the electron energy spectrum  $\frac{dN}{dE}$ , which is commonly referred to as the Doppler effect (or Doppler shift) on the energy spectrum.

Mathematically, this effect can be expressed as a convolution of the differential spectrum

$$\left(g \otimes \frac{dN}{dE}\right)(E) = \int_{-\infty}^{+\infty} g(E - \varepsilon) \frac{dN}{dE}(\varepsilon) d\varepsilon, \quad (5.6)$$

with  $E$  being the kinetic electron energy in the tritium rest frame, and  $\varepsilon$  the electron energy in the laboratory frame. The convolution kernel  $g$  is given by a Maxwellian distribution, which describes the thermal movement of the tritium gas. In its non-relativistic approximation [Höt12; Sha03], as it is implemented in the code, the Maxwellian  $g$  can be written as

$$g(E - \varepsilon) = g(\Delta E) = \frac{1}{\sigma_E \sqrt{2\pi}} e^{-\frac{1}{2} \left(\frac{\Delta E - U_b}{\sigma_E}\right)^2}, \quad (5.7)$$

with

$$\sigma_E = \sqrt{2Ek_B T m_e / M_{T_2}}. \quad (5.8)$$

The additional energy shift  $U_b \approx v_u \sqrt{2Em_e}$  is due to the position-dependent bulk velocity  $v_u$  of the tritium gas, which arises from the net gas flow through the beam tube of the WGTS from the injection point to the pumping ports. The convolution kernel can be understood as a shifted Gaussian distribution with a standard deviation of  $\sigma_E$ , determined by the temperature  $T$  of the source gas, the Boltzmann constant  $k_B$  and the energy  $E$  of the emitted electron.

For  $T = 30$  K and  $E = E_0$  close to the endpoint energy, the standard deviation of the Gaussian convolution kernel becomes  $\sigma_E \approx 130$  meV. This broadening of the energy spectrum is comparable to the neutrino mass, which KATRIN aims to determine. Figure 5.7 on page 98 shows the impact of the Doppler effect on the effective integrated spectrum and illustrates the importance of incorporating the effect into the calculations.

### 5.4 Negative Squared Neutrino Masses

Some statistical methods (section 6) demand the squared neutrino mass  $m_\nu^2$  to be treated as a free fit parameter without constraints to physically allowed regions, in order to account for statistical fluctuations of the observed data. For these purposes, equation 5.1 describing the differential  $\beta$  spectrum, requires a mathematical continuation into the unphysical region  $m_\nu^2 < 0$ :

$$\frac{dN}{dE} \propto \begin{cases} \sum_f P_f \varepsilon_f \sqrt{\varepsilon_f^2 - m_\nu^2} \Theta(\varepsilon_f - m_\nu) & \text{for } m_\nu^2 \geq 0 \\ \sum_f P_f (\varepsilon_f + m' \exp(-\frac{\varepsilon_f}{m'} - 1.0)) \sqrt{\varepsilon_f^2 - m_\nu^2} & \text{for } m_\nu^2 < 0 \end{cases} \quad (5.9)$$

$$\varepsilon_j = E_0 - E_f - E \quad (5.10)$$

$$m' = 0.716 \sqrt{-m_\nu^2} \quad (5.11)$$

$m'$  is scaled such that the extrapolation of  $\frac{dN}{dE}$  provides a symmetric log likelihood function or chi-square parabola around  $m_\nu^2 < 0$  [Wei93].

## 5.5 Integrated Spectrum

Due to its measuring principle (see section 2.1), KATRIN will observe an integrated  $\beta$ -decay spectrum of the kinetic electron energy. The expected observed signal rate at an applied retarding energy  $\dot{N}_S(qU)$  is an integral comprising the differential spectrum rate  $\frac{dN}{dE}$  and the response function  $R(E, qU)$  of the experimental apparatus:

$$\dot{N}_S(qU) = N_T \varepsilon_{\text{det}} \frac{\Omega}{4\pi} \int_{qU}^{E_0} \frac{dN}{dE}(E) R(E, qU) dE \quad (5.12)$$

$N_T$  is the number of tritium nuclei visible to the detector and  $\varepsilon_{\text{det}}$  the detection efficiency. The solid angle  $\Omega$  accounts for those electrons being emitted with a polar angle larger than  $\theta_{\text{max}}$ , and which are reflected before entering the spectrometer section:

$$\Omega = \frac{2\pi}{1 - \cos \theta_{\text{max}}} \quad (5.13)$$

The calculation of  $\dot{N}_S(qU)$  can be performed for specific segments of the tritium source or, using an appropriate mapping between source and detector (section 5.8), for individual detector pixels.

Eventually the mean number of  $\beta$ -decay electrons counted by the detector is determined by the time  $t_{qU}$  measured at a fixed retarding energy  $qU$ :

$$N_S(qU) = t_{qU} \cdot \dot{N}_S(qU) \quad (5.14)$$

A graphical comparison between differential and integrated  $\beta$ -decay spectrum is given in figure 5.5. In the following sections, the derivation and calculation of the response function  $R(E, qU)$  and the required modeling of gas dynamics in the tritium source are discussed.

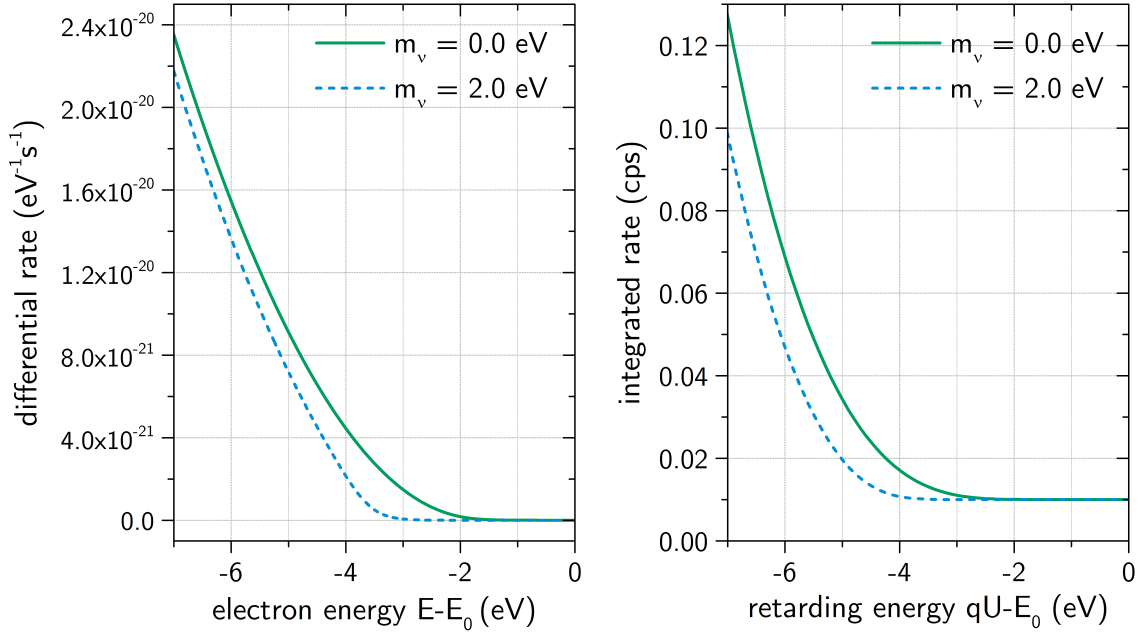


**Figure 5.5:** The differential spectrum  $\frac{dN}{dE}(E)$  (left) and integrated spectrum  $\dot{N}(qU)$  (right) is compared for a vanishing neutrino mass and  $m_\nu = 2000$  meV. The effects of the nuclear recoil and final states distribution effectively smear the endpoint region and lead to a shift away from the tritium endpoint  $E_0$ .

### 5.5.1 Transmission Function

The transmission characteristics of a MAC-E filter (section 2.2) can be described by the transmission function  $T(E, qU)$ . It gives the transmission probability for an electron with kinetic energy  $E$  to overcome the retarding energy  $qU$  and pass the filter's analyzing plane.

For electrons, which have been emitted isotropically, an analytical form can be quoted as follows [KAT05]:

$$T(E, qU) = \begin{cases} 0 & \text{for } E - qU \leq 0 \\ \frac{1 - \sqrt{1 - \frac{E - qU}{E} \frac{B_S}{B_A}}}{1 - \sqrt{1 - \frac{\Delta E}{E} \frac{B_S}{B_A}}} & \text{for } 0 < E - qU \leq \Delta E \\ 1 & \text{for } E - qU \geq \Delta E \end{cases} \quad (5.15)$$

Here  $B_S$  denotes the magnetic field strength in the source section and  $B_A$  the field strength in the analyzing plane of the MAC-E filter. This representation of  $T(E, qU)$  only holds for electrons with their momentum vector being randomly distributed within a polar angle  $0 \leq \theta \leq \theta_{\max}$  with respect to the guiding magnetic field line, that intersects perpendicular with the analyzing plane of the MAC-E filter.

The maximum polar angle  $\theta_{\max}$  is determined by the magnetic field strength  $B_S$  in the source and the maximum field strength  $B_{\max}$  between the source and the filter:

$$\sin \theta_{\max} = \sqrt{\frac{B_S}{B_{\max}}} \quad (5.16)$$

Electrons with a higher emission angle are reflected due to the magnetic mirror effect.

A characteristic property of the MAC-E filter is its energy resolution  $\Delta E$ , which manifests in the relative width of the analytical transmission function:

$$\Delta E = \frac{B_A}{B_{\max}} \quad (5.17)$$

For electrons near the endpoint energy of 18.6 keV, the width of the analytical transmission function becomes  $\Delta E = \frac{B_A}{B_{\max}} E = 0.93$  eV (also compare with figure 5.6).

#### Beyond the Analytical Description

At some point, the analytical form of the transmission function will not suffice to describe the transmission characteristics of the main spectrometer with high enough accuracy. Width and offset of the transmission function are determined by the local electrostatic potential and the magnetic field, which in turn have a radial dependence, relative to the

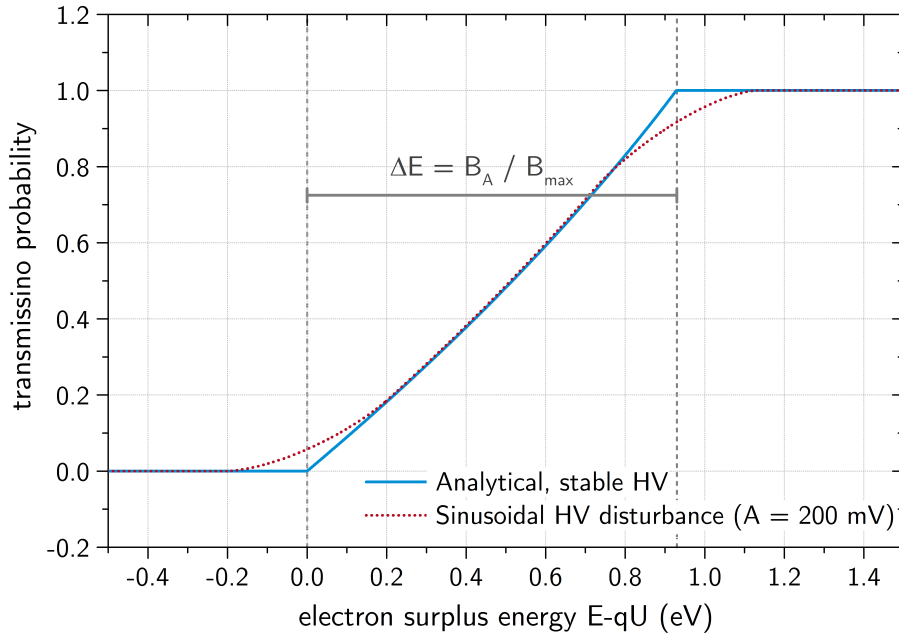


**Figure 5.6:** Transmission function for isotropically emitted electrons at a retarding energy of 18 570 eV. The solid curve depicts the analytical form of  $T(E, 18\,570\text{ eV})$ , the dotted 'broadened' curve incorporates a sinusoidal high voltage fluctuation of the retarding potential.

beam axis. Another effect, which is not covered by the analytical description and must be extracted from particle tracking simulations, is energy loss due to synchrotron radiation, caused by the electron gyration motion along the guiding field lines.

Particle tracking and field simulations, taking into account a detailed geometric model, have been performed to quantify these effects. Transmission measurements during the first SDS commissioning phase, employing an angular resolved electron gun, have shown a very good agreement with simulations and confirmed the understanding of the main spectrometer properties as a MAC-E filter [KAT14].

The code framework provides a class structure, which supports the inclusion of simulated and extrapolated measured transmission functions on a detector per-pixel basis. Using these tools, detailed studies on transmission properties and the implications for the neutrino mass sensitivity are ongoing and will be discussed in the doctoral thesis of Stefan Groh [Gro15].

### 5.5.2 Retarding Voltage Instabilities

A systematic effect which is known to cause problematic distortions of the integrated  $\beta$  spectrum, are short-term instabilities of the retardation voltage. Such instabilities will lead to a subtle broadening of the transmission function. If such an effect is not incorporated in the neutrino mass analysis, it causes a shift of the best-fit estimate towards small or even negative  $m_\nu^2$ , without showing a noticeable effect on the goodness-of-fit statistic [Ott08].

In order to study the effect within the statistical framework (see chapter 6.6), two analytical descriptions of a retarding voltage instability were implemented.

- A sinusoidal fluctuation of the transmission function  $T(E, qU)$  with amplitude  $A$ , which can be expressed as:

$$T_{\text{sine}}(E, qU) = \frac{1}{\pi} \int_{-\pi}^{\pi} T(E, qU + A \sin t) dt \quad (5.18)$$

- A Gaussian distortion of the HV amplitude. Under the assumption, that the retarding voltage is normally distributed with  $qU$  being the mean value and  $\sigma_{qU}$  the standard deviation, the transmission function can be convolved with a Gaussian distribution  $\mathcal{N}(x, qU, \sigma_{qU})$ <sup>1</sup>:

$$T_{\text{gauss}}(E, qU) = (\mathcal{N} \otimes T)(E, qU) = \int_{-\infty}^{\infty} \mathcal{N}(x, qU, \sigma_{qU}) T(E, x) dx \quad (5.19)$$

The effect of a sinusoidal HV fluctuation on the transmission function is illustrated in figure 5.6. The consequent modification of the integrated  $\beta$ -decay spectrum by such a fluctuation is shown in figure 5.7, next to other systematic effects.

---

1  $\mathcal{N}(x, \mu, \sigma) = \frac{1}{\sigma\sqrt{2\pi}} e^{-\frac{(x-\mu)^2}{2\sigma^2}}$

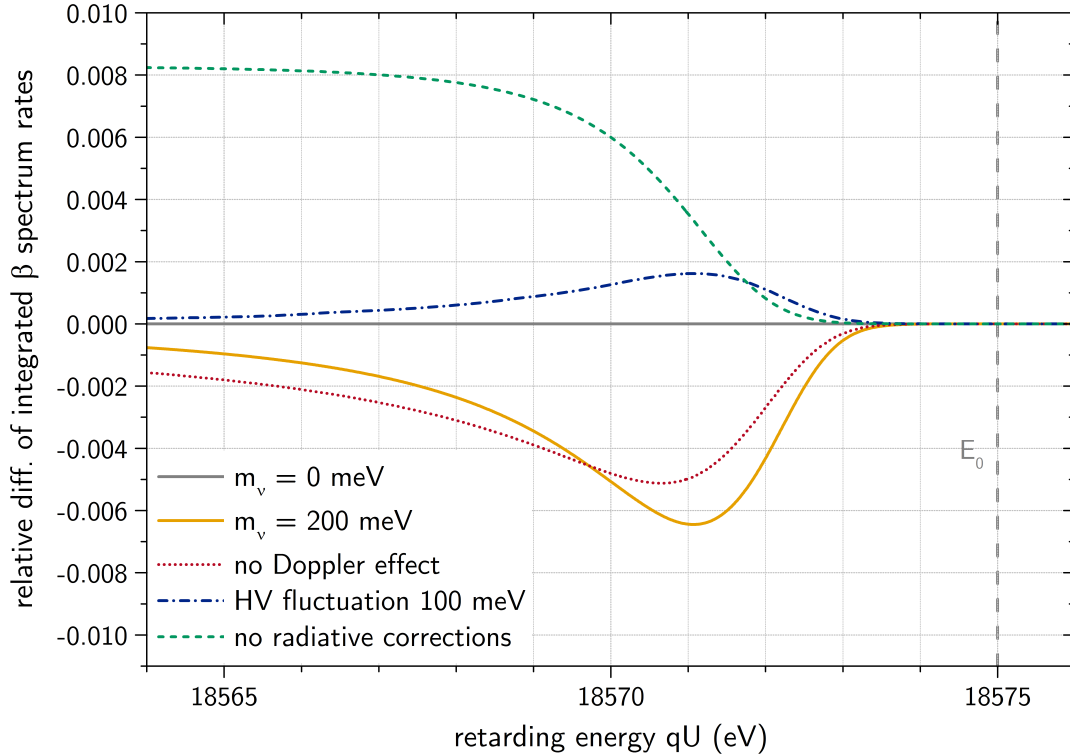


**Figure 5.7:** Comparison of various systematic effects on the integrated  $\beta$  spectrum, shown as the relative difference of rates. The scenario of a vanishing neutrino mass is used as reference. In case of the HV fluctuation, a sinusoidal disturbance with amplitude  $A = 100$  meV is assumed.

### 5.5.3 Source Simulations

The calculation of electromagnetic and gas dynamic properties of the source section is one of the major tasks of the source simulation code in the SSC software module. In its current form, the basis for this simulation was developed and used by Markus Hötzel in the context of his doctoral thesis [Höt12].

With the aim of having a customizable degree of detail, the source section can be subdivided into axial-symmetric segments, so-called *voxels*. Taking into account variations in the gas flow, temperature profile and magnetic fields of the WGTS, critical key parameters for the later calculation of the integrated spectrum are determined for each voxel.

Using the field calculators provided by the KEMField module (section 3.2.1) and a detailed geometric model of the WGTS, the magnetic field strengths  $B_S$  in the source are determined. They are used to define voxels of specific magnetic flux ( $B \cdot A$ ) and allow a mapping between effective areas of the source to the detector geometry. Another parameter determined by the field strengths is the maximum polar emission angle  $\theta_{\max}$  of the  $\beta$  electrons. It influences the shape of the transmission function  $T$ , scattering probabilities  $P_i$  and energy loss due to synchrotron radiation.

The temperature profile along the beam tube will be constantly monitored during the operation of KATRIN [Gro13] and used as input for the source simulations. Not only is the density of the source gas influenced by the temperature, but also the Doppler broadening of the differential  $\beta$  spectrum due to the thermal gas movement. The implemented calculation of this effect, as described in section 5.3, resorts to the temperature information held by each voxel.

Dedicated gas dynamics simulations, described in greater detail in [Höt12], provide information about the gas density and velocity. The currently implemented gas model is largely based on studies and calculations by Felix Sharipov [Sha09; Sha03]. They use a full solution of the Boltzmann equation to cover gas dynamics from a hydrodynamical regime (high pressure at the injection ports) up to a free-molecular regime (low pressure at the pumping ports).

The gas density in the WGTS (see figure 5.8) affects the scattering probabilities and the total number of tritium molecules, which constitutes the activity of a source voxel and thus the observable rate. The bulk velocity  $u_z$  of the gas along the beam line contributes an energy shift to the spectrum, which is incorporated in the Doppler effect calculation.

#### 5.5.4 Response Function

The response  $R$  denotes the probability of an electron, emitted in the WGTS with starting energy  $E$ , to eventually reach the detector, after having undergone inelastic scattering and overcoming the retarding potential with energy  $qU$ .

$$R(E, qU) = \int_0^E T(E - \varepsilon, qU) \cdot (P_0 \delta(\varepsilon) + P_1 f(\varepsilon) + P_2 (f \otimes f)(\varepsilon) + \dots) d\varepsilon \quad (5.20)$$

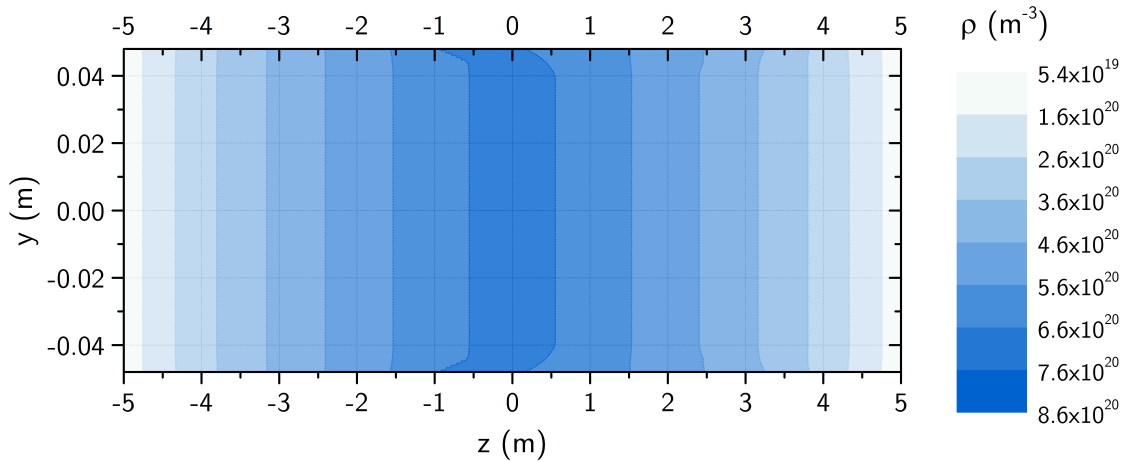


**Figure 5.8:** Gas density profile of the WGTS beam tube, calculated with SSC.

$P_0$  is the probability for an electron to reach the MAC-E filter without scattering. In case of (multiple) scattering, indicated by the probabilities  $P_i$  with  $i > 0$ , the energy loss function  $f(\varepsilon)$  has to be convolved  $i$  times and multiplied with the transmission function.

In the above notation of  $R$ , an isotropic distribution of electrons without significant change in direction after scattering is assumed. At nominal configuration ( $\rho d = 5 \cdot 10^{17} \text{ cm}^{-2}$ ) the response function, as pictured in figure 5.9, shows a steep rise defined by the width of the transmission function, up to a plateau of  $P_0 = 0.413$ . This peculiar shape is due to the fact, that inelastic scattering implies energy losses of at least 10 eV. As a consequence,  $\beta$ -decay rates, which are observed by KATRIN close to the endpoint region, will not be affected by systematic uncertainties connected to the knowledge of  $f(\varepsilon)$ . This is due to the fact that electrons reaching the detector within that energy range cannot have suffered any energy loss due to inelastic scattering.

### 5.5.5 Scattering Probabilities

In order to describe the complete response function, the energy loss due to manifold scattering ( $f \otimes f \otimes \dots$ ) has to be taken into account and the probabilities  $P_i$  for an electron to scatter off the source gas  $i$  times need to be calculated accordingly [Ase00]:

$$P_i(z, \theta) = \frac{(\lambda(z, \theta) \cdot \sigma_{\text{inel}})^i}{i!} e^{-\lambda(z, \theta) \cdot \sigma_{\text{inel}}} \quad (5.21)$$

The scattering probabilities  $P_i(z, \theta)$  are Poisson distributions, determined by the inelastic cross section  $\sigma_{\text{inel}}$  (section 5.5.6) and the effective column density  $\lambda(z, \theta)$ , that an electron has to traverse, when emitted under a polar angle  $\theta$  at longitudinal position  $z$  in the source of total length  $L$ :

$$\lambda(z, \theta) = \frac{1}{\cos \theta} \int_z^L \rho(z') dz' \quad (5.22)$$

The effective column density  $\lambda(z, \theta)$  can be understood as the number of tritium molecules per area, that an electron has to pass before leaving the WGTS. Consequently, electrons emitted at a higher polar angle  $\theta$  and closer to the rear end of the source, are more likely to scatter and will contribute less to the upper end of the  $\beta$  electron energy spectrum.

The mean scattering probabilities  $P_i^{\text{WGTS}}$  can be quoted as average values over all possible emission angles  $\theta$  (isotropic), weighted by the local density  $\rho(z)$ :

$$P_i^{\text{WGTS}} = \frac{1}{\rho d (1 - \cos \theta_{\text{max}})} \int_0^L dz \int_0^{\theta_{\text{max}}} d\theta \sin \theta \rho(z) P_i(z, \theta) \quad (5.23)$$

parameter	value
column density	$\rho d = 5 \cdot 10^{17} \text{ cm}^{-2}$
active source cross-section	$A_S = 53.3 \text{ cm}^2$
magnetic field strength (source)	$B_S = 3.6 \text{ T}$
magnetic field strength (maximum)	$B_{\text{max}} = 6.0 \text{ T}$
inelastic scattering cross section	$\sigma_{\text{inel}} = 3.45 \cdot 10^{-18} \text{ cm}^{-2}$
scattering probabilities	$P_0 = 41.33 \%$
	$P_1 = 29.27 \%$
	$P_2 = 16.73 \%$
	$P_3 = 7.91 \%$
	$P_4 = 3.18 \%$

**Table 5.1:** Electron mean scattering probabilities  $P_i$  for the WGTS reference configuration.

This calculation takes into account the maximum polar emission angle  $\theta_{\text{max}}$ , which depends on the local magnetic field strengths (see equation 5.16).  $\rho d$  denotes the total gas column density along the beam axis. In table 5.1 the mean scattering probabilities for up to 4-fold scattering in case of a nominal WGTS configuration are summarized.

### 5.5.6 Energy Loss

Any form of energy loss, which is suffered by the signal electrons before reaching the electrostatic analyzing plane, should either be avoided or, if inevitable, needs to be known precisely.

#### Inelastic Scattering

The most significant contribution to the energy loss is due to inelastic scattering of the  $\beta$ -decay electrons with  $\text{T}_2$  molecules while being guided through the source and the pumping section. At the nominal value of the source column density  $\rho d = 5 \cdot 10^{17} \text{ cm}^{-2}$ , about 59 % of the electrons will be affected. A prominent feature of inelastic scattering is, that it implies an energy loss of at least 10 eV per scattering process.

The energy loss function  $f(\varepsilon)$  is a normalized probability distribution

$$f(\varepsilon) \propto \frac{1}{\sigma_{\text{inel}}} \frac{d\sigma_{\text{inel}}}{d\varepsilon}, \quad (5.24)$$

with  $\varepsilon$  being the amount of energy lost during scattering. It depends on the inelastic scattering cross section  $\sigma_{\text{inel}}$  and the differential cross section  $\frac{d\sigma_{\text{inel}}}{d\varepsilon}$ .

Both quantities have been measured in an experimental setup, scattering electrons off gaseous tritium [Ase00]. The inelastic scattering cross section at an electron energy of 18.6 keV was determined with a precision of 2.1 %:

$$\sigma_{\text{inel}} = (3.40 \pm 0.07) \cdot 10^{-18} \text{ cm}^{-2} \quad (5.25)$$

A functional form was fitted to the energy loss function

$$f(\varepsilon) = \begin{cases} A_1 e^{-2\left(\frac{\varepsilon-\varepsilon_1}{w_1}\right)^2} & \text{for } \varepsilon < \varepsilon_c \\ A_2 \frac{w_2^2}{w_2^2 + 4(\varepsilon - \varepsilon_2)^2} & \text{for } \varepsilon \geq \varepsilon_c \end{cases} \quad (5.26)$$

with the parameters  $A_1 = 0.204 \pm 0.001$ ,  $w_1 = 1.85 \pm 0.02$ ,  $A_2 = 0.0556 \pm 0.0003$ ,  $w_2 = 12.5 \pm 0.1$  and  $\varepsilon_2 = 14.30 \pm 0.02$ , using  $\varepsilon_1 = 12.6$  fixed. The factor  $\varepsilon_c = 14.09$  was chosen to obtain a continuous function. The Gaussian part of this parameterized form  $f(\varepsilon)$  describes the energy loss due to excitation, the Lorentzian part accounts for ionization.

For the envisaged sensitivity of KATRIN, the energy loss function is required to be known to the  $10^{-3}$  level. A dedicated calibration measurement is planned, using the rear section electron gun (see section 2.7.1), to measure the response function at different column density configurations of the WGTS. With an elaborate deconvolution procedure applied to the gathered data, the energy loss function can then be untangled from the scattering probabilities and the transmission function [Kra11; Zie13].

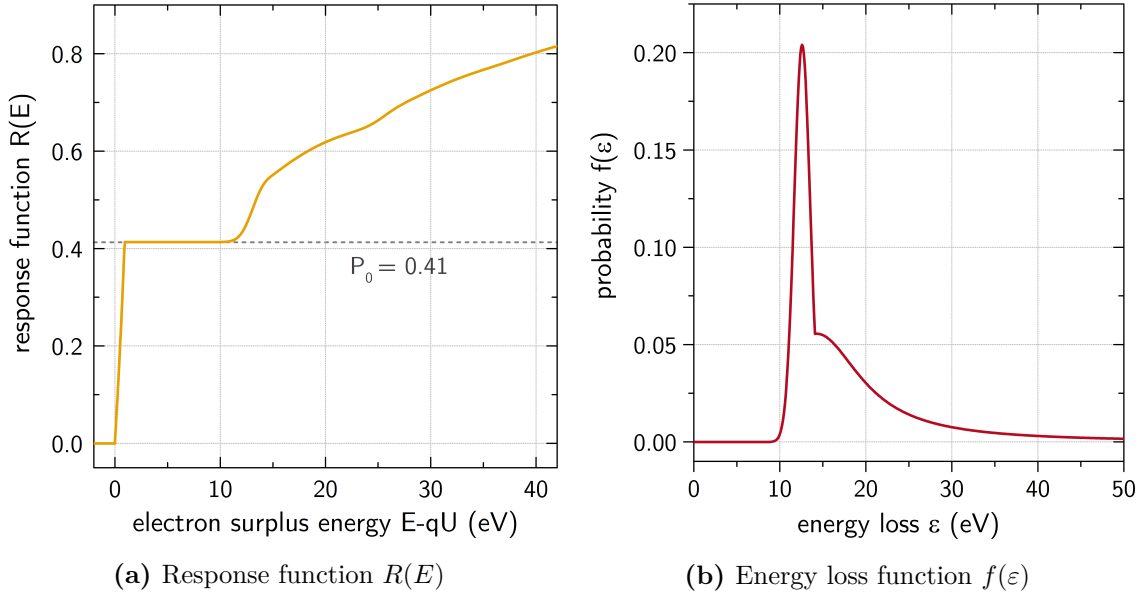


**Figure 5.9:** Response function  $R(E)$  (left) and energy loss function  $f(\varepsilon)$  (right). Since ionization of gaseous tritium implies energy loss not below 10 eV, the response function forms a plateau between 0.93 eV (the upper end of the transmission function) and about 10 eV. Only electrons, which have not scattered (probability  $P_0 = 0.41$ ), fall into this region.

### Elastic Scattering and Synchrotron Radiation

Elastic scattering off  $T_2$  molecules and emission of synchrotron radiation due to the gyration motion in the high magnetic field of the source and transport section are further sources of energy loss for  $\beta$  electrons. In general however, these losses are comparatively small.

The total elastic cross section of 18.6 keV electrons with  $T_2$  molecules is about 12 times smaller than the inelastic cross section, with an average energy loss of 16 meV per single scattering event and scattering angle of only  $3^\circ$  [KAT05]. In addition, the resulting energy loss can be reliably calculated:

$$\Delta E = 2 \frac{m}{M} E (1 - \cos \theta_p), \quad (5.27)$$

where  $m$  and  $M$  denote the electron and molecule masses,  $E$  the electron energy, and  $\theta_p$  is the polar scattering angle.

Energy losses due to synchrotron radiation can amount up to 100 meV in case of an electron being emitted at the rear end of the WGTS with the maximal polar angle of  $\sim 51^\circ$ . Detailed particle tracking simulations with electron trajectories through the complete KATRIN setup have been performed recently by Stefan Groh [Gro15] and are being incorporated into the response function calculation.

#### 5.5.7 Numerical Integration

Taking a closer look at the shape of the integrand in equation 5.12 (see figure 5.10), one can notice the almost linear, steep rise at the lower end of the integral, which is caused by the response function shape with its sharp transmission step at lower energies. Above the transmission width, the integrand suddenly drops with a parabolic decrease, originating from the functional form of the differential spectrum (equation 5.1).

Such an integrand shape requires special care, when attempting an accurate numerical integration. An obvious measure is the division of the integrand into two parts, in order to avoid any loss of accuracy close to the transition edge, where the integrand is largest.

In addition, an iterative numerical integrator, described in section 5.7, was implemented in order to guarantee consistent precision among the whole parameter space of interest and to ensure a numerically stable behavior of the likelihood function (section 6.1.2).

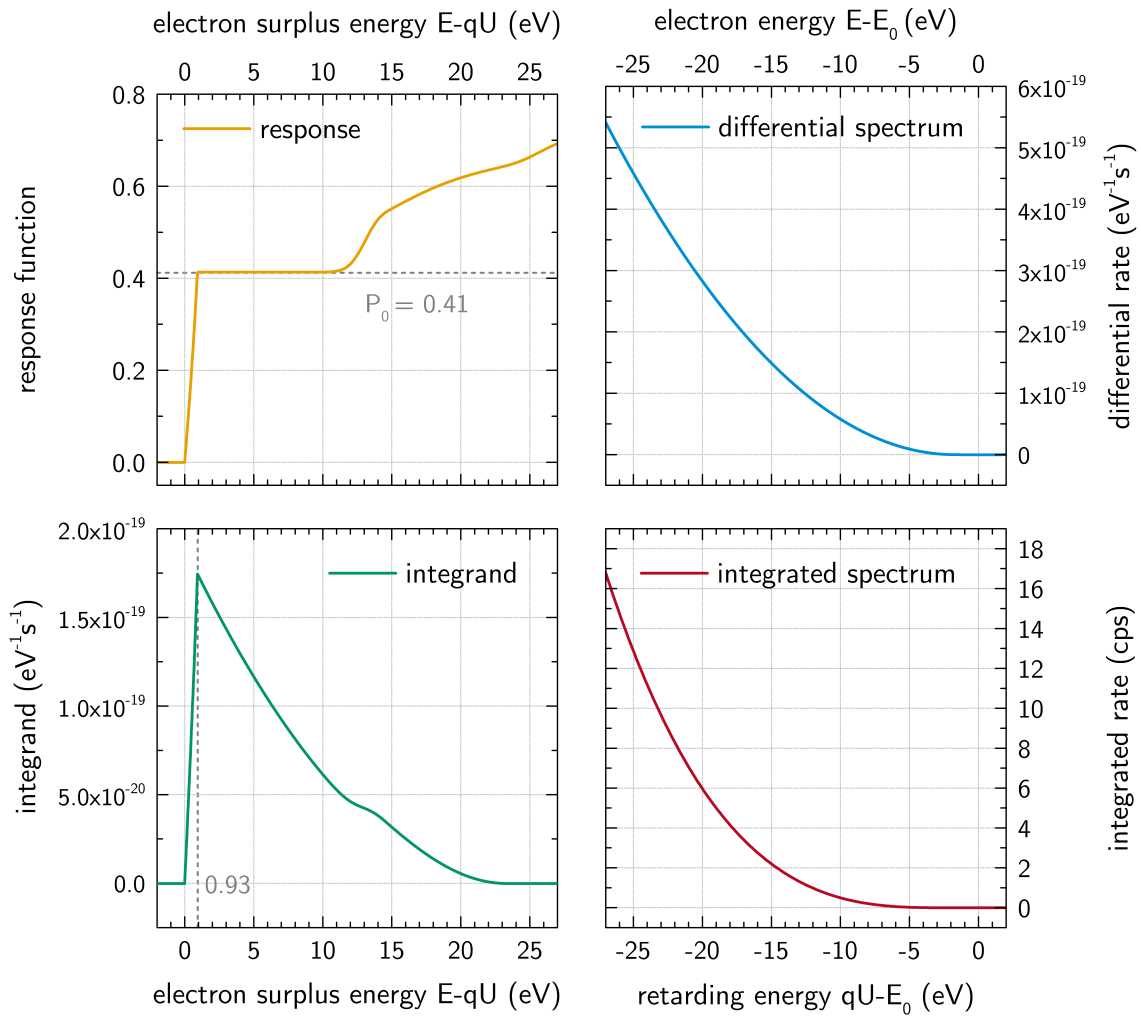


**Figure 5.10:** Top left: response function  $R(E, qU)$  dependent on the electron energy  $E$ . Top right: differential  $\beta$  spectrum  $dN/dE$ . Bottom left: integrand  $R(E, qU) \cdot dN/dE$ . Bottom right: integrated  $\beta$  spectrum  $\dot{N}(qU)$ .

## 5.6 Sterile Neutrinos

As outlined in section 1.4.1, the effective differential spectrum observed by a  $\beta$ -decay experiment is a superposition of several spectra, one for each neutrino mass eigenstate  $m_i$ , which mixes with the electron anti neutrino flavor eigenstate:

$$m_{\nu_e}^2 = \sum_i |U_{ei}|^2 m_i^2 \quad (5.28)$$

Thus the differential spectrum can be expressed as:

$$\frac{dN}{dE} = \sum_i |U_{ei}|^2 \frac{dN}{dE}(m_i) \quad (5.29)$$

Adding a sterile<sup>1</sup> neutrino to the picture is straightforward, since the code can incorporate an arbitrary number of neutrino mass eigenstates.

Considering that the mass splittings between the known three active mass eigenstates are too small to be resolved experimentally, they can be approximated in most KATRIN related calculations with an effective active neutrino mass squared

$$(m_a)^2 = \sum_{i=1}^3 |U_{ei}|^2 m_i^2 . \quad (5.30)$$

If one additional sterile neutrino mass is added in a 1+1 mixing scheme with  $m_s \gg |\Delta m_i|$  and a mixing coefficient of

$$|U_{es}| = \sin \theta_s , \quad (5.31)$$

the admixture of a sterile mass eigenstate to the electron neutrino can be expressed as

$$|\nu_e\rangle = \cos \theta_s |\nu_a\rangle + \sin \theta_s |\nu_s\rangle . \quad (5.32)$$

Our effective differential  $\beta$ -decay spectrum then becomes a superposition of

$$\frac{dN}{dE} = \cos^2 \theta_s \frac{dN}{dE}(m_a) + \sin^2 \theta_s \frac{dN}{dE}(m_s) \quad (5.33)$$

$$= (|U_{es}|^2 - 1) \frac{dN}{dE}(m_a) + |U_{es}|^2 \frac{dN}{dE}(m_s) . \quad (5.34)$$

---

<sup>1</sup> Neutrino mass eigenstates participating in weak interactions are named *active*. Mass eigenstates, which only appear through mass mixing, but not in weak interactions, are called *sterile*.

The effect of a heavy sterile neutrino state  $m_s$  on the differential  $\beta$ -decay spectrum is illustrated in figure 5.11. Its admixture produces a kink in the electron energy spectrum of size  $|U_{es}|^2$  at an energy  $E_0 - m_s$ , as well as a suppression of events at the endpoint of  $1 - |U_{es}|^2$ .

In neutrino oscillation experiments, where usually an appearance or disappearance probability is measured, the mixing angle  $\theta_s$  of an additional mass eigenstate is observed as an oscillation parameter  $\sin^2(2\theta_s)$  and commonly plotted as such:

$$\sin^2(2\theta_s) = 4|U_{es}|^2(1 - |U_{es}|^2) \quad (5.35)$$

The presented spectrum calculation code SSC is mainly suited for neutrino masses (active and sterile) in the eV range. This is not only due to the fact that the analytical description of the  $\beta$ -decay energy spectrum, including some of its approximations, is optimized for accuracy close to the endpoint region ( $E \gtrsim E_0 - 200 \text{ eV}$ ). Also systematic effects due to multiple scattering of  $\beta$  electrons in the source become more pronounced and less manageable at lower energies.

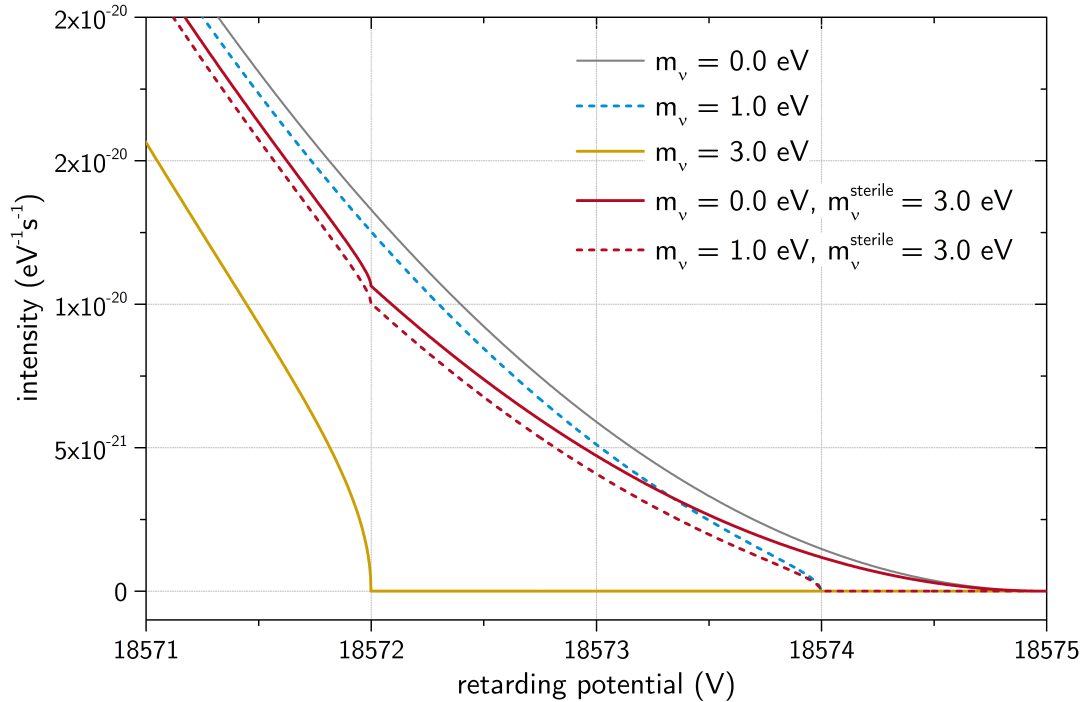


**Figure 5.11:** Comparison of differential  $\beta$ -decay spectra rates. For sterile neutrino contributions, the mixing coefficient assumed here is  $\sin^2 \theta_s = 0.1$ . Final states and the Doppler effect are neglected in these plots for better visualization.

## 5.7 Floating-point Accuracy and Numerical Stability

A floating-point method is an approximative representation of (non-integral) real numbers, used in computers. It inevitably means, that real numbers can only be represented with finite precision and that arithmetic operations suffer from limited accuracy. For calculations in SSC and KaFit, two particular cases require special attention:

- Many real numbers like 0.1 or 0.01 cannot be represented exactly in binary. If a small neutrino mass  $m_\nu$  for instance is squared and square-rooted repeatedly during numerical calculations, the accuracy of the result deteriorates.
- Summation and subtraction of nearly equal operands can lead to cancellation effects with high loss of accuracy. This effect needs to be considered when performing numerical integration or summation of a longer chi-square terms.

The cancellation problem is addressed with the Kahan summation algorithm (also known as compensated summation [Hig02]), which compensates accuracy losses by keeping a separate running variable to accumulate small errors. This algorithm was implemented as part of the KASPER library and is applied throughout the code for critical numerical operations like integration or incremental statistical computations.

In addition to the intrinsic limitations of machine floating point precision, the accuracy of the applied numerical methods, in particular numerical integration algorithms, has to be considered. In SSC, numerical integration has to be performed not only when incorporating systematics, such as the Doppler effect (section 5.3), energy loss (section

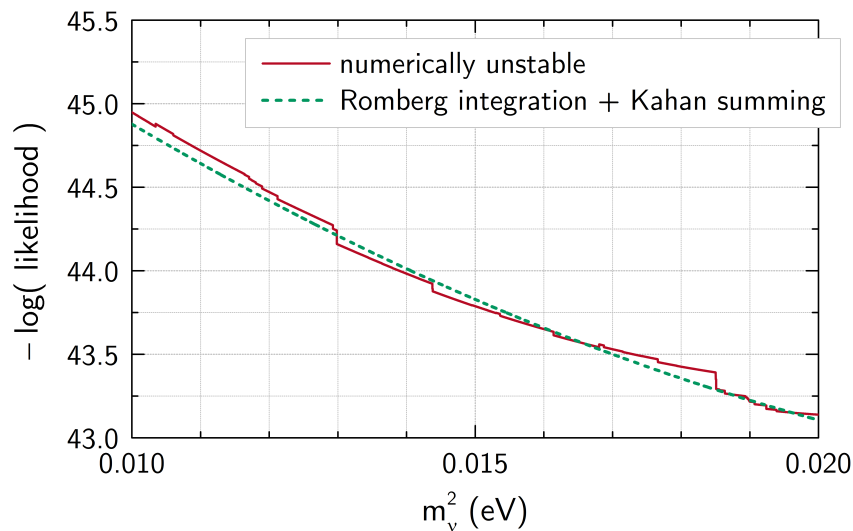


**Figure 5.12:** Likelihood shape on small scales of  $m_\nu^2$ . Using an iterative integration scheme and the Kahan summing method in numerically critical parts of the calculation, discontinuities in the likelihood function are avoided.

5.5.6) and distortions of the transmission function (section 5.5.2). The requirement for an accurate method is most obvious when calculating the integrated spectrum and dealing with a rather complicated integrand shape (section 5.5).

The likelihood function (section 6.1.2) in particular turned out to react extremely sensitive to numerical fluctuations of the integrated spectrum rate. Tiny modifications of fit parameters like  $m_\nu^2$  can result in sudden jumps of the integrated spectrum rate  $\dot{N}_S(qU)$ , which lead to discontinuities of the likelihood, as illustrated in figure 5.12. This behavior can occur, when ordinary trapezoidal integration methods with fixed step widths are used. Fitting algorithms, such as MIGRAD, which rely on a well behaved likelihood shape, are then likely to produce inconclusive results or fail.

A robust and flexible solution was found by implementing a configurable iterative integrator into the KASPER software framework, following the suggestions from [Pre07]. The integration algorithm successively refines the number  $N = 2^k$  ( $k \in \mathbb{N}$ ) of evaluated points of the integrand in  $k$  iterations, until a predefined precision is achieved (see figure 5.13). The intermediate results can be weighted to transform the trapezoidal rule into Simpson's or Romberg's rule with practically no computational overhead. The Simpson method essentially performs a parabolic extrapolation, the Romberg method a polynomial extrapolation of the successive refinements. In many cases, using either of these extrapolations can reduce the total number of required integrand evaluations  $N$  considerably.

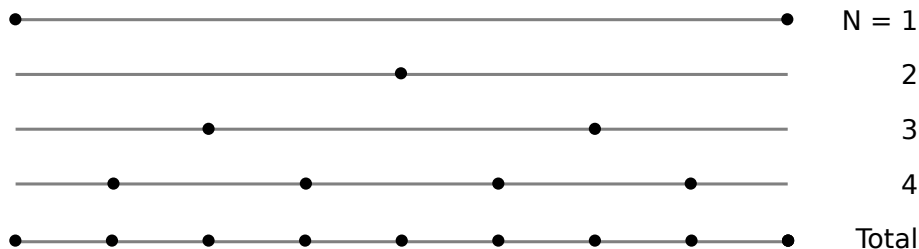


**Figure 5.13:** Sequential calls to the integrand by iterative integration schemes.

## 5.8 Detector Segmentation

All parts of the spectrum calculation code SSC and the statistical toolkit KaFit have been extended to accommodate a powerful diagnostic property of the KATRIN experiment, the segmentation of the main detector (section 2.6). Its layout is axisymmetric with 148 pixels forming a circular sensitive area of 90 mm in diameter (figure 5.14). The inner 4 pixels are referred to as the ‘bullseye’. The 12 contiguous rings contain 12 pixels each. Radii of bullseye and rings are chosen as such, that all pixels have equal surface area.

This detector layout is of specific interest in the data analysis, as it allows to incorporate radial dependencies of the source model, the transmission properties and the background. Not only can systematics and several background components be disentangled due to their different radial distribution. Pixels yielding a higher signal-to-background ratio can effectively improve statistical uncertainties in a neutrino mass estimation (see chapter 7.1).

The source simulation uses the information about source-specific magnetic fields to form an axial segmentation, which maps areas of equal magnetic flux to a specific detector pixel  $j$ . Those source segments (voxels) are then aggregated in longitudinal direction to calculate effective response functions  $R^j(E, qU)$  and differential rates  $\frac{dN^j}{dE}(E)$ , taking into account local gas density, velocity and temperature variations. The notation of the integrated spectrum rate (equation 5.12) can then be extended to

$$\dot{N}_S^j(qU) = N_T^j \varepsilon_{\text{det}}^j \frac{\Omega^j}{4\pi} \int_{qU}^{E_0} \frac{dN^j}{dE}(E) R^j(E, qU) dE. \quad (5.36)$$

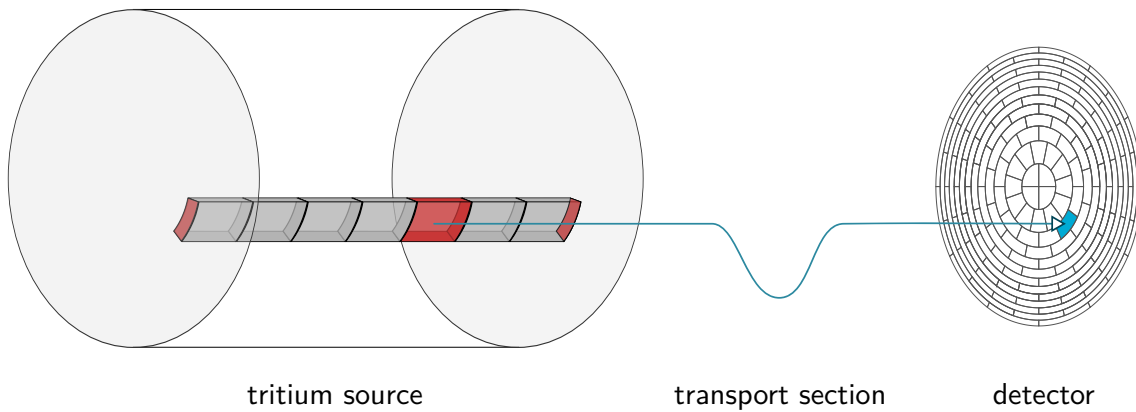


**Figure 5.14:** The source segmentation is performed dynamically along the beam direction, mapping source areas of equal magnetic flux to their corresponding visible detector pixel. Schematic not according to scale.

## 5.9 Background Models

Besides the signal rate  $\dot{N}_S^j(qU)$ , calculated for a retarding energy  $qU$  on a detector segment  $j$ , one has to take into account various forms of background. The design goal of KATRIN requires the overall background rate  $\dot{N}_{\text{bg}}$  to be constrained to about 10 mcps [KAT05]. Not only the absolute rate, but also the statistical nature of the background and its variation over time will have an impact on the statistical neutrino mass uncertainty.

With respect to the statistical studies outlined in chapter 6, the KaFit module provides an extensible framework to model various background types. Currently two major background contributions, which were studied during the SDS commissioning measurements, have been implemented in the code.

### 5.9.1 Cosmic Background

A major source of potential background arises from incident cosmic rays (primarily muons) which can eject secondary electrons from the inner surface of the spectrometers [Lei10]. The magnetic and electrostatic shielding of the MAC-E filter (section 2.2) should prevent most of the charged particles from entering the magnetic flux tube. Due to axial asymmetries of the field configuration and non-adiabatic movement however, a small fraction of the ejected electrons ( $E \lesssim 100$  eV) is able to drift into the sensitive part of the flux tube and produce background there through residual gas ionization or scattering. After acceleration by the electrostatic barrier this background component becomes indistinguishable from the  $\beta$ -decay signal.

Within the context of this thesis the cosmic background component is assumed to be of Poissonian nature<sup>1</sup>. In this approximation the modeling is straightforward: For each detector segment  $j$  an expected mean background rate  $\dot{N}_{\text{bg}}^j$  can be specified. When a toy measurement is simulated with a duration of  $t_{qU}$ , the number of counted background events is drawn from a Poissonian distribution:

$$N_{\text{bg}}^j = \text{Poisson} \left( t_{qU} \cdot \dot{N}_{\text{bg}}^j \right) \quad (5.37)$$

Accordingly, the standard deviation of absolute background count is

$$\sigma_{N,\text{pois}} = \sqrt{t_{qU} \cdot \dot{N}} = \sqrt{N}. \quad (5.38)$$

---

<sup>1</sup> Recent measurements of the incident muon flux at the KATRIN main spectrometer indicate a non-Poissonian time variance of the cosmic background [Lei14], which might be attributed to changes in the solar activity or atmospheric parameters. Implications on the neutrino mass sensitivity and a possibly adapted measurement strategy (see section 5.10.1) are currently under investigation.

### 5.9.2 Radon-Induced Background

Another source of background are high-energy electrons, which are produced during the nuclear  $\alpha$ -decay of the two radon isotopes  $^{219}\text{Rn}$  and  $^{220}\text{Rn}$  in the spectrometer [Frä10; Goe14; Mer12]. Such high energetic electrons, which are released inside the magnetic flux tube, can be stored in the main spectrometer over several hours due to the magnetic mirror effect. During this time period they scatter off residual gas multiple times, thereby producing low-energy secondary electrons ( $E < 100$  eV) through ionization. The secondaries are accelerated by the spectrometer retarding potential and when escaping the magnetic bottle, they can reach the detector within the energy region of interest.

Radon is to some extent emanated from the weld seams of the inner spectrometer surface. Another major source of radon emanation is the non-evaporable getter pump with its large porous surface. The NEG material is installed in the shape of getter strips, totaling a length of 3 km in the main spectrometer (section 2.5.2).

Sources and production mechanisms of radon-induced background have been studied in great detail during dedicated measurements at the pre-spectrometer [Wan13]. Active and passive suppression techniques have been established and were successfully tested during the SDS commissioning phase [KAT14], in particular by installation of  $\text{LN}_2$ -cooled copper baffles [Goe14] (see section 2.5.2).

Due to the above mentioned long storage time of high energy electrons produced in radon decays, this form of background exhibits a more complicated temporal structure ('radon spikes') than a purely Poissonian background. Even over longer measuring periods, the statistical variance of the background rate can be noticeably larger, which implies a stronger impact on the neutrino mass sensitivity. A detailed model of radon-induced background with a realistic description of its non-Poissonian character, is currently being developed [Oer14].

For purposes of this thesis, a simple and preliminary statistical model of radon induced background has been deduced from SDS commissioning measurements [KAT14]. Here, the pressure in the main spectrometer was artificially elevated by injecting gaseous argon, in order to reduce the cool-down time of primary electrons from radon decay to the order of milliseconds. The produced secondary electrons were observed in short bursts, which could be discriminated from cosmic background using cuts on the recorded inter-arrival times between detector events [Sch14]. A rate trend was extrapolated and the time difference between secondary electron production was scaled to reflect nominal vacuum conditions (see figure 5.15). From this rate trend, the standard deviation of the number of background events was estimated to be larger by a factor of  $\approx 3.6$  as compared to a Poissonian background with similar mean event count.

Assuming long enough measurement intervals of  $> 1$  h, radon-induced background counts in KaFit are currently drawn from a normal distribution with a standard deviation of

$$\sigma_{N,\text{radon}} \approx 3.6 \cdot \sqrt{N_{\text{radon}}} . \quad (5.39)$$

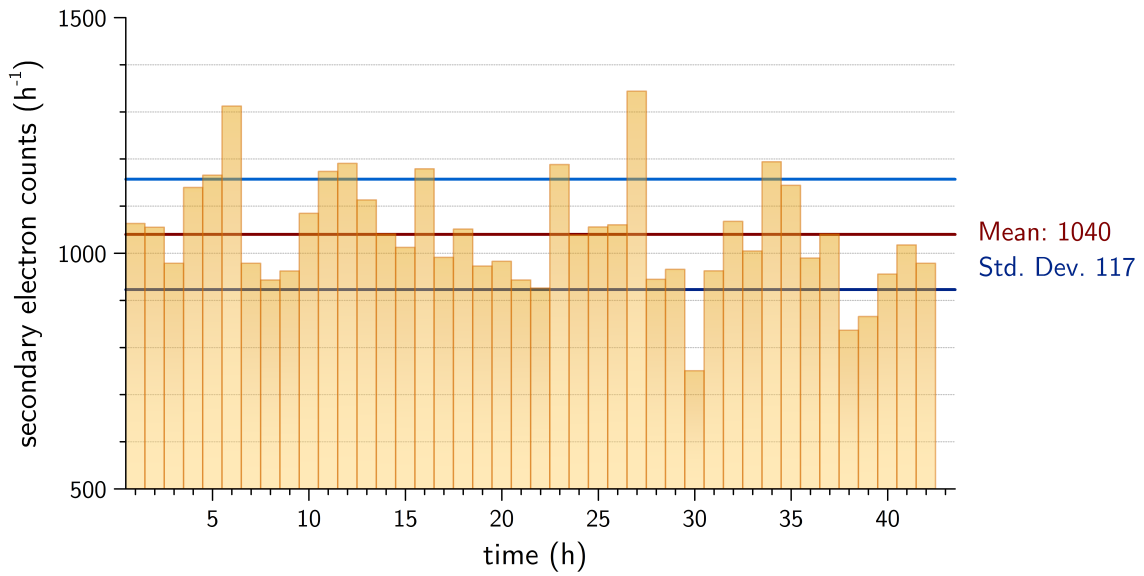


**Figure 5.15:** Empirical model of radon-induced secondary electron rates, extrapolated from high pressure SDS-I measurements. Data provided by Jan Oertlin [Oer14].

These basic models for cosmic and radon-induced background are used in the following chapters, when statistical methods are discussed with respect to the background model of a (simulated) KATRIN measurement (chapter 6), and when the neutrino mass sensitivities are reevaluated based on recent SDS-I commissioning data (chapter 7).

## 5.10 Measurement Simulation

Combining the methods described in this chapter, specifically the calculation of the expected integrated  $\beta$  signal and the background rate, the expected number of events in a KATRIN measurement can be estimated for any given set of retarding energies  $qU$  and the corresponding measurement times  $t_{qU}$ .

### 5.10.1 Measuring Time and Strategy

A measuring time distribution (MTD) is a set of measurement configurations  $\{t_{qU}\}$ , defining the amount of effective net measuring time  $t$ , which the KATRIN experiment should invest at a specific retarding energy setting  $qU$ . KaFit can be configured to simulate a full KATRIN run on the basis of any desired measuring time distribution. The sum  $\sum t_{qU}$  can for instance be chosen to cover the planned 3 full-beam years of effective measuring time, which corresponds to 5 calendar years<sup>1</sup>.

The numerical simulation of a KATRIN run in KaFit allows for another refinement. Measurement time, spent at a particular retarding potential, can be broken up into smaller, more realistic measurement intervals. In its current but extensible implementation, the code allows the user to define a maximum uninterrupted measurement time  $t_{qU}^{\max}$ . The various retarding energies  $qU$  are then scanned, either in ascending order or randomly, until in total the defined measurement time distribution is fulfilled.

Furthermore, the total full-beam measuring time  $\sum t_{qU}$  can be freely adjusted (for instance to a few weeks), while requiring the simulation to guarantee a full scan of the spectrum, attributing the correct fraction of time  $t_{qU}$  to each retarding energy  $qU$ .

Further investigations are planned with respect to time-dependent variances of background rates or long-term drifts of systematic parameters, which might imply a bias on certain measurements, if anything but a random scanning strategy is used.

### 5.10.2 Generating a KATRIN Run

For each  $t_{qU}$  in a given measurement time distribution  $\{t_{qU}\}$ , the expectation value of the number of counted electrons on a detector pixel  $j$  is:

$$\hat{N}_{qU}^j = \dot{N}_{qU}^j \cdot t_{qU} \quad (5.40)$$

A toy measurement  $N_{qU}^j$  is drawn from a Poissonian with expectation value  $\lambda = \hat{N}_{qU}^j$ , and a background contribution is added from its corresponding probability distribution:

$$N_{qU,\text{toy}}^j = \text{Poisson}\left(\hat{N}_{qU}^j\right) + N_{\text{bg}} \quad (5.41)$$

---

<sup>1</sup> ‘Full-beam’ measuring time does not include calibration and service time.

For the reference measuring time distribution from [KAT05] with 41 retarding potentials, a toy KATRIN run comprises 41 toy measurements (data points) accordingly. If the focal plane detector is sub-divided into its 13 rings, this number increases to 533. For the full geometry of 148 pixels, a simulated KATRIN run consists out of 6068 toy measurements.

In figure 5.16, the count rates of a randomly generated KATRIN measurement, comprising 41 data points, are compared to the theoretical predictions of a vanishing and a non-zero neutrino mass.

### 5.10.3 Performance

The computational performance of the spectrum calculation and run simulation is of particular interest when it comes to statistical analysis. Performing one single best-fit estimate on a set of data (using a MINUIT minimizer) requires at least around 200 evaluations of the likelihood function. Each likelihood evaluation causes several computations of the integrated spectrum rate, one at each retarding potential (about 40 to 70) for each de-

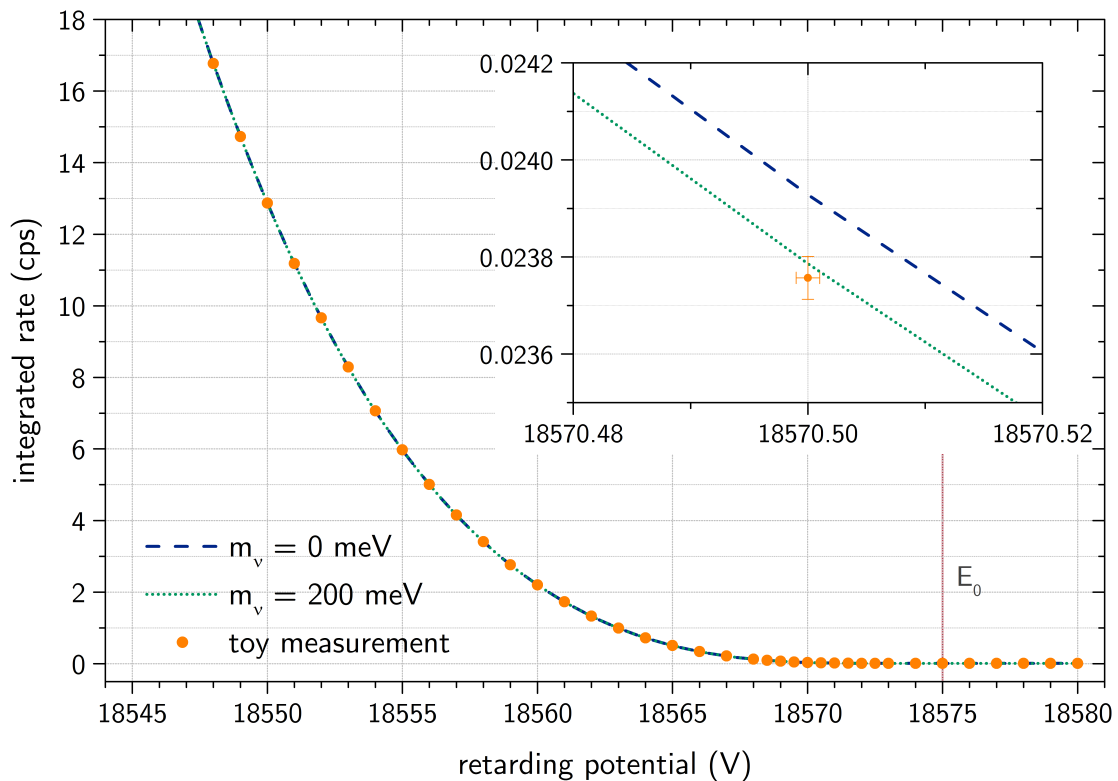


**Figure 5.16:** Comparison of two integrated  $\beta$ -decay spectra for  $m_\nu = 0$  meV and  $m_\nu = 200$  meV. The toy measurement was generated assuming  $m_\nu = 200$  meV and considering Poisson statistics for signal and background rates.

tector pixel (148), possibly accumulated over several longitudinal source voxels (10 to 50). Performing a Bayesian analysis of a measurement and sampling a posterior probability distribution (see chapter 6) can require up to  $10^6$  evaluations of the likelihood function.

Depending on the configured detail of the source modeling and inclusion of systematic effects and the binning of the final states distribution, a simulation of a complete KATRIN run (one likelihood evaluation) can take between  $\mathcal{O}(1\text{ ms})$  to  $\mathcal{O}(10\text{ s})$  computation time on a single CPU core (Intel® Xeon™ E5630 @ 2.53 GHz).

A configuration, which is reasonably accurate for most mass sensitivity studies, and thus includes final states with 0.1 eV binning, the Doppler effect and a minimal segmentation of the source, takes about  $\mathcal{O}(100\text{ ms})$ . In this case the likelihood function can be evaluated in under 1 s for a given parameter set.

### Summary

In this chapter, the implemented methods for the calculation of  $\beta$ -decay spectra were presented. They cover classical Fermi theory and a large number of corrections and systematical effects, which are essential in order to allow a reliable prediction of expected count rates for any desired (and possibly unknown) physical parameter, such as the squared neutrino mass. Consequently, the accuracy and completeness of the spectra calculations are a crucial requirement for nearly all of the statistical methods presented in the following chapter, including the inference of a neutrino mass from observed data.



# CHAPTER 6

---

## Statistical Methods

---

This chapter focuses on a series of statistical tools, which were developed and integrated into the KATRIN analysis framework as part of the present thesis. First a short introduction into basic statistical concepts and terms will be given, as these are required to understand the procedure of inferring a neutrino mass from observed data. Several Frequentist and Bayesian methods are explained and compared, also in scenarios involving systematic effects and the search for sterile neutrinos in  $\beta$ -decay spectroscopy.

A set of specially implemented Markov Chain Monte Carlo (MCMC) algorithms is presented in section 6.3, which are not only suited for  $\beta$  spectrum fitting, but in particular for the treatment of high-dimensional problems. Based on these tools, a new Monte Carlo (MC) method for the optimization of KATRIN's measuring time distribution will be introduced in section 6.4 and evaluated for various measurement scenarios.

### KaFit

The statistical methods, outlined in this chapter, were implemented as part of the KASPER software framework and organized inside a module named KaFit. It is seamlessly integrated with the spectrum calculation module SSC, the particle tracking module Kassiopeia, the electro-magnetic field solvers from KEMField and the data access module KaLi, thus connecting all the pieces of the global software framework, required to study the systematic properties of KATRIN. In addition it provides a set of statistical methods to allow the extraction of a neutrino mass from observed data. A simplified schematic overview of KaFit in this context is given in figure 6.1

KaFit's functions are organized and provided in extensible, object-oriented class hierarchies, so that they can be used by other parts of the KASPER software framework. The Markov Chain Monte Carlo (MCMC) methods presented in section 6.3 for instance, are being used as function minimizers in independent applications, such as radon decay model studies [Goe14] or transmission analysis [Gro15].

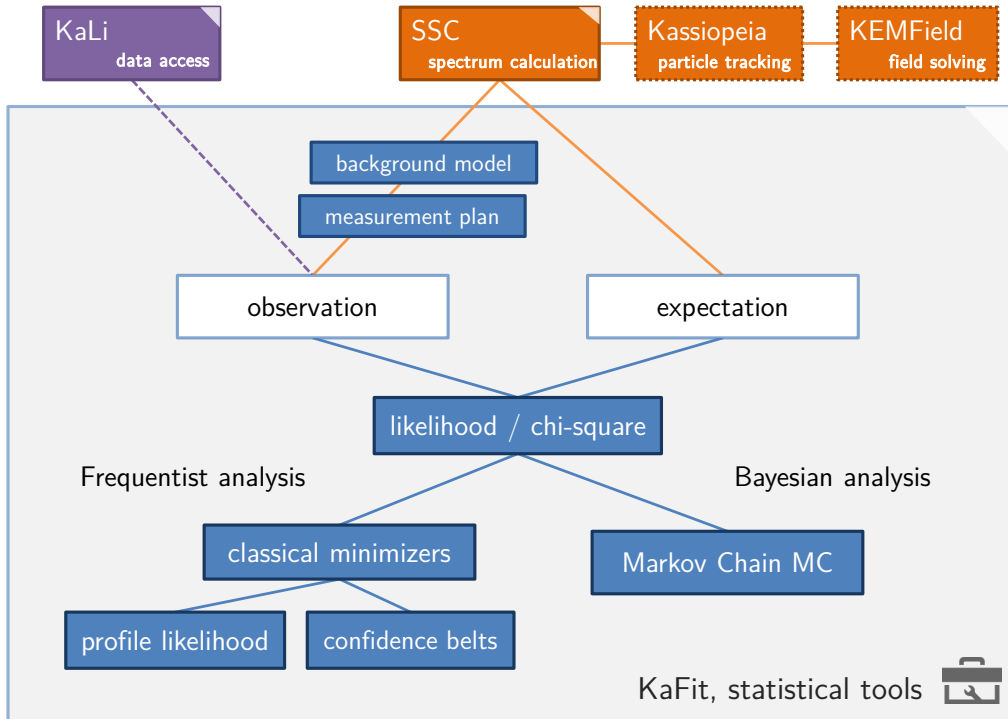


**Figure 6.1:** Schematic diagram of the components within KaFit, required for parameter inference and confidence interval construction.

## 6.1 Parameter Inference

The KATRIN experiment is designed to achieve a sensitivity on the absolute neutrino mass scale of  $m_\nu < 200$  meV at 90% confidence level (C.L.). The sensitivity of a neutrino mass experiment is a statement about the combined statistical and systematic uncertainties and a quantifying measure of how capable the experiment will be in ruling out a vanishing neutrino mass or setting an upper limit for that parameter.

KATRIN will observe an integrated  $\beta$ -decay spectrum and perform a shape analysis (see figure 6.2) to estimate the parameter of interest, namely  $m_\nu$ . Due to the statistical nature of an *observation*, KATRIN cannot *measure* the true value of  $m_\nu$  with absolute certainty, but has to make a *best-fit estimate* and state a confidence interval (Frequentist approach) or publish a posterior probability density function of  $m_\nu$  (Bayesian approach). This process is commonly referred to as parameter estimation or inference.

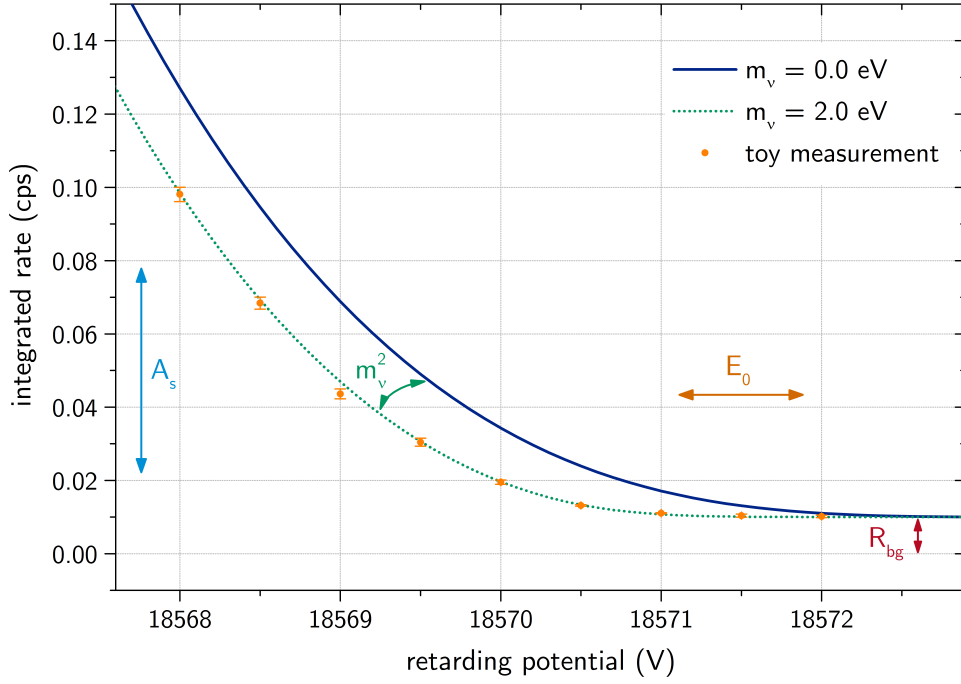


**Figure 6.2:** Illustration of the standard four-parameter spectrum fit of  $\beta$ -decay data. The four unknown parameters, squared neutrino mass  $m_\nu^2$ , tritium endpoint energy  $E_0$ , the signal amplitude  $A_S$  and the background rate  $R_{bg}$  are adjusted to fit the theoretical spectrum shape to the observed experimental data. In this example the error bars show the statistical count rate error after 1 month of data-taking at KATRIN.

### 6.1.1 Definition of Sensitivity

KATRIN's sensitivity on  $m_\nu$ , as defined in the Technical Design Report (TDR) [KAT05], can be understood as the total uncertainty on  $m_\nu$  in the scenario of a vanishing neutrino mass. In other words: If a completed measurement yields a best fit estimate of  $\hat{m}_\nu$  which is higher than the stated sensitivity, KATRIN is able to exclude the null hypothesis of a vanishing neutrino mass.

Assuming a Gaussian distribution of  $m_\nu^2$  estimates, the 90 % C.L. sensitivity on  $m_\nu$  can be written as

$$S_{m_\nu}(90\%) = \sqrt{1.645 \cdot \sigma_{m_\nu^2, \text{tot}}}, \quad (6.1)$$

with

$$\sigma_{m_\nu^2, \text{tot}} = \sqrt{(\sigma_{m_\nu^2, \text{stat}})^2 + (\sigma_{m_\nu^2, \text{sys}})^2} \quad (6.2)$$

being the quadratically combined statistical and systematic uncertainty on  $m_\nu^2$ . For Gaussian distributed quantities, the factor 1.645 translates a  $1.0\sigma$  (68.3 %) to a  $1.645\sigma$  (90 %) confidence interval.

### 6.1.2 KATRIN Likelihood Function

The likelihood function  $L$  plays a key role in statistical methods of parameter inference. It is the probability model of how likely a particular outcome of an experiment and a measurement is.

$$L(\Theta_{\text{theo}}|\mathbf{N}_{\text{obs}}) = P(\mathbf{N}_{\text{obs}}|\Theta_{\text{theo}}) = \prod_i p(N_{\text{obs},i}|\Theta_{\text{theo}}) \quad (6.3)$$

In other words: The likelihood  $L(\Theta|\mathbf{N})$  of a set of model parameters  $\Theta$ , given a set of observations  $\mathbf{N}$ , is equal to the probability  $P(\mathbf{N}|\Theta)$  of observing the outcome  $\mathbf{N}$ , given those parameters  $\Theta$  as input (including  $m_\nu$ ).  $p(N_i|\Theta)$  denotes the probability of making a single observation  $N_i$  under the assumption of  $\Theta$ .

For KATRIN the likelihood function comprises a complete description of  $\beta$ -decay theory and the behavior of the experimental apparatus, including the tritium source model, transmission characteristics, detection efficiency, background model, systematic effects and statistical properties. In a minimal description the vector  $\Theta$  consists of four parameters: Our parameter of interest, the squared neutrino mass  $m_\nu^2$ , and three nuisance parameters (the tritium endpoint energy  $E_0$ , the signal amplitude  $A_S$  and the mean background rate  $R_{\text{bg}}$ , see figure 6.2). The summing index  $i$  denotes the retarding potentials  $qU$ , at which the integrated  $\beta$  spectrum will be observed with  $N_i$  events.

Writing down the likelihood in terms of observed signal events  $N_{i,\text{obs}}$  and the expected event counts  $N_{i,\text{theo}}$  at the corresponding experimental configuration  $i$ , under the assumption of certain theoretical parameters  $(m_\nu^2, E_0, A_S, R_{\text{bg}})$ , equation 6.3 becomes:

$$L(m_\nu^2, E_0, A_S, R_{\text{bg}}|\mathbf{N}_{\text{obs}}) = \prod_i p(N_{\text{obs},i}|N_{\text{theo},i}(qU_i, m_\nu^2, E_0, A_S, R_{\text{bg}})) \quad (6.4)$$

In figure 6.3 the likelihood for a random KATRIN toy measurement is shown. For this particular example, the likelihood maximum is shifted away from the true set of input parameters  $(m_\nu^2, E_0, A_S, R_{\text{bg}})$  that were used to generate the measurement. This is naturally to be expected due to the statistical nature of the observables  $\mathbf{N}$ .

It is important to understand, that the likelihood function does not and cannot state, how likely a particular true value of  $m_\nu^2$  is for an observed data set  $\mathbf{N}$ . However, by comparing the observations of the experiment with the predictions of the likelihood as a function of various input parameters  $\Theta$ , one can carefully make an estimate about the true value of the parameters of interest.

Those values of  $m_\nu^2$ ,  $E_0$ ,  $A_S$  and  $R_{\text{bg}}$ , which result in the global maximum of  $L$ , are the best-fit estimators, including the estimator of interest  $\hat{m}_\nu^2$ . Even though the other, so-called *nuisance* parameters are of only secondary interest to us, they are not sufficiently well known in advance, and must be treated as unknown free parameters during a fit procedure.

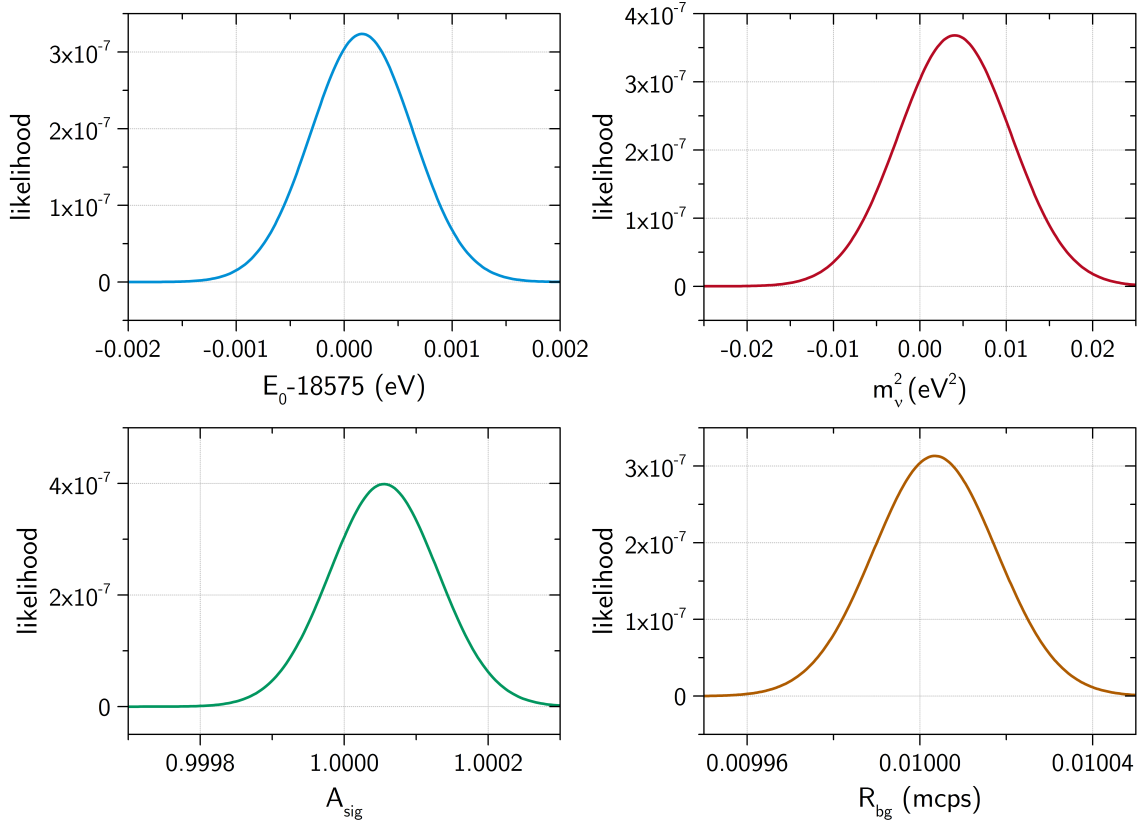


**Figure 6.3:** 1D projections of the likelihood  $L(m_v^2, E_0, A_S, R_{\text{bg}}|\mathbf{N})$  for a random toy measurement ( $\mathbf{N}$ ) with true  $m_v^2 = 0.0 \text{ eV}^2$ .

It is common practice and numerically more convenient, to not maximize the likelihood  $L$ , but to minimize the negative log likelihood instead:

$$-\log L(\boldsymbol{\Theta}|\mathbf{N}) = -\log \prod_i p(N_i|\boldsymbol{\Theta}) = -\sum_i \log p(N_i|\boldsymbol{\Theta}) \quad (6.5)$$

### 6.1.3 Chi-Square Statistic

In many cases, the probability distribution  $p(x|\mu)$  for an observation  $x$  to occur, when  $\mu = \mu(\boldsymbol{\Theta})$  is expected, can be approximated by a Gaussian distribution

$$\mathcal{N}(x, \mu, \sigma) = \frac{1}{\sigma\sqrt{2\pi}} \exp -\frac{(x - \mu)^2}{2\sigma^2}, \quad (6.6)$$

with  $\mu$  being the expectation value and  $\sigma$  its standard deviation. This approximation is also valid for Poissonian distributions with an expectation value  $\mu \gtrsim 25$  and  $\sigma = \sqrt{\mu}$ .

The likelihood function from equation 6.3 can then be written as

$$-2 \log L = -2 \log \prod_i \mathcal{N}(x_i, \mu_i, \sigma_i) = \sum_i \left( \frac{x_i - \mu_i(\boldsymbol{\Theta})}{\sigma_i} \right)^2 + h.c. = \chi^2. \quad (6.7)$$

If we set  $\sigma_i = \sqrt{\mu_i}$ , this term equals the well known Pearson's chi-square statistic [Pla83].

In this representation the chi-square function for a KATRIN minimal four parameter fit reads

$$\chi^2(m_\nu^2, E_0, A_S, R_{\text{bg}} | \mathbf{N}_{\text{obs}}) = \sum_{i(qU)} \left( \frac{N_{\text{obs},i} - N_{\text{theo},i}(m_\nu^2, E_0, A_S, R_{\text{bg}})}{\sigma_i} \right)^2. \quad (6.8)$$

$\sigma_i$  is the expected statistical uncertainty of an observation  $N_{\text{obs},i}$ . In case of purely Poissonian signal  $N_{\text{sig}}$  and background  $N_{\text{bg}}$ , it can be written as

$$\sigma_i = \sqrt{N_{\text{theo},i}} = \sqrt{(\sigma_i^{\text{sig}})^2 + (\sigma_i^{\text{bg}})^2} = \sqrt{N_{\text{theo},i}^{\text{sig}} + N_{\text{theo},i}^{\text{bg}}}. \quad (6.9)$$

### Poisson Likelihood Chi-square

Since in most cases KATRIN data (in particular  $\beta$  electrons) will obey Poisson statistics, an alternative form of a Poisson likelihood chi-square statistic  $\chi_{\lambda,p}^2$ , introduced by Baker and Cousins [Bak84], was implemented in our statistical framework:

$$\chi_{\lambda,p}^2 = 2 \sum_i \mu_i - x_i + x_i \log(x_i/\mu_i), \quad (6.10)$$

This statistic yields parameter and error estimates, which are identical to those of the maximum likelihood method. Furthermore it can be used for goodness-of-fit testing, since its minimum asymptotically obeys a classical chi-square distribution.

#### 6.1.4 Negative Squared Neutrino Masses

The shape of the  $\beta$ -decay spectrum (see equation 1.30) depends on the squared neutrino mass  $m_\nu^2$ , which consequently also is the observable, that can be estimated from a chi-square minimization. If one allows the likelihood function and the kinematic model of  $\beta$ -decay to extrapolate for negative  $m_\nu^2$  (i.e. tachyonic neutrinos), the best-fit estimate of  $m_\nu^2$  can very well fall into this unphysical region and be considered a statistical fluctuation of the observed data.

In particle physics and especially previous neutrino mass experiments, various strategies have been discussed to deal with parameter estimates and confidence intervals that extend into unphysical regions [Bon00; Wil88]. Frequentist methods advocate the inclusion of unphysical regions, mostly however with special treatment during the confidence belt

construction (see section 6.2.2), to avoid result intervals falling outside physical regions. A Bayesian physicist (section 6.2.4) might choose to state complete disbelief in negative  $m_\nu^2$  beforehand and not bother with the above mentioned likelihood extrapolation at all.

Special attention has to be paid to unaccounted systematic effects which might distort the observations in a way to mimic smaller or even negative  $m_\nu^2$ . For instance, high voltage fluctuations on the retarding potential are known to produce such an effect, without worsening the goodness-of-fit chi-square statistic [Ott08].

### 6.1.5 Systematic Uncertainties

In the KATRIN design report [KAT05] a comprehensive list of all identified and quantifiable systematic uncertainties is given (see table 6.1). It was found that the sum of all systematic uncertainties on  $m_\nu^2$  added quadratically does not exceed a value of  $\sigma_{\text{sys, tot}} \approx 0.01 \text{ eV}^2$ . No single value gives rise to a shift in the measured squared neutrino mass  $m_\nu^2$  larger than  $\Delta m_\nu^2 = 0.0075 \text{ eV}^2$ .

source of systematic shift	achievable / projected accuracy	systematic shift $\sigma_{\text{sys}}(m_\nu^2)$ ( $10^{-3} \text{ eV}^2$ )
description of final states	$f < 1.01$	$< 6$
$\text{T}^-$ ion concentration	$< 2 \cdot 10^{-8}$	$< 0.1$
unfolding of the energy loss function $f(\varepsilon)$		$< 6$
monitoring of column density $\rho d$	$\Delta T/T < 2 \cdot 10^{-3}$	$< \frac{\sqrt{5} \cdot 6.5}{10}$
	$\Delta \Gamma/\Gamma < 2 \cdot 10^{-3}$	
	$\Delta \varepsilon_T/\varepsilon_T < 2 \cdot 10^{-3}$	
	$\Delta p_{\text{inj}}/p_{\text{inj}} < 2 \cdot 10^{-3}$	
	$\Delta p_{\text{ex}}/p_{\text{ex}} < 0.06$	
background slope	$< 0.5 \text{ mHz/keV}$ (Troitsk)	$< 1.2$
HV variations	$\Delta HV/HV < 3 \text{ ppm}$	$< 5$
WGTS potential variations	$\Delta U < 10 \text{ meV}$	$< 0.2$
WGTS mag. field variations	$\Delta B_S/B_S < 2 \cdot 10^{-3}$	$< 2$
elastic $e^- - \text{T}_2$ scattering		$< 5$
<b>identified syst. uncertainties</b>	$\sigma_{\text{sys, tot}} = \sqrt{\sum \sigma_{\text{sys}}^2} \approx 0.01 \text{ eV}^2$	

**Table 6.1:** Summary of sources of systematic errors, taken from [KAT05], page 217.

To account for unidentified systematic effects, that might arise in a complete and final neutrino mass analysis, a conservative limit for the total systematic uncertainty of KATRIN was chosen:

$$\sigma_{\text{sys, tot}} \lesssim 0.017 \text{ eV}^2 \quad (6.11)$$

### 6.1.6 Sensitivity Calculation from Ensemble Tests

In [KAT05] the statistical uncertainty on  $m_\nu^2$  of KATRIN was investigated by performing ensemble tests. In this method a larger number of KATRIN measurements is simulated, with the resulting rates  $N_i$  being randomly distributed according to Poisson statistics. In each case a best-fit estimate of  $\hat{m}_\nu^2$  is determined by maximizing the likelihood function, or equivalently minimizing the chi-square function.

The statistical uncertainty of  $m_\nu^2$  can then be calculated from the resulting distribution of best-fit estimates (see figure 6.4 for an example). From such a distribution, a 68 % fraction of the samples can be picked to construct a central and continuous  $1\sigma$  error interval resulting in

$$\sigma_{\text{stat}}(m_\nu^2) = 0.018 \text{ eV}^2 .$$

Together with an estimated systematic uncertainty of

$$\sigma_{\text{sys}}(m_\nu^2) = 0.017 \text{ eV}^2 ,$$

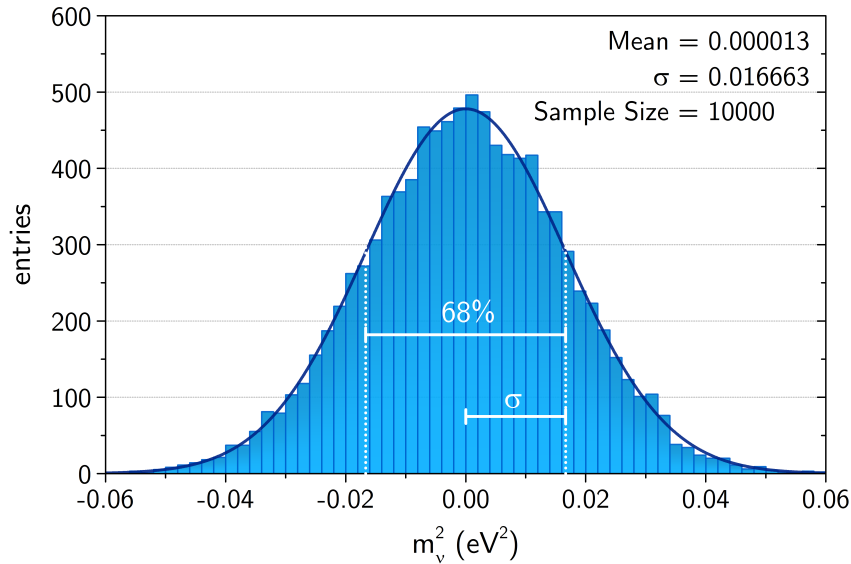


**Figure 6.4:** Distribution of best-fit estimates of  $m_\nu^2$  from an ensemble test with simulated  $m_\nu = 0 \text{ eV}$ . A Gaussian distribution with  $\sigma_{\text{stat}}(m_\nu^2) = 0.0166$  was fitted to the histogram.

these ensemble tests yield the often cited reference value for the KATRIN sensitivity of  $m_\nu = 200 \text{ meV}$  (90 % C.L.).

In the doctoral thesis of Markus Hötzel [Höt12] a reevaluation of the statistical uncertainty was performed. Using the same simulation parameters and measuring time distribution as in the Technical Design Report (TDR) (see table 6.2), but more recent final states distributions [Dos08] and larger ensembles, a statistical uncertainty of

$$\sigma_{\text{stat}}(m_\nu^2) = (0.0165 \pm 0.0001) \text{ eV}^2$$

was calculated, which resulted in a sensitivity of

$$m_\nu = 198 \text{ meV} \text{ (90 \% C.L.)} .$$

Since the publication of the TDR, the calculation of tritium  $\beta$ -decay spectra, the description of the most relevant systematics of the KATRIN apparatus (see section 5), and the formulation of our probability model has evolved and become more accurate. Repeating the above sensitivity evaluation with a complete model of the tritium source, inclusion of the Doppler effect and radiative corrections, the statistical uncertainty slightly improves to

$$\sigma_{\text{stat}}(m_\nu^2) = (0.0162 \pm 0.0001) \text{ eV}^2 , \quad (6.12)$$

parameter	setting
column density	$\rho d = 5 \cdot 10^{17} \text{ cm}^{-2}$
inelastic scattering cross section	$\sigma_{\text{inel}} = 3.45 \cdot 10^{-18} \text{ cm}^{-2}$
scattering probabilities	$P_0 = 0.413339$
	$P_1 = 0.292658$
	$P_2 = 0.167331$
	$P_3 = 0.079129$
	$P_4 = 0.031776$
active source cross-section	$A_S = 53.3 \text{ cm}^2$
magnetic field strengths	$B_S = 3.6 \text{ T}$
	$B_{\text{max}} = 6.0 \text{ T}$
	$B_A = 3 \cdot 10^{-4} \text{ T}$
tritium purity	$\varepsilon_T = 0.95$
background rate	$\dot{N}_{\text{bg}} = 0.01 \text{ cps}$
detection efficiency	$\varepsilon_{\text{det}} = 0.9$
measurement interval	$[E_0 - 30 \text{ eV}, E_0 + 5 \text{ eV}]$
Doppler effect	neglected
physical boundaries	extrapolation to negative $m_\nu^2$
tritium endpoint energy	$E_0 = 18\,575 \text{ eV}$

**Table 6.2:** Reference simulation parameters for ensemble tests.

which results in a sensitivity of

$$m_\nu = 197 \text{ meV (90 \% C.L.)} . \quad (6.13)$$

In case of the standard 4 parameter likelihood fit, the confidence intervals calculated from ensemble tests are in very good agreement with alternative methods implemented in KASPER, including likelihood ratio intervals (profile likelihood method, section 6.2.3) and Bayesian credibility intervals (Markov Chain Monte Carlos, section 6.3).

## 6.2 Confidence Intervals

The definition of confidence intervals (basically error limits) for parameters still is a controversial subject, especially between the schools of Frequentists and Bayesians. Both Frequentist (referred to as classical) and Bayesian methods are within themselves mathematically consistent, and in many cases they yield similar intervals. Their interpretation of probability however is fundamentally different.

A Frequentist will claim complete objectivity, by only making statements about the possible repetitions of the same experiment and the statistical fluctuations it produces. In doing so, the understanding of probability is the relative frequency of the experiment's possible outcome.

The Bayesian's view on probability is related to some personal degree of belief. Here, one attempts to report a probability on the actual parameter value, by only considering the one existent outcome of his experiment. However, a Bayesian is required to make a prior assumption on the parameter beforehand, which is unacceptable for a Frequentist.

It is not the purpose of this thesis to engage in a philosophical discussion about whether to favor one method over the other. However, we would like to point the interested reader to an article, summarizing the technical subtleties between several classical and Bayesian methods [Zec02]. The paper has a strong emphasis on physics experiments, including those dealing with nuisance parameters and non-physical confidence limits.

Within the next two sections a brief outline will be given of the two relevant classical methods within KATRIN's analysis framework: The Unified Approach and the Profile Likelihood method. Both are well-established Frequentist methods, which are explicitly recommended by the Particle Data Group [Ber12]. The Unified Approach will most certainly find application, when an actual neutrino mass measurement is to be published by the KATRIN collaboration within a Frequentist approach. The Profile Likelihood method is a reliable and yet computationally fast way of calculating error intervals. Therefore it is an important tool in more complex tasks presented later on in this thesis, like the measuring time optimization (section 6.4).

Following the introduction to Frequentist methods, we will move on to the focus of the present work, and introduce the Bayesian approach in section 6.2.4 and discuss its practical applications within KATRIN data analysis.

### 6.2.1 Neyman Construction

The defining property of classical confidence intervals is *coverage*: A method is said to yield a confidence interval with confidence level  $\alpha$  if, were the experiment to be repeated many times, at least a fraction of  $\alpha$  of the resulting intervals would cover the true parameter value, no matter what that value is.

Generally, Frequentist confidence intervals  $[\mu_1, \mu_2]$  are computed by constructing a *confidence belt* according to the Neyman construction scheme [Nak10], as illustrated in figure 6.5: For each true value  $\mu$  of a parameter of interest, an interval  $[x_1, x_2]$  (horizontal lines) of possible observed or measured values of that parameter is chosen, such that

$$\int_{x_1}^{x_2} P(x|\mu) dx = \alpha \quad (6.14)$$

By intersecting the belt at a measured value  $x$ , the confidence interval of  $[\mu_1, \mu_2]$  (vertical lines) is obtained.

The Neyman construction scheme doesn't determine  $x_1$  and  $x_2$  uniquely. Classical two-sided central intervals for instance have the additional property

$$P(x_1|\mu) = P(x_2|\mu) .$$

If the observable  $x$  however lies far within an unphysical region, such intervals can become small or even empty.

Results of unphysical or suspiciously small central confidence intervals have led to an undesirable behavior among physicists, called *flip-flopping*: Depending on the outcome of an experiment, the flip-flopper decides whether to compute a one-sided (upper / lower) limit or a two-sided interval after looking at the data. Not only does it seem subjective to switch the analysis method depending on the observation. Such an approach effectively violates the coverage condition of equation 6.14 in some areas of the confidence belt [Fel98].

### 6.2.2 Unified Approach by Feldman and Cousins

A solution to the problem of flip-flopping in the presence of physical parameter boundaries has been suggested by Feldman and Cousins by introducing an alternative ordering principle [Fel98]. When constructing a confidence belt (see figure 6.5), the intervals of  $[x_1, x_2]$  (horizontal lines) are determined by choosing the points of  $x$  in order of decreasing likelihood ratio

$$R(x, \mu) = \frac{P(x|\mu)}{P(x|\mu_{\text{best}})} . \quad (6.15)$$

Here,  $\mu_{\text{best}}$  is the value that maximizes the likelihood and at same time still is within the allowed region.

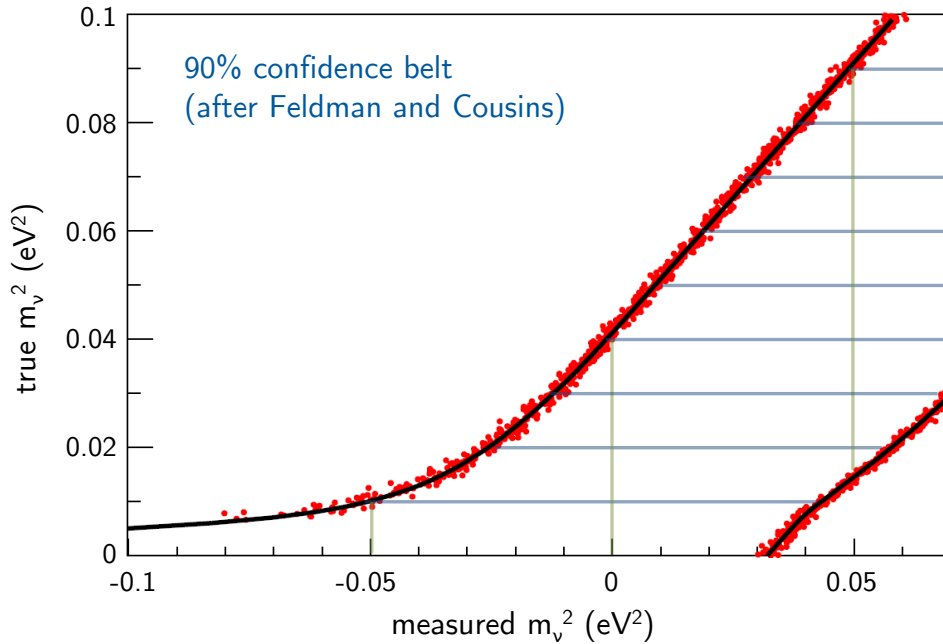


**Figure 6.5:** Frequentist confidence belt constructed after the Neyman scheme, using the likelihood ratio ordering suggested by Feldman and Cousins. After a neutrino mass measurement (best-fit estimate) has been done, the vertical lines inside the belt instruct, whether an upper limit or two-sided confidence interval should be published. A systematic uncertainty on  $m_\nu^2$  of  $0.017 \text{ eV}^2$  has been added in quadrature. Based on data from [Höt12].

The construction method by Feldman and Cousins provides smooth transitions from one-sided to two-sided confidence intervals and guarantees correct coverage. Also, small or vanishing upper limits due to a lucky best-fit estimate, lying far in the unphysical region, are prevented.

Among Frequentist methods, the unified approach is the one method recommended by the particle data group [Ber12]. It was also used in the final Mainz neutrino mass analysis to construct and publish an upper limit  $m_{\nu_e} < 2.3 \text{ eV}$  (95 % C.L.), where the best-fit value of  $m_{\nu_e}^2 = -0.6 \text{ eV}^2$  happened to be negative [Kra05].

The Feldman and Cousins method was first implemented in the software module KaFit by Markus Hötzel [Höt12]. The ordering principle is realized by generating a set of toy MC experiments and comparing their best-fit chi-square values. The confidence belt in figure 6.5 was computed using this implementation.

### 6.2.3 Profile Likelihood Method

As in the case of KATRIN, the likelihood  $L(\Theta, \pi)$  often contains several parameters, of which only some, namely  $\Theta$  are of interest. While the other nuisance parameters  $\pi$  might only be of secondary scientific importance, they can influence the estimate of the parameters of interest and their error limits.

An inappropriate suggestion for the elimination of the nuisance parameters  $\boldsymbol{\pi}$  would be to replace them by their best fit estimate, thus neglecting any correlation between the nuisance and the interesting parameters. In the extreme case of full correlation, the errors of  $\boldsymbol{\Theta}$  would shrink towards zero.

A likelihood-ratio based approach of estimating confidence intervals with a more sensible treatment of nuisance parameters is the so-called profile likelihood method [Rol05]. With a function  $\hat{\boldsymbol{\pi}}(\boldsymbol{\Theta})$  that maximizes the likelihood with respect to its nuisance parameters, one defines the profile likelihood

$$L_p(\boldsymbol{\Theta}) = L(\boldsymbol{\Theta}, \hat{\boldsymbol{\pi}}(\boldsymbol{\Theta})), \quad (6.16)$$

which solely depends on  $\boldsymbol{\Theta}$ . Using the best-fit estimate  $\hat{\boldsymbol{\Theta}}$ , a likelihood ratio test statistic  $\lambda(\boldsymbol{\Theta})$  can be defined

$$\lambda(\boldsymbol{\Theta}) = \frac{L_p(\boldsymbol{\Theta})}{L_p(\hat{\boldsymbol{\Theta}})}. \quad (6.17)$$

Following Wilk's theorem [Wil38],  $-2 \log \lambda$  converges in distribution to a  $\chi^2$  random variable. This is the theoretical basis for the extraction of confidence limits from the likelihood function: Similar to the  $\chi^2$  method, the area around the minimum of  $-2 \log L_p$  can be analyzed to find those values of  $\boldsymbol{\Theta}$ , where  $-2 \log L_p$  increases by a specific factor, defined by the quantiles of a  $\chi^2$  distribution with one degree of freedom. For instance, to find the  $1 \sigma$  intervals of a single parameter  $\Theta$ , one would scan the profile likelihood to determine values of  $\Theta$ , where  $-2 \Delta \log L_p(\Theta) = -2 \log \lambda = 1$ .

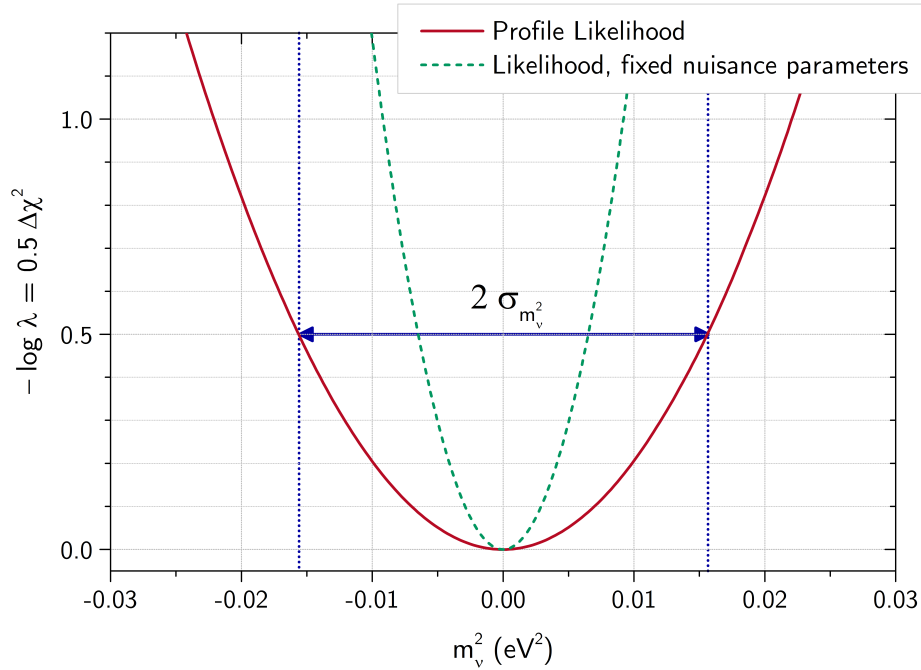
According to [Rol05] this method has proven to result in confidence intervals with good coverage for many applications, even close to unphysical borders. It can also be applied to the Feldman and Cousins ordering principle (section 6.2.2) to deal with more than one nuisance parameter.

Figure 6.6 shows the profile likelihood ratio for a typical KATRIN likelihood function. The extrapolation to negative  $m_\nu^2$  is chosen in such a way, that the profile likelihood  $L_p(\boldsymbol{\Theta})$  becomes symmetric in the point of the best-fit estimate  $\hat{m}_\nu^2$ . For details on the mathematical extrapolation we refer to section 5.4.

An implementation of the profile likelihood method, which is well known to many particle physicists, is the program MINOS, a component of the ROOT analysis framework [Ant09]. It is often used in conjunction with the minimizer MINUIT, to perform a sensible error estimate, especially in the presence of correlated nuisance parameters. The KATRIN software module KaFit integrates the most recent version of MINUIT and MINOS into our analysis framework and provides a unified programming interface to these tools.

#### 6.2.4 Bayesian Inference

Bayesian statisticians derive the posterior probability density function (p.d.f.)  $P(\boldsymbol{\Theta}|X)$  of a parameter of interest  $\boldsymbol{\Theta}$  from the likelihood function  $L(X|\boldsymbol{\Theta})$  and a prior probability  $\pi(\boldsymbol{\Theta})$ .



**Figure 6.6:** Profile likelihood ratio  $\lambda$  as a function of  $m_\nu^2$ , compared to a likelihood ratio with nuisance parameters fixed at the best-fit estimate of  $m_\nu^2$ .

This is in contrast to Frequentist methods, where only a best fit estimate  $\hat{\Theta}$  together with a confidence interval is stated, derived from assumptions on the relative frequency of the experiment's outcomes. Frequentists however argue, that the need for a prior assumption on the parameter yet to be estimated, is not objective.

Bayesian inference computes the posterior probability according to *Bayes' theorem*, which derives from basic axioms of probability:

$$P(\Theta|\mathbf{X}) = \frac{L(\mathbf{X}|\Theta) \cdot \pi(\Theta)}{p(\mathbf{X})}$$

- $\mathbf{X}$  is a set of observed data points.
- $\Theta$  is a vector of parameters, including those of interest, as well as nuisance parameters.
- $P(\Theta|\mathbf{X})$  constitutes the desired posterior probability density function (p.d.f.) of the parameters after having observed a certain set of data.
- The likelihood function  $L(\mathbf{X}|\Theta)$  is our probability model for data  $\mathbf{X}$  to be observed under the assumption of  $\Theta$ .

- $\pi(\Theta)$  is the prior probability of the parameters before any data is observed. The need for this subjective prior assumption on a parameter, that is yet to be determined, is subject of intense discussions between Frequentist and Bayesian statisticians. The simplest choice for the prior assumption can be a *flat* prior (identity) to state complete ignorance on the parameter, or a step function to exclude unphysical ranges of values.
- $p(\mathbf{X})$  can be seen as a normalization factor, which in most cases is difficult or even impossible to calculate. It is the distribution of the observed data marginalized over the parameters, also called the marginalized likelihood or evidence.

The probabilistic interpretation of a Bayesian result, namely  $P(\Theta|\mathbf{X})$ , is related to a personal degree-of-belief, because it requires the input of a prior density  $\pi$ . Another noteworthy difference from a Frequentist approach is that Bayesian inference obeys the *Likelihood Principle*, which states, that only the likelihood of the *actual observation* should matter for parameter inference.

Besides the publication of the full p.d.f.  $P(\mathbf{X}|\mu)$ , one can optionally construct any (confidence) interval of the parameter of interest  $[\mu_1, \mu_2]$ , so that

$$\int_{\mu_1}^{\mu_2} P(\mathbf{X}|\mu) d\mu = \alpha . \quad (6.18)$$

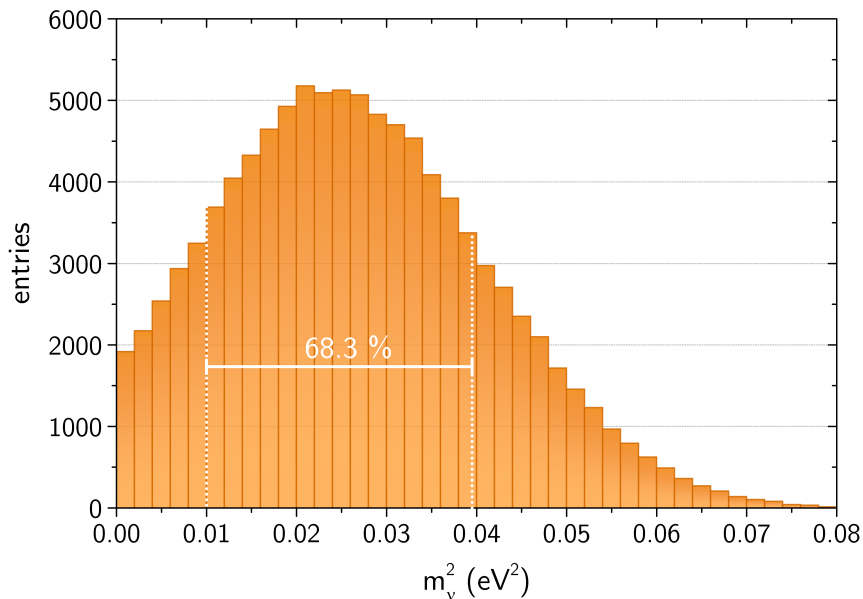


**Figure 6.7:** Exemplary bayesian posterior probability density function (p.d.f.) for  $m_v^2$ . The corresponding toy measurement was generated with  $m_{v\text{true}}^2 = 0.04 \text{ eV}^2$ . Sampled with the MCMC code introduced in section 6.3. The dashed lines mark the 68.3% HDR interval.

In a Bayesian context these intervals are often referred to as *credibility intervals* with  $\alpha$  being the *credibility level*. A common choice of  $[\mu_1, \mu_2]$  is the high density region (HDR), which is the smallest possible credibility interval  $[\mu_1, \mu_2]$  to give the posterior probability  $\alpha$ . An example for a p.d.f. with the corresponding HDR interval is shown in figure 6.7.

Frequentists often accuse Bayesian methods of being subjective, due to their choice of a prior. Again, we do not presume to advocate for one method or the other from a philosophical point of view. Frequentist methods are inarguably consistent within themselves. But in case of physical boundaries (as in case of squared mass terms) many classical methods produce differing results among one another, some of them with counter-intuitively small confidence intervals, that do not represent the precision of the experiment. Solutions to this problem, like the Unified Approach, require some arbitrary assumptions and extrapolation of the likelihood for unphysical regions of negative squared masses. Things become even more complicated in the presence of nuisance parameters, where some classical methods can produce intervals with undercoverage.

Bayesian methods on the other hand offer a technically simple and very universal approach. Forbidden parameter regions are excluded by the choice of the prior. Nuisance parameters are integrated out correctly and automatically when using MCMCs (section 6.3). Asymmetric and complex likelihoods are easier to treat in a Bayesian framework, because the computed posterior probability distributions, published together with the likelihood function, comprehensively reflect all relevant information.

### 6.2.5 Comparison of Neutrino Mass Confidence Intervals

The discussed methods for confidence interval construction can yield very similar results, if the observed data gives a positive best-fit  $m_\nu^2$  estimate. If however chances are unfortunate, and the best-fit falls into an unphysical region (due to statistical fluctuations), the differences between classical and Bayesian methods become apparent.

In figure 6.8, some of the implemented statistical methods are compared against each other for the cases of the best-fit value of  $m_\nu^2$  being negative, zero and positive. Only the statistical uncertainty at a confidence level of 90 % is considered here.

The *classical* method uses 2-sided central intervals, which in extreme cases can completely fall into the unphysical region, or simply become very small. Feldman and Cousins's *unified* approach dictates a more reasonable 1-sided limit in such scenarios.

*Bayesian* limits were calculated using the MCMC implementation, described in the following section 6.3. A flat prior on  $m_\nu^2 \geq 0.0 \text{ eV}^2$  was chosen. The stated limits were constructed by integrating the marginalized posterior probability distribution of  $m_\nu^2$ , following equation 6.18 to obtain a credibility level of  $\alpha = 90 \%$ .

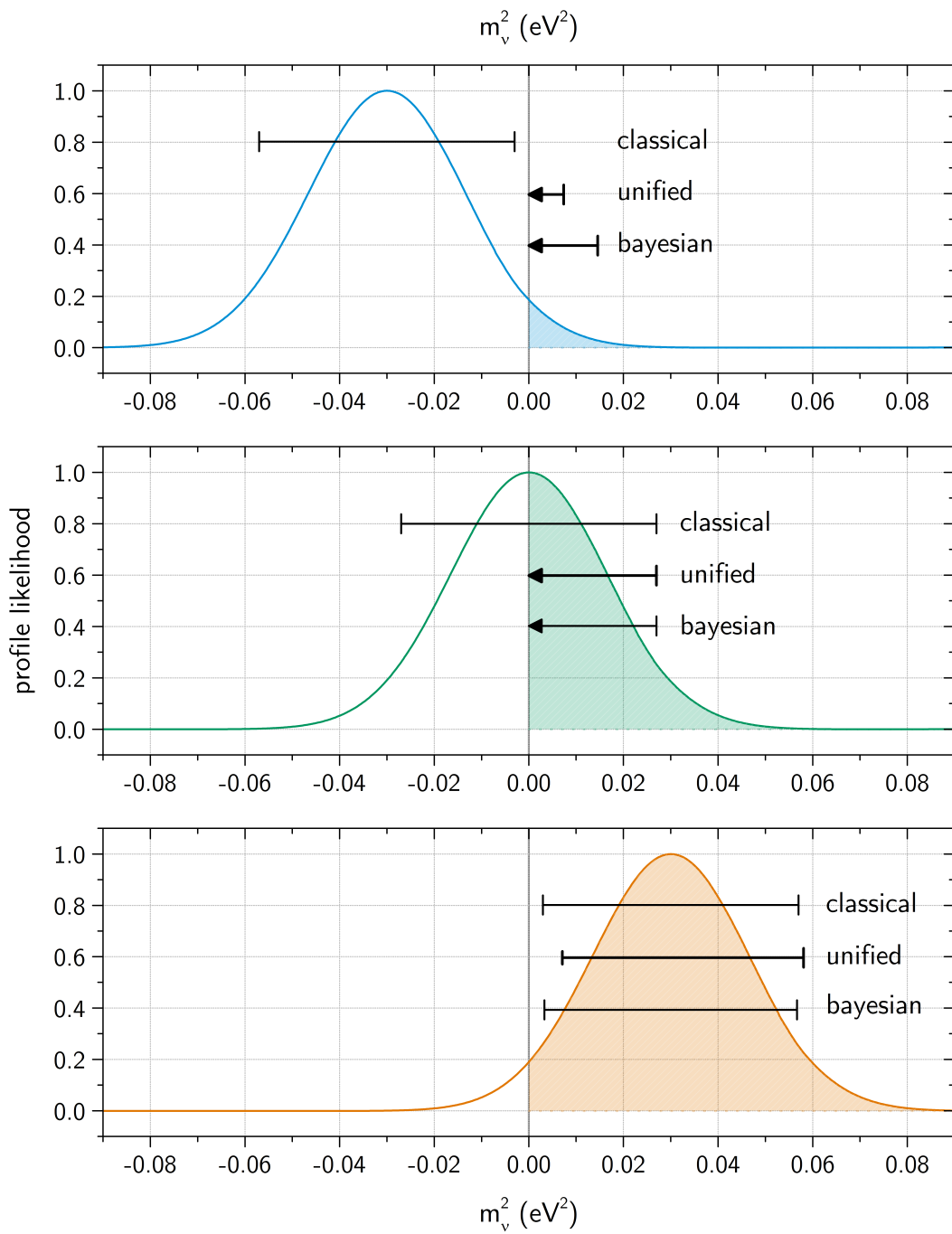


**Figure 6.8:** Profile likelihood  $L_p$  as a function of  $m_\nu^2$ . The marked intervals compare statistical confidence intervals (90% C.L.) for various methods. The best-fit estimates for  $m_\nu^2$  are  $-0.03 \text{ eV}^2$  (top),  $0.00 \text{ eV}^2$  (middle) and  $+0.03 \text{ eV}^2$  (bottom).

### 6.3 Markov Chain Monte Carlo Methods

MCMC methods are a class of efficient mathematical algorithms, which are widely employed to sample from probability distributions in a Bayesian framework. They have become popular not only in statistical physics, but also in cosmology, high energy and astroparticle physics, to deal with complex high-dimensional and multi-modal systems, that are hard to solve for classical statistical methods.

MCMCs were first introduced in 1953 by Metropolis et al. [Met53] as a mathematical tool for obtaining samples from probability distributions, for which direct sampling is difficult, especially when the number of dimensions is high. In contrast to other MC methods, Markov chain based algorithms are constructed to produce a random walk of statistically correlated samples. The obtained sequence of samples can then be used to calculate an integral (e.g. an expectation value) or approximate the desired distribution by generating a histogram. Nuisance parameters are automatically integrated out during this procedure and do not require special treatment.

#### 6.3.1 Metropolis-Hastings Algorithm

A well-known MCMC algorithm, which has become the basis of many existing MCMC sampling schemes, is the Metropolis-Hastings algorithm, introduced in 1970 [Has70]. It can draw samples from any distribution  $P(\boldsymbol{\theta})$ , with  $\boldsymbol{\theta}$  being a vector of parameters with dimensionality  $d$ . The only requirement is, that the user can compute a function  $f(\boldsymbol{\theta})$ , which is proportional to the density of  $P(\boldsymbol{\theta})$ . This means, that the algorithm circumvents the requirement of knowing the normalization of  $f(\boldsymbol{\theta})$ , which makes it particularly useful for Bayesian inference:

$$P(\boldsymbol{\theta}) = \frac{L(\mathbf{X}|\boldsymbol{\theta}) \cdot \pi(\boldsymbol{\theta})}{p(\mathbf{X})} = \frac{f(\boldsymbol{\theta})}{c} \quad (6.19)$$

The algorithm works by generating a sequence of samples  $\{\boldsymbol{\theta}_t\}$ , which after a so-called *burn-in* period converges towards the target distribution  $P(\boldsymbol{\theta})$ . Advancing from a point  $\boldsymbol{\theta}_t$  in the chain, the algorithm draws a candidate point  $\mathbf{Z}$  from a proposal distribution  $q(\mathbf{Z}|\boldsymbol{\theta}_t)$ . Next, the candidate point is accepted or rejected depending on the Metropolis acceptance ratio:

$$\alpha(\boldsymbol{\theta}_t, \mathbf{Z}) = \min \left[ \frac{f(\mathbf{Z})}{f(\boldsymbol{\theta}_t)} \cdot \frac{q(\boldsymbol{\theta}_t, \mathbf{Z})}{q(\mathbf{Z}, \boldsymbol{\theta}_t)}, 1 \right] \quad (6.20)$$

The factor  $\frac{q(\mathbf{Z}, \boldsymbol{\theta}_t)}{q(\boldsymbol{\theta}_t, \mathbf{Z})}$  compensates for an asymmetry in the proposal function. Often a simple Gaussian is chosen for  $q$ , which is centered around  $\boldsymbol{\theta}_t$ . In that case, the asymmetry factor simply is 1. If the candidate is accepted, the next point in the chain is set to  $\boldsymbol{\theta}_{t+1} = \mathbf{Z}$ . Otherwise, the old state is kept and duplicated  $\boldsymbol{\theta}_{t+1} = \boldsymbol{\theta}_t$ . The fact that the next state within the sequence only depends on the preceding one, is the defining property of a *Markov chain*.

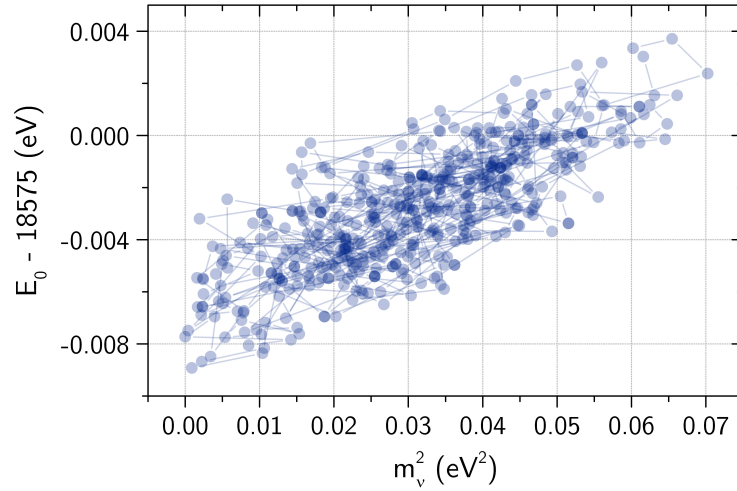


**Figure 6.9:** The random walk behavior of an MCMC process is illustrated using the example of a four parameter KATRIN likelihood function. A sequence of 500 samples from the middle of the sampled chain is plotted in a 2D projection of the parameter space. In this stage the MCMC has adjusted to a stationary distribution, spending more time in areas of higher probability. Darker points imply subsequent identical samples due to rejected proposals.

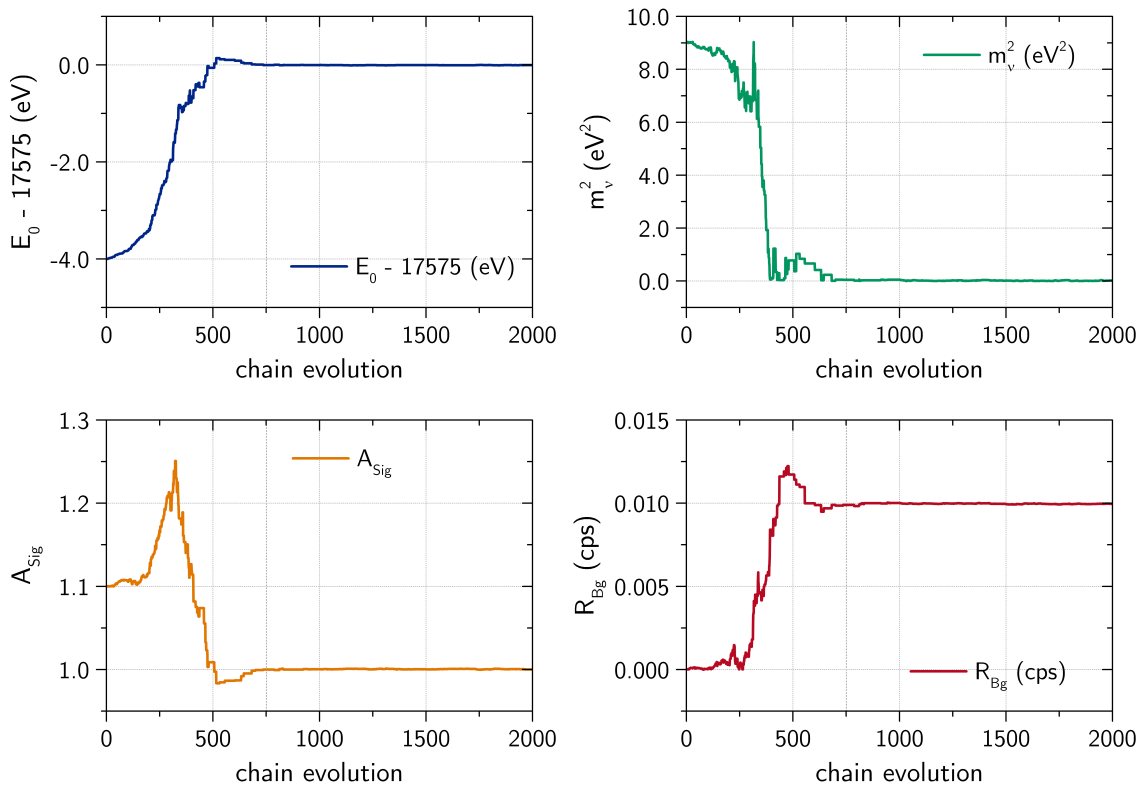


**Figure 6.10:** Burn in phase of a MCMC. The four parameters are set to quite extreme start values with a corresponding chi-square value of  $\sim 10^5$ . After about 600 steps, the chain has converged towards the target distribution in all of the four parameter dimensions.

The transition probability of a Metropolis-Hastings algorithm fulfills the condition of *detailed balance*. It guarantees that the Markov chain can asymptotically reach a stationary distribution  $P(\boldsymbol{\theta})$ . For a deeper explanation and the complete mathematical proof, the reader is referred to selected references of the comprehensive literature available on the topic [Gre05; Mac03; Pre07].

An exemplary section of an MCMC random walk through a standard KATRIN parameter space is shown in figure 6.9. The characteristic burn-in phase and convergence behavior can be seen figure 6.10, where the evolution for each parameter in the chain is plotted.

### 6.3.2 Proposal Distribution and Acceptance Rate

The efficiency of the sampler is mostly determined by the choice of the proposal distribution, sometimes called the transition kernel. Its width controls the jumping distance from one state in the Markov chain to the next. A large jumping distance will usually lead to a low *acceptance rate*  $\alpha$ , the fraction of accepted proposals. In this case, the parameter state of the chain will only rarely change. A too small jumping distance on the other hand (in general connected to high acceptance rates) will lead to a long burn-in phase and a strong auto-correlation of the sampled sequence with obvious random-walk behavior. In both cases, large portions of the sampled states have to be discarded or thinned out and the MCMC has to run for a long time in order to produce a good enough approximation

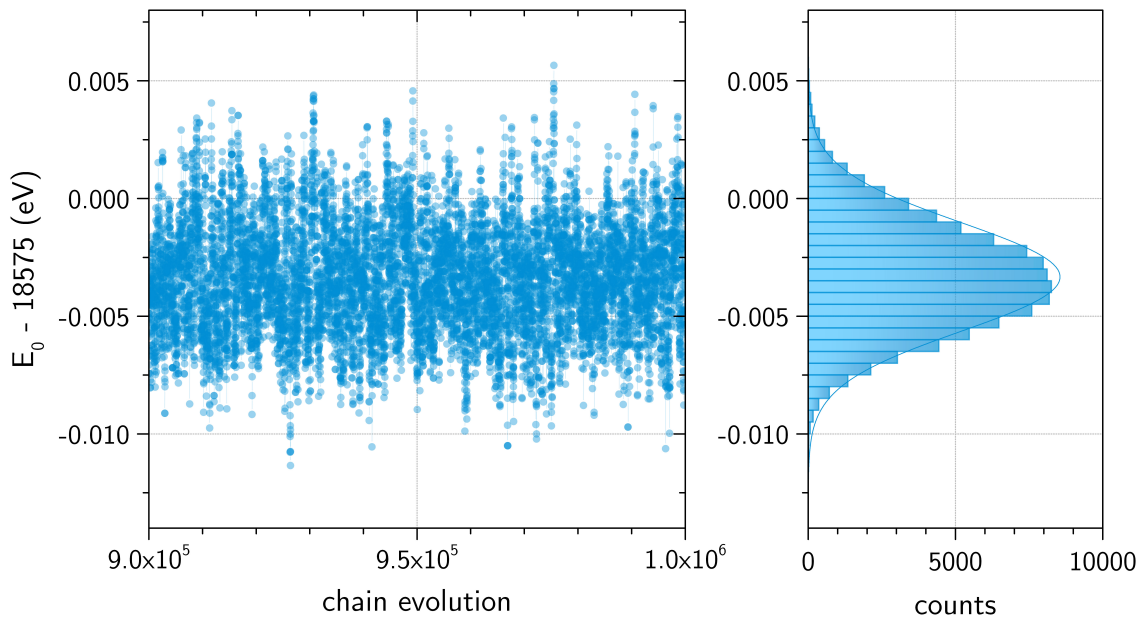


**Figure 6.11:** Evolution of a specific parameter ( $E_0$  in this case). The corresponding marginalized probability density function is approximated by a histogram of all sampled parameter values.

of the target distribution. It has been shown theoretically, that for Gaussian-like target distributions, the optimal acceptance rate is about 50 % for one dimension, decreasing to about 23 % for four or more dimensions [Rob97].

### 6.3.3 Implementation and Performance

The Metropolis-Hastings algorithm was the first MCMC sampling scheme to be integrated into the KASPER software framework as part of the KaFit sensitivity studies module. The implementation of the algorithm is straightforward, but nevertheless very robust and universal in its application.

Like most other components of KASPER, the Markov Chain code is organized in a modular way with simple interfaces to other KASPER functionality. The KATRIN likelihood function with all the spectrum and systematics simulation code behind it, is easily ‘plugged in’ to be used for comprehensive Bayesian inference. Some other applications inside KASPER merely use the MCMC code as a high-dimensional function minimizer.

A specific MCMC simulation can be set up with XML configuration files or directly via its programming interface. Parameters are defined in exactly the same way as for the MINUIT minimizer. In addition to the standard Metropolis-Hastings scheme, several other strategies, described further below, can be chosen and configured.

Within the KASPER framework, the implemented MCMC methods have proven to be robust and versatile tools for parameter inference or simply function minimization. In case of higher dimensional functions with strongly correlated parameters, possibly with multiple local extrema, classical minimizers tend to struggle (like the ‘Simplex’ or ‘Migrad’ algorithms provided by MINUIT). Properly configured MCMCs however, manage to explore such functions efficiently, and map them out in a way allowing graphical by-eye inspection of their properties and intuitive statistical analyses (see figures 6.11, 6.12 and 6.13).

#### Proposal Functions and Automatic Adaption

The code allows the definition of various proposal distributions for the Metropolis-Hastings sampling scheme. In most KATRIN-specific applications however, a multivariate Gaussian distribution, centered around the current state of the Markov Chain, proved to be the most universal and easily tunable solution. The widths of the Gaussian for each dimension of the parameter space can be specified by the user. If strong parameter correlations are to be expected, a full covariance matrix for the proposal distribution can be specified.

Finding the optimal proposal widths manually can be challenging. As already discussed above, those configuration values are crucial for the performance of the sampler. The code implemented for this thesis features an adaption mechanism which periodically analyzes the acceptance rate of the chain. In its most basic mode, the adaption mechanism will then gradually adjust the proposal widths to yield an optimal acceptance rate. Optionally, the full covariance matrix can be extracted from the parameter states, sampled within the last

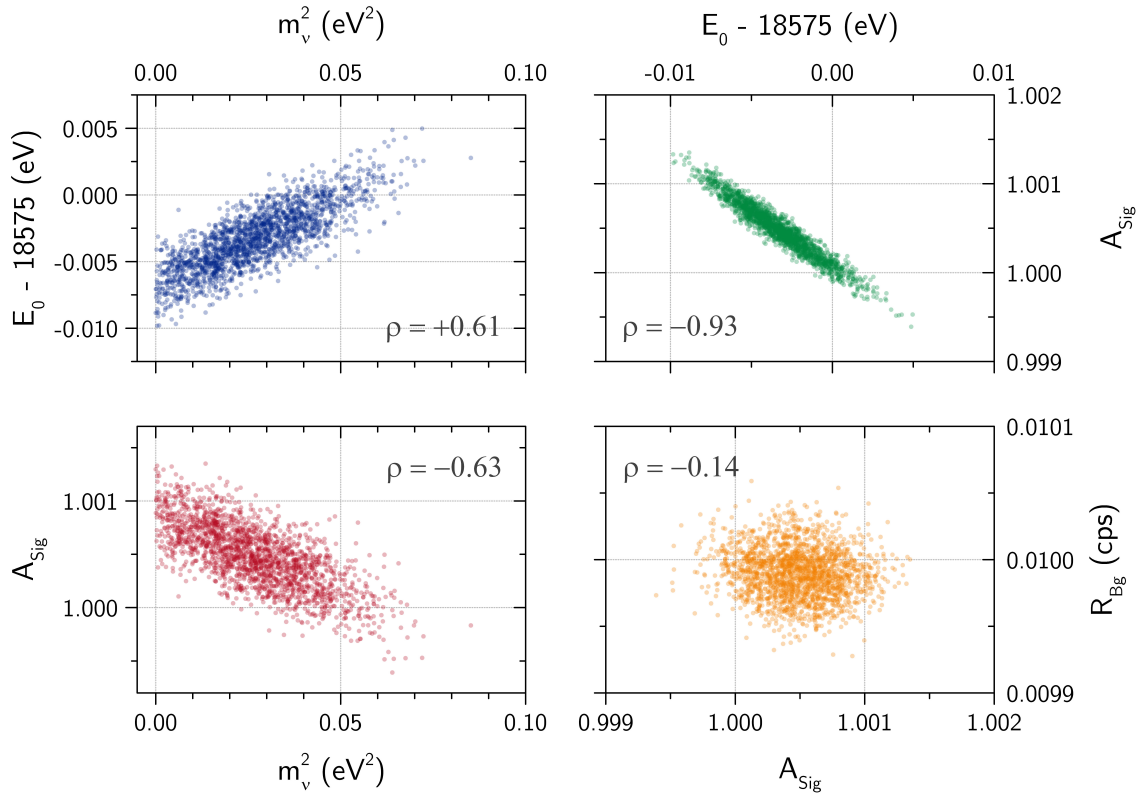


**Figure 6.12:** 2D scatter plots of selected parameter combinations (squared neutrino mass  $m_\nu^2$ , tritium endpoint  $E_0$ , signal amplitude  $A_{\text{sig}}$ , background rate  $R_{\text{bg}}$ ) and their correlation coefficients  $\rho$ . The scatter plots are rendered from an MCMC analysis of a single random KATRIN toy measurement with a true value of  $m_\nu^2 = 0.04 \text{ eV}^2$  and a prior on positive  $m_\nu^2$ .

adaption cycle. Using the covariances, not only the scale, but also the orientation of the proposal distribution is adjusted. Such an adaption can of course only be done during the burn-in phase, since such a run-time modification violates the detailed balance condition.

### Parallel Tempering

By definition and construction, MCMCs are capable of escaping local extrema and exploring a wider region of the parameter space. However, for farther separated minima, a jump from one to the other can become very unlikely, and the simulation might not explore the full parameter space during its lifetime. A possible solution would be to run several MCMCs with different start positions and combine the sampled results into one histogram.

A more elegant solution, implemented as proposed in [Gre05], is parallel tempering: Multiple copies of the simulation are run in parallel. Each sampler is assigned a different temperature  $T$ , which effectively deflates the sampling distribution by a factor  $\beta = \frac{1}{T}$ . At certain intervals, a state exchange of adjacent chains is proposed in such a way, that the

convergence conditions of the coldest chain with  $T = 1$  is preserved. This mechanism enables the MCMC to perform jumps between different modes of the sampling distribution at the cost of having to compute additional (heated) chains, which are discarded in the end.

### Evaluating Convergence and Statistical Quantities

After an MCMC run has been completed, the code provides a large set of functions to extract diagnostics and statistical data from the sampled sequences. Certain quantities are essential in order to judge convergence and quality of the sampled distribution:

- Autocorrelation function

The autocorrelation  $R(k)$  describes the correlation of states within the chain at two different times  $t$  and  $t + k$  with time lag  $k$ :

$$R(k) = \frac{1}{(N - k)\sigma^2} \sum_{t=0}^{N-k} (\boldsymbol{\theta}_t - \boldsymbol{\mu})(\boldsymbol{\theta}_{t+k} - \boldsymbol{\mu}), \quad (6.21)$$

$\boldsymbol{\mu}$  is the mean of the parameter  $\boldsymbol{\theta}$  and  $\sigma^2$  the variance. Markov Chains generated by random-walk algorithms like the Metropolis-Hastings show strong correlations over several tens or hundreds of nearby samples. In figure 6.13 autocorrelation functions for each parameter of an exemplary MCMC run are shown.

- Autocorrelation time

Adjacent samples within a time lag  $t_R$ , the autocorrelation time, are considered to be not independent:

$$t_R = 1 + 2 \sum_{k=1}^N R(k) \quad (6.22)$$

- Effective sample size

This parameter is given by the total number of samples divided by the autocorrelation time:

$$ESS = \frac{N}{t_R}$$

By discarding the majority of samples and considering only every  $(t_R)$ th sample, an independent set of uncorrelated samples can be extracted. In general, this is the favored procedure in order to get a reasonable estimate of the target probability distribution. Also, the effective sample size is commonly used to benchmark the efficiency of an MCMC algorithm and its transition kernel.

- Gelman Rubin Diagnostic [Gel92]

This is a diagnostic quantity indicating the convergence of multiple parallel chains towards the same distribution.

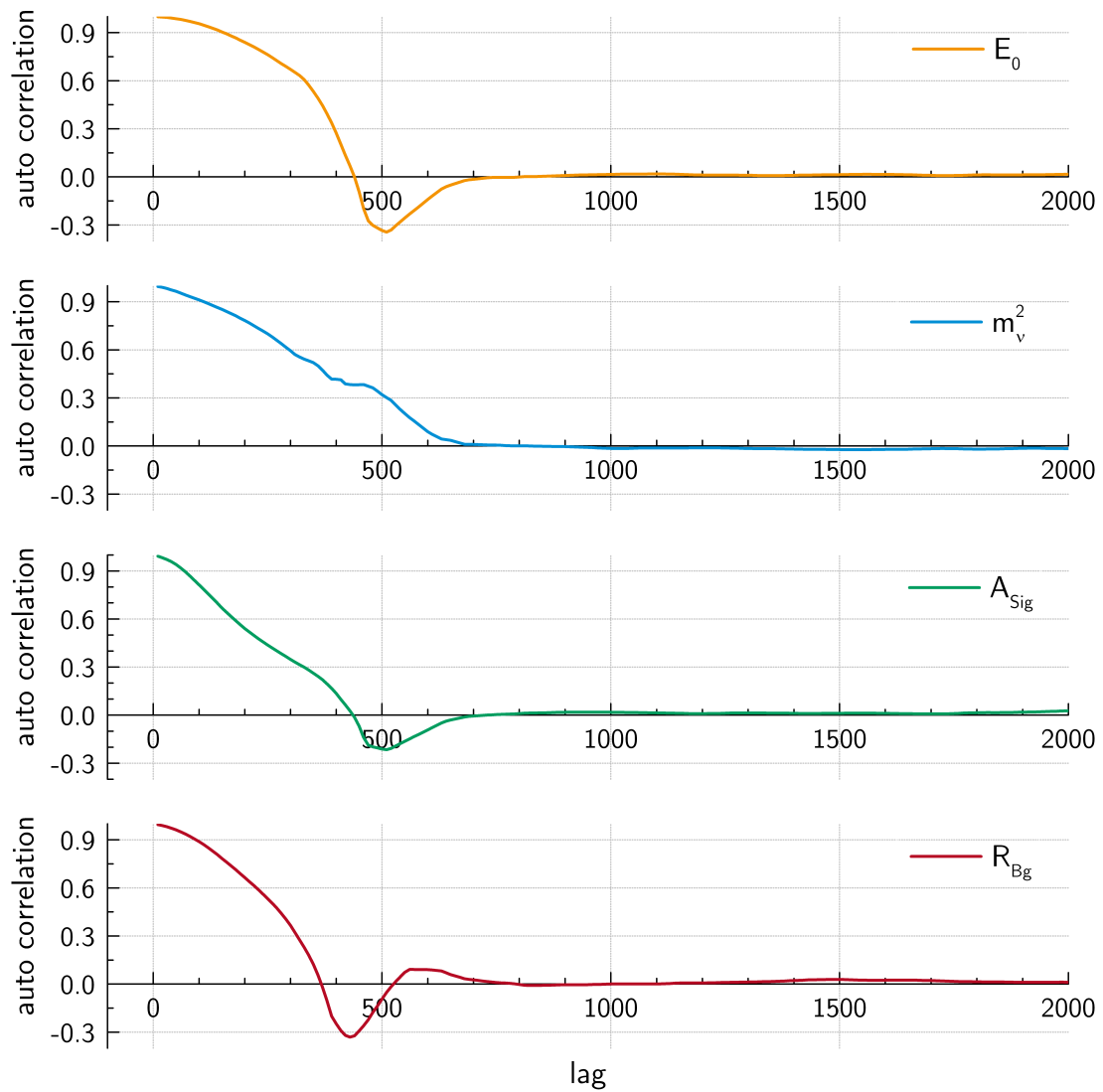


**Figure 6.13:** Autocorrelation functions  $R(k)$  for each fit parameter ( $m_{\nu}^2$ ,  $E_0$ ,  $A_{\text{Sig}}$ ,  $R_{\text{Bg}}$ ) of an MCMC analysis of a simulated KATRIN measurement. The lag  $k$  denotes the distance (number of chain evolutions) between two states of the Markov Chain. Usually, the behavior of  $R(k)$  relates to the length of the burn-in phase, which in this example is  $\approx 700$ .

In addition, basic statistical analysis is automatically performed on the sampled data:

- Covariance and correlation coefficients
- Medians for each parameter and statistical moments like the mean and variance
- Marginalized distributions for each parameter
- Calculation of credibility intervals

All the information gathered during the sampling procedure can be exported to either ASCII files or ROOT compatible data formats (see figure 6.14).

### 6.3.4 Hamiltonian MCMC

A more complex sampling scheme, implementing Hamiltonian dynamics, was added to the KASPER MCMC package as part of the diploma thesis of Sebastian Schams [Sch13a]. A Hamiltonian MCMC attempts to speed up convergence by introducing fictitious momentum variables. Given that the state space is continuous, the sampler creates discretized trajectories, which in some applications are more efficient compared to the diffuse random walk behavior of the simpler Metropolis Hastings algorithm [Nea11].

However, this approach introduces additional configuration parameters (masses of the momentum variables), which require careful manual tuning. Also it relies on the first order derivatives of the likelihood, demanding additional computing time, especially if they have to be approximated numerically. Furthermore the algorithm exhibits some sensitivity towards local steep gradients arising from small-scale numerical fluctuations in our likelihood function (see section 5.7).

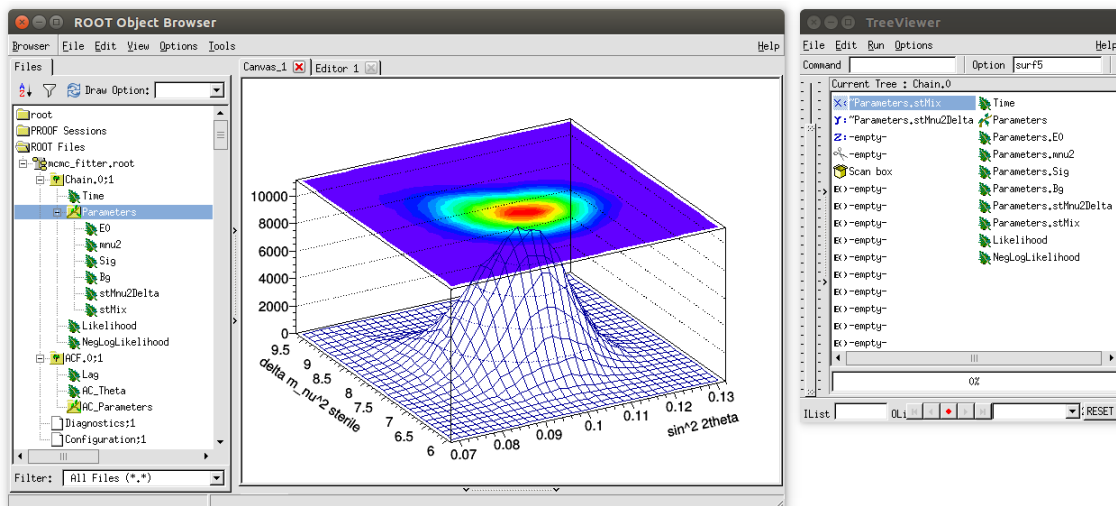


**Figure 6.14:** Analysis of MCMC output, using the TTreeView tool provided by ROOT [Ant09]. With the graphical user interface various types of histograms can quickly be generated for any parameter configuration.

### 6.3.5 Self Adaptive Differential Evolution MCMC

Even though it has been argued so far, that the Metropolis Hastings algorithm is one of the most robust and universal sampling schemes, the mixing of the Markov Chain can be disturbingly slow in parameter spaces of high dimensionality ( $d \gtrsim 10$ ). The expression of slow mixing refers to chains that converge very slowly and show strong auto-correlation over long distances. Frequently this is caused by an inappropriate choice of scale and orientation of the proposal distribution, which is used to generate the candidate states for the next move. In principal the user would have to provide the full parameter covariance matrix for the proposal distribution a priori, in order to ensure efficient mixing. However in practice, especially for higher number of dimensions, this is nearly impossible.

The most recently implemented sampling scheme in KASPER attempts to address this problem, without discarding the robustness towards difficult likelihood surfaces. It is based on the Differential Evolution Adaptive Metropolis (DREAM) algorithm [Vru09], first published in 2009. At its core, it still uses the Metropolis-Hastings ratio to decide about the acceptance of a candidate proposal. For the generation of proposals however, a population of multiple chains is used, with at least as many chains as parameter dimensions running in parallel.

#### Self Adaption

The only input, the user has to provide, is a sensible spread for the starting positions of the different Markov chains. From then on, at each generation the algorithm uses the current samples of the chains to determine the parameter covariances and most appropriate jump sizes dynamically, in order to generate the next proposal step for each chain.

#### Subspace Sampling

Often it is not optimal to modify all dimensions simultaneously. DREAM implements a randomized subspace sampling strategy with a set of so called crossover probabilities, that are automatically tuned during the burn-in phase. Also within the burn-in phase, outlier chains with aberrant trajectories are reset to the best member of the population to speed up convergence.

#### Delayed Rejection

Another feature, called Delayed Rejection [Haa06], has been added to this sampling scheme, which increases the acceptance rates and therefore improves the target distribution estimate. Upon rejection of the first proposal, a second trial move is generated from a deflated covariance matrix. The Metropolis acceptance probability has to be modified for the second proposal, in order to restore the condition of detailed balance.

## 6.4 Optimizing the Measuring Time Distribution

The expected number of events

$$N_{\text{theo},i} = \dot{N}_{\text{int}}(qU_i, m_\nu^2, E_0, A_S, R_{\text{bg}}) \cdot t_i$$

to be measured by KATRIN is determined by the integrated energy spectrum of  $\beta$ -decay electrons with rate  $\dot{N}_{\text{int}}$  at a given retarding potential  $qU_i$  and the measuring time  $t_i$  distributed to that configuration. The total measuring time  $\sum_i t_i$  is constrained by the planned time budget of 3 effective (5 calendar) years of data taking. The time distribution  $t_i$ , as well as the interval of  $qU$  around the endpoint energy, have a considerable affect on the shape of the likelihood function, and in consequence on the statistical uncertainty of  $m_\nu$ .

Several attempts have been made so far, to minimize the statistical uncertainties by modifying the measuring time distribution (MTD). Authors of the TDR computed a set of non-flat time distributions (for background rates  $R_{\text{bg}} = 10$  mcps), which achieve an improvement on the statistical uncertainty of about 20 % (see figure 6.15). The largest amount of measuring time is accounted for values of the retarding energy  $qU$  close to the endpoint region, where the spectral shape is most sensitive to deformations due to a non-zero neutrino mass  $m_\nu$ , and where the signal-to-background ratio of about 2 : 1 is sufficiently large. The region beyond the endpoint is required to deduce the background rate  $R_{\text{bg}}$ , whereas the region at lower retarding potentials determines the endpoint  $E_0$  and the amplitude of the signal  $A_S$ .

Systematic effects are a limiting factor, when choosing an interval of the retarding energy  $qU$  around the tritium endpoint  $E_0$ . According to estimates in the TDR, systematic uncertainties, especially due to electron scattering in the tritium source, are best understood and sufficiently under control above  $qU \geq E_0 - 30$  eV. Therefore, in most of the following calculations the retarding potential will be constrained for this region to an interval of  $qU \in [E_0 - 30 \text{ eV}, E_0 + 5 \text{ eV}]$ , meaning that no measuring time will be allocated outside that interval. This definition also allows for better comparability of the reevaluated neutrino mass sensitivities with calculations from previous theses and the TDR [KAT05].

### 6.4.1 Motivation

Calculations of spectra with alternative background models or the inclusion of sterile neutrinos (see figure 6.15) suggest, that the measuring time distribution (MTD) has to be adapted to scenarios, which differ from the reference configuration. Now that more flexible and accurate procedures for spectra calculation are available within the KATRIN software framework, and that the first commissioning data at various background rates have been taken, the need for an appropriate optimization tool became apparent. Ideally the optimization scheme should make use of the full likelihood and spectrum model available and deduce the optimal time distribution, in terms of neutrino mass sensitivity, autonomously and in a reproducible manner.

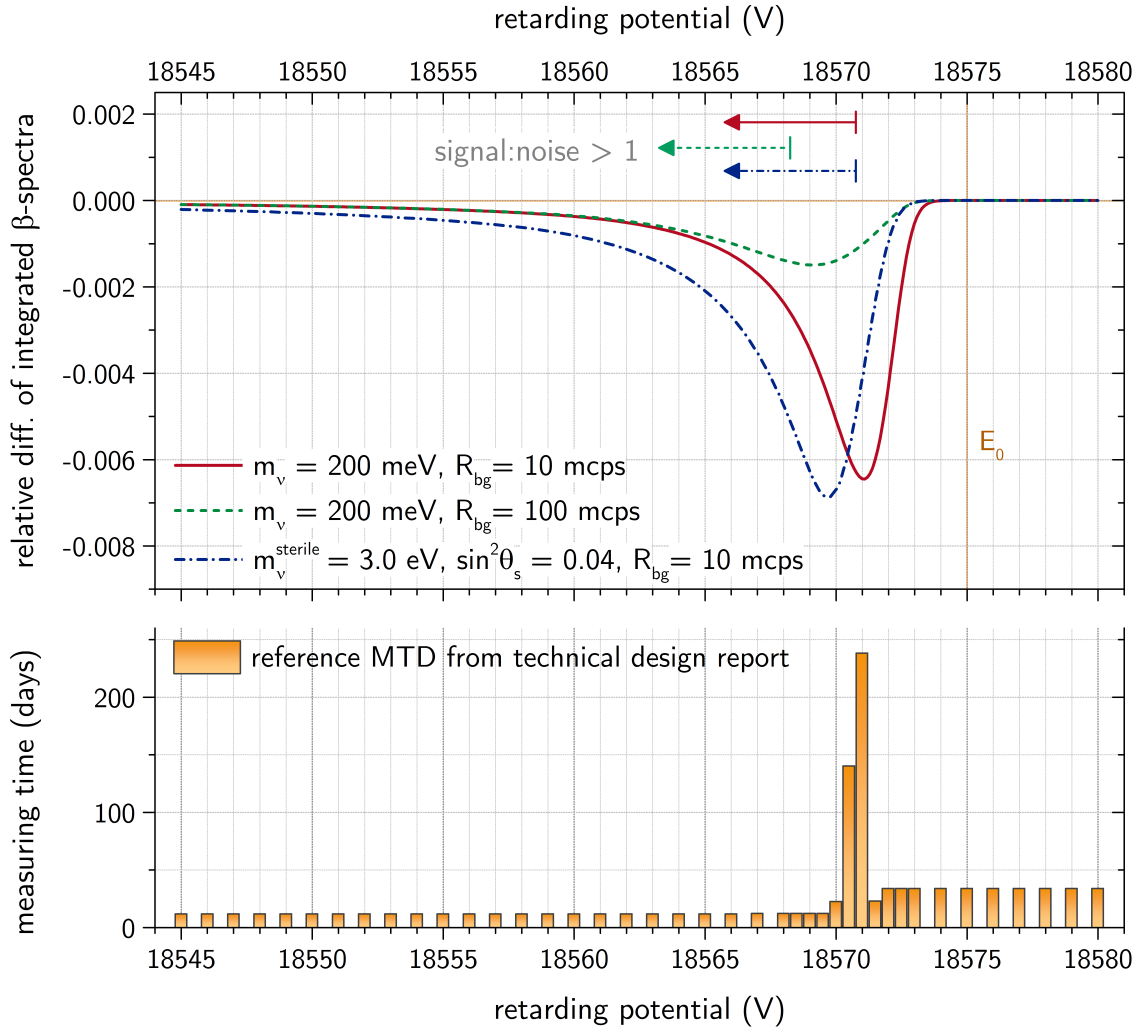


**Figure 6.15:** Top: Relative differences of integrated spectra with the scenario of a vanishing neutrino mass and background of 10 mHz as reference. Bottom: The measuring time distribution proposed by the KATRIN design report [KAT05].

#### 6.4.2 Functional Description

First, a functional description of the optimization task is suggested by defining an objective function:

$$f(\{t_i\}) = f(t_1, \dots, t_N) = \left(\frac{\sigma_{m_\nu}}{a}\right)^2 + \left(\frac{\sum t_i - T_{\max}}{b}\right)^2 \quad (6.23)$$

$f$  is a function of the individual measuring times  $t_i$ , each one attributed to a specific retarding potential  $qU_i$  in the measurement configuration. The parameter  $\sigma_{m_\nu}$  denotes the statistical uncertainty on the measured neutrino mass,  $T_{\max}$  is the maximum total data-taking time. Graphically the first summand of the objective function  $f(\{t_i\})$  describes a

parabola, which becomes minimal for small  $\sigma_{m_\nu}$ . The sum over all time bins is constrained by the second summand, a penalty term. The constant factors  $a$  and  $b$  are arbitrary parameters, that can be used to tune the priorities and steepness of the objective function.

With the objective function  $f$  implemented and a fixed set of measurement potentials  $qU_i$  defined, the next step is to find those parameter values  $\hat{t}_i$ , which result in a global minimum of  $f(\{t_i\})$ .

An important detail of this approach is the calculation of  $\sigma_{m_\nu}$ . It is foreseeable that this quantity will have to be recalculated for every tested set of  $\{t_i\}$  during the minimization procedure with sufficient precision. Full blown ensemble tests (see section 6.1.6), requiring thousands of minimization procedures each, are not feasible. A first attempt of calculating only a handful of fixed points of the likelihood function did produce wrong results, because it neglected the complicated correlation between  $m_\nu^2$  and the nuisance fit parameters  $E_0$ ,  $R_{bg}$  and  $A_S$ .

The profile likelihood method, described in section 6.2.3, turned out to be the most appropriate choice at this point: For each set of fixed  $\{t_i\}$ , the expectation values of a toy KATRIN measurement are calculated and used to analyze the shape of the profile likelihood. This way, a representative value for  $\sigma_{m_\nu}$  can be calculated, while taking into account its correlation with the nuisance parameters. The technical implementation of this method makes use of the external MINOS library, which requires around 100 to 200 evaluations of the likelihood function in order to obtain a result.

### 6.4.3 Minimization Technique

Depending on the number of time bins  $\{t_i\}$  chosen, we are faced with the minimization of a high-dimensional function. If a 0.5 eV binning is demanded in the retarding potential interval  $[E_0 - 30 \text{ eV}, E_0 + 5 \text{ eV}]$ , the objective function has 71 parameters. If one adopts the binning scheme suggested in the TDR, with a 1.0 eV binning, adding 5 additional bins close to the endpoint region, the parameter count still comes to 41.

The MCMC code, described in section 6.3 and implemented as part of this thesis, was chosen to perform this task. Since the objective function  $f(\{t_i\})$  does not constitute a probability distribution, all Bayesian inference capabilities of the MCMC sampler are neglected in this case. The MCMC is merely utilized and configured as a minimizer, relying on its capabilities to handle local minima and possibly non-continuous functions. The self-adaptive features of the code are of great help, since the parameter correlations (between the  $\{t_i\}$ ) and step widths of this particular problem are difficult to tune in advance by hand.

#### MCMC Transition Kernel

A customized transition kernel was implemented, which modifies only a subset of the parameters (MTD bins) at a time, again by randomly proposing the next step from a Gaussian centered around the start value. However, the remaining unmodified parameters are rescaled to keep the total measuring time  $\sum t_i$  at its original value. Executing the

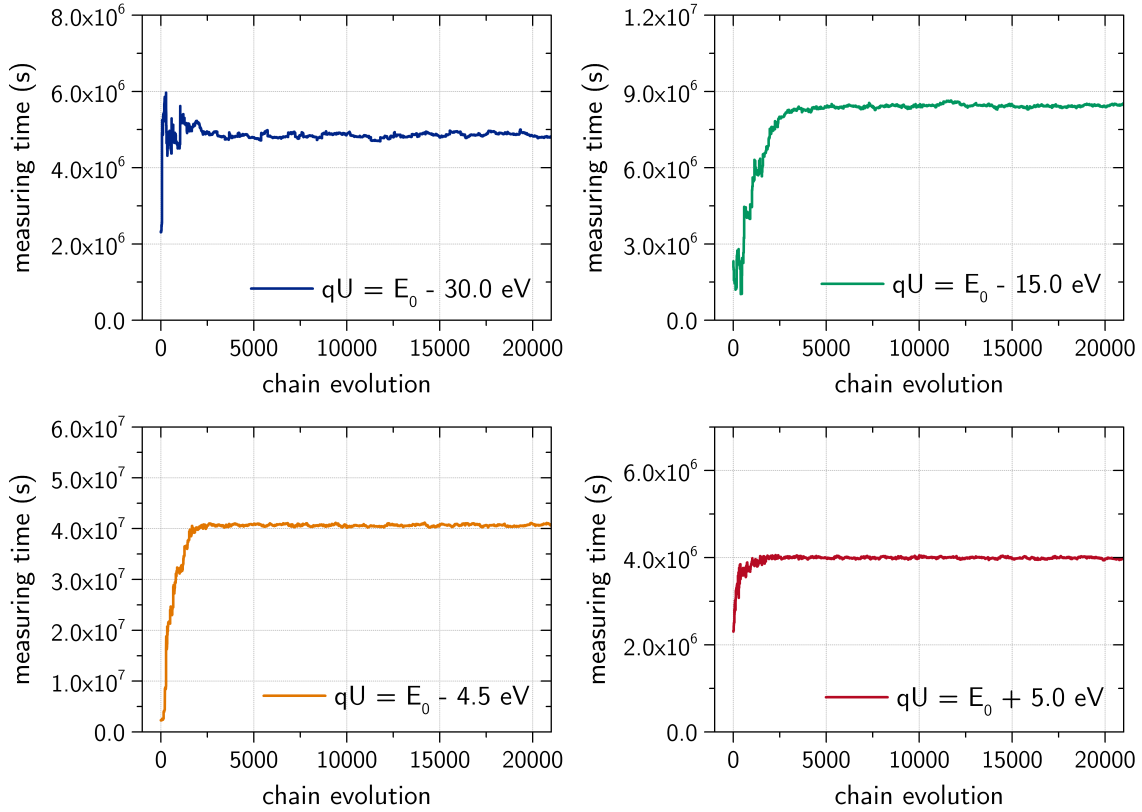


**Figure 6.16:** Evolution of the Markov Chain Monte Carlo in four bins of the measuring time distribution. The leftmost energy bin  $qU = E_0 - 30\text{ eV}$  and the bin most sensitive to a mass-related spectrum distortion  $qU = E_0 - 4.5\text{ eV}$  exhibit the fastest convergence towards a sharp minimum.

MCMC using the described transition kernel, has shown the fastest convergence and best mixing behavior so far. A stationary distribution around the optimum of the objective function is usually reached after a few hundred MCMC steps, as illustrated by figure 6.16.

#### 6.4.4 Results

The optimized MTDs, which will be discussed in the following, were extracted from MCMC simulations with at least 100 000 evolution steps. After discarding the first 10 000 samples from the burn-in phase, a 5 % fraction of the remaining samples is selected, which are closest to the optimum of the objective function (in other words produce the best  $m_\nu$  sensitivity). The selected samples are averaged to smoothen out statistical fluctuations of the MC simulation. An additional correction ensures a minimum measuring time of at least 3 days per retarding potential, which is about 3 % of the total effective measuring time of 3 years.

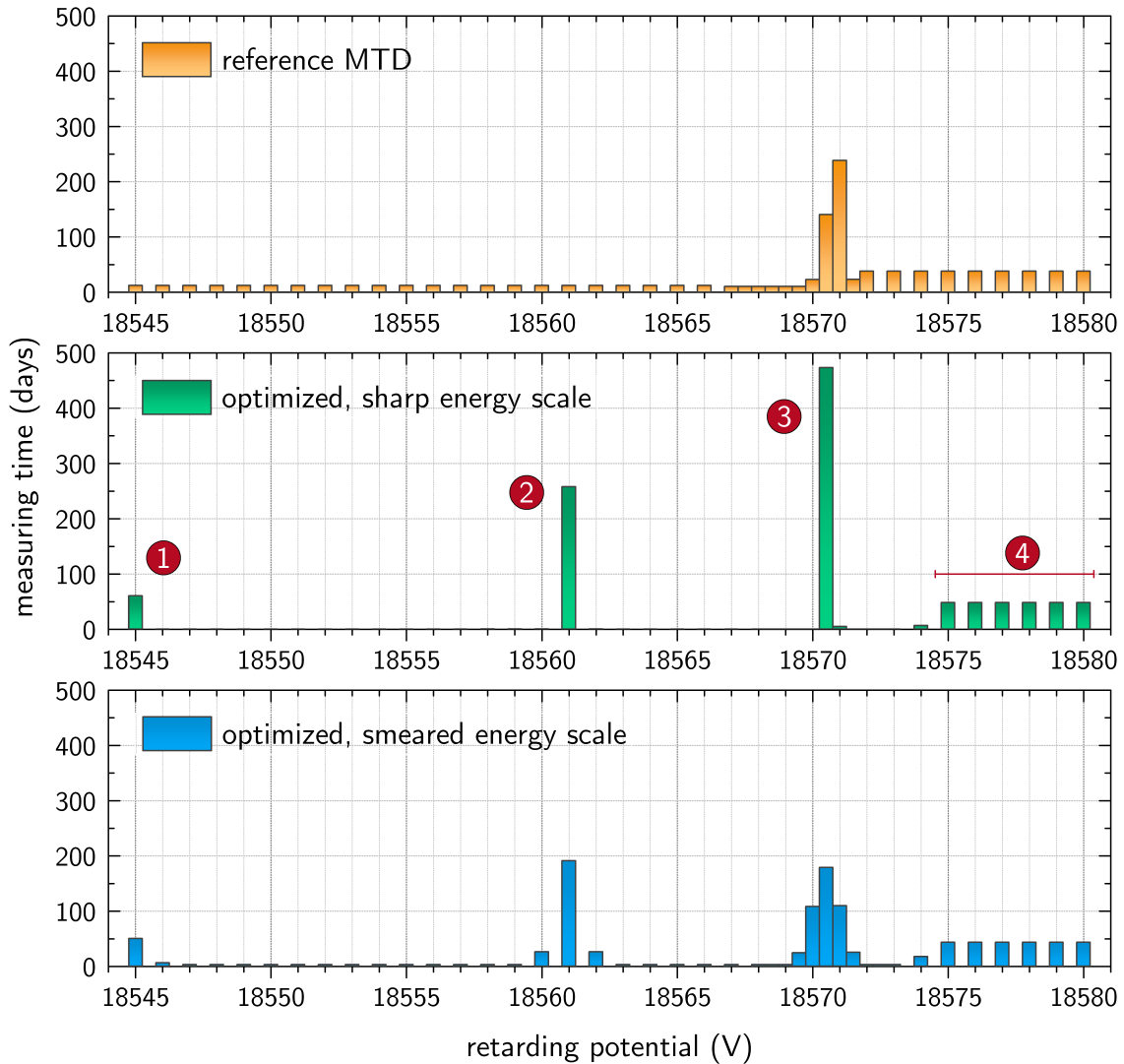


**Figure 6.17:** Comparison of MTDs with 41 bins in a 10 mcps background scenario with tritium endpoint  $E_0 = 18575$  eV.

**a** (top): Reference distribution from the design report.

**b** (middle): Optimized MTD, assuming that the retarding energy scale  $qU$  is precisely known with respect to the tritium endpoint  $E_0$ .

**c** (bottom): Optimized MTD, incorporating an uncertainty on  $(qU - E_0)$  of  $\sigma(E_0) = 0.5$  eV. For an explanation of the numbered features 1, 2, 3, 4, see the main text.

Using the recipe outlined above, the simulation generates the results shown in figure 6.17 (b). It is noticeable, that compared to the reference distribution (a), most of the available time is sharply distributed among four very specific areas, indicated by the numbered red markers. The optimization algorithm will precisely reproduce these four features in subsequent simulations in both their position and attributed time:

- ① The leftmost time bin ( $qU = E_0 - 30 \text{ eV}$ ) corresponds to the setting, where the highest signal count and thus the lowest relative error in the rate is expected. Therefore, from a statistical point of view, it is the most effective point in a parameter fit procedure, to determine the tritium endpoint  $E_0$  and the signal amplitude  $A_S$  of the  $\beta$ -decay spectrum.  
However, one important factor hasn't been quantified and incorporated so far: Certain systematics, especially energy losses of signal electrons in the source, will produce a larger uncertainty on the spectrum shape, the farther away from the endpoint the spectrum energy is analyzed (also see section 5.5.4).
- ② The second feature ( $qU = E_0 - 14 \text{ eV}$ ) is required to disentangle the two parameters  $E_0$  and  $A_S$ . If the optimization algorithm is modified to treat either one of them as a fixed parameter during the fit procedure, this feature vanishes completely. The reference time distribution does not emphasize a particular bin in this region, but evenly distributes the measuring time over a broader range of 20 eV.
- ③ As to be expected, most of the measuring time is attributed to the region closely below the endpoint, where a non-zero neutrino mass causes the most prominent shape deformation of the spectrum. The optimizer accounts about 195 days (17.8 %) to a single retarding energy of  $qU = E_0 - 4.5 \text{ eV}$ .
- ④ Time attributed to the energy interval above the endpoint region is used to determine the average background rate precisely. The noticeable difference compared to the reference distribution is, that the new optimizer does not allocate any significant time in the 3 eV interval directly below  $E_0$ . There the event rate is still dominated by background, but contains a small fraction of signal electrons, which would 'pollute' a pure background measurement.

### Uncertainty on the Endpoint Energy Scale

The distribution shown in 6.17 (b) stands out with sharp and emphasized bins. At first, this might appear counter intuitive, but can be explained. The optimization scheme outlined above implicitly assumes, that the position of the tritium endpoint  $E_0$  is a priori known precisely, and that the scale of the retarding energy  $qU$  can be chosen accordingly. With the objective of minimizing the statistical uncertainties involved in the KATRIN four parameter fit, the MTD optimizer now allocates as much individual time  $t_i$  to as few retarding potential settings  $i(qU)$  as possible. Accordingly, at least four distinct bins or regions in the MTD are needed to allow a spectrum shape analysis with four free fit parameters ( $m_\nu^2, E_0, A_S, R_{\text{bg}}$ ).

Currently, the best value for  $E_0$  is derived from Penning trap measurements of gaseous  $T_2$  and  ${}^3\text{HeT}$  molecules [Nag06]. With a mass difference  $\Delta M({}^3\text{He}, T)$ , measured by cyclotron resonance, the endpoint energy of molecular tritium can be calculated [Ott08]:

$$E_0(T_2) = (18\,571.8 \pm 1.2) \text{ eV} \quad (6.24)$$

KATRIN is expected to improve the measurement of  $E_0$  up to  $\pm 2$  meV after 3 years measuring time and  $\pm 20$  meV after 1 month (table 6.6). Nevertheless, a certain choice on the retarding voltage scale ( $qU - E_0$ ) has to be made, when starting the first neutrino mass measurements. To take into account the prior uncertainty on the energy scale and alleviate any error due to the choice of binning, a Gaussian smearing with  $\sigma(qU) = 0.5$  eV is applied to the calculated measuring time distributions. Together with the requirement to have at least 3 days of measuring time per bin, this results in a broader distribution, pictured in figure 6.17 (c).

Using these new MTDs in the ensemble method outlined in section 6.1.6, the statistical uncertainties on  $m_\nu^2$  can be recalculated in order to benchmark the performance of the optimized MTDs. Table 6.3 summarizes the results for the nominal background rate of  $R_{\text{bg}} = 10$  mcps.

MTD	$\sigma(m_\nu^2)$	improv.	$\sigma(E_0)$
x) flat time distribution	0.024 24 eV <sup>2</sup>		0.002 31 eV
a) reference configuration, design report	0.016 46 eV <sup>2</sup>	32.1 %	0.002 52 eV
b) optimized with precise energy scale	0.014 15 eV <sup>2</sup>	41.6 %	0.001 91 eV
c) optimized with smeared energy scale	0.014 90 eV <sup>2</sup>	38.5 %	0.001 92 eV

**Table 6.3:** Statistical uncertainties on  $m_\nu^2$  and  $E_0$  (68.3 % C.L.), calculated with the corresponding MTDs from figure 6.17. The background rate is  $R_{\text{bg}} = 10$  mcps. Relative improvements are stated with respect to a flat time distribution.

### Energy Dependent Systematics

The optimization scheme presented in this chapter produces mathematically consistent and reproducible results with respect to the statistical characteristics of a neutrino mass spectrum shape fit. However in its current form, the model does not incorporate systematic uncertainties on the observed spectrum rates.

Particularly systematic effects connected with the energy loss of  $\beta$  electrons (section 5.5.6) will play an important role, because they cause a larger systematic uncertainty on the spectrum rate, the farther away from the tritium endpoint  $E_0$  the spectrum is analyzed. This was already the reason for restricting the measuring interval to  $qU \geq E_0 - 30$  eV. Within that interval the energy dependency of such systematic uncertainties, which has not been quantified or modeled so far, might introduce a ‘penalty’ on retarding voltage settings

$t_i$  at the lower end of the scanned interval. This limitation to a purely statistical treatment of the problem has to be kept in mind, when looking at the result MTDs discussed in the following.

### Extended Retarding Energy Interval

In figure 6.18 two optimized MTDs are depicted, one for the reference energy interval  $[E_0 - 30 \text{ eV}, E_0 + 5 \text{ eV}]$  and one MTD for an extended interval of  $[E_0 - 35 \text{ eV}, E_0 + 5 \text{ eV}]$ . The measuring time allocated for the disentanglement of  $A_S$  and  $E_0$ , shifts to a lower retarding potential by  $\sim 2 \text{ eV}$ . As expected, the uncertainties on  $E_0$  and  $m_\nu^2$  improve due to a lower minimum retarding energy. A comparison of the statistical uncertainties for both energy intervals is given in table 6.4.

MTD	retarding energy	$\sigma(m_\nu^2)$	improv.	$\sigma(E_0)$
a) optim. for 35 eV interval	$[E_0 - 30 \text{ eV}, E_0 + 5 \text{ eV}]$	$0.01494 \text{ eV}^2$		$0.00191 \text{ eV}$
b) optim. for 40 eV interval	$[E_0 - 35 \text{ eV}, E_0 + 5 \text{ eV}]$	$0.01412 \text{ eV}^2$	5.5 %	$0.00172 \text{ eV}$

**Table 6.4:** Statistical uncertainties on  $m_\nu^2$  and  $E_0$  (68.3% C.L.) for different retarding energy intervals. The background rate is  $R_{\text{bg}} = 10 \text{ mcps}$ . See figure 6.18 for the applied MTDs.

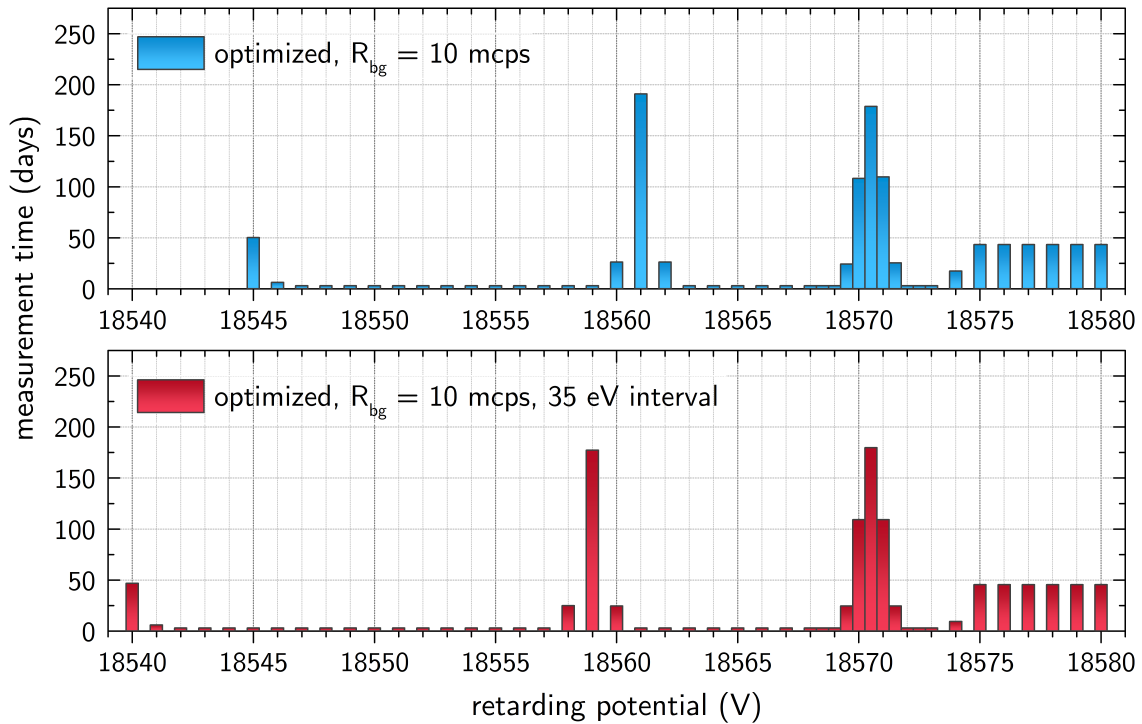


**Figure 6.18:** **a** (top): MTD optimized for the default energy interval  $[E_0 - 30 \text{ eV}, E_0 + 5 \text{ eV}]$ . **b** (bottom): MTD optimized for an extended energy interval  $[E_0 - 35 \text{ eV}, E_0 + 5 \text{ eV}]$ .

### Elevated Background Rates and Sterile Neutrinos

Optimized MTDs for the  $\beta$  spectra depicted in figure 6.15 (100 mcps background and sterile neutrino search) are shown in figure 6.19. As one would intuitively expect from looking at the relative differences of integrated  $\beta$  spectra, the focus of the optimized MTDs in the endpoint region follows the point of a maximum shape distortion of the spectrum, due to a non-zero neutrino mass.

The shift towards lower energies, reflecting the point of an optimal signal-to-noise ratio, becomes even more pronounced for higher background rates, as they were measured during the SDS-I commissioning phase (see section 7.1). Optimized MTDs for a 614 mcps and a 940 mcps background scenario are shown in figure 6.20. A comprehensive side-by-side comparison of the resulting improvements in sensitivities for the elevated background scenarios will be given in section 7.2.

The sensitivity on sterile neutrino mass eigenstates  $m_s^2$  depends on the mixing coefficient  $\sin^2 \theta_s = |U_{es}|^2$ , which will be explained in more detail in the following section 6.5. For a mixing of  $\sin^2 \theta_s = 0.036$ , a comparison of  $m_s^2$  sensitivities for the reference and optimized MTD is given in table 6.5.

MTD	$\sigma(m_s^2)$	improvement
a) reference configuration, design report	0.4749 eV <sup>2</sup>	
b) optimized for eV sterile neutrino masses	0.4268 eV <sup>2</sup>	10.1 %

**Table 6.5:** Statistical uncertainties for light sterile neutrino masses  $m_s^2$  (68.3% C.L.) with a mixing coefficient of  $\sin^2 \theta_s = 0.036$ . The background rate is  $R_{bg} = 10$  mcps. Active neutrino masses are assumed to be negligibly small with  $\sum m_i = 0$ .

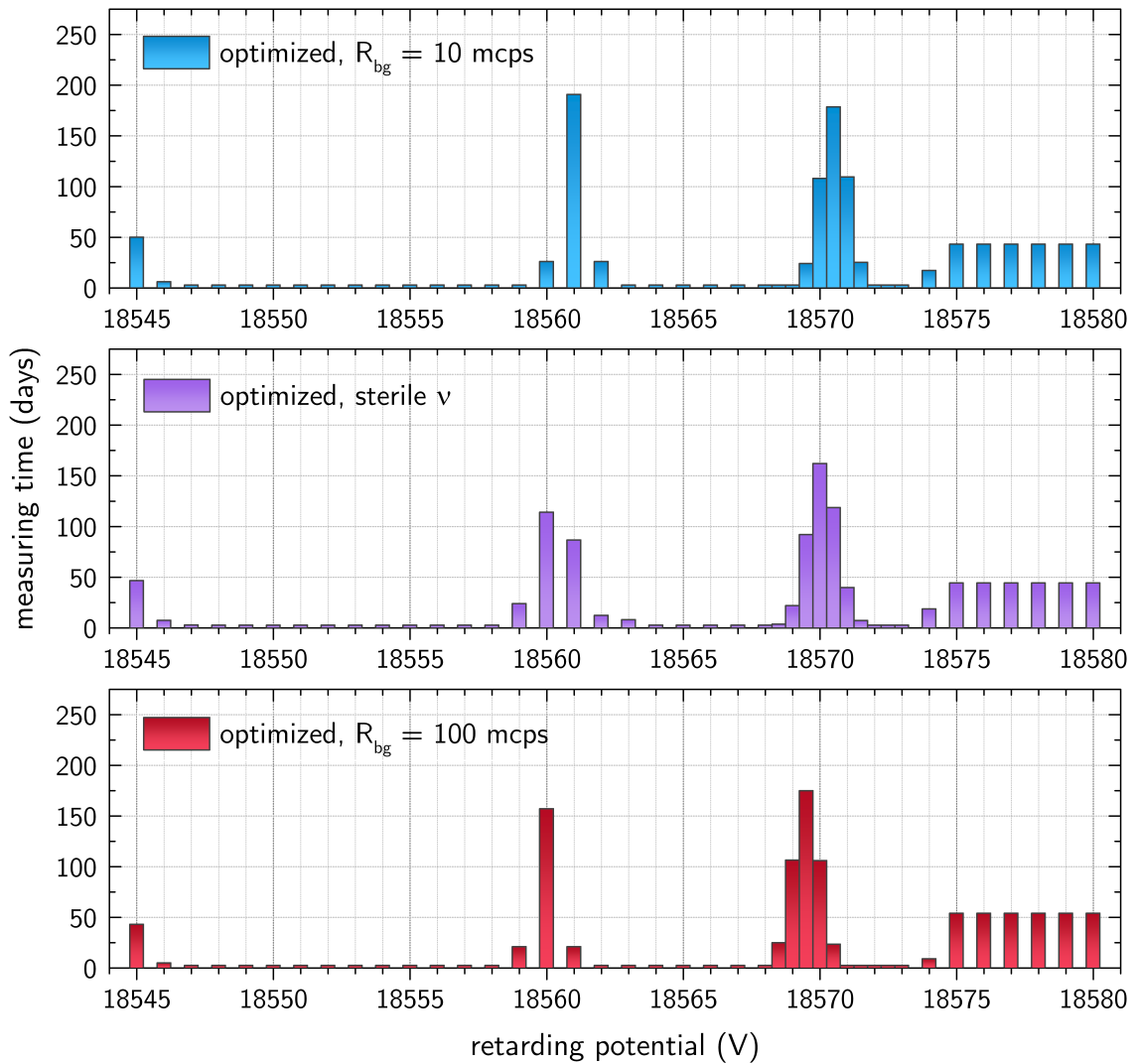


**Figure 6.19:** **a** (top): MTD for active neutrino search at  $R_{bg} = 10$  mcps.  
**b** (middle): MTD for sterile neutrino search (small masses) at  $R_{bg} = 10$  mcps.  
**c** (bottom): MTD for active neutrino search at  $R_{bg} = 100$  mcps.

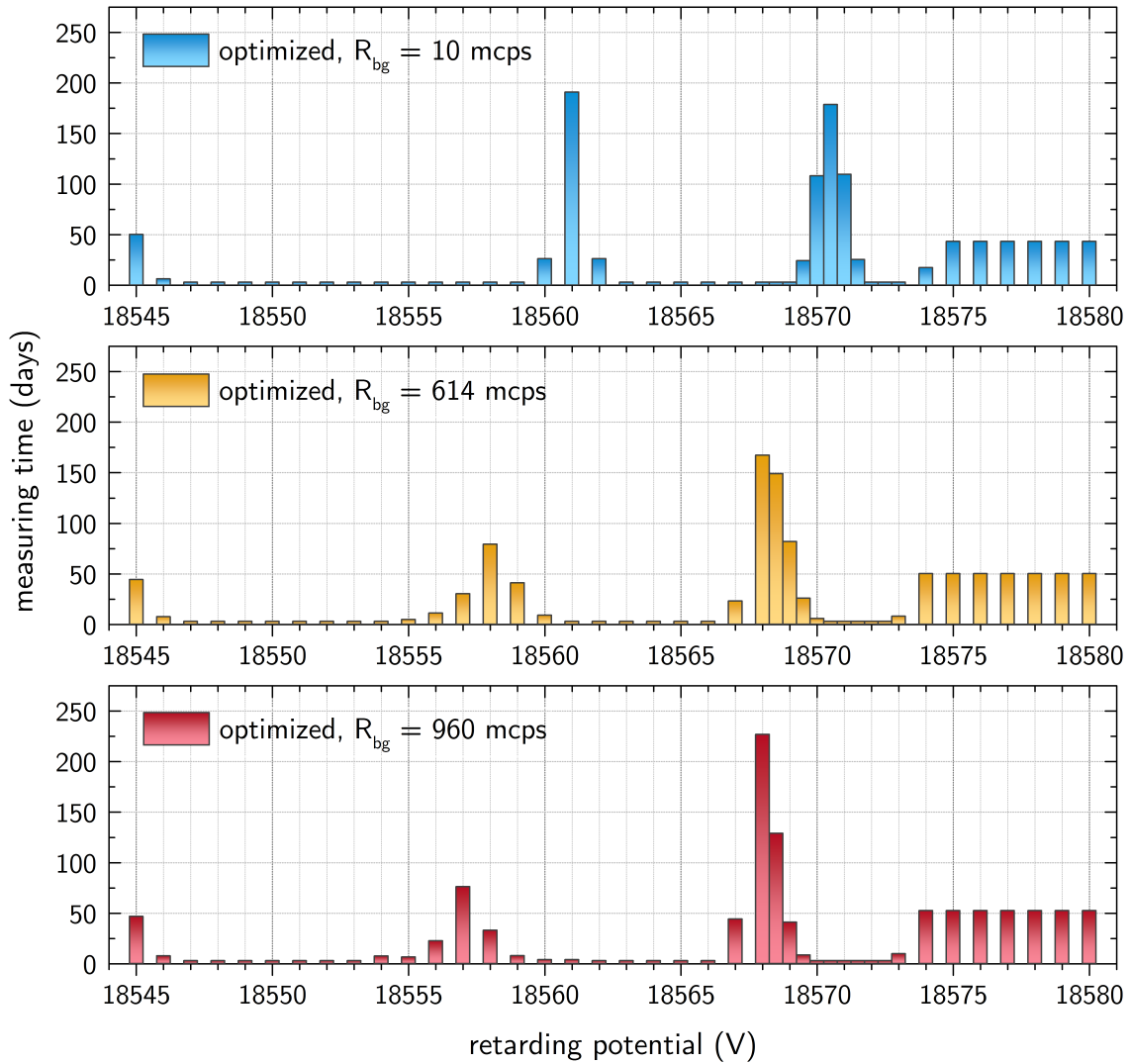


**Figure 6.20:** **a** (top): MTD for cosmic background with  $R_{bg} = 10$  mcps.  
**b** (middle): MTD for cosmic background with  $R_{bg} = 614$  mcps.  
**c** (bottom): MTD for cosmic and radon-induced background with  $R_{bg} = 960$  mcps.

### 6.4.5 Outlook

The objective of computing an MTD, which yields the smallest statistical uncertainty on  $m_\nu^2$  during a spectrum shape analysis, was achieved with the help of a mathematical description, thereby reducing the problem to a (high-dimensional) function minimization. This method produces a very pronounced result with most measuring time allocated to only a few of the available retarding voltage settings. For a realistic measurement plan, it will be advisable to account enough measuring time for those intervals of the spectrum, that are not of direct use for the neutrino mass extraction. A solid and sufficiently complete scan of the spectrum is desirable to exclude unexpected anomalies or systematic effects, especially in the very beginning of the data-taking phase.

The optimization method presented in this thesis cannot yet be claimed to hold the final answer to a well-balanced measurement strategy. But it provides the algorithmic basis and the required statistical tools to generate an optimal measurement time distribution for a correctly formulated problem. For the first month of data-taking one might for instance use a broader time distribution as suggested in figure 6.21, and later switch to a more focused strategy, when the actual position of the tritium endpoint with respect to the retarding energy is sufficiently determined. The statistical uncertainties on  $m_\nu^2$  and  $E_0$  for the optimized one month MTD are listed in table 6.6.

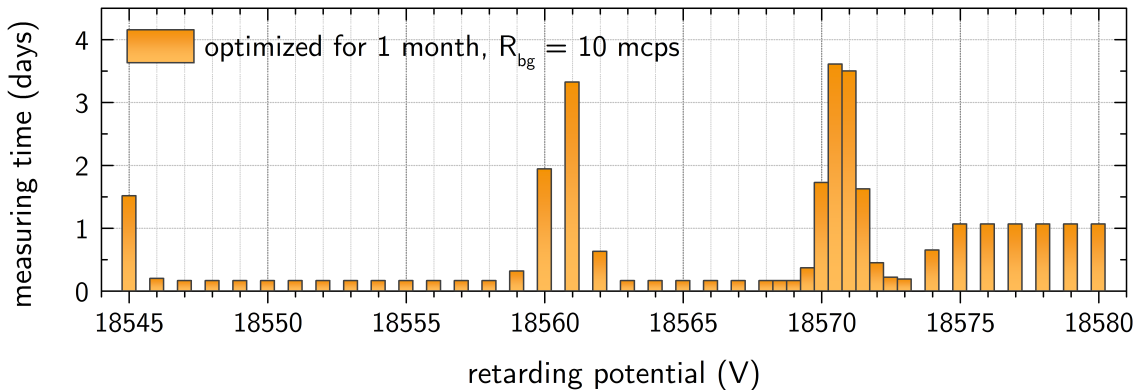


**Figure 6.21:** Suggested MTD for the first month of data-taking. The minimum measuring time per setting is 6 hours ( $\sim 1\%$ ). An uncertainty on the tritium endpoint of  $\sigma_{E_0} = 1$  eV is accounted for.

MTD	$\sigma(m_\nu^2)$	improv.	$\sigma(E_0)$
a) reference configuration, design report	$0.1004 \text{ eV}^2$		$0.0153 \text{ eV}^2$
b) broad scanning strategy, optimized for 1 month	$0.0947 \text{ eV}^2$	5.7%	$0.0126 \text{ eV}^2$

**Table 6.6:** Statistical uncertainties on  $m_\nu^2$  and  $E_0$  (68.3% C.L.), calculated for 1 month (31 days) of total measuring time. The background rate is  $R_{\text{bg}} = 10$  mcps.

### 6.4.6 From Time Distribution to Measuring Strategy

Extensions of the optimization tool are already being planned and prepared. The detailed modeling of energy-dependent systematic effects is only one aspect. Currently, the parameter space to be optimized is restricted to the measuring times  $t_i$  accounted for a retarding voltage setting  $qU(i)$ . But in principle the parameter space can be extended by any other experimental configuration parameter, also such with non-trivial correlations.

The focal plane detector for instance can be tuned to operate at a higher detection efficiency at the cost of an increased intrinsic background. Finding the right compromise for each region of the  $\beta$  spectrum with regard to the neutrino mass analysis is an open problem, which should be addressed in a combined optimization strategy.

Another question is about how to divide the overall measuring time at one setting into reasonable operational runs and in what order to scan different points in the energy spectrum. Calibration and monitoring procedures, as well as active background removal methods will prove more or less efficient, depending on how they are scheduled in between measuring intervals. Long-term drifts of key parameters, such as the HV retarding energy and fluctuations of the background rates, strongly suggest the spectrum to be scanned randomly rather than in an ascending / descending order. A detailed study of an optimal scanning strategy is currently being prepared, based on the statistical methods and the code framework presented in this work.

## 6.5 Sterile Neutrino Sensitivity

In section 1.5 it was pointed out that recent experimental observations have hinted towards the existence of a fourth sterile neutrino. As illustrated in section 5.6 of this thesis, the admixture of an additional heavy neutrino state  $m_s$  to the electron antineutrino  $\bar{\nu}_e$  in the eV range produces a kink in the electron  $\beta$ -decay energy spectrum at around  $E_0 - m_s$ .

The KATRIN likelihood can easily be extended to incorporate such a scenario, by adding two additional fit parameters: A sterile neutrino mass  $m_s^2$  and the mixing coefficient  $\sin^2 \theta_s = |U_{es}|^2$ .

$$L(m_\nu^2, E_0, A_S, R_{bg} | \mathbf{N}) \longrightarrow L_s(m_\nu^2, E_0, A_S, R_{bg}, m_s^2, \sin^2 \theta_s | \mathbf{N})$$

However, doing so would add a certain degree of degeneracy to the likelihood:

- For  $\sin^2 \theta_s = 0.5$  and data  $\mathbf{N}$  implying no sterile neutrino, the two mass parameters can be chosen freely, as long as they add up to a constant sum.
- For  $\sin^2 \theta_s \neq 0.5$  and data  $\mathbf{N}$  implying the existence of a sterile neutrino, the likelihood will show two identical maxima for each mass term.

Instead it seems reasonable to express the sterile neutrino as a mass splitting term  $\Delta m_s^2$ , relative to the active neutrino mass, with  $\Delta m_s > 0$  eV:

$$L_s(m_\nu^2, E_0, A_S, R_{bg}, \Delta m_s^2, \sin^2 \theta_s | \mathbf{N}) .$$

In this picture, the definition of nuisance parameters changes. If our goal is to study the sensitivity on our parameter of interest, which is the sterile neutrino mass  $m_s^2$  for a fixed mixing coefficient  $\sin^2 \theta_s$ , then the effective active neutrino mass  $m_{\nu_e}^2$  can be treated as one of the other nuisance parameters.

### 6.5.1 Technical Challenges

With such a parameter configuration, a degeneracy in the mass parameters can still arise, when the mixing  $\sin^2 \theta_s$  becomes small. Classical minimizers, either simplex or functional algorithms, as provided by the MINUIT tool, struggle to find a reasonable minimum in  $-\log L_s$ , if not some of the parameters are fixed or artificially constrained. The same holds for profile likelihood analyses performed by MINOS. In a sterile neutrino analysis, where the active mass is treated as a free nuisance parameter, MINOS can demand well up to 10 000 function evaluations, if it succeeds at all.

MCMCs explore the parameter space more robustly and converge to a target distribution in most cases (figure 6.22a). The sampled marginalized probability distributions for the mixing coefficient and the two involved masses can be inspected for hints towards the existence of a sterile neutrino (figure 6.22b).

### 6.5.2 Sensitivity Contours

Using the profile likelihood method, the likelihood ratio between the hypothesis of a sterile neutrino (with given mass  $m_s$  and mixing coefficient  $\sin^2 \theta_s$ ) and the null hypothesis of no sterile neutrino are calculated. Repeating the calculation for a grid of  $m_s$  and  $\sin^2 \theta_s$  values, sensitivity contour plots can be constructed. In figure 6.23 exclusion curves for a sterile mass contribution to the electron neutrino measured by KATRIN are shown, in one case using the reference MTD from the design report, in the other case using a slightly adapted, optimized MTD for small sterile masses (figure 6.19b).

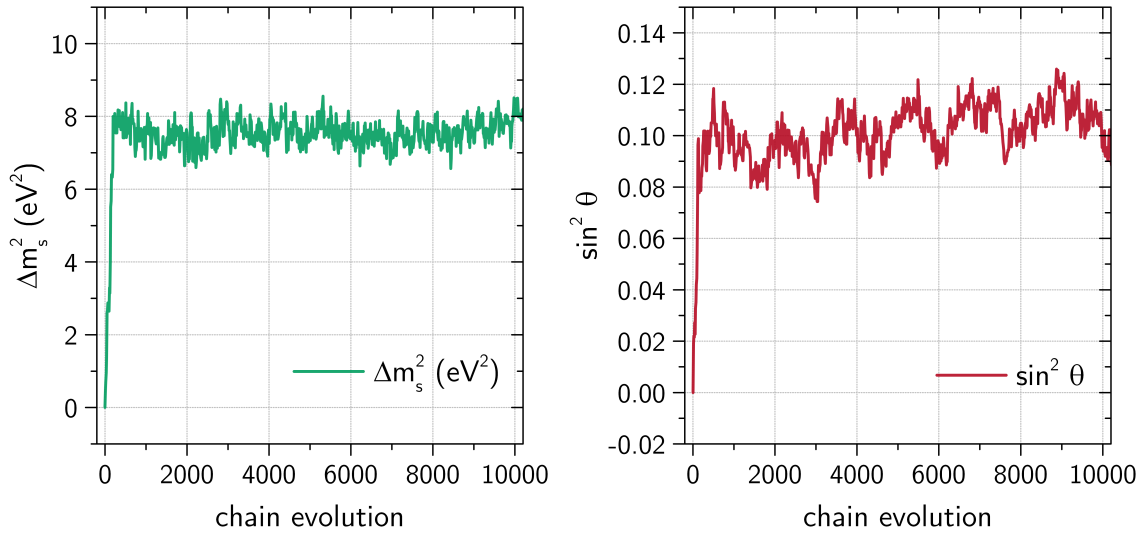
### 6.5.3 Resolving the Reactor Antineutrino Anomaly

A combined analysis of reactor data, gallium solar neutrino calibration experiments and MiniBooNE data, performed by Mention et al. [Men11], has favored a 3+1 mixing hypothesis for certain regions in the  $\Delta m_s^2$  and  $\sin^2 2\theta_s$  plane (also compare figure 1.11 in section 1.5). The best-fit values of this analysis are

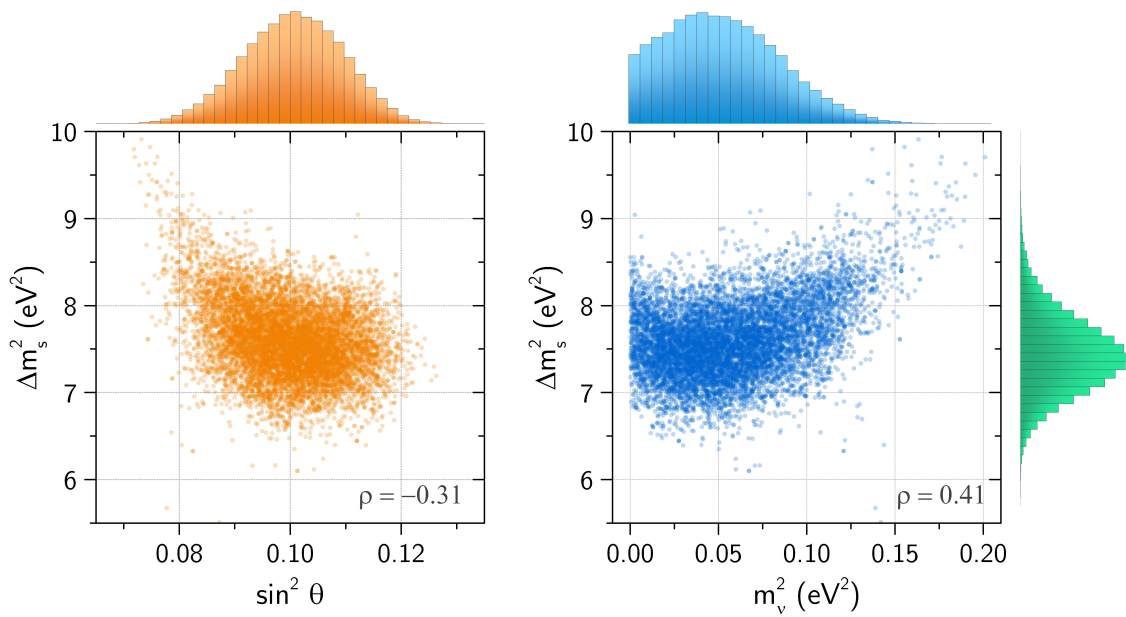
$$\Delta m_s^2 > 1.5 \text{ eV}^2 \quad \text{and} \quad \sin^2 2\theta_s = 0.14 \pm 0.08 \text{ (95 \% C.L.)} . \quad (6.25)$$

The oscillation parameter  $\sin^2 2\theta_s = 0.14$  corresponds to a mixing matrix coefficient of

$$|U_{es}|^2 = \sin^2 \theta_s = 0.036 . \quad (6.26)$$

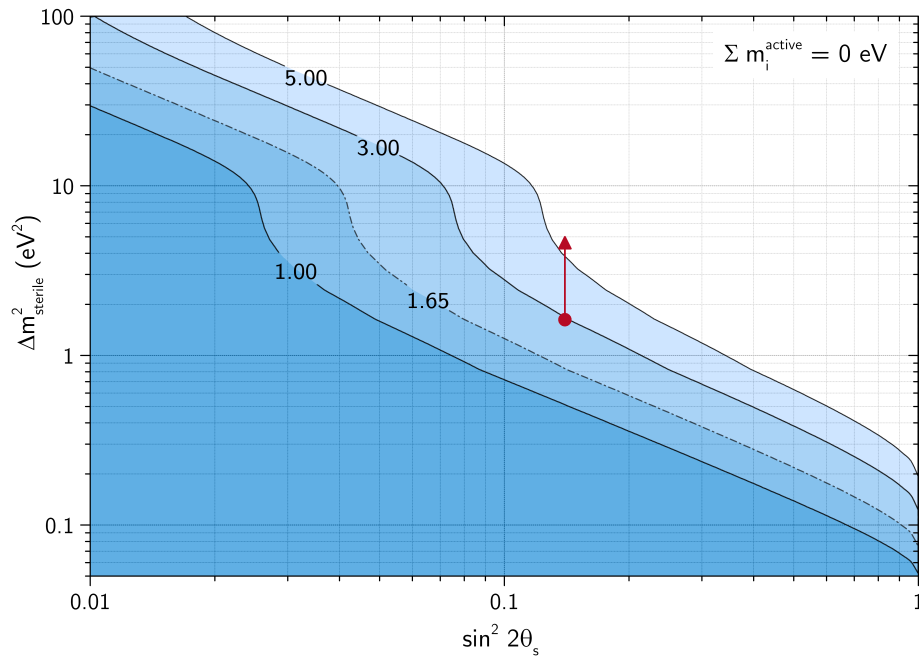


(a) MCMC evolution of the squared mass difference  $\Delta m_s^2$  between active and sterile neutrino.

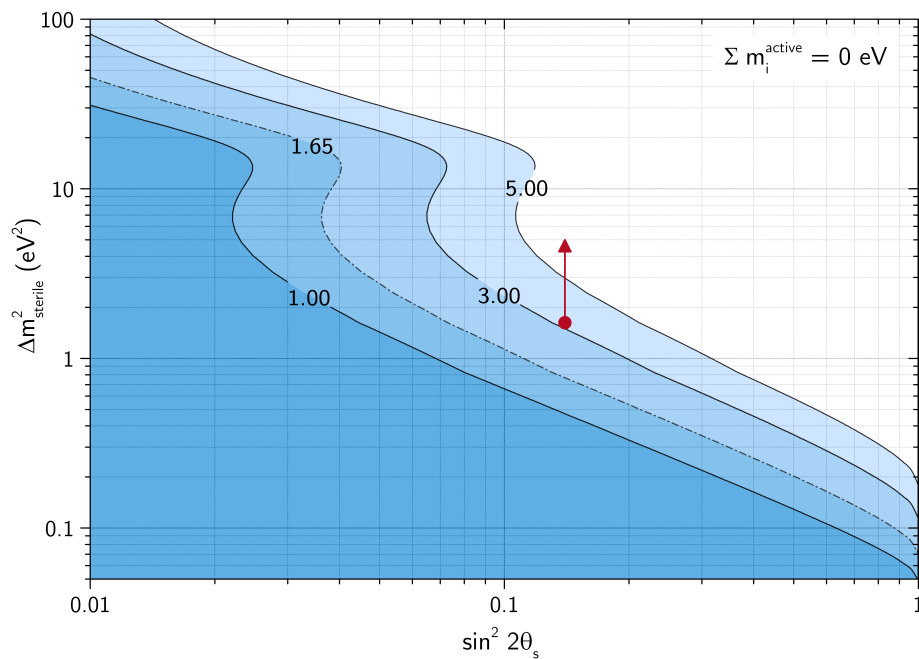


(b) Scatter plots and marginalized probability distributions of the squared mass difference  $\Delta m_s^2$ , the mixing coefficient  $\sin^2 \theta_s$  and the active neutrino mass  $m_\nu^2$ . Correlation coefficients are denoted by  $\rho$ .

**Figure 6.22:** MCMC analysis of a 1+1 sterile neutrino mixing scenario. The underlying toy experiment was generated with  $m_\nu^2 = 0.04 \text{ eV}^2$  and  $m_s = 9.0 \text{ eV}^2$ , which corresponds to a squared mass difference of  $\Delta m_s^2 = 7.84 \text{ eV}^2$ . The mixing coefficient is  $\sin^2 \theta_s = 0.1$ .



(a) Reference measuring time distribution for an active neutrino mass.



(b) Optimized measuring time distribution for sterile neutrino masses  $< 3$  eV.

**Figure 6.23:** Sensitivity contours for the detection of a sterile neutrino by KATRIN. The solid lines show the confidence levels in Gaussian standard deviations  $\sigma$ . The dashed line indicates the 90% ( $1.645\sigma$ ) confidence level contour. The sum of active neutrino masses is assumed to be zero. A systematic uncertainty on the neutrino mass of 130 meV has been added in quadrature. The parameter range favored by a combined analysis of reactor antineutrino anomaly data [Men11] is indicated by the vertical red line.

For such a mixing and under the assumption of comparatively small active neutrino masses  $m_1 \sim m_2 \sim m_3 \ll m_s$ , the methods presented in this thesis yield a sterile neutrino mass sensitivity for KATRIN of

$$\Delta m_s^2 = 0.753 \text{ eV}^2 \text{ (90 \% C.L.)} . \quad (6.27)$$

Based on these results, the KATRIN experiment will have a promising chance of probing the reactor antineutrino anomaly in a direct kinematic measurement.

## 6.6 Correlated Systematics

One of the most severe challenges for kinematic neutrino mass experiments are unaccounted or not precisely determined systematics. High voltage fluctuations on the MAC-E filter retarding potential for instance, are known to cause a bias on the estimated  $m_\nu^2$  towards small or negative values, without affecting the goodness-of-fit statistic [Ott08]. Similar effects can occur for any systematic parameter, which shows a strong correlation with  $m_\nu^2$ , or which is able to mimic a similar shape deformation of the  $\beta$ -decay spectrum.

### 6.6.1 Ensemble Method

The simplest approach to the problem is ensemble testing: A larger set of toy measurements is simulated with some predefined 'true' value of a systematic parameter. When fitting  $m_\nu^2$ , the systematic is deliberately assumed to have a differing 'wrong' value. The impact of the investigated systematic on the measured neutrino mass will then show up as a shift of the distribution of best-fit  $m_\nu^2$  estimates.

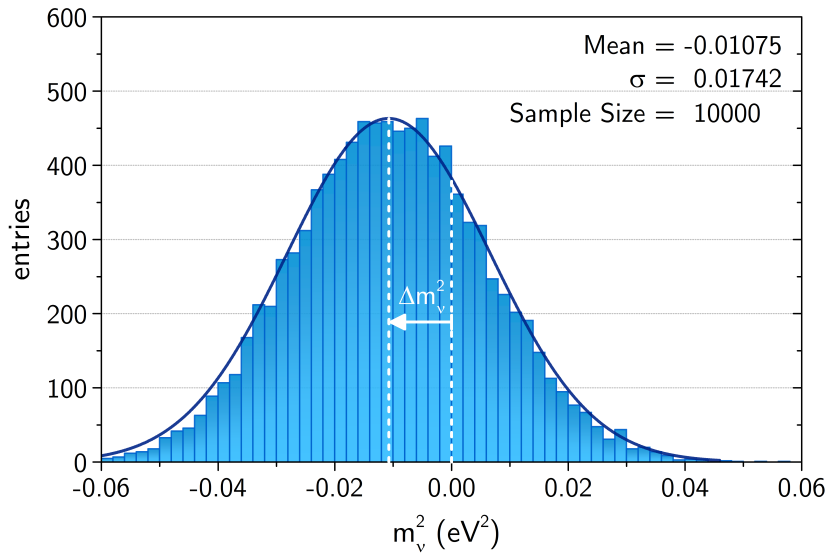


**Figure 6.24:** Distribution of best-fit estimates of  $m_\nu^2$  from an ensemble test with simulated  $m_\nu^2 = 0.0 \text{ eV}^2$ . The toy experiments were generated with a retarding voltage fluctuation of  $A_{\text{hv}} = 100 \text{ mV}$ . The distribution of measured  $m_\nu^2$  is shifted by  $\approx -A_{\text{hv}}$ .

An example for a sinusoidal retarding voltage fluctuation is shown in figure 6.24 (also see section 5.5.2). With an amplitude  $A_{\text{hv}}$  and a cycle duration  $T$  considerably smaller than the measuring time, the time-dependent retarding energy is described as

$$qU(t) = qU + A_{\text{hv}} \sin(t/T) . \quad (6.28)$$

The observed shift in the distribution of estimated squared neutrino masses is in very good agreement with the value expected from analytical approximations [Wie12]:

$$\Delta m_{\nu}^2 \approx -A_{\text{hv}} \quad (6.29)$$

### 6.6.2 Additional Free Fit Parameter

In a different approach, it can be informative to study the effect of a systematic, when it is treated as a free, unknown nuisance parameter in the likelihood or chi-square function, similar to the signal amplitude  $A_{\text{S}}$  or tritium endpoint  $E_0$ . In some cases, the fit algorithm might be able to estimate the additional parameter correctly from the spectrum shape. Then the statistical uncertainty on the additional nuisance parameter propagates and consequently increases the uncertainty on  $m_{\nu}^2$ . An exemplary calculation is given table 6.7, where the inelastic scattering cross section  $\sigma_{\text{inel}}$  of the signal electrons (section 5.5.6) is treated as a free parameter.

This method becomes ineffective however, when a strong correlation between the new nuisance parameter and  $m_{\nu}^2$  cannot be broken by the fitting algorithm. This is the case for a retarding voltage fluctuation  $A_{\text{hv}}$ , for instance. When a classical minimizer like MINUIT attempts to analyze the chi-square function, it can arbitrarily compensate between  $m_{\nu}^2$  and  $A_{\text{hv}}$ . The minimizer will fail in its objective to find a well-defined minimum or to calculate other statistical quantities like the correlation factors.

stat. uncertainties	4 fit parameters	5 fit parameters
$m_{\nu}^2$	0.014 94 eV <sup>2</sup>	0.023 47 eV <sup>2</sup>
$E_0$	0.001 92 eV	0.005 10 eV
$A_{\text{S}}$	$2.624 \cdot 10^{-4}$	$9.747 \cdot 10^{-4}$
$R_{\text{bg}}$	$1.880 \cdot 10^{-5}$ cps	$1.887 \cdot 10^{-5}$ cps
$\sigma_{\text{inel}}$		$1.9498 \cdot 10^{-20}$ cm <sup>-2</sup>

**Table 6.7:** Statistical uncertainties on the standard four fit parameters and the electron-tritium inelastic scattering cross-section  $\sigma_{\text{inel}} = 3.4 \cdot 10^{-18}$  cm<sup>-2</sup>, when treated as an additional free fit parameter. The values were calculated with MINOS (profile likelihood method), using an optimized measuring time distribution (figure 6.17c).

MCMCs on the other hand do not require to find one specific function optimum. A properly configured Markov Chain analysis will scan the more likely regions of the parameter space, explore the relation between the two correlated parameters and calculate a full correlation matrix. Figure 6.25 (left) shows a 2D scatter plot of  $m_\nu^2$  and  $A_{\text{hv}}$  samples from an MCMC analysis of the above mentioned voltage fluctuation scenario.

### 6.6.3 Pull Method

The knowledge about the error  $\sigma_\zeta$  of a systematic quantity  $\zeta$  can be incorporated into the likelihood and chi-square function using the so-called *pull* method. The systematic is treated as a variable fit parameter  $\zeta$ , while adding a penalty (pull) term to the likelihood, which effectively constrains the new fit parameter to a Gaussian distribution with standard deviation  $\sigma_\zeta$ .

With this extension the KATRIN chi-square term can then be written as follows:

$$\chi^2(m_\nu^2, E_0, A_S, R_{\text{bg}}, \zeta | \mathbf{N}) = \sum_{i(qU)} \left( \frac{N_i - N_i^{\text{theo}}(m_\nu^2, E_0, A_S, R_{\text{bg}})}{\sigma_i} \right)^2 + \left( \frac{\hat{\zeta} - \zeta}{\sigma_\zeta} \right)^2 \quad (6.30)$$

The best estimate on a systematic  $\hat{\zeta}$  might be obtained from a calibration measurement for instance. Again  $\sigma_\zeta$  is the assumed error on  $\zeta$ .

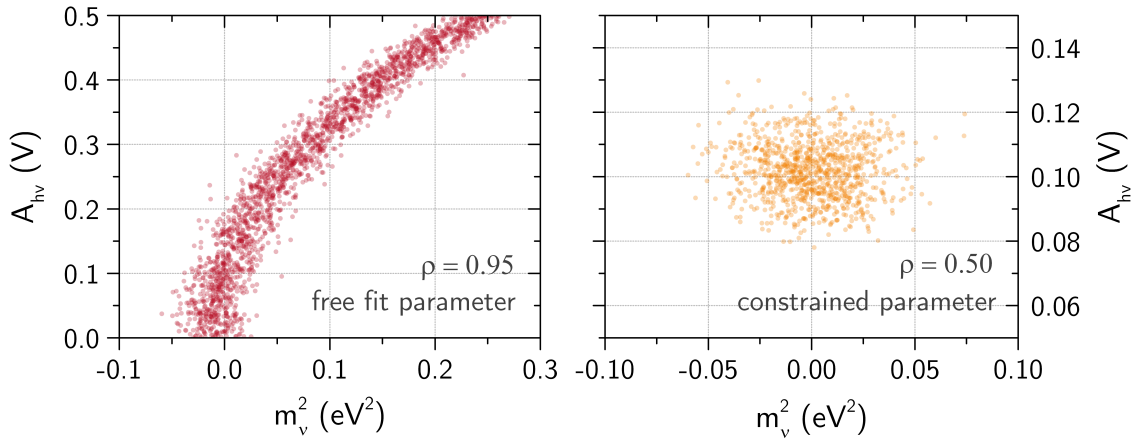


**Figure 6.25:** 2D scatter plots from MCMCs with a high voltage fluctuation  $A_{\text{hv}}$  as an additional fit parameter. The true value of  $A_{\text{hv}}$  (sinusoidal) is in both cases 100 mV and  $m_\nu^2 = 0$  meV. The prior on  $m_\nu^2$  is flat, so negative squared masses are allowed.

**Left:**  $A_{\text{hv}}$  is a free fit parameter, showing nearly full correlation with the squared neutrino mass  $m_\nu^2$ . The sampled parameter space forms a valley with constant chi-square at its bottom.

**Right:** The pull method is applied, constraining the fit parameter  $A_{\text{hv}}$  to a Gaussian with  $\sigma(A_{\text{hv}}) = 10$  meV.

stat. uncertainties	4 fit parameters	4 + 4 fit parameters
$m_\nu^2$	0.0152 eV <sup>2</sup>	0.0208 eV <sup>2</sup>
$E_0$	0.00234 eV	0.00401 eV
$A_S$	$3.039 \cdot 10^{-4}$	$7.278 \cdot 10^{-4}$
$R_{\text{bg}}$	$1.852 \cdot 10^{-5}$ cps	$1.985 \cdot 10^{-5}$ cps
$\varepsilon_T$		0.00992
$A_{\text{hv}}$		9.05 mV
$\sigma_{\text{inel}}$		$1.9360 \cdot 10^{-20}$ cm <sup>-2</sup>
$T$		0.0985 K

**Table 6.8:** Statistical uncertainties on the standard four fit parameters and four additional constrained parameters (pull method): tritium purity  $\varepsilon_T = 0.95 \pm 0.01$ , HV fluctuation  $A_{\text{hv}} = (100 \pm 10)$  mV, inelastic scattering cross-section  $\sigma_{\text{inel}} = (3.40 \pm 0.07) \cdot 10^{-18}$  cm<sup>-2</sup> and source temperature  $T = (30.0 \pm 0.1)$  K. The results were calculated from marginalized probability distributions, which were sampled by an MCMC simulation with flat priors.

Repeating the parameter inference and error estimation with this method, the systematic error can propagate and change the error intervals of the other fit parameters, depending on how these are correlated with each other. In figure 6.25 two MCMC simulations are compared, in one case with a high voltage fluctuation treated as a free fit parameter, in the other case with a constraint according to the pull method. Table 6.8 lists the results of another MCMC simulation, which incorporates uncertainties on four systematic parameters by extending the chi-square with the corresponding pull terms.

## Summary

In this chapter a selection of Frequentist and Bayesian statistical methods, implemented as part of the software module KaFit, were presented and evaluated for neutrino mass analyses. An MCMC framework was introduced, allowing for robust Bayesian inference of higher-dimensional problems, in particular  $\beta$ -decay parameter fitting involving strongly correlated systematics or sterile neutrino mixing.

With the help of these versatile MCMC algorithms, a new MC optimization technique was developed, which autonomously performs an adaption of the measuring time distribution to improve the statistical uncertainty on neutrino mass fit parameters, depending on background scenarios and involved systematics. Applying the statistical toolset to the case of sterile neutrino analysis, the discovery potential of an eV-scale sterile neutrino was investigated.

# CHAPTER 7

---

## Sensitivities Reevaluated

---

Applying the methods presented in preceding chapters, a reevaluation of KATRIN's neutrino mass sensitivity is performed below. Using a set of optimized measuring time distributions and considering the radial dependency of observed background electrons, some noticeable improvements can be achieved. In the following, the sensitivities are calculated for the expected nominal background rate of 10 mcps and compared to the rates observed with the preliminary KATRIN setup during the first SDS commissioning measurements [KAT14].

### 7.1 SDS Background Measurements

The overall background rate is an important parameter with strong impact on the statistical uncertainty of a neutrino mass measurement. Background electrons, reaching the detector in a similar energy window as the  $\beta$ -decay signal electrons, impair the signal-to-noise ratio and increase statistical fluctuations on the measured event rates.

A major source of background are secondary electrons ejected from the vessel walls by transiting cosmic ray muons. For a small fraction of these electrons, the magnetic and electrostatic shielding of the main spectrometer can be ineffective, allowing them to enter the sensitive part of the magnetic flux tube. There they generate background by an ionizing collision, with a low-energy electron being accelerated by the retarding potential and guided in the direction of the detector (section 5.9.1).

Another source of background are high-energy electrons, which are produced inside the magnetic flux tube by decays of radon atoms emanating from the main spectrometer vessel walls and the getter pumps. These high energetic particles can be stored in the magnetic bottle of the main spectrometer over several hours and repeatedly scatter off residual gas, producing secondaries, which can reach the detector in the energy region-of-interest (section 5.9.2). Radon-induced background exhibits larger variance in rate (Radon spikes) as compared to the Poissonian background produced by cosmic radiation.

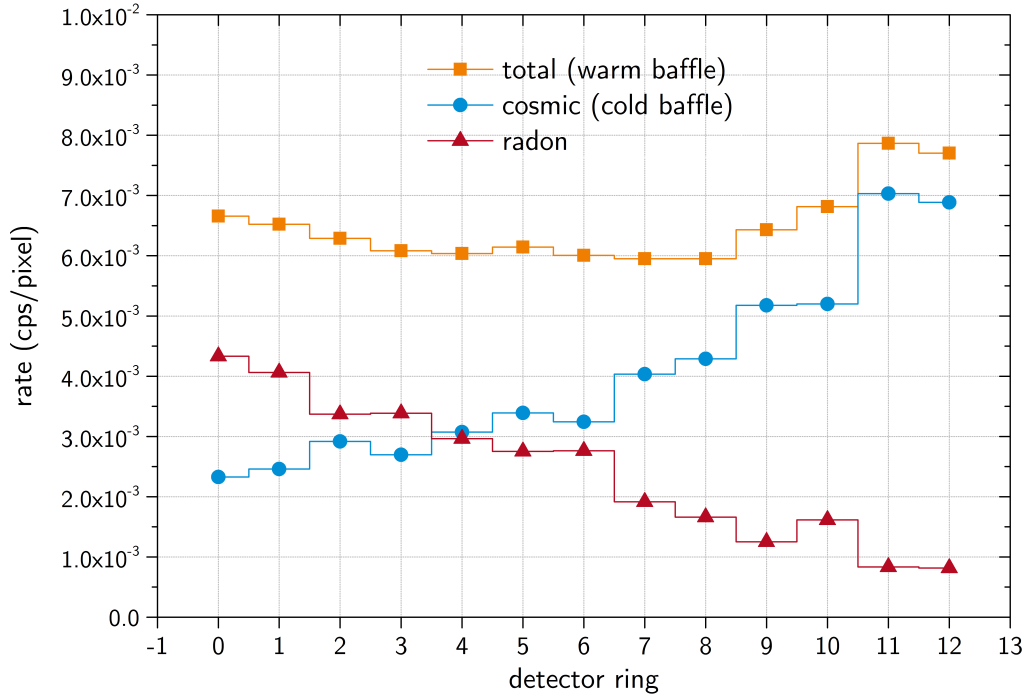


**Figure 7.1:** Background rates recorded during SDS-I commissioning and plotted for individual rings of the main detector. Index 0 = bullseye, 12 = outer ring.

The following calculations are based on long-term (at least 4 h) SDS commissioning measurements with a nominal 3.8 G field setup in the main spectrometer analyzing plane<sup>1</sup>. All rates are normalized to account for non-active and shadowed detector pixels. The analysis logic for these background measurements is implemented with the BEANS framework (section 4.4) and was kindly provided by Johannes Schwarz [Sch14].

With no radon suppression method active, an overall background rate of

$$R_{\text{bg}}^{\text{total}} = (960 \pm 4) \text{ mcps} \quad (7.1)$$

was measured in a 24 h run during SDS commissioning. Cooling down the getter pump baffles (see section 2.5.2) and thus preventing radon  $^{219}\text{Rn}$  from entering the spectrometer volume, and removing  $^{219}\text{Rn}$  and  $^{220}\text{Rn}$  emanating from the vessel walls, leads to a decrease of the background rate to

$$R_{\text{bg}}^{\text{cosmic}} = (614 \pm 7) \text{ mcps} , \quad (7.2)$$

<sup>1</sup> The magnetic field settings were the following: First pre-spectrometer magnet at 3.0 T, second pre-spectrometer magnet (before main-spectrometer) at 4.3 T, pinch magnet (after main-spectrometer) at 5.0 T, detector magnet at 3.5 T. Air coils are configured to create a nearly symmetric field configuration with 3.8 G in the analyzing plane.

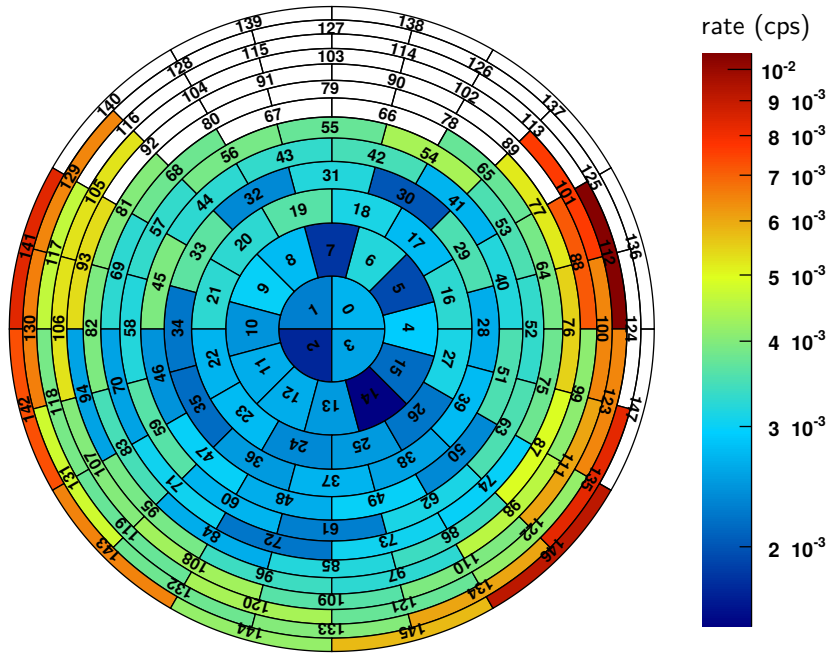


**Figure 7.2:** Pixel-view of accumulated detector events during a 12 h background measurement with active radon suppression (see main text). The total background rate amounts to 457 mcps. When correcting for the number of shadowed and non-active pixels (white), the rate normalizes to 614 mcps.

measured over a duration of 4 h. When assuming, that the remaining background is dominated by secondary electrons produced by cosmic rays<sup>1</sup> and that most of the radon induced background has been eliminated by the NEG pump port baffles, we obtain:

$$R_{\text{bg}}^{\text{radon}} = R_{\text{bg}}^{\text{total}} - R_{\text{bg}}^{\text{cosmic}} = (346 \pm 6) \text{ mcps} \quad (7.3)$$

All measured background rates are again summarized in table 7.1. In figure 7.1 the rates attributed to cosmic and radon-induced background mechanisms are compared for each ring of the segmented main detector. A pixel-view of the detector for the 4 h cold baffle measurement is shown in figure 7.2.

<sup>1</sup> The elevated background rate of 614 mcps due to cosmic secondaries is attributed to an electrical short circuit in the HV feedline of the main spectrometer electrode wire system. This leads to an impaired shielding against incident charged particles. With a (partial) repair of the electrode system successfully completed in advance of the next measurement phase, the overall background is expected to be further reduced to eventually meet the desired reference value of  $\sim 10$  mcps in 2015, in conjunction with active background removal methods.

configuration	total background rate	background type
inactive baffle	$(960 \pm 4)$ mcps	total
active baffle	$(614 \pm 7)$ mcps	cosmic secondaries
difference	$(346 \pm 6)$ mcps	radon induced

**Table 7.1:** Background rates measured during SDS-I commissioning.

### Sensitivity Calculation

Using the reference measuring time distribution (MTD) in the ensemble method outlined in section 6.1.6, a total of 10 000 KATRIN toy experiments was generated for five different background scenarios:  $R_{\text{bg}} = 10$  mcps,  $R_{\text{bg}} = 100$  mcps,  $R_{\text{bg}} = 614$  mcps (cosmic) and  $R_{\text{bg}} = 960$  mcps (radon).

From the standard deviation of best-fit  $m_{\nu}^2$  estimates, the statistical uncertainty  $\sigma(m_{\nu}^2)$  is determined for each scenario and summarized in column 1 of table 7.2a. The corresponding 90 % C.L. and  $5\sigma$  neutrino mass sensitivities are also listed in column 1 of tables 7.2b and 7.2c on the same page 169.

As to be expected, the neutrino mass sensitivity is diminished with increasing background rate.

### 7.2 Measuring Time Optimization

In order to perform a reasonable mass sensitivity evaluation with background rates significantly higher than the reference value of  $R_{\text{bg}} = 10$  mcps, an optimized measurement time distribution has to be applied. Using the Markov Chain based optimization method introduced in section 6.4, a set of adapted measurement time distributions has been calculated for different background scenarios.

The optimized time distributions yield better sensitivities, if reevaluated with the ensemble testing method. For  $R_{\text{bg}} = 10$  mcps the statistical uncertainty on the squared neutrino mass decreases to

$$\sigma_{\text{stat}}(m_{\nu}^2) = (0.0149 \pm 0.0001) \text{ eV}^2, \quad (7.4)$$

which is an improvement of 9.7%. As to be expected, the effect is even more significant for higher background levels.

The reevaluated statistical uncertainties for each background scenario are listed in column 2 of table 7.2a. For the corresponding total neutrino mass sensitivities, summarized in column 2 of table 7.2b and 7.2c, a systematic uncertainty of  $\sigma_{\text{sys}} = 0.017 \text{ eV}^2$  was added in quadrature. In some cases, where the systematic dominates the statistical uncertainty, the relative improvement turns out to be less prominent.

For the envisaged background rate of  $R_{\text{bg}} = 10$  mcps, the evolution of the neutrino mass sensitivity over the accumulated measuring time is shown in figure 7.3 on page 168. The curves illustrate the theoretical improvement in the neutrino mass sensitivity, when using an optimized measuring time distribution, presented in this thesis, over the reference or a flat distribution.

### 7.3 Background Radial Dependency

The SDS background measurements (see figures 7.1 and 7.2) show a clear dependency of the measured rates on the radial distance from the detector center. For cosmic background this seems plausible, since electrons ejected from the spectrometer tank wall are unlikely to advance to the center of the magnetic flux tube. This background characteristic can be incorporated into the parameter estimation, thanks to the radial segmentation of the focal plane detector.

The observed signal and background rates for each detector ring are then considered in a dedicated term of the likelihood or chi-square function

$$\chi^2(m_\nu^2, E_0, A_S, R_{\text{bg}} | \mathbf{N}) = \sum_{i(qU)} \sum_r \left( \frac{N_{i,r} - N_{i,r}^{\text{theo}}(m_\nu^2, E_0, A_S, R_{\text{bg}}^{\text{avg}})}{\sigma_{i,r}} \right)^2, \quad (7.5)$$

with  $r \in \{0, \dots, 12\}$  denoting the detector ring index. The fit parameter  $R_{\text{bg}}^{\text{avg}}$  is now used to proportionally rescale the previously determined background rate distribution across the detector rings.

Chi-square terms from detector rings with a lower background rate effectively contribute with a higher weight (lower uncertainty) and improve the resulting sensitivities, especially at higher mean background rates. For  $R_{\text{bg}} = 10$  mcps the statistical uncertainty on the squared neutrino mass is further decreased to

$$\sigma_{\text{stat}}(m_\nu^2) = (0.0142 \pm 0.0001) \text{ eV}^2, \quad (7.6)$$

which constitutes an additional relative improvement of 4.2%. Column 3 of tables 7.2a to 7.2c contains the updated sensitivity values from radial-dependent calculations for all of the presented background scenarios.

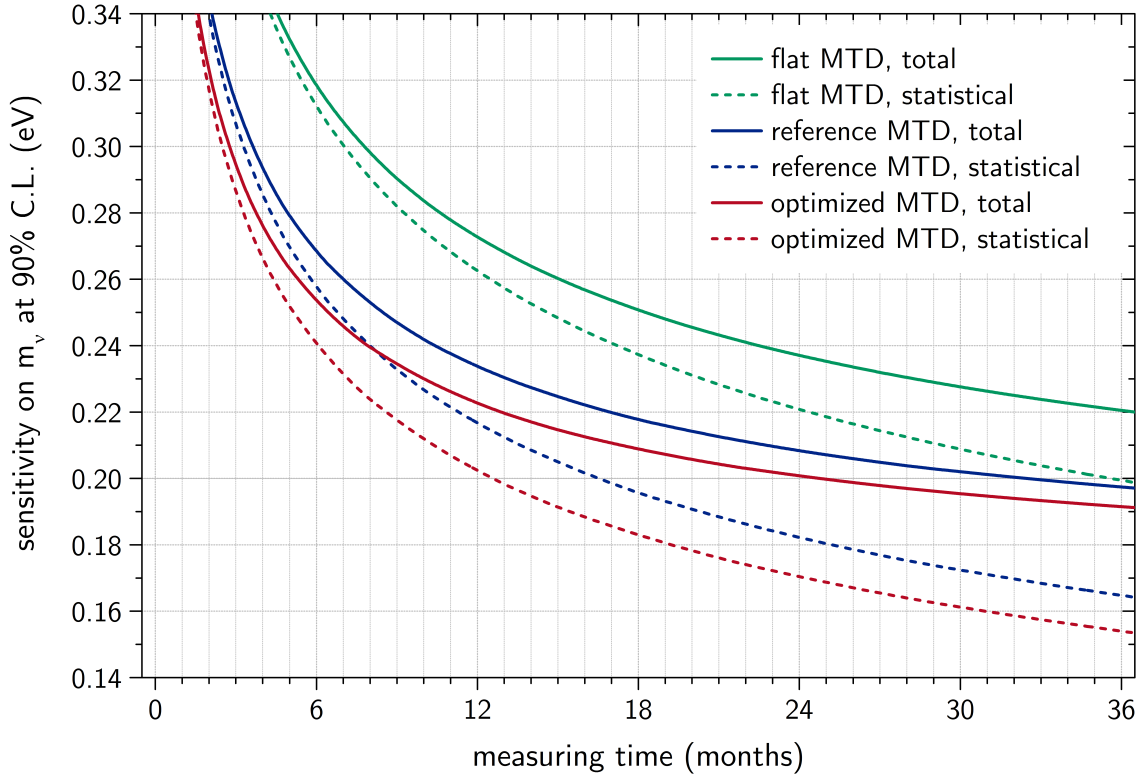


**Figure 7.3:** Evolution of  $m_{\nu_e}$  statistical (dashed line) and total (solid line) sensitivities at 90% C.L. over accumulated measuring time for three different MTDs. The total sensitivities incorporate a systematic uncertainty of  $\sigma_{\text{sys}}(m_{\nu_e}) = 130 \text{ meV}$  ( $\sigma_{\text{sys}}(m_{\nu_e}^2) = 0.017 \text{ eV}^2$ ) added in quadrature. Note that the observable is the squared neutrino mass  $m_{\nu_e}^2$ .

## Conclusion

The presented analysis shows, that a careful evaluation of the MTD and the inclusion of additional background-discriminating parameters, such as the radial dependence of events, as measured by the focal plane detector, allow to push the sensitivity of KATRIN beyond the reference value of 200 meV (90% C.L.).

background	stat. uncertainty ( $1\sigma$ ) $\pm 0.0001\text{ eV}^2$			
	1: reference MTD	2: optimized MTD	3: radial dep.	improv.
10 mcps, cosmic	0.0165 eV <sup>2</sup>	0.0149 eV <sup>2</sup>	<b>0.0142 eV<sup>2</sup></b>	13.9 %
100 mcps, cosmic	0.0342 eV <sup>2</sup>	0.0286 eV <sup>2</sup>	0.0265 eV <sup>2</sup>	22.5 %
614 mcps, cosmic	0.0737 eV <sup>2</sup>	0.0535 eV <sup>2</sup>	0.0485 eV <sup>2</sup>	34.2 %
960 mcps, cosmic + radon	0.1854 eV <sup>2</sup>	0.1283 eV <sup>2</sup>	0.1216 eV <sup>2</sup>	34.5 %

(a)  $1\sigma$  statistical uncertainties on  $m_\nu^2$ .

background	sensitivity (90 % C.L.) $\pm 1\text{ meV}$			
	1: reference MTD	2: optimized MTD	3: radial dep.	improv.
10 mcps, cosmic	197 meV	193 meV	<b>191 meV</b>	2.9 %
100 mcps, cosmic	254 meV	234 meV	228 meV	10.2 %
614 mcps, cosmic	352 meV	304 meV	291 meV	17.4 %
960 mcps, cosmic + radon	554 meV	461 meV	452 meV	18.6 %

(b) 90 % C.L. total sensitivities for  $m_\nu$ , including a systematic uncertainty of  $\sigma_{\text{sys}}(m_\nu) = 130\text{ meV}$  added in quadrature.

background	sensitivity ( $5\sigma$ ) $\pm 1\text{ meV}$			
	1: reference MTD	2: optimized MTD	3: radial dep.	improv.
10 mcps, cosmic	343 meV	337 meV	<b>333 meV</b>	2.9 %
100 mcps, cosmic	443 meV	408 meV	398 meV	10.2 %
614 mcps, cosmic	614 meV	530 meV	507 meV	17.4 %
960 mcps, cosmic + radon	974 meV	806 meV	790 meV	18.6 %

(c)  $5\sigma$  total sensitivities, including a systematic uncertainty of  $\sigma_{\text{sys}}(m_\nu) = 130\text{ meV}$  added in quadrature.

**Table 7.2:** Summary of reevaluated statistical uncertainties and total sensitivities for  $m_\nu$ , comparing the reference measuring time distribution (MTD) from the design report with optimized MTDs and the incorporation of radial dependent event rates. The relative improvements are stated with respect to the reference MTD.



# CHAPTER 8

---

## Summary and Conclusion

---

The KATRIN experiment is designed to measure the effective electron neutrino mass  $m_{\nu_e}$  with an unprecedented sensitivity of 200 meV at 90 % C.L. or 350 meV at  $5\sigma$  C.L. respectively, after five calendar years of data taking. This ambitious goal assumes stringent constraints on systematic parameters, which need to be determined precisely and be incorporated into all relevant parts of the analysis. The distributed system of diverse sensors and detectors demands a well-conceived data management and analysis framework.

With the first commissioning data at hand, a comprehensive set of statistical tools is required in order to investigate the impact of systematic effects on the neutrino mass sensitivity. Also, such tools are needed to evaluate the effectiveness of background removal techniques or to discuss possible optimizations of the measuring time distribution.

It was set out as a goal for this thesis, to identify and address the technical and physical requirements for KATRIN data analysis, not only considering the recent commissioning phase but also the upcoming neutrino mass measurements. In the following a short summary of this work will be given, outlining the implemented data analysis framework and statistical methods.

### Data Analysis Infrastructure

In cooperation with software developers from the KATRIN collaboration, a unified C++ analysis and simulation software framework, called *KASPER*, has been created, enforcing common code standards and interoperability between all its components.

For the purposes of transparent data processing and secure access mechanisms, a multi-tier network architecture has been designed and implemented. The C++ web-service application *KDBServer* is in charge of collimating, processing and making KATRIN data available for local and remote analysis. It utilizes object-oriented techniques and industry standard protocols to communicate with databases and serve data requests from client applications.

The data access library *KaLi* as a prominent part of KASPER provides a convenient yet powerful interface to this web-service layer. Any type of recorded, simulated or manually entered data can be requested through simple function calls. Powerful analysis logic is thus reduced to very few lines of code, as the library hides the complicated details of data preparation and network transfer from the user.

Many applications within KASPER, such as particle tracking Monte Carlos, the detector analysis suite and the statistical tools presented in this thesis, now utilize this infrastructure to access event triggered data, sensor readout, calibration data and positioning information. The system was successfully tested and productively used by collaborators worldwide during the SDS commissioning phase. Since then the data management system has been in continuous operation.

### Spectrum Calculation and Measurement Simulation

In preparation of the more complex statistical studies, performed in this thesis, the source and spectrum calculation code *SSC* was restructured to integrate properly with other modules of the analysis and simulation framework.

Additional *systematic effects*, like high voltage and temperature fluctuations, uncertainties on the isotopic tritium purity and electron scattering cross-section were parameterized and incorporated into the code. Another extension of the  $\beta$  spectrum calculation now allows for the definition of an arbitrary number of neutrino mass eigenstates. This feature can be used for instance, for the admixture of one or more *sterile neutrino states*.

The accuracy and numerical stability of SSC, especially the calculation of integrated  $\beta$  spectra, was improved considerably due to the introduction of adaptive Simpson and Romberg integration algorithms. Also the computational performance was increased by at least one order of magnitude with a dynamical rebinning of the tritium  $\beta$ -decay final state distributions.

A new mapping scheme between volumes of the tritium source section and the corresponding main detector pixels was introduced, in order to incorporate radial and angular rate variances into the spectra calculations and consequently the sensitivity studies. For the simulation of KATRIN neutrino measurements, an extensible class structure was introduced, allowing compositions of Poissonian and non-Poissonian *background models*. Several measurement strategies were implemented, which define the scanning order and duration of specific retarding energies in the  $\beta$ -decay spectrum.

### Statistical Methods for Sensitivity Studies

In the course of this thesis, a suite of diverse statistical tools, called *KaFit*, has been developed and a series of sensitivity studies were realized along with it. KaFit integrates closely with the spectrum calculation code to compute integrated  $\beta$ -decay spectra and background rates for various theoretical and experimental parameter configurations. The connection to KATRIN's database is realized through the data access module KaLi, and prepared for the upcoming neutrino mass measurements.

A crucial ingredient of this statistical toolset is the KATRIN likelihood function or chi-square function respectively, which is required for Frequentist or Bayesian approaches of *parameter inference* – in case of KATRIN meaning the extraction of a neutrino mass and the error bars of its estimate from observed  $\beta$  spectrum rates. The likelihood model has been enhanced substantially in order to accommodate critical systematics, sterile neutrino mixing scenarios and more complex spectrum scanning strategies.

KaFit utilizes the MINUIT2 function minimizer and the related MINOS profile likelihood algorithm from CERN for parameter fits on single data sets or larger ensemble tests (repeated KATRIN neutrino mass measurement simulations). Several construction methods for Frequentist *confidence intervals* are provided, including the established Feldman-Cousins method.

One specific focus of this work was set on Bayesian analysis methods. A highly customizable system of *Markov Chain Monte Carlo (MCMC)* algorithms was implemented and applied to high-dimensional problems. Especially when the default four-dimensional parameter space of the KATRIN likelihood ( $m_\nu^2, E_0, A_S, R_{\text{bg}}$ ) is extended by sterile neutrino mixing parameters ( $\Delta m_s, \sin^2 \theta_s$ ) or additional (correlated) systematics, the MCMCs performed more robust and versatile, compared to classical minimizers. The output of such a Bayesian analysis is a set of *posterior probability distributions* of the parameters of interest, which can be used to construct so-called credibility intervals.

Using MCMCs as powerful high-dimensional minimizers, a new optimization technique for KATRIN's *measuring time distribution (MTD)* was presented. For a predefined set of retarding potentials, at which the  $\beta$ -decay spectrum should be investigated, the optimization algorithm will autonomously distribute the available full-beam measuring time of 3 years, to yield the best statistical neutrino mass sensitivity. Revised measuring time distributions were calculated and presented for various background scenarios and sterile neutrino search in the eV range.

Taking advantage of the segmentation of the main detector and considering the radial dependency of background events, as observed during the SDS commissioning phase, a further improvement of the sensitivity could be achieved. With the above mentioned optimizations, the statistical uncertainty for the squared neutrino mass in case of the envisaged background level of  $R_{\text{bg}} = 10$  mcps was reevaluated to

$$\sigma_{\text{stat}}(m_\nu^2) = (0.0142 \pm 0.0001) \text{ eV}^2 .$$

This is an improvement of 13.9% compared to previous calculations, which were based on the reference measuring time distribution from the technical design report. Taking into account the originally budgeted and now slightly dominating systematic uncertainty of  $\sigma_{\text{sys}}(m_\nu^2) = 0.017 \text{ eV}^2$ , the corresponding total sensitivity on  $m_\nu$  amounts to

$$\sigma_{\text{tot}}(m_\nu) = (191 \pm 1) \text{ meV} .$$

The detection potential of a sterile neutrino mass eigenstate in the eV range has been investigated with an adapted measuring time distribution. It was found, that the KATRIN experiment has a good chance of probing a 3+1 mixing hypothesis in the parameter space currently favored by combined analyses of reactor and gallium calibration data (commonly referred to as the *reactor antineutrino anomaly*). For an admixture of one sterile neutrino with  $|U_{es}|^2 = \sin^2 \theta_s = 0.036$  to the electron anti-neutrino  $\bar{\nu}_e$  and under the assumption of comparatively small active neutrino mass eigenstates, the following sterile neutrino mass sensitivity was calculated:

$$\Delta m_s^2 = 0.753 \text{ eV}^2 \text{ (90 \% C.L.)}$$

All components of KaFit, especially the function minimizers, are provided as extensible class structures. They are independently used by other KATRIN collaborators in custom applications, for instance, in parameter fitting of radon emanation models or optimization of electro-magnetic field configurations of the spectrometers.

## Conclusion

A comprehensive data processing and analysis framework for the KATRIN experiment has been designed, implemented and integrated with existing simulation logic. During the recent commissioning measurements it has become the foundation of nearly all analysis tools utilized in the collaboration.

Frequentist and Bayesian statistical methods were evaluated for neutrino mass sensitivity studies and prepared for the analysis of actual  $\beta$  decay data. A new MC optimization technique was presented, performing an adaption of the measurement strategy, depending on the physics objective and extent of systematic effects. It was shown, that significant potential for the improvement of KATRIN's statistical sensitivity exists.

## Outlook

The statistical models and software tools developed in the course of this thesis will be of major importance during the commissioning and operation of the KATRIN experiment. They already constitute the basis of crucial simulation and analysis applications, used by students and senior scientists in the KATRIN collaboration on a daily basis.

Several studies, regarding the treatment of long-term variations in systematic parameters and background rates in KATRIN's measurement plan, have recently been initiated. Based on the optimization techniques presented in this thesis, it is planned to develop a more detailed measurement strategy, including the ideal order and durations of single data-taking runs, as well as calibration and background removal phases.

KATRIN's goal of determining the absolute neutrino mass scale with an unprecedented precision and probing new physics beyond the SM, does not only push hardware requirements to their technological limit. As emphasized in this work, a reliable data analysis chain together with a well-conceived probabilistic model and the appropriate statistical tools are of no less importance.

# APPENDIX A

---

## KDBServer Technical Supplements

---

### A.1 Object Relational Mappings in the KATRIN Database

The C++ web service KDBServer, providing KATRIN's server-side data processing and management functionalities (see section 3.4.1), utilizes the programming techniques of *Object-Relational Mapping (ORM)* and *argument binding*, in order to access various KATRIN-related SQL databases.

The classical method of searching and extracting data from an SQL database is, to more-or-less manually concatenate SQL queries and laboriously extract numbers and strings from the returned result:

```
1 // define the SQL query
2 SqlStatement mySqlQuery = someSqlConnection.prepare( "SELECT XXX, NNN,
3 validity_start, function_ID, calibration_data, quantity, flags, ... FROM
4 calibration_000 LEFT JOIN katrin_number ON calibration_000.katrin_ID =
5 katrin_number.ID WHERE user_ID = 5" );
6
7 // execute the query
8 mySqlQuery.execute();
9
10 // setup local variables for the result values
11 int XXX;
12 long long int validity_start;
13 string quantity;
14 ...
15
16 // iterate over all rows from the result and fetch the column values
17 while ( mySqlQuery->nextRow() )
18 {
19     mySqlQuery->getResult(0, &XXX);
20     mySqlQuery->getResult(2, &validity_start);
21 }
```

```

18  mySqlQuery->getResult(5, &quantity);
19  ...
20
21  // print to console
22  cout << XXX << ": " << validity_start << ... << endl;
23  }

```

ORM is a more sophisticated technique in object oriented programming languages for the purpose of mapping whole objects to a relational database. Using functions provided by the *Wt* library (section 3.4.1), a mapping scheme is implemented in KDBServer, relating every database table to a corresponding C++ class.

For calibration data for instance (see figure 3.8), the server-side class definition and its mapping to the corresponding SQL table look as follows:

```

1  struct Calibration : Wt::Dbo::Dbo<Calibration>
2  {
3      // define the member variables of this class
4
5      long long int fEntryTime;
6      long long int fValidityStart;
7      int fSwVersion;
8      int fUserId;
9      optional<int> fModificationId;
10
11     string fQuantity;
12     string fUnit;
13     int fType;
14     vector<unsigned char> fData;
15     long long int fTimeOffset;
16     int fFlags;
17     int fConfiguration;
18
19     // smart pointer to an object describing the KATRIN number
20     Wt::Dbo::ptr<KatrinNumber> fKatrinNumber;
21
22     template <class Action> void persist(Action& a)
23     {
24         // map every member variable to a database column:
25         Wt::Dbo::field(a, fEntryTime, "entry_time");
26         Wt::Dbo::field(a, fValidityStart, "validity_start");
27         Wt::Dbo::field(a, fSwVersion, "SW_version");
28         Wt::Dbo::field(a, fUserId, "user_ID");
29         Wt::Dbo::field(a, fModificationId, "modification_ID");
30         Wt::Dbo::field(a, fQuantity, "quantity");
31         Wt::Dbo::field(a, fUnit, "unit");
32         Wt::Dbo::field(a, fType, "function_ID");
33         Wt::Dbo::field(a, fFlags, "flags");
34         Wt::Dbo::field(a, fData, "calibration_data");

```

```

35     Wt::Dbo::field(a, fTimeOffset, "time_offset");
36     Wt::Dbo::field(a, fConfiguration, "configuration");
37
38     // map the relations between calibrations and katrin numbers
39     Wt::Dbo::belongsTo(a, fKatrinNumber, "katrin_ID");
40 }
41 };

```

Functions and types provided by the Wt library are prefixed by the namespace `Wt::Dbo::`. The function `persist` is invoked by the underlying Wt library to establish the link between a class member (such as `fTimeOffset`) and the respective column name of the database table (`"time_offset"`).

Line 39 in the above code example illustrates, how a relation between two tables is established. Here the calibration table has a column named `"katrin_ID"`, which points to the KATRIN number table. Within the C++ class model, this relation is reflected by a special pointer to a KATRIN number object `"Wt::Dbo::ptr<KatrinNumber>"`.

Once such a mapping scheme has been established for all database tables and the corresponding classes, queries to the database become much more convenient. Reading a list of calibration entries for instance might look as follows:

```

1 // set up the query to find a list of calibration entries
2 Wt::Dbo::Query<Calibration> myQuery = someDbSession.find<Calibration>();
3
4 // filter for a specific user
5 myQuery.where( "user_ID = ?" ).bind( 5 );
6 // constrain time interval
7 myQuery.where( "validity_start < ?" ).bind( KLTimeStamp::Now() - KLDays(5) );
8
9 list<Wt::Dbo::Ptr<Calibration> > myResultList = myQuery.resultList();
10
11 // iterate over a list of result objects
12 for ( Wt::Dbo::Ptr<Calibration> myCalibration : myResultList )
13 {
14     // print some info to console
15     cout << myCalibration->fKatrinNumber << " : " << myCalibration->fType << endl;
16
17     // update some field, which will automatically be written to the database
18     myCalibration->fQuantity = "voltage";
19 }

```

Not only is the above pictured way of accessing the database from C++ in better accordance with an object-oriented programming style. It is considerably more failsafe and robust in practical use. The complicated SQL queries are reliably assembled by the library underneath and translated into so-called prepared SQL statements.

Parameters are added to a statement through a mechanism called *argument binding*, as used in lines 5 and 7. The library Wt ensures that parameters, to be inserted into the SQL query, will be correctly handled and converted, depending on their type (integer, float, binary, etc.) and the actual database system currently in use. Last, but not least, the method of binding arguments to a prepared SQL statement fulfills an important security aspect. It makes the system practically invulnerable towards a common form of attacks, called SQL code injection, where malicious SQL code is inserted into the SQL query by an unauthorized client. Such an attack is only possible, when there is no distinction between SQL commands (the statement) and its parameters (arguments).

All KATRIN data types, which are persisted in the database (see figure 3.8), are implemented with an ORM scheme similar to the one outlined in the above example.

## A.2 SOAP Communication with KATRIN Web Services

Remote access to the services provided by KDBServer, including access to KATRIN data, is realized through the Simple Object Access Protocol (SOAP), which is an XML based messaging protocol. The external library gSoap (see section 3.4.1) is used to handle underlying transport protocols, as well as compression and encryption techniques.

Users of the KATRIN C++ analysis and simulation framework KASPER (section 3.2.1) can establish communication with KDBServer through a defined set of functions, provided by the KASPER module KaLi (section 4.2.1). However, since the SOAP interface implemented by KDBServer is standards-compliant and supported by most modern programming languages, access from other applications is possible.

The process of messaging is invoked through a technique called Remote Procedure Call (RPC): A user program running on a local machine invokes a function, which then is not executed locally but translated into an XML message and sent over the network to the web service. The code deployed on the remote server evaluates the function call and sends the return value back to the client, again in an XML representation. The user program now ends the function call and returns the result data to the user in a programmable format. This process is in most cases completely transparent to the user.

### A.2.1 A SOAP Messaging Example

The following XML document (a SOAP envelope) is a simplified example of how a remote procedure call is realized between a client application and the server. In this case, detector event data from a run with the id 'fpd1875' is requested.

```
1 <?xml version="1.0" encoding="UTF-8"?>
2 <soap:Envelope>
3   <soap:Body>
4     <TransferData>
5       <Actor Type="KALICLIENT" Id="student-pc" Version="2.0.10" />
6       <Query type="ReadQuery">
7         <Procedure>112</Procedure>
8         <Id>fpd00001875.root</Id>
9       </Query>
10    </TransferData>
11  </soap:Body>
12 </soap:Envelope>
```

KDBServer parses the request, verifies that the client is authorized, and gathers the requested data. When the procedure was successfully evaluated, the following response is sent to the client:

```
1 <?xml version="1.0" encoding="UTF-8"?>
2 <soap:Envelope>
3   <soap:Body>
4     <TransferDataResponse>
5       <Actor Type="KDBSERVER" Id="katrin-kit-server1" Version="2.0.30" />
6       <Result>
7         <Status>0</Status>
8         <Procedure>112</Procedure>
9         <Run Id="fpd00001875">
10          <TimeInterval End="1348743391000000000" Start="1348739790000000000" />
11          <SubRun End="1348743391000000000" Start="1348739790000000000" />
12          <Header Name="kali"># OrcaStreamType: 5264 # ... </Header>
13          <NumberOfSubRuns>1</NumberOfSubRuns>
14        </Run>
15        <File Id="fpd00001875.root" Type="File">
16          <xmime5:contentType>application/octet-stream</xmime5:contentType>
17          <Md5>90fecb6d5475d90271367a6fcfd144aa</Md5>
18          <Size>17538748</Size>
19          <SoapAttachment><xop:Include href="fpd00001875.root"/></SoapAttachment>
20        </File>
21      </Result>
22    </TransferDataResponse>
23  </soap:Body>
24 </soap:Envelope>
```

In the above example, the XML response document does not contain the complete result data. The tag `<SoapAttachment>` links to a binary attachment (the detector event data), which is transferred along with the XML document.

The recipient of the response message could be, for instance, an analysis tool built upon the KASPER framework (section 3.2.1). In that case, the XML message is automatically translated into the corresponding C++ objects and returned to the user as a function result, which can be used for further analysis.

---

## Bibliography

---

- [Abd09] J. N. ABDURASHITOV et al.: ‘Measurement of the solar neutrino capture rate with gallium metal. III. Results for the 2002–2007 data-taking period’. *Phys. Rev. C* 80 (1 July 2009), p. 015807. DOI: [10.1103/PhysRevC.80.015807](https://doi.org/10.1103/PhysRevC.80.015807).
- [Abd02] J. ABDURASHITOV et al.: ‘Solar neutrino flux measurements by the Soviet-American gallium experiment (SAGE) for half the 22-year solar cycle’. English. *Journal of Experimental and Theoretical Physics* 95.2 (2002), pp. 181–193. DOI: [10.1134/1.1506424](https://doi.org/10.1134/1.1506424).
- [Abe13] K. ABE et al.: ‘Evidence of electron neutrino appearance in a muon neutrino beam’. *Phys. Rev. D* 88 (3 Aug. 2013), p. 032002. DOI: [10.1103/PhysRevD.88.032002](https://doi.org/10.1103/PhysRevD.88.032002).
- [Abe11] K. ABE et al.: ‘Indication of Electron Neutrino Appearance from an Accelerator-produced Off-axis Muon Neutrino Beam’. *Phys.Rev.Lett.* 107 (2011), p. 041801. DOI: [10.1103/PhysRevLett.107.041801](https://doi.org/10.1103/PhysRevLett.107.041801).
- [Abe08] S. ABE et al.: ‘Precision Measurement of Neutrino Oscillation Parameters with KamLAND’. *Phys.Rev.Lett.* 100 (2008), p. 221803. DOI: [10.1103/PhysRevLett.100.221803](https://doi.org/10.1103/PhysRevLett.100.221803).
- [Ade13] P. ADE et al.: ‘Planck 2013 results. I. Overview of products and scientific results’. (2013). DOI: [10.1051/0004-6361/201321529](https://doi.org/10.1051/0004-6361/201321529).
- [Agu09] A. AGUILAR-AREVALO et al.: ‘A Search for Electron Antineutrino Appearance at the  $\Delta m^2 \sim 1 \text{ eV}^2$  Scale’. *Phys.Rev.Lett.* 103 (2009), p. 111801. DOI: [10.1103/PhysRevLett.103.111801](https://doi.org/10.1103/PhysRevLett.103.111801).
- [Ahm02] Q. R. AHMAD et al.: ‘Direct Evidence for Neutrino Flavor Transformation from Neutral-Current Interactions in the Sudbury Neutrino Observatory’. *Phys. Rev. Lett.* 89 (1 June 2002), p. 011301. DOI: [10.1103/PhysRevLett.89.011301](https://doi.org/10.1103/PhysRevLett.89.011301).
- [Ahn10] J. AHN et al.: ‘RENO: An Experiment for Neutrino Oscillation Parameter  $\theta_{13}$  Using Reactor Neutrinos at Yonggwang’. (2010).
- [Ahn06] M. AHN et al.: ‘Measurement of Neutrino Oscillation by the K2K Experiment’. *Phys.Rev.* D74 (2006), p. 072003. DOI: [10.1103/PhysRevD.74.072003](https://doi.org/10.1103/PhysRevD.74.072003).
- [Alt05] M. ALTMANN et al.: ‘Complete results for five years of GNO solar neutrino observations’. *Phys.Lett.* B616 (2005), pp. 174–190. DOI: [10.1016/j.physletb.2005.04.068](https://doi.org/10.1016/j.physletb.2005.04.068).

- [Ams14] J. AMSBAUGH, J. BARRETT, A. BEGLARIAN, T. BERGMANN, H. BICHSEL, et al.: ‘Focal-plane detector system for the KATRIN experiment’. *Submitted to NIM A* (2014).
- [An12] F. P. AN, J. Z. BAI, et al.: ‘Observation of Electron-Antineutrino Disappearance at Daya Bay’. *Phys. Rev. Lett.* 108 (17 Apr. 2012), p. 171803. DOI: [10.1103/PhysRevLett.108.171803](https://doi.org/10.1103/PhysRevLett.108.171803).
- [Ant09] I. ANTICHEVA, M. BALLINTIJN, B. BELLENOT, M. BISKUP, R. BRUN, N. BUNCIC, P. CANAL, D. CASADEI, O. COUET, and V. FINE: ‘ROOT – A C++ framework for petabyte data storage, statistical analysis and visualization’. *Computer Physics Communications* 180.12 (Dec. 22, 2009), pp. 2499–2512. DOI: [10.1016/j.cpc.2009.08.005](https://doi.org/10.1016/j.cpc.2009.08.005).
- [Ard06] F. ARDELLIER et al.: ‘Double Chooz: A Search for the neutrino mixing angle  $\theta(13)$ ’. (2006).
- [Ark02] N. ARKANI-HAMED, S. DIMOPOULOS, G. DVALI, and J. MARCH-RUSSELL: ‘Neutrino masses from large extra dimensions’. *Phys.Rev.* D65 (2002), p. 024032. DOI: [10.1103/PhysRevD.65.024032](https://doi.org/10.1103/PhysRevD.65.024032).
- [Arm03] B. ARMBRUSTER, G. DREXLIN, K. EITEL, T. JANNAKOS, J. KLEINFELLER, et al.: ‘Improved limits on anti- $\nu(e)$  emission from  $\mu^+$  decay’. *Phys.Rev.Lett.* 90 (2003), p. 181804. DOI: [10.1103/PhysRevLett.90.181804](https://doi.org/10.1103/PhysRevLett.90.181804).
- [Ase00] V. N. ASEEV et al.: ‘Energy loss of 18 keV electrons in gaseous T<sub>2</sub> and quench condensed D<sub>2</sub> films’. *European Physical Journal D* 10 (1 2000), pp. 39–52. DOI: [10.1007/s100530050525](https://doi.org/10.1007/s100530050525).
- [Ase11] V. N. ASEEV et al.: ‘Upper limit on the electron antineutrino mass from the Troitsk experiment’. *Phys. Rev. D* 84 (11 Dec. 2011), p. 112003. DOI: [10.1103/PhysRevD.84.112003](https://doi.org/10.1103/PhysRevD.84.112003).
- [Ath98] C. ATHANASSOPOULOS et al.: ‘Evidence for  $\nu_\mu \rightarrow \nu_e$  neutrino oscillations from LSND’. *Phys.Rev.Lett.* 81 (1998), pp. 1774–1777. DOI: [10.1103/PhysRevLett.81.1774](https://doi.org/10.1103/PhysRevLett.81.1774).
- [Atk06] P. ATKINS and J. de PAULA: *Atkins’ Physical Chemistry*. Vol. 8. Oxford University Press, 2006.
- [ATL12] ATLAS COLLABORATION: ‘Observation of a new particle in the search for the Standard Model Higgs boson with the ATLAS detector at the LHC’. *Physics Letters B* 716.1 (2012), pp. 1–29. DOI: [10.1016/j.physletb.2012.08.020](https://doi.org/10.1016/j.physletb.2012.08.020).
- [Aug96] AUGER COLLABORATION: *The Pierre Auger Project Design Report*. Tech. rep. FERMILAB-PUB-96-024. Batavia, IL: FERMILAB, 1996.
- [Bah99] J. N. BAHCALL, P. I. KRASTEV, and A. Y. SMIRNOV: ‘Is a large mixing angle MSW effect the solution of the solar neutrino problems?’ *Phys. Rev. D* 60 (9 Oct. 1999), p. 093001. DOI: [10.1103/PhysRevD.60.093001](https://doi.org/10.1103/PhysRevD.60.093001).
- [Bah05] J. N. BAHCALL, A. M. SERENELLI, and S. BASU: ‘New solar opacities, abundances, helioseismology, and neutrino fluxes’. *Astrophys.J.* 621 (2005), pp. L85–L88. DOI: [10.1086/428929](https://doi.org/10.1086/428929).

- [Bak84] S. BAKER and R. COUSINS: ‘Clarification of the use of chi-square and likelihood functions in fits to histograms’. *Nuclear Instruments and Methods in Physics Research* 221.2 (Apr. 1, 1984), pp. 437–442. DOI: [10.1016/0167-5087\(84\)90016-4](https://doi.org/10.1016/0167-5087(84)90016-4).
- [Bar12] J. BARRY, W. RODEJOHANN, and H. ZHANG: ‘Sterile Neutrinos for Warm Dark Matter and the Reactor Anomaly in Flavor Symmetry Models’. *JCAP* 1201 (2012), p. 052. DOI: [10.1088/1475-7516/2012/01/052](https://doi.org/10.1088/1475-7516/2012/01/052).
- [Bat14] R. A. BATTYE and A. MOSS: ‘Evidence for massive neutrinos from CMB and lensing observations’. *Phys.Rev.Lett.* 112 (2014), p. 051303. DOI: [10.1103/PhysRevLett.112.051303](https://doi.org/10.1103/PhysRevLett.112.051303).
- [Beh] J. BEHRENS. Doctoral thesis, in preparation. University of Münster.
- [Ben13] C. L. BENNETT et al.: ‘Nine-year Wilkinson Microwave Anisotropy Probe (WMAP) Observations: Final Maps and Results’. *The Astrophysical Journal Supplement Series* 208.2 (2013), p. 20.
- [Ber03] L. BERGSTRÖM and A. GOOBAR: *Cosmology and particle astrophysics; 2nd ed.* Berlin: Springer, 2003.
- [Ber12] J. BERINGER and others (PARTICLE DATA GROUP): ‘Review of Particle Physics’. *Physical Review D* 86.1 (July 2012). 2013 partial update for the 2014 edition, pp. 010001+. DOI: [10.1103/physrevd.86.010001](https://doi.org/10.1103/physrevd.86.010001).
- [Beu11] F. BEUTLER, C. BLAKE, M. COLLESS, D. H. JONES, L. STAVELEY-SMITH, L. CAMPBELL, Q. PARKER, W. SAUNDERS, and F. WATSON: ‘The 6dF Galaxy Survey: baryon acoustic oscillations and the local Hubble constant’. *Monthly Notices of the Royal Astronomical Society* 416.4 (2011), pp. 3017–3032. DOI: [10.1111/j.1365-2966.2011.19250.x](https://doi.org/10.1111/j.1365-2966.2011.19250.x).
- [Bla13] K. BLAUM, A. DOERR, C. DUELLMANN, K. EBERHARDT, S. ELISEEV, et al.: ‘The Electron Capture  $^{163}\text{Ho}$  Experiment ECHO’. (2013).
- [Bog85] D. BOGDAN, A. FAESSLER, A. PETROVICI, and S. HOLAN: ‘Neutrino masses and right-handed current in the neutrinoless double beta decay  $^{76}\text{Ge} \rightarrow ^{76}\text{Se} + 2e^-$ ’. *Physics Letters B* 150 (Jan. 1985), pp. 29–34. DOI: [10.1016/0370-2693\(85\)90131-5](https://doi.org/10.1016/0370-2693(85)90131-5).
- [Bon00] J. BONN, B. BORNSCHEIN, L. BORNSCHEIN, L. FICKINGER, O. KAZACHENKO, et al.: ‘Newest results from the Mainz neutrino mass experiment’. *Phys.Atom.Nucl.* 63 (2000), pp. 969–974. DOI: [10.1134/1.855733](https://doi.org/10.1134/1.855733).
- [Bor10] B. BORNSCHEIN: ‘KATRIN Numbering System for equipment, components and related documents’. KATRIN internal document, 10-IG-1070-4. 2010.
- [Bro96] M. R. BROWN: *FastCGI Specification*. 1996. URL: <http://www.fastcgi.com/devkit/doc/fcgi-spec.html>.
- [Ced06] A. CEDILNIK, B. GEVECI, K. MORELAND, J. P. AHRENS, and J. M. FAVRE: ‘Remote Large Data Visualization in the ParaView Framework.’ *EGPGV*. Ed. by A. HEIRICH, B. RAFFIN, and L. P. P. dos SANTOS. Eurographics Association, 2006, pp. 163–170.

- [Cen14] CENTER FOR EXPERIMENTAL NUCLEAR PHYSICS AND ASTROPHYSICS: *Annual Report*. University of Washington, 2014.
- [Cha14] J. CHADWICK: ‘Intensitätsverteilung im magnetischen Spektrum der  $\beta$ -Strahlen von Radium B+C’. *Verhandlungen der Deutschen Physikalischen Gesellschaft* 16 (1914), pp. 383–91.
- [Chi14] S. CHILIGARYAN: *ADEI, Advanced Data Extraction Infrastructure*. Institute for Data Processing and Electronics, KIT. 2014. URL: <http://dside.dyndns.org/adei>.
- [CMS12] CMS COLLABORATION: ‘Observation of a new boson at a mass of 125 GeV with the CMS experiment at the LHC’. *Physics Letters B* 716.1 (2012), pp. 30–61. DOI: [10.1016/j.physletb.2012.08.021](https://doi.org/10.1016/j.physletb.2012.08.021).
- [Cor14] T. J. CORONA: ‘Simulated and measured background studies and their impact on the KATRIN neutrino mass sensitivity’. Doctoral thesis, in preparation. Chapel Hill, USA: University of North Carolina, 2014.
- [Dan62] G. DANBY, J.-M. GAILLARD, K. GOULIANOS, L. M. LEDERMAN, N. MISTRY, M. SCHWARTZ, and J. STEINBERGER: ‘Observation of High-Energy Neutrino Reactions and the Existence of Two Kinds of Neutrinos’. *Phys. Rev. Lett.* 9 (1 July 1962), pp. 36–44. DOI: [10.1103/PhysRevLett.9.36](https://doi.org/10.1103/PhysRevLett.9.36).
- [Dav94] R. DAVIS: ‘A review of the homestake solar neutrino experiment’. *Progress in Particle and Nuclear Physics* 32 (1994), pp. 13–32. DOI: [10.1016/0146-6410\(94\)90004-3](https://doi.org/10.1016/0146-6410(94)90004-3).
- [Daw14] B. DAWES, D. ABRAHAMS, and R. RIVERA: *boost C++ libraries*. 2014. URL: <http://www.boost.org>.
- [Dec90] D. DECAMP et al.: ‘A Precise Determination of the Number of Families With Light Neutrinos and of the  $Z$  Boson Partial Widths’. *Phys.Lett.* B235 (1990), p. 399. DOI: [10.1016/0370-2693\(90\)91984-J](https://doi.org/10.1016/0370-2693(90)91984-J).
- [Deu96] L. P. DEUTSCH and J.-L. GAILLY: *ZLIB Compressed Data Format Specification version 3.3*. Internet RFC 1950. May 1996.
- [Dev13] P. S. B. DEV, S. GOSWAMI, M. MITRA, and W. RODEJOHANN: ‘Constraining neutrino mass from neutrinoless double beta decay’. *Phys. Rev. D* 88 (9 Nov. 2013), p. 091301. DOI: [10.1103/PhysRevD.88.091301](https://doi.org/10.1103/PhysRevD.88.091301).
- [Dos08] N. DOSS and J. TENNYSON: ‘Excitations to the electronic continuum of  $^3\text{HeT}^+$  in investigations of  $T_2$   $\beta$ -decay experiments’. *Journal of Physics B: Atomic, Molecular and Optical Physics* 41.12 (June 28, 2008), pp. 125701+. DOI: [10.1088/0953-4075/41/12/125701](https://doi.org/10.1088/0953-4075/41/12/125701).
- [Dos06] N. DOSS, J. TENNYSON, A. SAENZ, and S. JONSELL: ‘Molecular effects in investigations of tritium molecule  $\beta$  decay endpoint experiments’. *Phys. Rev. C* 73 (2 Feb. 2006), p. 025502. DOI: [10.1103/PhysRevC.73.025502](https://doi.org/10.1103/PhysRevC.73.025502).
- [Ell02] S. R. ELLIOTT and P. VOGEL: ‘Double beta decay’. *Ann.Rev.Nucl.Part.Sci.* 52 (2002), pp. 115–151. DOI: [10.1146/annurev.nucl.52.050102.090641](https://doi.org/10.1146/annurev.nucl.52.050102.090641).

- [Emw14] EMWEB: *Wt, a C++ Web Toolkit*. 2014. URL: <http://www.webtoolkit.eu/wt/blog>.
- [Erh14] M. ERHARD et al.: ‘High voltage monitoring with a solenoid retarding spectrometer of the KATRIN experiment’. *Submitted to Journal of Instrumentation* (2014).
- [Fel98] G. J. FELDMAN and R. D. COUSINS: ‘A Unified approach to the classical statistical analysis of small signals’. *Phys.Rev. D* 57 (1998), pp. 3873–3889. DOI: [10.1103/PhysRevD.57.3873](https://doi.org/10.1103/PhysRevD.57.3873).
- [Fer34] E. FERMI: ‘Versuch einer Theorie der Betastrahlen’. *Z. Phys.* 88 (1934), pp. 161–177. DOI: [10.1007/BF01351864](https://doi.org/10.1007/BF01351864).
- [Fra14] F. FRAENKLE, F. GLUECK, and K. VALERIUS ET AL.: ‘Penning discharge in the KATRIN pre-spectrometer’. *New Journal of Physics* (2014). Submitted for internal review.
- [Frä10] F. FRÄNKLE: ‘Background Investigations of the KATRIN Pre-Spectrometer’. Doctoral thesis. KIT, 2010.
- [Fuk98] Y. FUKUDA et al.: ‘Evidence for Oscillation of Atmospheric Neutrinos’. *Phys. Rev. Lett.* 81 (8 Aug. 1998), pp. 1562–1567. DOI: [10.1103/PhysRevLett.81.1562](https://doi.org/10.1103/PhysRevLett.81.1562).
- [Fuk96] Y. FUKUDA et al.: ‘Solar neutrino data covering solar cycle 22’. *Phys.Rev.Lett.* 77 (1996), pp. 1683–1686. DOI: [10.1103/PhysRevLett.77.1683](https://doi.org/10.1103/PhysRevLett.77.1683).
- [Fuk13] K. FUKUTANI and T. SUGIMOTO: ‘Physisorption and ortho-para conversion of molecular hydrogen on solid surfaces’. *Progress In Surface Science* 88 (Dec. 2013), pp. 279–348. DOI: [10.1016/j.progsurf.2013.09.001](https://doi.org/10.1016/j.progsurf.2013.09.001).
- [Fur14] D. FURSE, S. GROH, et al.: ‘Kassiopeia: A Modern, Extensible C++ Particle Tracking Package’. (2014). Submitted for internal review.
- [Gan13] A. GANDO et al.: ‘Reactor on-off antineutrino measurement with KamLAND’. *Phys. Rev. D* 88 (3 Aug. 2013), p. 033001. DOI: [10.1103/PhysRevD.88.033001](https://doi.org/10.1103/PhysRevD.88.033001).
- [Gar11] A. GARCÍA et al.: ‘The Large Scale Data Facility: Data Intensive Computing for scientific experiments.’ *Proceedings of The 12th IEEE International Workshop on Parallel and Distributed Scientific and Engineering Computing (PDSEC-11/IPDPS-11)*, IEEE Computer Society (2011), pp. 1467–1474.
- [Gel79] M. GELL-MANN, P. RAMOND, and R. SLANSKY: ‘Complex Spinors and Unified Theories’. *Conf.Proc.* C790927 (1979), pp. 315–321.
- [Gel92] A. GELMAN and D. B. RUBIN: ‘Inference from Iterative Simulation Using Multiple Sequences’. *Statistical Science* 7.4 (1992), pp. 457–472. DOI: [10.2307/2246093](https://doi.org/10.2307/2246093).
- [Gla61] S. GLASHOW: ‘Partial Symmetries of Weak Interactions’. *Nucl.Phys.* 22 (1961), pp. 579–588. DOI: [10.1016/0029-5582\(61\)90469-2](https://doi.org/10.1016/0029-5582(61)90469-2).
- [Glü13] F. GLÜCK, G. DREXLIN, B. LEIBER, S. MERTENS, A. OSIPOWICZ, et al.: ‘Electromagnetic design of the large-volume air coil system of the KATRIN experiment’. *New J.Phys.* 15 (2013), p. 083025. DOI: [10.1088/1367-2630/15/8/083025](https://doi.org/10.1088/1367-2630/15/8/083025).

- [Goe14] S. GOERHARDT: ‘Background Reduction Methods and Vacuum Technology at the KATRIN Spectrometers’. Doctoral thesis. KIT, 2014.
- [Gol58] M. GOLDHABER, L. GRODZINS, and A. W. SUNYAR: ‘Helicity of Neutrinos’. *Phys. Rev.* 109 (3 Feb. 1958), pp. 1015–1017. DOI: [10.1103/PhysRev.109.1015](https://doi.org/10.1103/PhysRev.109.1015).
- [Gre05] P. C. GREGORY: *Bayesian logical data analysis for the physical sciences: a comparative approach with Mathematica support*. Cambridge University Press, 2005.
- [Gri69] V. GRIBOV and B. PONTECORVO: ‘Neutrino astronomy and lepton charge’. *Physics Letters B* 28 (Jan. 1969), pp. 493–496. DOI: [10.1016/0370-2693\(69\)90525-5](https://doi.org/10.1016/0370-2693(69)90525-5).
- [Gro15] S. GROH: ‘Global tracking of electrons and transmission properties of the KATRIN experiment’. Doctoral thesis, in preparation. KIT, 2015.
- [Gro13] S. GROHMANN, T. BODE, M. HÖTZEL, H. SCHÖN, M. SÜSSER, and T. WAHL: ‘The thermal behaviour of the tritium source in KATRIN’. *Cryogenics* 55–56 (2013), pp. 5–11. DOI: [10.1016/j.cryogenics.2013.01.001](https://doi.org/10.1016/j.cryogenics.2013.01.001).
- [Gro11] S. GROHMANN, T. BODE, H. SCHÖN, and M. SÜSSER: ‘Precise temperature measurement at 30 K in the KATRIN source cryostat’. *Cryogenics* 51.8 (2011), pp. 438–445. DOI: [10.1016/j.cryogenics.2011.05.001](https://doi.org/10.1016/j.cryogenics.2011.05.001).
- [Haa06] H. HAARIO, M. LAINE, A. MIRA, and E. SAKSMAN: ‘DRAM: Efficient adaptive MCMC’. *Statistics and Computing* 16.4 (Dec. 1, 2006), pp. 339–354. DOI: [10.1007/s11222-006-9438-0](https://doi.org/10.1007/s11222-006-9438-0).
- [Hai88] T. HAINES et al.: ‘Neutrinos from SN1987a in the IMB detector’. *Nuclear Instruments and Methods in Physics Research Section A: Accelerators, Spectrometers, Detectors and Associated Equipment* 264.1 (1988), pp. 28–31. DOI: [10.1016/0168-9002\(88\)91097-2](https://doi.org/10.1016/0168-9002(88)91097-2).
- [Ham99] W. HAMPEL et al.: ‘GALLEX solar neutrino observations: Results for GALLEX IV’. *Phys.Lett.* B447 (1999), pp. 127–133. DOI: [10.1016/S0370-2693\(98\)01579-2](https://doi.org/10.1016/S0370-2693(98)01579-2).
- [Has70] W. K. HASTINGS: ‘Monte Carlo sampling methods using Markov chains and their applications’. *Biometrika* 57.1 (Apr. 1, 1970), pp. 97–109. DOI: [10.1093/biomet/57.1.97](https://doi.org/10.1093/biomet/57.1.97).
- [Hee08] D. van HEESCH: *Doxygen: Source code documentation generator tool*. 2008. URL: <http://www.stack.nl/~dimitri/doxygen>.
- [Hig07] H. HIGAKI, K. ITO, W. SAIKI, Y. OMORI, and H. OKAMOTO: ‘Properties of non-neutral electron plasmas confined with a magnetic mirror field’. *Phys. Rev. E* 75 (6 June 2007), p. 066401. DOI: [10.1103/PhysRevE.75.066401](https://doi.org/10.1103/PhysRevE.75.066401).
- [Hig64] P. W. HIGGS: ‘Broken Symmetries and the Masses of Gauge Bosons’. *Phys. Rev. Lett.* 13 (16 Oct. 1964), pp. 508–509. DOI: [10.1103/PhysRevLett.13.508](https://doi.org/10.1103/PhysRevLett.13.508).
- [Hig02] N. J. HIGHAM: *Accuracy and stability of numerical algorithms (2. ed.)*. SIAM, 2002, pp. I–XXX, 1–680.

- [Hir87] K. HIRATA et al.: ‘Observation of a neutrino burst from the supernova SN1987A’. *Phys. Rev. Lett.* 58 (14 Apr. 1987), pp. 1490–1493. DOI: [10.1103/PhysRevLett.58.1490](https://doi.org/10.1103/PhysRevLett.58.1490).
- [Höt12] M. HÖTZEL: ‘Simulation and analysis of source-related effects for KATRIN’. Doctoral thesis. KIT, 2012.
- [Hug08] K. HUGENBERG: ‘Design of the electrode system of the KATRIN main spectrometer’. Diploma thesis. University of Münster, 2008.
- [Jan] A. JANSEN. Doctoral thesis, in preparation. KIT.
- [Käf12] W. KÄFER: ‘Sensitivity studies of the KATRIN experiment’. Doctoral thesis. KIT, 2012.
- [KAT05] KATRIN COLLABORATION: ‘KATRIN design report’. *FZKA Scientific Report 7090* (2005).
- [KAT14] KATRIN COLLABORATION: ‘Results of the first KATRIN SDS measurement phase’. *Internal report* (2014).
- [Kit14] KITWARE: *CMake, a cross-platform, open-source build system*. 2014. URL: <http://www.cmake.org>.
- [Kla04] H. KLAPDOR-KLEINGROTHAUS, I. KRIVOSHEINA, A. DIETZ, and O. CHKVORETS: ‘Search for neutrinoless double beta decay with enriched  $^{76}\text{Ge}$  in Gran Sasso 1990–2003’. *Physics Letters B* 586.3–4 (2004), pp. 198–212. DOI: [10.1016/j.physletb.2004.02.025](https://doi.org/10.1016/j.physletb.2004.02.025).
- [Kod01] K. KODAMA et al.: ‘Observation of tau neutrino interactions’. *Phys.Lett.* B504 (2001), pp. 218–224. DOI: [10.1016/S0370-2693\(01\)00307-0](https://doi.org/10.1016/S0370-2693(01)00307-0).
- [Kra11] C. KRANZ: ‘Optimierung der Methoden und Messprozeduren zur Entfaltung der Energieverlustfunktion beim KATRIN-Experiment’. Diploma thesis. University of Münster, 2011.
- [Kra05] C. KRAUS, B. BORNSCHEIN, L. BORNSCHEIN, J. BONN, B. FLATT, et al.: ‘Final results from phase II of the Mainz neutrino mass search in tritium beta decay’. *Eur.Phys.J.* C40 (2005), pp. 447–468. DOI: [10.1140/epjc/s2005-02139-7](https://doi.org/10.1140/epjc/s2005-02139-7).
- [Kro14] P. A. KROCHIN YEPEZ: ‘Investigations on the influence of the ortho-para tritium ratio on the neutrino mass sensitivity of KATRIN’. Bachelor thesis. KIT, 2014.
- [Lei14] B. LEIBER: ‘Investigations of background due to secondary electron emission in the KATRIN-experiment’. Doctoral thesis. KIT, 2014.
- [Lei10] B. LEIBER: ‘Non-axially symmetric field and trajectory calculations for the KATRIN-experiment’. Diploma thesis. KIT, 2010.
- [Les06] J. LESGOURGUES and S. PASTOR: ‘Massive neutrinos and cosmology’. *Phys.Rept.* 429 (2006), pp. 307–379. DOI: [10.1016/j.physrep.2006.04.001](https://doi.org/10.1016/j.physrep.2006.04.001).
- [Lob85] V. LOBASHEV and P. SPIVAK: ‘A method for measuring the electron antineutrino rest mass’. *Nuclear Instruments and Methods in Physics Research Section A: Accelerators, Spectrometers, Detectors and Associated Equipment* 240.2 (Oct. 1985), pp. 305–310. DOI: [10.1016/0168-9002\(85\)90640-0](https://doi.org/10.1016/0168-9002(85)90640-0).

- [Lon02] D. A. LONG: *A Unified Treatment of the Theory of Raman Scattering by Molecules*. John Wiley & Sons, Ltd, 2002. DOI: [10.1002/0470845767](https://doi.org/10.1002/0470845767).
- [Lor02] T. J. LOREDO and D. Q. LAMB: ‘Bayesian analysis of neutrinos observed from supernova SN 1987A’. *Phys. Rev. D* 65 (6 Feb. 2002), p. 063002. DOI: [10.1103/PhysRevD.65.063002](https://doi.org/10.1103/PhysRevD.65.063002).
- [Luc00] L. L. LUCAS and M. P. UNTERWEGER: ‘Comprehensive review and critical evaluation of the half-life of tritium’. *J. Res. Natl. Inst. Stand. Technol.* 105.4 (2000), pp. 541–549. DOI: [10.6028/jres.105.043](https://doi.org/10.6028/jres.105.043).
- [Mac03] D. J. C. MACKAY: *Information Theory, Inference and Learning Algorithms*. First Edition. Cambridge University Press, Oct. 6, 2003.
- [Mak62] Z. MAKI, M. NAKAGAWA, and S. SAKATA: ‘Remarks on the Unified Model of Elementary Particles’. *Progress of Theoretical Physics* 28 (Nov. 1962), pp. 870–880. DOI: [10.1143/PTP.28.870](https://doi.org/10.1143/PTP.28.870).
- [Men11] G. MENTION, M. FECHNER, T. LASSERRE, T. MUELLER, D. LHUILLIER, et al.: ‘The Reactor Antineutrino Anomaly’. *Phys.Rev.* D83 (2011), p. 073006. DOI: [10.1103/PhysRevD.83.073006](https://doi.org/10.1103/PhysRevD.83.073006).
- [Mer12] S. MERTENS: ‘Study of Background Processes in the Electrostatic Spectrometers of the KATRIN experiment’. Doctoral thesis. KIT, 2012.
- [Mer13] S. MERTENS, G. DREXLIN, F. FRÄNKLE, D. FURSE, F. GLÜCK, et al.: ‘Background due to stored electrons following nuclear decays in the KATRIN spectrometers and its impact on the neutrino mass sensitivity’. *Astropart.Phys.* 41 (2013), pp. 52–62. DOI: [10.1016/j.astropartphys.2012.10.005](https://doi.org/10.1016/j.astropartphys.2012.10.005).
- [Met53] N. METROPOLIS, A. W. ROSENBLUTH, M. N. ROSENBLUTH, A. H. TELLER, and E. TELLER: ‘Equation of State Calculations by Fast Computing Machines’. *The Journal of Chemical Physics* 21.6 (Dec. 23, 1953), pp. 1087–1092. DOI: [10.1063/1.1699114](https://doi.org/10.1063/1.1699114).
- [Mik87] MIKHEEV, S.P. AND SMIRNOV, A. YU.: ‘Resonance Oscillations of Neutrinos in Matter’. *Sov.Phys.Usp.* 30 (1987), pp. 759–790. DOI: [10.1070/PU1987v030n09ABEH002961](https://doi.org/10.1070/PU1987v030n09ABEH002961).
- [Moh07] R. N. MOHAPATRA et al.: ‘Theory of neutrinos: a white paper’. *Reports on Progress in Physics* 70.11 (2007), p. 1757.
- [Moh06] R. MOHAPATRA, S. NASRI, and H.-B. YU: ‘Grand unification of  $\mu$ - $\tau$  symmetry’. *Phys.Lett.* B636 (2006), pp. 114–118. DOI: [10.1016/j.physletb.2006.03.049](https://doi.org/10.1016/j.physletb.2006.03.049).
- [Nag06] S. NAGY, T. FRITIOFF, M. BJÖRKHAGE, I. BERGSTRÖM, and R. SCHUCH: ‘On the Q-value of the tritium  $\beta$ -decay’. *EPL (Europhysics Letters)* (May 1, 2006), pp. 404+. DOI: [10.1209/epl/i2005-10559-2](https://doi.org/10.1209/epl/i2005-10559-2).
- [Nak10] K. NAKAMURA et al.: ‘Review of particle physics’. *J.Phys.* G37 (2010), p. 075021. DOI: [10.1088/0954-3899/37/7A/075021](https://doi.org/10.1088/0954-3899/37/7A/075021).
- [Nea11] R. M. NEAL: *MCMC Using Hamiltonian Dynamics*. CRC Press, May 2011. DOI: [10.1201/b10905-6](https://doi.org/10.1201/b10905-6).

- [Nuc12] A. NUCCIOTTI: ‘Neutrino mass calorimetric searches in the MARE experiment’. *Nucl.Phys.Proc.Suppl.* 229-232 (2012), pp. 155–159. DOI: [10.1016/j.nuclphysbps.2012.09.025](https://doi.org/10.1016/j.nuclphysbps.2012.09.025).
- [Oer14] J. OERTLIN: ‘Analysis of Radon-Induced Background during First Measurements at the KATRIN Main Spectrometer’. Diploma thesis. KIT, 2014.
- [Oli07] T. E. OLIPHANT: ‘Python for Scientific Computing’. *Computing in Science & Engineering* 9.3 (2007), pp. 10–20.
- [Ora14] ORACLE CORPORATION: *MYSQL, a relational database management system*. 2014. URL: <http://www.mysql.com>.
- [Osi12] A. OSIPOWICZ, W. SELLER, J. LETNEV, P. MARTE, A. MULLER, et al.: ‘A mobile Magnetic Sensor Unit for the KATRIN Main Spectrometer’. *JINST* 7 (2012), T06002. DOI: [10.1088/1748-0221/7/06/T06002](https://doi.org/10.1088/1748-0221/7/06/T06002).
- [Ott08] E. OTTEN and C. WEINHEIMER: ‘Neutrino mass limit from tritium beta decay’. *Rept.Prog.Phys.* 71 (2008), p. 086201. DOI: [10.1088/0034-4885/71/8/086201](https://doi.org/10.1088/0034-4885/71/8/086201).
- [Par08] S. J. PARKE: ‘CP Violation in the Neutrino Sector’. (2008).
- [PHP14] PHP GROUP: *Hypertext Preprocessor*. 2014. URL: <http://www.php.net>.
- [Phy14] PHYSICS AND ASTRONOMY DEPARTMENT, UNIVERSITY OF NORTH CAROLINA AT CHAPEL HILL: *ORCA, Object-oriented Real-time Control and Acquisition*. 2014. URL: [http://orca.physics.unc.edu/~markhowe/Orca\\_Help/Home.html](http://orca.physics.unc.edu/~markhowe/Orca_Help/Home.html).
- [Pic92] A. PICARD et al.: ‘A solenoid retarding spectrometer with high resolution and transmission for keV electrons’. *Nuclear Instruments and Methods in Physics Research Section B: Beam Interactions with Materials and Atoms* 63.3 (Feb. 1992), pp. 345–358. DOI: [10.1016/0168-583x\(92\)95119-c](https://doi.org/10.1016/0168-583x(92)95119-c).
- [Pla83] R. L. PLACKETT: ‘Karl Pearson and the Chi-Squared Test’. *International Statistical Review / Revue Internationale de Statistique* 51.1 (1983), pp. 59–72. DOI: [10.2307/1402731](https://doi.org/10.2307/1402731).
- [Pon57] B. PONTECORVO: ‘Mesonium and anti-mesonium’. *Sov.Phys. JETP* 6 (1957), p. 429.
- [Pra11] M. PRALL: ‘The Katrin experiment and the pre-spectrometer at reduced retarding potential’. *Progress in Particle and Nuclear Physics* 66.2 (2011). Particle and Nuclear Astrophysics International Workshop on Nuclear Physics, 32nd Course, pp. 418–423. DOI: [10.1016/j.ppnp.2011.01.044](https://doi.org/10.1016/j.ppnp.2011.01.044).
- [Pre07] W. H. PRESS, S. A. TEUKOLSKY, W. T. VETTERLING, and B. P. FLANNERY: *Numerical Recipes 3rd Edition: The Art of Scientific Computing*. 3rd ed. Cambridge University Press, Sept. 10, 2007.
- [Rac37] G. RACAH: ‘Sulla Simmetria Tra Particelle e Antiparticelle’. Italian. *Il Nuovo Cimento* 14.7 (1937), pp. 322–328. DOI: [10.1007/BF02961321](https://doi.org/10.1007/BF02961321).
- [Rei60] F. REINES, C. L. COWAN, F. B. HARRISON, A. D. MCGUIRE, and H. W. KRUSE: ‘Detection of the Free Antineutrino’. *Phys. Rev.* 117 (1 Jan. 1960), pp. 159–173. DOI: [10.1103/PhysRev.117.159](https://doi.org/10.1103/PhysRev.117.159).

- [Rep83] W. REPKO and C.-E. WU: ‘Radiative corrections to the end point of the tritium  $\beta$  decay spectrum’. *Physical Review C* 28.6 (Dec. 1983), pp. 2433–2436. DOI: [10.1103/physrevc.28.2433](https://doi.org/10.1103/physrevc.28.2433).
- [Rob97] G. O. ROBERTS, A. GELMAN, and W. R. GILKS: ‘Weak convergence and optimal scaling of random walk Metropolis algorithms’. *The Annals of Applied Probability* 7.1 (Feb. 1997), pp. 110–120. DOI: [10.1214/aoap/1034625254](https://doi.org/10.1214/aoap/1034625254).
- [Rol05] W. A. ROLKE, A. M. LÓPEZ, and J. CONRAD: ‘Limits and confidence intervals in the presence of nuisance parameters’. *Nuclear Instruments and Methods in Physics Research Section A: Accelerators, Spectrometers, Detectors and Associated Equipment* 551.2–3 (2005), pp. 493–503. DOI: [10.1016/j.nima.2005.05.068](https://doi.org/10.1016/j.nima.2005.05.068).
- [Röl12] M. RÖLLIG: ‘Studien zu einem Röntgendetektorsystem zur Bestimmung der Aktivität in der KATRIN Tritiumquelle’. Diploma thesis. KIT, 2012.
- [Rov13] P. ROVEDO: ‘Muon induced secondary electrons at the KATRIN experiment - Detector installation and setup & data analysis’. Diploma thesis. KIT, 2013.
- [Sae00] A. SAENZ, S. JONSELL, and P. FROELICH: ‘Improved Molecular Final-State Distribution of  $\text{HeT}^+$  for the  $\beta$  Decay Process of  $\text{T}_2$ ’. *Physical Review Letters* 84.2 (Jan. 2000), pp. 242–245. DOI: [10.1103/physrevlett.84.242](https://doi.org/10.1103/physrevlett.84.242).
- [Sal68] A. SALAM: ‘Weak and Electromagnetic Interactions’. *Conf.Proc.* C680519 (1968), pp. 367–377.
- [Sch13a] S. SCHAMS: ‘Data Analysis Tools and Sterile Neutrino Investigations for the KATRIN Experiment’. Diploma thesis. KIT, 2013.
- [Sch80] J. SCHECHTER and J. W. F. VALLE: ‘Neutrino masses in  $\text{SU}(2) \times \text{U}(1)$  theories’. *Phys. Rev. D* 22 (9 Nov. 1980), pp. 2227–2235. DOI: [10.1103/PhysRevD.22.2227](https://doi.org/10.1103/PhysRevD.22.2227).
- [Sch13b] M. SCHLÖSSER: ‘Accurate calibration of the Raman system for the Karlsruhe Tritium Neutrino Experiment’. Doctoral thesis. KIT, 2013.
- [Sch14] J. SCHWARZ: ‘Implementation of the Main Detector System for the KATRIN Experiment’. Doctoral thesis. KIT, 2014.
- [Sco35] F. A. SCOTT: ‘Energy Spectrum of the Beta-Rays of Radium E’. *Phys. Rev.* 48 (5 Sept. 1935), pp. 391–395. DOI: [10.1103/PhysRev.48.391](https://doi.org/10.1103/PhysRev.48.391).
- [Sha09] F. SHARIPOV et al.: *Influence of temperature variations and acoustic waves on the column density. Calculations of the velocity distribution function*. KATRIN internal report. 2009.
- [Sha03] F. SHARIPOV: *Numerical calculations of tritium flow through the KATRIN beam line*. KATRIN internal report. 2003.
- [Sim81] J. SIMPSON: ‘Measurement of the beta energy spectrum of  $\text{H}_3$  to determine the antineutrino mass’. *Physical Review D* 23.3 (Feb. 1981), pp. 649–662. DOI: [10.1103/physrevd.23.649](https://doi.org/10.1103/physrevd.23.649).

- [Sis04] M. SISTI, C. ARNABOLDI, C. BROFFERIO, G. CERUTI, O. CREMONESI, et al.: ‘New limits from the Milano neutrino mass experiment with thermal microcalorimeters’. *Nucl.Instrum.Meth.* A520 (2004), pp. 125–131. DOI: [10.1016/j.nima.2003.11.273](https://doi.org/10.1016/j.nima.2003.11.273).
- [Sle13] M. SLEZÁK, S. BAUER, O. DRAGON, M. ERHARD, K. SCHLÖSSER, A. ŠPALEK, D. VÉDOS, and M. ZBOŘIL: ‘Electron line shape of the KATRIN monitor spectrometer’. *Journal of Instrumentation* 8.12 (2013), T12002. DOI: [10.1088/1748-0221/8/12/T12002](https://doi.org/10.1088/1748-0221/8/12/T12002).
- [Sle] M. SLEZÁK. Doctoral thesis, in preparation. Charles University in Prague, Faculty of Mathematics and Physics.
- [Sof14] SOFTWARE FREEDOM CONSERVANCY: *Git Distributed Revision Control*. 2014. URL: <http://git-scm.com>.
- [Tra14] TRAC OPEN SOURCE PROJECT: *trac, Integrated SCM and Project Management*. 2014. URL: <http://trac.edgewall.org>.
- [Tri03] A. TRIDGELL and M. POOL: *RSYNC: fast incremental file transfer*. 2003. URL: <http://samba.anu.edu.au/rsync>.
- [Ubi09] M. UBIETO-DÍAZ, D. RODRÍGUEZ, S. LUKIC, S. NAGY, S. STAHL, and K. BLAUM: ‘A broad-band FT-ICR Penning trap system for KATRIN’. *International Journal of Mass Spectrometry* 288.1–3 (2009), pp. 1–5. DOI: [10.1016/j.ijms.2009.07.003](https://doi.org/10.1016/j.ijms.2009.07.003).
- [Val10] K. VALERIUS: ‘The wire electrode system for the KATRIN main spectrometer’. *Prog.Part.Nucl.Phys.* 64 (2010), pp. 291–293. DOI: [10.1016/j.ppnp.2009.12.032](https://doi.org/10.1016/j.ppnp.2009.12.032).
- [Val11] K. VALERIUS, H. HEIN, H. BAUMEISTER, M. BECK, K. BOKELOH, et al.: ‘Prototype of an angular-selective photoelectron calibration source for the KATRIN experiment’. *JINST* 6 (2011), P01002. DOI: [10.1088/1748-0221/6/01/P01002](https://doi.org/10.1088/1748-0221/6/01/P01002).
- [Van08] R. A. VAN ENGELEN: ‘A framework for service-oriented computing with C and C++ Web service components’. *ACM Trans. Internet Technol.* 8.3 (2008), pp. 1–25. DOI: [10.1145/1361186.1361188](https://doi.org/10.1145/1361186.1361188).
- [Van02] R. A. VAN ENGELEN and K. A. GALLIVAN: ‘The gSOAP toolkit for Web services and peer-to-peer computing networks’. *Cluster Computing and the Grid 2nd IEEE/ACM International Symposium CCGRID2002* (2002), pp. 117–124.
- [Vöc] S. VÖCKING. Doctoral thesis, in preparation. University of Münster.
- [Vru09] J. A. VRUGT, C. J. F. ter BRAAK, C. G. H. DIKS, B. A. ROBINSON, J. M. HYMAN, and D. HIGDON: ‘Accelerating Markov chain Monte Carlo simulation by differential evolution with self-adaptive randomized subspace sampling’. *International Journal of Nonlinear Sciences and Numerical Simulation* 10.3 (2009), pp. 273–290.
- [Wan13] N. WANDKOWSKY: ‘Study of background and transmission properties of the KATRIN spectrometers’. Doctoral thesis. KIT, 2013.

- [Wei67] S. WEINBERG: ‘A Model of Leptons’. *Phys. Rev. Lett.* 19 (21 Nov. 1967), pp. 1264–1266. DOI: [10.1103/PhysRevLett.19.1264](https://doi.org/10.1103/PhysRevLett.19.1264).
- [Wei93] C. WEINHEIMER et al.: ‘Improved limit on the electron-antineutrino rest mass from tritium  $\beta$ -decay’. *Physics Letters B* 300.3 (1993), pp. 210–216. DOI: [10.1016/0370-2693\(93\)90355-L](https://doi.org/10.1016/0370-2693(93)90355-L).
- [Wie12] V. WIEDMANN: ‘Systematische Untersuchungen zur Hochspannungsstabilisierung am KATRIN Monitorspektrometer’. Diploma thesis. KIT, 2012.
- [Wik06] WIKIMEDIA COMMONS: *Standard Model of Elementary Particles*. 2006. URL: [http://commons.wikimedia.org/wiki/File:Standard\\_Model\\_of\\_Elementary\\_Particles.svg](http://commons.wikimedia.org/wiki/File:Standard_Model_of_Elementary_Particles.svg) (visited on 06/12/2014).
- [Wil88] J. F. WILKERSON, T. J. BOWLES, D. A. KNAPP, M. P. MALEY, R. G. H. ROBERTSON, and D. L. WARK: ‘Limit on mass from free molecular tritium beta decay’. *Nuclear Physics A* 478 (Feb. 1988), pp. 439–446. DOI: [10.1016/0375-9474\(88\)90878-0](https://doi.org/10.1016/0375-9474(88)90878-0).
- [Wil38] S. S. WILKS: ‘The Large-Sample Distribution of the Likelihood Ratio for Testing Composite Hypotheses’. English. *The Annals of Mathematical Statistics* 9.1 (1938), pages.
- [Wol09] J. WOLF: ‘Size Matters: The Vacuum System of the KATRIN Neutrino Experiment’. *Journal of the Vacuum Society of Japan* 52.5 (2009).
- [Wol12] J. WOLF: ‘The KATRIN Numbering Scheme’. KATRIN internal document. 2012.
- [Wol78] WOLFENSTEIN, L.: ‘Neutrino Oscillations in Matter’. *Phys.Rev.* D17 (1978), pp. 2369–2374. DOI: [10.1103/PhysRevD.17.2369](https://doi.org/10.1103/PhysRevD.17.2369).
- [Wu57] C. S. WU, E. AMBLER, R. W. HAYWARD, D. D. HOPPES, and R. P. HUDSON: ‘Experimental Test of Parity Conservation in Beta Decay’. *Phys. Rev.* 105 (4 Feb. 1957), pp. 1413–1415. DOI: [10.1103/PhysRev.105.1413](https://doi.org/10.1103/PhysRev.105.1413).
- [Wym14] M. WYMAN, D. H. RUDD, R. A. VANDERVELD, and W. HU: ‘Neutrinos help reconcile Planck with the Local Universe’. *Physical Review Letters* 112.5 (Jan. 2, 2014). DOI: [10.1103/physrevlett.112.051302](https://doi.org/10.1103/physrevlett.112.051302).
- [Neu14] *XXVI. International Conference on Neutrino Physics and Astrophysics*. Boston, USA, 2014.
- [Zec02] G. ZECH: ‘Frequentist and Bayesian confidence intervals’. English. *EPJ direct* 4.1 (2002), pp. 1–81. DOI: [10.1007/s1010502c0012](https://doi.org/10.1007/s1010502c0012).
- [Zie13] S. ZIEGLER: ‘Die Extraktion der Energieverlustfunktion beim KATRIN Experiment’. Diploma thesis. KIT, 2013.
- [Zub11] K. ZUBER: *Neutrino Physics, Second Edition*. Series in High Energy Physics, Cosmology and Gravitation. Taylor & Francis, 2011.

---

## List of Figures

---

1.1	Radium $\beta$ -decay energy spectrum . . . . .	1
1.2	Standard Model of Elementary Particles . . . . .	3
1.3	Neutrino flavor mixing and mass hierarchy . . . . .	8
1.4	KamLAND neutrino spectrum . . . . .	10
1.5	Cosmic neutrino energy density . . . . .	13
1.6	Neutrino less double beta decay spectrum . . . . .	15
1.7	Schematic of the tritium $\beta^-$ decay . . . . .	17
1.8	Feynman diagram of the neutron $\beta$ -decay . . . . .	17
1.9	Idealized differential $\beta$ spectrum . . . . .	18
1.10	Reactor antineutrino anomaly . . . . .	22
1.11	Sterile neutrino exclusion contours . . . . .	23
2.1	KATRIN official logo . . . . .	25
2.2	KATRIN experimental setup . . . . .	26
2.3	MAC-E filter working principle . . . . .	28
2.4	Main spectrometer wire system . . . . .	32
2.5	NEG pump and baffle CAD drawing . . . . .	32
2.6	Focal plane detector setup . . . . .	33
2.7	Focal plane detector silicon wafer . . . . .	33
2.8	Monitor spectrometer CAD drawing . . . . .	34
2.9	ORCA DAQ operation screenshot . . . . .	36
2.10	ADEI Slow Control web interface . . . . .	37
3.1	Multi-tier IT architecture . . . . .	41
3.2	KASPER configuration with CMake . . . . .	42
3.3	KASPER analysis and simulation software components . . . . .	44
3.4	Instrumentation and data producers . . . . .	47
3.5	ORCA run processing . . . . .	49
3.6	TTreeView, event data inspection with ROOT . . . . .	49
3.7	Slow Control cache tables . . . . .	52
3.8	KATRIN database layout . . . . .	53
3.9	KDBServer, service oriented architecture . . . . .	58
3.10	Remote procedure calls . . . . .	60

4.1	KDBServer web frontend - run list . . . . .	66
4.2	KDBServer web frontend - run details . . . . .	67
4.3	KDBServer web frontend - position table . . . . .	68
4.4	KDBServer web frontend - sensor editor . . . . .	68
4.5	KaLi XML communication and offline caching . . . . .	71
4.6	Energy calibration of the main detector . . . . .	77
4.7	Slow Control sensor monitoring . . . . .	78
4.8	Monitor spectrometer K-32 filter spectrum . . . . .	79
4.9	BEANS event rate analysis . . . . .	81
4.10	Kassiopeia particle tracking simulation . . . . .	82
4.11	Magnetic fieldline monitoring . . . . .	83
5.1	Comparison of differential $\beta$ spectra . . . . .	88
5.2	Final states, angular momenta . . . . .	89
5.3	Final states, ortho:para ratio . . . . .	90
5.4	Final states, rebinning algorithm . . . . .	92
5.5	Differential and integrated $\beta$ spectrum . . . . .	95
5.6	Transmission function . . . . .	96
5.7	Comparison of systematic effects on the integrated $\beta$ spectrum . . . . .	98
5.8	WGTS density profile . . . . .	99
5.9	Response and energy loss function . . . . .	102
5.10	From differential to integrated $\beta$ spectrum . . . . .	104
5.11	Differential spectra with sterile neutrino mixing . . . . .	106
5.12	Likelihood discontinuities . . . . .	107
5.13	Iterative numerical integration . . . . .	108
5.14	Source and detector segmentation . . . . .	109
5.15	Empirical radon background model . . . . .	112
5.16	Integrated spectrum and toy measurements . . . . .	114
6.1	KaFit components . . . . .	118
6.2	KATRIN four-parameter spectrum fit . . . . .	119
6.3	Exemplary $\beta$ -decay likelihood functions . . . . .	121
6.4	Ensemble testing, distribution of $m_\nu^2$ estimates . . . . .	124
6.5	Feldman and Cousins confidence belt . . . . .	128
6.6	Profile Likelihood . . . . .	130
6.7	Posterior probability density function . . . . .	131
6.8	Confidence Intervals . . . . .	133
6.9	MCMC random walk behavior . . . . .	135
6.10	MCMC convergence . . . . .	135
6.11	MCMC parameter sampling . . . . .	136
6.12	MCMC parameter correlations . . . . .	138
6.13	Autocorrelation functions . . . . .	140
6.14	Analysis of MCMC output using ROOT utilities . . . . .	141
6.15	Relative differences of $\beta$ spectra and measuring time . . . . .	144
6.16	Convergence during MTD optimization . . . . .	146

---

6.17	MTDs for 10 mcps background . . . . .	147
6.18	MTD for an extended energy interval . . . . .	150
6.19	MTD for 100 mcps background and sterile neutrino search . . . . .	152
6.20	MTDs for elevated background rates . . . . .	153
6.21	MTD for the first month of neutrino mass data-taking . . . . .	154
6.22	MCMC analysis of 1+1 sterile neutrino mixing . . . . .	157
6.23	Sterile neutrino sensitivity contours . . . . .	158
6.24	Ensemble method, HV fluctuations . . . . .	159
6.25	MCMC scatter plots, HV fluctuations . . . . .	161
7.1	Background rates from SDS-I commissioning . . . . .	164
7.2	Pixel-view of the main detector . . . . .	165
7.3	Sensitivities over accumulated measuring time . . . . .	168



---

## List of Tables

---

1.1 Neutrino oscillation parameters . . . . .	7
3.1 Source code metrics . . . . .	45
3.2 Active Slow Control readout channels . . . . .	51
5.1 WGTS scattering probabilities . . . . .	101
6.1 Systematic uncertainties . . . . .	123
6.2 Simulation parameters for ensemble tests . . . . .	125
6.3 Statistical uncertainties for 10 mcps background . . . . .	149
6.4 Statistical uncertainties for an extended energy interval . . . . .	150
6.5 Statistical uncertainties for sterile neutrino masses . . . . .	151
6.6 Statistical uncertainties after the first month of data-taking . . . . .	154
6.7 Statistical uncertainties, systematic as free parameter . . . . .	160
6.8 Statistical uncertainties, pull method . . . . .	162
7.1 Background rates from SDS-I commissioning . . . . .	166
7.2 Reevaluated sensitivities . . . . .	169



---

## Acronyms

---

ADEI	Advanced Data Extraction Infrastructure
AJAX	Asynchronous JavaScript and XML
API	Application Programming Interface
C.L.	confidence level
CMB	cosmic microwave background
DAQ	Detector Data Acquisition
DIME	Direct Internet Message Encapsulation
DREAM	Differential Evolution Adaptive Metropolis
FLT	first-level trigger
FPD	focal plane detector
FPGA	Field Programmable Gate Array
FSD	Final State Distribution
GPU	Graphics Processing Unit
HTTP	Hypertext Transfer Protocol
HV	high voltage
IPE	Institute for Data Processing and Electronics
KaLi	Katrin data access Library
KATRIN	Karlsruhe TRitium Neutrino
KIT	Karlsruhe Institute of Technology
LHC	Large Hadron Collider
LSDF	Large Scale Data Facility
MAC-E	Magnetic Adiabatic Collimation combined with an Electrostatic
MC	Monte Carlo

---

MCMC	Markov Chain Monte Carlo
MSW	Mikheyev-Smirnov-Wolfenstein
MTD	measuring time distribution
NEG	non-evaporable getter
ORCA	Object-oriented Real-time Control and Acquisition
ORM	Object-Relational Mapping
PCS7	Siemens SIMATIC Process Control System 7
PMNS	Pontecorvo-Maki-Nakagawa-Sakata
RAID	Redundant Array of Independent Disks
RPC	Remote Procedure Call
SCS	Slow Control System
SDS	Spectrometer and Detector Section
SLT	second-level trigger
SM	Standard Model of elementary particles
SOAP	Simple Object Access Protocol
SQL	Structured Query Language
SSC	Source and Spectrum Calculation
SSL	Secure Sockets Layer
SSM	standard solar model
STL	Standard Template Library
TDR	Technical Design Report
TMP	Turbo Molecular Pump
UHV	ultra high vacuum
WGTS	Windowless Gaseous Tritium Source
WSDL	Web Services Description Language
XML	Extensible Markup Language
ZEUS	Central Acquisition and Control

---

## Index

---

- accelerator neutrinos, 9
- acceptance rate, 136
- ADEI, 36
- adiabatic conversion, 27
- analyzing plane, 27
- argument binding, 175
- atmospheric mixing, 7
- atmospheric neutrinos, 8
- autocorrelation, 139
  
- background
  - cosmic, 163
  - measurements, 163
  - radon-induced, 163
  - rate, 120
- background models, 110
- baffles, 33
- Bayes' theorem, 130
- Bayesian statistics, 126, 129
- BEANS, 80
- best-fit estimate, 118
- beta decay kinematics, 16
- beta decay theory, 1
- bug-tracking, 46
- burn-in phase, 134
  
- calibration data, 54
- channel mapping, 55
- chi-square, 121
- client-server architecture, 39
- code injection, 177
- code standards, 41
- commissioning milestones, 37
  
- conclusion, 174
- confidence
  - belt, 127
  - interval, 126
  - level, 127
- constrained fit parameter, 161
- correlated systematics, 159
- cosmic microwave background, 110
- cosmic neutrino background, 12
- cosmology, 12
- credibility interval, 131
- cryogenic pumping, 30
  
- DAQ mode, 48
- data acquisition, 35
- data sources, 46
- data tier, 46
- database
  - administration, 66
  - search requests, 73
- delayed rejection, 142
- density profile, 98
- detailed balance, 134
- detector
  - analysis, 80
  - energy calibration, 77
  - section, 33
- detector segmentation, 109, 167
- differential beta spectrum, 86
- differential pumping, 30
- Dirac particle, 5
- discovery, 2
- Doppler effect, 93

- doxygen, 42, 76
- elastic scattering, 103
- electron gun measurements, 102
- energy loss, 101
- energy resolution, 96
- ensemble testing, 124, 159
- estimator, 120
- event data analysis, 73
- event rates, 55
  
- Feldman and Cousins, 127
- Fermi function, 87
- Fermi's golden rule, 16
- Fermi, Enrico, 1
- fieldline monitoring, 83
- file repository, 62
- final states
  - distribution, 88
  - rebinning, 91
- flavor eigenstates, 4
- floating-point accuracy, 107
- focal plane detector, 33
- FPGA, 35
- Frequentist statistics, 126
  
- gas dynamics, 99
- Git repository, 45
- Glashow-Weinberg-Salam model, 2
- gSOAP, 59, 179
  
- hamiltonian MCMC, 141
- Higgs mechanism, 2
- high voltage fluctuations, 97
- history, 1
- holmium, 19
  
- incoherent sum, 17
- inelastic scattering, 101
- integrated beta spectrum, 94
- integrating high-pass filter, 28
- introduction, i
- IT infrastructre, 39
- iterative integration, 108
  
- KaFit, 86, 117
  
- Kahan summing, 107
- KaLi, 69
- KARMEN, 21
- KASPER, 42
- Kassiopeia, 82
- KATRIN
  - experimental setup, 25
  - principle, 26
- KATRIN numbering, 47
- KDBServer, 44, 57
- KLCalibration, 75
- KLDatabaseFilter, 73
- KLDataManager, 71
- KLRun, 73
- KLSlowControl, 74
  
- LARA, 30, 56
- likelihood
  - function, 120
  - principle, 131
- log group, 50
- log likelihood, 120
- logic tier, 57
- LSND, 21
  
- MAC-E filter, 27
- magnetic mirror effect, 29
- main spectrometer, 31
- Majorana particle, 5
- Markov Chain Monte Carlo, 134, 145
- mass eigenstates, 4
- massive neutrinos, 10
- measurement simulation, 113
- measuring time distribution, 113, 143, 166
- Metropolis-Hastings algorithm, 134
- middle tier, 57
- MiniBooNE, 21
- MobSU, 55
- monitor spectrometer, 34
  - analysis, 79
- MSW effect, 6
- multi-tier architecture, 39
  
- near-time analysis, 65
- NEG pump, 31, 111

- negative squared neutrino mass, 93, 122
- neutrino mass, 10
  - confidence intervals, 132
  - limits, 20
  - squared, 120
- neutrino oscillation, 4
- neutrino-less double beta decay, 14
- Neyman construction, 127
- nuclear recoil, 87
- nuisance parameter, 120, 128
- null hypothesis, 119
- numerical integration, 103
- numerical stability, 107
  
- object-relational mapping, 58, 59, 175
- offline caching, 72
- ORCA, 35, 48
- ortho-para ratio, 89
- oscillation, 4
  - length, 6
  - parameters, 7
  - probability, 5
- outline, iii
- outlook, 174
  
- parallel tempering, 138
- parameter inference, 118
- particle tracking, 82
- Pauli, Wolfgang, 1
- PMNS matrix, 5, 17
- Poisson likelihood, 122
- Poltergeist experiments, 2
- positioning data, 55
- posterior probability, 129
- postulation, 1
- pre-spectrometer, 31
- probabilistic model, 120
- profile likelihood, 128, 145
- proposal function, 136, 137, 145
- pull method, 161
  
- radial event rate dependency, 167
- radiative corrections, 87
- radon-induced background, 111
- Raman, 56
- reactor antineutrino anomaly, 21, 156
- reactor neutrinos, 9
- rear section, 34
- remote procedure call, 60, 70
- replication, 63
- response function, 99
- retarding potential, 27, 31
- rhenium, 19
- Romberg integration, 108
- ROOT, 42
- rovibronic excitations, 88
- RPC, 179
- run
  - browser, 65
  - data, 48
  - index, 55
  - processing, 48
  
- scattering probability, 100
- SDS commissioning phase, 37
- seesaw mechanism, 11
- self adaptive MCMC, 142
- sensitivity, 119, 163, 169
- sensor catalog, 54
- service oriented architecture, 60
- signal amplitude, 120
- Simpson integration, 108
- single beta decay, 16
- Slow Control
  - analysis, 74
  - database, 50
  - monitoring, 78
  - processing, 61
  - system, 35
- SOAP, 59, 179
  - xml envelope, 179
- solar mixing, 7
- solar neutrino problem, 4
- solar neutrinos, 8
- source simulation, 98
- source-detector mapping, 109
- spectrometer, 27
- spectrum calculation, 85
- spin degeneracy, 89
- SQL database, 52
- SSC, 85

- Standard Model, 2
- statistical methods, 117
- step width adaption, 137
- sterile neutrinos, 21, 105, 155
  - sensitivity contours, 156
- STL iterators, 70
- structure formation, 13
- summary, 171
- supernova neutrinos, 9
- surrogate key, 54
- synchrotron radiation, 103
- systematic uncertainties, 123
  
- target distribution, 134
- temperature profile, 98
- trac, 46
- transaction safety, 59
- transmission function, 95
  
- transport section, 30
- tritium, 19
- tritium endpoint, 120, 148
- tritium source section, 29
  
- unified approach, 127
  
- version control, 52
  
- web interface, 65
- web service, 57, 59
- WGTS, 29, 98
- wire electrodes, 31
- Wt, 58
  
- XML messaging, 179
  
- Zlib compression, 61

---

## Acknowledgments

---

I thankfully acknowledge, that I was given the opportunity of joining the KATRIN collaboration in a determining development phase of the experiment, and to work in an enriching and vivid scientific environment. I would like to express my gratitude to everyone, who made this thesis possible and provided me with friendly and professional support. In particular I would like to thank

- Prof. Guido Drexlin for his enthusiastic mentoring, continued support and confidence in my work,
- Prof. Michael Feindt for the evaluation of this thesis as second reviewer,
- Dr. Joachim Wolf for his supervision and his great effort in proofreading this document,
- the Studienstiftung des Deutschen Volkes for granting my PhD scholarship,
- Dr. Alan Poon for inviting me to visit Lawrence Berkeley National Laboratory (LBNL) and guiding me in statistical methods and analysis techniques,
- the Karlsruhe House of Young Scientists (KHYS) for financially supporting my stay abroad for its duration of five months,
- Dr. Markus Hötzel and Sebastian Schams for the fruitful and enjoyable teamwork, especially during our memorable time at LBNL,
- Dr. Joe Formaggio for inviting me to the Massachusetts Institute of Technology (MIT) and encouraging me in pursuing Bayesian statistics,
- Stefan Groh, my office coworker, for his reliable support and friendship, for proofreading this thesis, and for regularly updating my office name tag,
- Dr. Sanshiro Enomoto for his inspiring and substantial input to large parts of the data processing framework,
- Martin Slezák for his untiring efforts in beta testing data access and analysis in KaLi 2.0,

- Sebastian Vöcking for his patient C++ advice and essential contributions to KDBServer and KaLi 1.0,
- our young US colleagues Daniel Furse, T.J. Corona, John Barrett and Dr. Diana Parno for the fruitful cooperation and the most rewarding collaboration meetings,
- Moritz Erhard, Marcel Kraus and Nikolaus Trost for ensuring the essential coffee supply, and Jan Örtlin for introducing a sweets stock,
- Johannes Schwarz for enduring my persistent questions and complaining in our temporary shared office while writing our theses,
- our dynamic scientific group for the encouraging teamwork, professional advice and also a very enjoyable time, including all colleagues of the Institute of Experimental Nuclear Physics (IEKP), the Karlsruhe Tritium Laboratory (TLK) and the University of Münster.

Finally, I would like to express my deepest gratitude to my family and my wonderful wife Anja for their patience, continuous encouragement and nourishing dinners on long days.

